

VNIVERSITAT DE VALÈNCIA

Facultat de Física

Departament d'Òptica i Optometria i Ciències de la Visió



---

Design of anisotropic nanostructures  
for light control

---

**Ph.D. Thesis**

*Programa de Doctorat en Física*

*Author:*

**Carlos Díaz Aviñó**

*Supervisors:*

**Carlos J. Zapata Rodríguez**

**Mahin Naserpour**

Valencia, July 2018



**UNIVERSITAT DE VALÈNCIA**  
**FACULTAT DE FÍSICA**

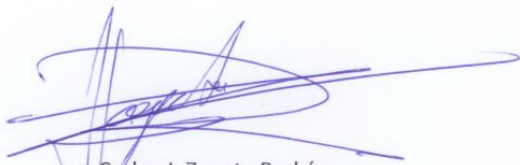
**DEPARTAMENT D'ÒPTICA I OPTOMETRIA**  
**I CIÈNCIES DE LA VISIÓ**

**D. Carlos J. Zapata Rodríguez**, Profesor Titular del Departament d'Òptica i Optometria i Ciències de la Visió de la Universitat de València, y **Dña. Mahin Naserpour**, doctora por la Universidad de Shiraz (Irán)

**INFORMAN:**

Que la presente memoria, titulada **Design of anisotropic nanostructures for light control**, ha sido elaborada por **D. Carlos Díaz Aviñó** bajo su dirección en la Facultat de Física de la Universitat de València, y constituye su Tesis para optar al grado de Doctor en Física con mención internacional.

Y, para que así conste, firman el presente certificado:



Carlos J. Zapata Rodríguez



Mahin Naserpour

Valencia, 28 de Mayo de 2018



*Dedicada a mis padres Amparo y Rubén,  
a mi hermano Luis y a mi mujer Beatriz  
por su apoyo incondicional  
y su inconmensurable motivación.*



# Acknowledgements

I want to thank my supervisors Prof. Carlos J. Zapata Rodríguez and Mahin Naserpour for accepting me as their student. Also, it is worth to mention their dedication to make possible the elaboration of this Ph.D. Thesis. Their guidance, support and patience is highly appreciated, particularly in helping me with the realization of this work.

Special mention to the UMDO group at the Institute of Materials Science ICMUV and their members Prof. Juan P. Martínez Pastor and Dr. Isaac Suárez Álvarez for letting me to learn and develop experience in laboratory research. And my sincere thanks to Dr. Alejandro Molina Sánchez and the Physics and Materials Science Research Unit in the University of Luxembourg to allow me to stay with them and acquire very great knowledge about material properties and material computational research.

## IV

The experience lived along these years has been very stimulating and grateful.

Finally, I want to give a great acknowledge to my family and friends for their support no matter where and when. Without you this would have been impossible.



# Resumen

El rápido avance en métodos de micro- y nanofabricación, tanto teórica como experimentalmente, han hecho posible a día de hoy que podamos controlar el flujo de luz con una precisión sin precedentes. Los metamateriales y las metasuperficies son nanoestructuras compuestas a partir de celdas unidad diseñadas, de forma que permitan manipular la luz con una respuesta estipulada. Como resultado de esto, los metamateriales han proporcionado un gran número de posibles aplicaciones nuevas que antes eran inconcebibles. En esta Tesis Doctoral nos hemos centrado en el uso de estos metamateriales excepcionales para conseguir, específicamente, partículas indetectables y también para controlar el modelado de haces de luz.

El objetivo principal de esta Tesis es proponer nuevas estructuras fotónicas basadas en metamateriales multicapa metal-dieléctricos que, gracias a su alta anisotropía de forma, son capaces de generar distribu-

## VI

ciones de luz altamente localizadas, así como respuestas ópticamente inertes en el campo lejano. Hemos analizado el mecanismo para conseguir la cancelación de la dispersión en nanopartículas con simetría cilíndrica. Es posible ajustar con gran precisión la cancelación de la dispersión a diferentes longitudes de onda para conseguir invisibilidad si tenemos un control preciso tanto de la morfología como de la combinación apropiada de los materiales. Por otro lado, teniendo un diseño adecuado de metarrecubrimientos de tamaño alrededor del nanómetro, podemos conseguir una fuerte focalización de ondas electromagnéticas con gran apertura numérica. Además, dado un campo convergente estos metarrecubrimientos pueden aumentar de forma significativa la apertura numérica. Es más, usando las metasuperficies diseñadas se puede moldear el haz para transformar ondas convergentes de gran angular en haces acelerados que prevean su forma.

El trabajo que hemos llevado a cabo no se limita exclusivamente a desarrollos basados en fundamentos teóricos y simulaciones numéricas, sino que también nos involucramos en tareas experimentales. Siguiendo esta dirección, estudiamos las ondas de superficie de Dyakonov (DSWs), que se pueden encontrar en la interfase entre un medio birrefringente y otro isótropo. La excitación ocurre en el campo cercano bajo fotoluminiscencia, y la prueba de la existencia de las DSWs se

basa en la determinación experimental de su constante de propagación compleja, cuya parte imaginaria es significativamente menor que la encontrada tanto en modos guiados como en *leaky modes*.



# Abstract

The rapid theoretical and experimental advances in micro- and nanofabrication methods has currently made possible the governing of light flow with unprecedented control. Metamaterials and metasurfaces are engineered nanostructures composed by designed building blocks with the ability to manipulate light under a prescribed response. As a result, metamaterials provide a high number of novel potential applications which were previously inconceivable. This Ph.D. Thesis explores on some uses of these exceptional metamaterials, specifically to achieve optical undetectability and controlled beamshaping.

The main objective of this Thesis is the proposal of new photonic structures based on metal-dielectric multilayered metamaterials, which due to their high form anisotropy are capable of generating highly localized light distributions, as well as optically inert responses in the far field. The mechanism of scattering cancellation is thoroughly an-

alyzed in nanoparticles of cylindrical symmetry. With an accurate control of a multilayered morphology and a proper combination of materials, it is possible to fine-tune the scattering cancellation at different wavelengths to achieve invisibility. Secondly, an adequate design of a nonplanar metacoating in the nanoscale gives us the ability of achieving tight focusing of high numerical-aperture electromagnetic waves. Moreover, the use of the engineered metasurfaces may execute a beam shaping to transform wide-angle converging waves into shape-preserving accelerating beams.

The work developed here is not limited exclusively to developments based on theoretical foundations and numerical simulations, but also an attempt to immerse into the experimental labor. In this direction we studied the Dyakonov surface waves (DSWs), which can be found at the interface between a birefringent medium and another isotropic medium. The excitation occurs in the near field under photoluminescence, and the evidence of the existence of the DSWs is based on the experimental determination of its complex propagation constant, whose imaginary part is significantly smaller compared to that found in the guided and leaky modes in the surrounding media.

# Contents

<b>Resumen</b>	<b>V</b>
<b>Abstract</b>	<b>IX</b>
<b>Contents</b>	<b>XI</b>
<b>1 Introducción (Español)</b>	<b>1</b>
1.1 Metamateriales . . . . .	2
1.2 Estructuras para camuflaje . . . . .	8
1.3 Cancelación de la dispersión . . . . .	10
1.4 Metalentes y metasuperficies . . . . .	15
1.5 Ondas superficiales en medios anisótropos . . . . .	19
1.6 Objetivos de la Tesis . . . . .	21
1.7 Publicaciones de la Tesis . . . . .	26

<b>2</b>	<b>Introduction (English)</b>	<b>33</b>
2.1	Metamaterials . . . . .	34
2.2	Cloaking structures . . . . .	39
2.3	Scattering cancellation . . . . .	41
2.4	Metalenses and metasurfaces . . . . .	45
2.5	Optical surface waves in anisotropic substrates . . . . .	49
2.6	Thesis objectives . . . . .	51
2.7	Publications of the Thesis . . . . .	55
<b>3</b>	<b>Methodology</b>	<b>61</b>
3.1	Mie theory . . . . .	62
3.1.1	Particles with multilayered coating . . . . .	63
3.2	The effective medium approach . . . . .	68
3.2.1	Hyperbolic media . . . . .	71
3.3	Anisotropic waveguides . . . . .	73
3.3.1	Dispersion equation of DSWs . . . . .	74
3.3.2	A thin dielectric waveguide on an anisotropic substrate . . . . .	78
3.4	Finite Element Method (FEM) . . . . .	79
3.4.1	Commercial software based on FEM . . . . .	82
<b>4</b>	<b>Results and analysis</b>	<b>85</b>



4.1	Anisotropic particles . . . . .	86
4.1.1	Invisibility in hyperbolic nanotubes . . . . .	87
4.1.2	Non-homogenized cylindrical nanoparticles . . . . .	98
4.1.3	Optimized nanostructure . . . . .	106
4.2	Anisotropic metasurfaces . . . . .	119
4.2.1	Ultrathin high-index metasurfaces for shaping focused beams . . . . .	119
4.2.2	Beamshaping under high numerical aperture . . . . .	123
4.2.3	Accelerating converging waves in the near field . . . . .	128
4.3	Anisotropic waveguides . . . . .	134
4.3.1	Fabrication techniques . . . . .	135
4.3.1.1	Deposition process . . . . .	135
4.3.1.2	Doctor blade and baking process . . . . .	136
4.3.1.3	Sample characterization . . . . .	138
4.3.1.4	Spin-coating . . . . .	142
4.3.2	Experimental results . . . . .	144
4.3.3	Theoretical results . . . . .	151
<b>5</b>	<b>Conclusions</b>	<b>157</b>
	<b>Bibliography</b>	<b>165</b>
	<b>Publications annex</b>	<b>193</b>



# Capítulo 1

## Introducción (Español)

El control del flujo luminoso es actualmente posible con un dominio sin precedentes gracias al progreso de diferentes métodos de micro- y nanofabricación [1]. Los metamateriales y las metasuperficies son nanoestructuras diseñadas formadas por elementos básicos concebidos, también llamados meta-átomos, con la habilidad de manipular la luz con una respuesta prescrita. Como resultado, los metamateriales dejan la puerta abierta a un número notable de aplicaciones potenciales que tradicionalmente eran inimaginables. Gracias a ello, no estamos necesariamente limitados por la respuesta electromagnética de los materiales encontrados en la naturaleza y sus componentes químicos. Como alternativa, podemos modificar el tamaño y la forma de las unidades

básicas del metamaterial, ajustar la composición y la morfología de la estructura óptica, y obtener nuevas funcionalidades. Las propiedades excepcionales de los metamateriales y dispositivos fotónicos basados en la óptica de transformación, que fueron concebidos gracias a los metamateriales, permiten tener un índice de refracción negativo, obtener imágenes con una resolución por debajo de la longitud de onda, diseñar concentradores de luz efectivos, e idear camuflajes ópticos. En esta Tesis avanzamos en esta dirección y proponemos nuevas estructuras fotónicas las cuales, debido a su morfología anisótropa, son capaces de generar distribuciones de luz altamente localizadas, así como respuestas ópticamente inertes en el campo lejano.

## 1.1 Metamateriales

Una de las capacidades humanas más provechosas para nosotros es la habilidad de ver, hecho que está presente en nuestra vida diaria y el cual involucra la propagación de las ondas electromagnéticas. Las ondas se propagan, y también interactúan con los materiales. Se pueden observar efectos muy interesantes de la interacción luz-materia, como colores iridiscentes en los cuerpos de algunos escarabajos y conchas marinas, o distribuciones de color fantásticas en las alas de una mari-

posa [2, 3]. Estos fenómenos ocurren debido a la interacción de la luz con las distribuciones estructurales periódicas que forman los cuerpos. Es posible reproducir este tipo de estructuras periódicas en un laboratorio mediante materiales dieléctricos y plasmónicos. La plasmónica tiene gran importancia y está siendo aplicada actualmente en nanotecnología [4]. Ciertos fenómenos únicos como confinamiento por debajo de la longitud de onda [5], amplificación de las ondas evanescentes [6], transmisión extraordinaria [7], dispersión hiperbólica en compuestos metálicos complejos [8], y resonancias en nanopartículas y meta-átomos [9] han causado un impacto tremendo. Este tipo de estructuras conduce a numerosos dispositivos y aplicaciones en fotónica como superlentes [10], nanoantenas [11], guías con tamaños por debajo de la longitud de onda [12], estructuras de camuflaje/invisibilidad [13], sensores optimizados para la detección de agentes químicos y biológicos [14], y metamoléculas quirales [15] que trabajan en el infrarrojo cercano y el rango óptico, grabados de color con resoluciones hasta el límite de difracción [16], metasuperficies perforadas [17] o antenas ópticas con forma de V [18] para la modificación del frente de ondas mediante nanoestructuras resonadoras [19], y confinamiento de luz en celdas solares de capa fina [20]. Todos estos dispositivos y aplicaciones están basados en la habilidad de controlar y manipular la propagación

del campo electromagnético.

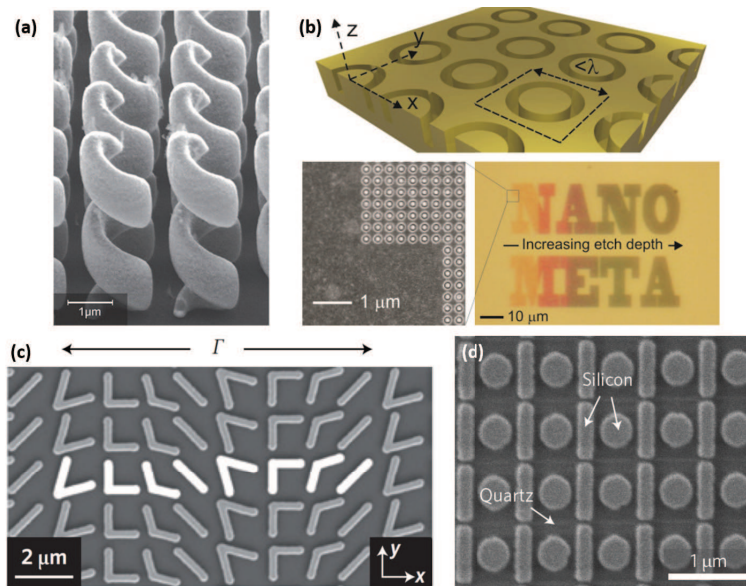


Figura 1.1: (a) Metamaterial quiral fabricados por inscripción láser directa [15]. (b) Matriz de calcografía genérica de metamaterial de metamoléculas de anillos simples con tamaños por debajo de la longitud de onda inscritos en una superficie metálica para generar color metálico estructural [21]. (c) Imagen obtenida por microscopía de barrido con electrones de una metasuperficie que consiste en una matriz de antenas ópticas de oro con forma de V fabricadas sobre una oblea de silicio, donde  $\Gamma = 11\mu\text{m}$  [22] (d) Metasuperficie de silicio que presenta una resonancia Fano, donde se muestra un fuerte aumento en la generación del tercer armónico [23].

Una de nuestras metas es controlar la desviación de la luz. Podemos ver este efecto si cogemos un vaso de agua y ponemos un bolígrafo en él. Utilizando los materiales apropiados, aquellos con la permitividad eléctrica ( $\epsilon$ ) y permeabilidad magnética ( $\mu$ ) adecuadas para el caso

que queremos estudiar, podemos controlar la propagación de las ondas de luz. Con este propósito, normalmente no encontramos materiales naturales disponibles con los valores deseados de  $\varepsilon$  y  $\mu$ . En estos casos tenemos que diseñar materiales artificiales que nos permitan controlar la propagación de la luz. Los materiales se combinan en una estructura más pequeña que la longitud de onda utilizada para conseguir los parámetros electromagnéticos necesarios con el fin de manipular las ondas. La combinación de estos materiales da estructuras llamadas “metamateriales”.

Los metamateriales se pueden comportar como materiales hiperbólicos, que presentan una relación de dispersión que soporta frecuencias espaciales muy altas. Los materiales hiperbólicos presentan una anisotropía óptica poco común [24], una característica crítica para conseguir, por ejemplo, una imagen superresolvente [25–28] y un volumen focal mucho más pequeño que  $\lambda^3$  [28, 29]. Este tipo de metamateriales serán de provecho para nosotros con el objetivo de alcanzar un efecto de invisibilidad.

La producción de metamateriales en el visible e infrarrojo necesita de una miniaturización extrema que impone restricciones severas en los procesos de fabricación, permitiendo el ensamblaje de geometrías elementales. Posiblemente, la geometría más simple es la nanoestructura

multicapa metal-dieléctrico, que ha sido analizada teóricamente [30] y fabricada [31] copiosamente. En el análisis teórico de nanomateriales estratificados con tamaños por debajo de la longitud de onda, se emplea generalmente una aproximación de medio efectivo (EMA, del inglés *Effective Medium Approximation*) [32, 33] y dicha aproximación es explotada para el diseño de dispositivos plasmónicos [34, 35]. Sin embargo, esta aproximación se ha demostrado que falla cuando se emplea con ondas polarizadas con campos magnéticos transversales (TM) [36–38], es decir, cuando el campo magnético es perpendicular a la dirección de la periodicidad de la nanoestructura metal-dieléctrico (MD). En este caso, aparecen efectos no locales bajo la condición de que la anchura de las capas metálicas se reduce e incluso sobrepasa la profundidad de penetración del metal [39]. Considerando que la tecnología actual ha dado un salto en la fabricación de nanoestructuras multicapa con capas metálicas uniformes y espaciados inferiores a 10 nm [40, 41] y que la profundidad de penetración para un metal como la plata (oro) está alrededor de los 24 nm (31 nm) a  $\lambda = 600$  nm, podemos concluir que los efectos no locales tienen lugar generalmente en disposiciones plasmónicas realistas.

Uno de los efectos más destacados motivado por la no-localidad de la respuesta óptica es la existencia de un modo extraordinario adicional



en la polarización TM [42–45]. Bajo ciertas condiciones, un haz puede dividirse en dos paquetes de ondas en una interfase aire/metamaterial, de forma que uno de ellos sufra refracción positiva y el otro haz se refracte con ángulos negativos. Junto con la refracción simple exhibida por ondas incidentes con polarización transversal eléctrica (TE), los materiales multicapa metalodieléctricos pueden manifestar trirrefringencia. En otras palabras, se necesitan tres índices de refracción para tipificar dicho comportamiento exótico. Conviene destacar que los cristales fotónicos adecuados también muestran propiedades multirrefringentes, aunque los detalles estructurales del medio (constantes de red) sean en la escala del rango de longitudes de onda ópticas [46].

En todos estos estudios previos llevados a cabo en metamateriales MD trirrefringentes se ha especificado una descripción detallada de la dirección de propagación de haces multirrefractados. No obstante, la distribución de flujo energético que corresponde a cada haz refractado no está clara, especialmente en la polarización TM. Una evaluación precisa de la transmisividad y reflectividad puede proporcionar un conocimiento más profundo derivado de los efectos no-locales del metamaterial.

## 1.2 Estructuras para camuflaje

Desde un punto de vista diferente, conviene señalar que un índice de refracción inhomogéneo puede proporcionarnos cierto control sobre el camino óptico de haces luminosos, como ocurre por ejemplo en lentes de gradiente de índice [47]. Para manipular este índice de refracción necesitamos diseñar metamateriales con una permitividad y permeabilidad requeridas, las cuales también pueden ser anisótropas. Para un material anisótropo, la respuesta de la luz depende de su polarización [48]. En particular, el camuflaje óptico se consigue manipulando la propagación de la luz, y llegó a ser muy popular entre los miembros de la comunidad científica después de la publicación de sendos artículos [49, 50]. En ellos se propusieron diversos métodos para el diseño de dispositivos para camuflaje basados en el método de transformación óptica (TOM, del inglés *Transformation Optics Method*). Este tipo de dispositivos permiten que la luz incidente se desvíe bordeando la estructura a aislar ópticamente, y así mantener las mismas características de propagación como si no hubiera nada en el volumen objetivo [51]. Uno puede introducir cualquier objeto para ocultarlo dentro de esa estructura, de forma que la luz viaja alrededor de ella y ningún observador fuera del dispositivo ve perturbación alguna del campo luminoso. El desarrollo de estas ideas en forma de tapices de

camuflaje, así como camuflajes tipo piel, se han demostrado recientemente de forma experimental (ver fig. 1.2).

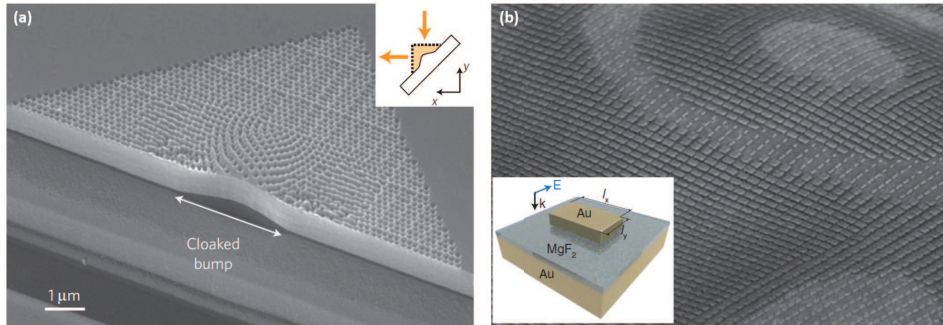


Figura 1.2: (a) Imagen de microscopía de barrido por electrones de un tapiz de camuflaje fabricado. Diseño de tapiz de camuflaje que transforma un espejo con un bache en un espejo virtualmente plano [52]. (b) Una metasuperficie de camuflaje tipo piel para un objeto 3D con forma arbitraria. Recuadro interior: Ilustración 3D de una nanoantena utilizada para la construcción de la metasuperficie [53].

Teniendo en cuenta el TOM en su concepto original, la estructura considerada posee comúnmente una anisotropía considerablemente alta. Los parámetros del material tomarán valores extremos en algunas regiones del camuflaje, cosa que hace imposible la selección de materiales naturales para este propósito [54]. Además, la permitividad y permeabilidad deben ser similares en las regiones exteriores de la estructura para satisfacer la condición de correspondencia en impedancia. Afortunadamente, usando metamateriales es posible ajustar la anisotropía tanto de la permeabilidad como de la permitividad del

material [55]. Ésta es la relación del camuflaje con los metamateriales: la estructura para conseguir un camuflaje perfecto está formada por metamateriales. Los primeros metamateriales utilizados para demostrar el camuflaje fueron resonadores con forma de anillo incompleto [51], y son probablemente las estructuras más utilizadas para este propósito [56–58]. El enorme progreso realizado en el desarrollo de nuevas estructuras para camuflaje ha transformado completamente el escenario actual. Los avances en ciencia e industria hacen posible el estudio y la fabricación de nuevos y más pequeños camuflajes y sensores invisibles, todos ellos realizados con metamateriales [59–61]. Con estos novedosos dispositivos y técnicas, el camuflaje para invisibilidad está atrayendo la atención de investigadores en todo el mundo.

### 1.3 Cancelación de la dispersión

Aunque el camuflaje perfecto es un método sumamente estudiado para suprimir completamente la visibilidad de un objeto, contamos con vías suplementarias para, al menos, minimizar su percepción electromagnética. Un método alternativo especialmente adaptado para partículas pequeñas y acuñado como cancelación de la dispersión conduce a la invisibilidad mediante la reducción al mínimo de la sec-

ción eficaz de dispersión para una estructura que puede estar parcialmente compuesta por metamateriales [62]. La idea básica consiste en hacer una partícula indetectable cubriéndola con revestimientos o metasuperficies ultrafinas, de forma que la dispersión del dispositivo sea mucho más reducida que si no llevara la cubierta nanoestructurada [63–66]. Se propusieron estructuras como nanohilos de silicio cubiertos de oro [67] para reducir la dispersión de la luz en detectores e incrementar la señal óptica al mismo tiempo, como se ilustra en la fig. 1.3. Más recientemente, también se han propuesto camuflajes con superficies de grosor atómico utilizando grafeno para frecuencias de THz [68, 69].

La disminución de la dispersión en metarrecubrimientos se puede atribuir a diferentes aspectos de la interacción luz-materia. De hecho, la polarizabilidad local de distintos componentes de un objeto de tamaño moderado y signo opuesto puede ser cancelada en una configuración diseñada apropiadamente [63, 71–77]. Como ejemplo, consideremos un nanohilo, con núcleo y cubierta, de permitividad interna (externa)  $\varepsilon_1$  ( $\varepsilon_2$ ) y radio de curvatura  $r_1$  ( $r_2$ ) embebido en una región de permitividad  $\varepsilon_3$ , el cual exhibe una polarizabilidad [78]

$$\alpha = 4\pi\varepsilon_0 \frac{[(\varepsilon_1 - \varepsilon_2)(\varepsilon_2 + \varepsilon_3)r_1^2 + (\varepsilon_1 + \varepsilon_2)(\varepsilon_2 - \varepsilon_3)r_2^2]}{(\varepsilon_1 - \varepsilon_2)(\varepsilon_2 - \varepsilon_3)r_1^2 + (\varepsilon_1 + \varepsilon_2)(\varepsilon_2 + \varepsilon_3)r_2^2}, \quad (1.1)$$

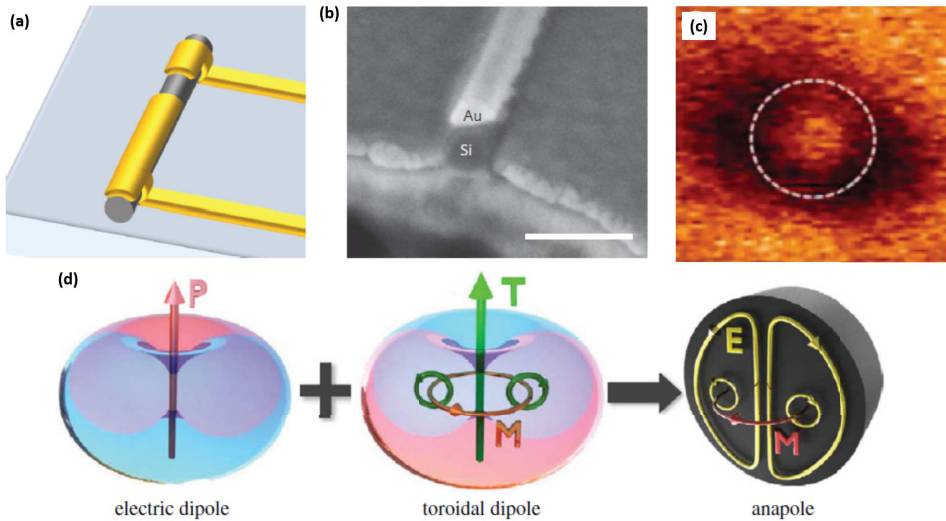


Figura 1.3: (a) Esquema de un fotodetector de nanohilos de oro/silicio. (b) Imagen SEM de un nanohilo de silicio con un diámetro de 50 nm con *recubrimiento* de oro de 20 nm de espesor. Barra de escala, 100 nm [67]. (c) Distribución de campo cercano para los modos anapolares excitados en un nanodisco de silicio bajo incidencia plana [70]. (d) La interferencia destructiva de un dipolo eléctrico (izquierda) y un dipolo toroidal (derecha) llevan a la formación de un modo anapolar no radiativo.

donde  $\varepsilon_0$  es la permitividad en el vacío. Por lo tanto, la polarizabilidad puede extinguirse teóricamente para una combinación específica de los parámetros del recubrimiento  $r_2$  y  $\varepsilon_2$ . El vector de polarización en cada uno de los materiales elementales es antiparalelo con respecto al resto, lo que implica que se induce un momento dipolar de fase opuesta. Tenemos un interés especial en la inclusión de recubrimientos con epsilon cercano a cero en el rango espectral deseado. Esta inclu-

sión puede conllevar una reducción significativa del espectro de dispersión de la estructura y también crear un efecto pantalla en el espacio colindante [79]. Centrándonos en dispersores con simetría cilíndrica en el eje  $z$ , compuestos por materiales dieléctricos y plasmónicos, los efectos de las polarizabilidades opuestas se aprecian sobre todo en campos de onda con polarización  $TM^z$ , mientras que las resonancias Fano, otra aproximación para la cancelación de la dispersión, puede ser usada simplemente en configuraciones con polarización  $TE^z$ . Las propiedades del patrón característico de una resonancia Fano pueden ser motivadas por la cancelación de la dispersión de una nanopartícula dispersora previamente diseñada. En este caso particular, la emisión de ondas electromagnéticas por el objeto crea una interferencia entre la dispersión no resonante de la partícula y la dispersión debida a modos de Mie [80]. Este efecto también se ha observado en nanopartículas de alto índice sin recubrimientos adicionales [81].

Es importante mencionar que la dispersión de ondas electromagnéticas por una partícula dada más pequeña que la longitud de onda la podemos describir mediante una descomposición multipolar del campo electromagnético que permite caracterizar la intensidad de dispersión por la interferencia de los modos multipolares dominantes. Dichos efectos de interferencia multipolar podrían involucrar multipolos eléctricos

cos, magnéticos y toroidales, que conducen, por ejemplo, a anapolos ópticos no radiativos [70], como se ilustra en la fig. 1.3. Este mecanismo reciente desarrollado para la reducción de la eficiencia de dispersión de un objeto es actualmente un área de investigación muy activa, aunque queda fuera del ámbito de esta Tesis.

Hay un tipo particular de nanoestructura para invisibilidad que llamó nuestra atención, el cual está basado en metamateriales hiperbólicos caracterizados por una anisotropía de forma enorme, y que tiene forma de nanotubo del tamaño de la longitud de onda [82]. Las capas de metal y dieléctrico están diseñadas para permitir a la luz propagarse a través de la estructura sin que la onda incidente se distorsione, tanto para luz incidente con polarización TE, como con polarización TM. Según el estudio preliminar, cuando la permitividad efectiva del nanotubo hiperbólico es cercana a cero en la dirección angular, la dispersión se reduce significativamente, induciéndose un efecto de invisibilidad. La propuesta original se centró en el análisis de cómo el factor de llenado metálico y el diámetro interno del nanotubo afectaba a la cancelación de la dispersión. Estos resultados han sido comparados también considerando un nanotubo con dispersión hiperbólica, a modo de modelización teórica, y se aprecia que la invisibilidad del nanotubo por capas puede ser bastante ajustada, por lo que se podría



utilizar en dispositivos nanofotónicos que se fabriquen en un futuro. En esta tesis profundizamos en las propiedades de estas nanoestructuras, y estudiamos cómo otros parámetros entre los que destacamos los efectos de borde o la permitividad tanto del medio interior como del medio exterior alteran la dispersión de los nanocilindros.

## 1.4 Metalentes y metamateriales concentradores de luz

También estamos interesados en dispositivos focalizadores basados en metasuperficies y metalentes. El funcionamiento de un gran número de dispositivos ópticos, como lentes, prismas, axiconos, y moduladores espaciales de luz, está basado en controlar el frente de onda de un haz luminoso modificando su fase, amplitud y estado de polarización. Los efectos de propagación son los responsables de la formación del haz llevada a cabo mediante los componentes ópticos antes mencionados. En este caso, los metamateriales volumétricos pueden presentar un problema: normalmente presentan grandes pérdidas [85]. Una alternativa consiste en diseñar metamateriales ultrafinos que permitan a las ondas pasar a través de ellos con una reducción considerable de los efectos dispersivos del material. Las metapantallas perforadas o

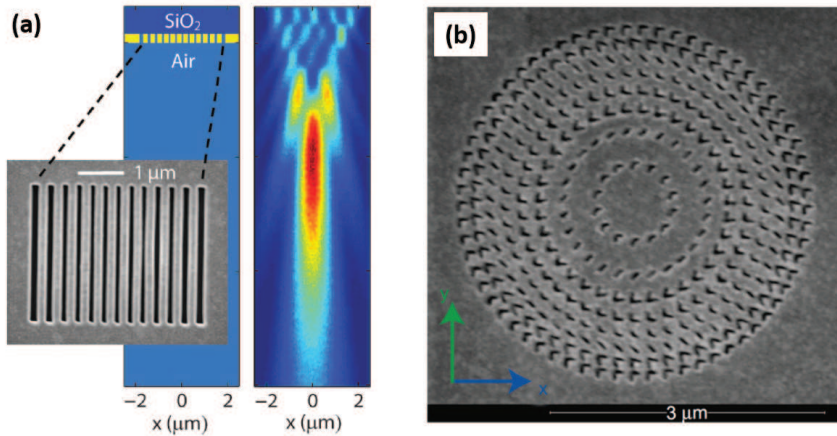


Figura 1.4: (a) Lente plana basada en una matriz de rendijas a nanoescala en una película metálica. La lente consiste en una capa ópticamente gruesa de 400 nm de oro (amarillo) con rendijas de aire de anchos diferentes (de 80 a 150 nm) (azul claro) fresadas sobre un sustrato de sílice fundido (azul oscuro) [83]. (b) Imagen SEM de una metalente plasmónica plana que consiste en una película de oro de 30 nm de grosor perforada concéntricamente, con una distancia focal de  $2.5 \mu\text{m}$  bajo una longitud de onda de 676 nm [84].

las metasuperficies basadas en nanorresonadores son buenas elecciones actualmente, como se ilustra en las figs. 1.4 y 1.5. Por ende, es posible controlar las propiedades de la luz, como la dirección de la onda e incluso transformar una onda evanescente en una homogénea. Por ejemplo, un metamaterial multicapa metal-dieléctrico soporta la propagación de las ondas para índices de refracción efectiva-

damente altos [45]

$$n_{\text{eff}} = \text{Re} \sqrt{\frac{\varepsilon_d \varepsilon_m}{\varepsilon_d f_m + \varepsilon_m (1 - f_m)}} \quad (1.2)$$

donde  $\varepsilon_m$  y  $\varepsilon_d$  denotan la permitividad del metal y del dieléctrico, respectivamente, con características ajustables mediante la simple variación del factor de llenado del metal  $f_m$  en el metamaterial. Por tanto, los campos que pasan a través de dichos metamateriales metal-dieléctricos experimentan variaciones rápidas de fase del campo dispersado incluso teniendo en cuenta una distancia de propagación inferior a la longitud de onda. Es más, algunas metasuperficies proporcionan corrientes electromagnéticas inducidas que producen una distribución de campo electromagnético concreta como respuesta a un frente de ondas electromagnéticas incidente conocido [86, 87]. Con estas metasuperficies, que son el equivalente en 2D de los metamateriales, uno puede tener un control excepcional de los frentes de onda de haces ópticos, y presentan la ventaja de estar compuestos por celdas unidad más pequeñas que la longitud de onda, con grosor también inferior a la longitud de onda. Esto nos permite moldear a voluntad el frente de onda incidente y controlar las ondas electromagnéticas mediante variaciones espaciales introducidas en las celdas unidad [88–92].

Es bien sabido que la resolución espacial de un campo electro-

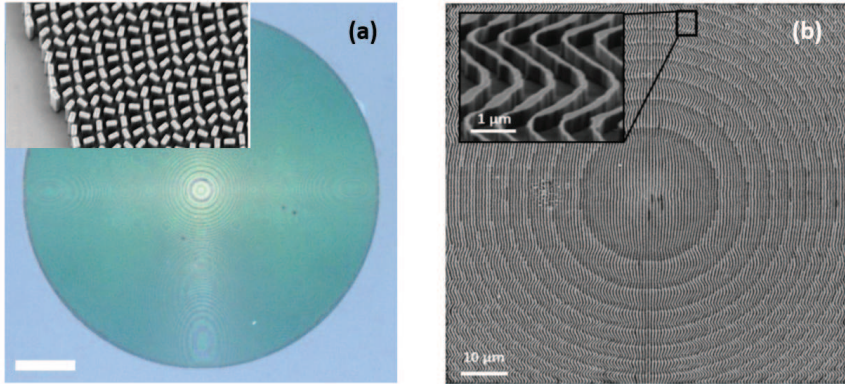


Figura 1.5: (a) Metalente diseñada para la longitud de onda de 660 nm, que consiste en nanoaletas de  $\text{TiO}_2$  sobre un sustrato de vidrio. Barra de escala,  $40 \mu\text{m}$  [93]. (b) Lente basada en red de difracción con  $f = 100 \mu\text{m}$  fabricada con técnicas de microfabricación en silicio estándar [94].

magnético difractado está acotada por el límite de difracción de la luz [95], el cual tiene un fuerte impacto en aplicaciones como almacenamiento de datos o microscopía de campo lejano [96,97]. Se han realizado muchos intentos para conseguir alcanzar este límite en resolución, e incluso sobrepasarlo, empleando metasuperficies planas [98–100]. Aparte de usar configuraciones planas, hay algunos otros diseños con geometrías curvilíneas que permiten un rendimiento mejor para moldear las ondas ópticas [101–103]. En particular, las ondas de gran apertura óptica se pueden transformar en haces no paraxiales adifraccionales. Estos haces muestran también una fuerte aceleración espacial [104,105]. Dentro de nuestra línea de investigación, esto fue llevado

a cabo utilizando metamateriales MD con la misma curvatura que la onda focal, por lo que podemos conseguir ondas aceleradas altamente localizadas. Mediante el uso de la misma configuración cilíndrica (o esférica, utilizando el diseño apropiado) del haz incidente evitamos un modelado inadecuado del haz que puede ser inducido por aberraciones ópticas. Conviene mencionar que no sólo los metamateriales de alto índice efectivo son capaces de moldear adecuadamente una onda plana para convertirlos en ondas de Bessel con trayectorias no cerradas, sino también los metarrecubrimientos con epsilon cercano a cero, los cuales pueden ser implementados por ejemplo sobre sustratos transparentes plano-cóncavos [106, 107].

## 1.5 Ondas superficiales en medios anisótropos

La interfase plana que separa dos materiales diferentes contribuye significativamente en muchos fenómenos ópticos. Una onda electromagnética superficial puede viajar a lo largo de toda la interfase, pero en cada lado de la superficie su amplitud es imperceptible siempre que observemos suficientemente lejos de la interfase. La relevancia del concepto de onda electromagnética superficial se expuso por primera

vez en 1907 cuando Zenneck [108] lanzó un estudio teórico en el cual exploraba la posibilidad de encontrar ondas guiadas en la interfase que separa la atmósfera y la tierra o una gran masa de agua. Este caso particular está centrado en ondas de radio, cuya región del espectro electromagnético se encuentra lejos del régimen óptico en el cual estamos interesados, pero la base física de este fenómeno es la misma, dada la invariancia escalar en las ecuaciones de Maxwell. Es más, el plasmón polaritón de superficie (SPP, del inglés *Surface Plasmon Polariton*) se ha extendido a día de hoy, dominando el escenario nanotecnológico actual en el espectro visible, y permitiendo así avances importantes en técnicas de nanofabricación existentes para la creación de sensores biológicos o químicos, por mencionar uno de los ejemplos más significativos [109]. Mientras la interfase de un material plasmónico y uno polarizable soporta SPPs, también es posible encontrar otros tipos de ondas superficiales propagándose por la interfase de dos materiales polarizables distintos.

Podemos encontrar un tipo particular de onda de superficie en la interfase de dos materiales dieléctricos homogéneos, siempre que al menos uno de ellos sea anisótropo, incluso aunque cualquier componente de la permitividad diádica tenga una parte real que sea positiva para ambos materiales. Después de que Dyakonov analizara en

1988 [110] los modos ligados que aparecían en la interfase entre un material dieléctrico uniáxico y un material dieléctrico isótropo surgió cierto interés en la propagación de ondas guiadas en la superficie de dos materiales dieléctricos homogéneos. De hecho, la birrefringencia de forma inherente en metamateriales proporcionaría un control preciso de estas ondas superficiales de Dyakonov (DSWs, del inglés *Dyakonov Surface Waves*) [111–114]. Una de las características más prominentes de las DSWs es su oblicuidad, es decir, la propagación de la onda de superficie siempre se produce oblicuamente con respecto al eje de anisotropía del dieléctrico uniáxico. También existen pruebas experimentales de este fenómeno, que en ocasiones aparece en connivencia con las pérdidas del material.

## 1.6 Objetivos de la Tesis

El objetivo general de esta Tesis es el diseño de dispositivos fotónicos y disposiciones basadas en estructuras con alta anisotropía, las cuales están formadas por una combinación adecuada de elementos dieléctricos y metálicos. Entre las aplicaciones potenciales que pueden aprovecharse de esta propiedad de anisotropía de forma en metamateriales, en esta Tesis nos centramos en dos de ellas: 1) nanorreso-

nadores para aplicaciones en invisibilidad óptica, y 2) metalentes y metasuperficies para localización espacial de luz. Finalmente, también nos proponemos llevar a cabo ciertos experimentos que pudieran confirmar la existencia de ondas de superficie en sustratos anisótropos, para los que, en esta propuesta preliminar, ha sido utilizado un medio anisótropo natural,  $\text{TeO}_2$ . Obviamente, la extensión de estas ideas a metasustratos con forma anisótropa parece inmediata.

Primero estudiaremos el mecanismo de cancelación de la dispersión en partículas con tamaños más pequeños que la longitud de onda, especialmente en geometrías simples: estamos interesados en cilindros multicapa infinitamente largos. Estudios previos mostraron que una reducción drástica de la dispersión puede llevarse a cabo mediante la interferencia destructiva de señales ópticas causada por una combinación adecuada de capas de metal y dieléctrico. Debido a la anisotropía geométrica de los nanorresonadores que se investigan, la dinámica electromagnética diferirá para iluminación con onda plana suponiendo bien polarización TE o bien TM. Utilizando morfologías controladas y combinaciones adecuadas de materiales llegamos a un ajuste fino de la cancelación de la dispersión a diferentes longitudes de onda. Por ejemplo, la plata y el  $\text{TiO}_2$  se consideran materiales adecuados para la reducción de la señal de dispersión en el régimen visible, aun-



que la aplicación del modelo de Drude para materiales plasmónicos proporcionará resultados más genéricos. La estimación analítica de la eficiencia de dispersión para una polarización dada de la luz incidente será desarrollada mediante el método de Lorenz-Mie. Dado que la utilización de un gran número de capas puede hacer el procedimiento estándar tedioso, se desarrollará una formulación de matrices de transferencia para una estimación más rápida [115–117]. Además, programas comerciales como MatLab y Mathematica serán ampliamente utilizados para resolver nuestros problemas matemáticos. El software de cálculo COMSOL Multiphysics será particularmente útil; consiste en una herramienta de simulación para la resolución de problemas de ondas electromagnéticas, que también será empleado a lo largo de esta Tesis, el cual es capaz de resolver numéricamente las ecuaciones de Maxwell y por tanto proporciona simulaciones precisas del comportamiento de dispersión de nuestras nanoestructuras.

En segundo lugar, nos encontraremos con graves restricciones geométricas de las metalentes planas para alcanzar aperturas numéricas extremadamente altas. Nuestras propuestas consisten en modelar una superficie cóncava, usando redes metal-dieléctrico, seguido de un diseño adecuado de metarrecubrimientos curvos para conseguir nuestros objetivos. Para nosotros es especialmente importante conseguir una

focalización extrema de ondas electromagnéticas basada en aperturas numéricas (NAs) altas, además destacando una increíble miniaturización de los componentes fotónicos. Por tanto, necesitamos utilizar el concepto básico de anisotropía extrema observado en los metamateriales multicapa metal-dieléctricos para diseñar recubrimientos más pequeños que la longitud de onda con un cierto gradiente de índice para que funcionen bajo una alta eficiencia como dispositivos focalizadores de alta apertura numérica [118]. Además, la curvatura del frente de onda de un campo electromagnético convergente puede ser convenientemente modificada para incrementar significativamente la apertura numérica de la arquitectura óptica [119]. Asimismo, la manipulación de un haz dado puede extenderse a campos localizados más generales en el régimen no paraxial. En particular, estamos interesados en transformar ondas convergentes de gran apertura angular en un haz acelerado que conserve la forma, especialmente cuando la anchura del haz permanece cerca del límite de difracción [120].

Es importante notar que los efectos no locales encontrados en metamateriales altamente anisótropos pueden inducir cambios en el comportamiento fotónico estimado con teorías de medio efectivo. Este tipo de análisis se llevó a cabo previamente a la admisión en el Programa de Doctorado en Física, durante la realización del curso de Máster en

Física Avanzada, también en la Universidad de Valencia. En particular, analizamos un metamaterial “volumétrico” compuesto por capas delgadas alternas de metal y dieléctrico que claramente manifiestan trirrefringencia [121]. Debido a la excitación colectiva de plasmones polaritones de superficie en capas metálicas más pequeñas que la longitud de onda, uno puede observar simultáneamente dos ondas de Bloch con un comportamiento contrapropagante. Dichas observaciones en experimentos numéricos han ayudado a diseñar correctamente los dispositivos fotónicos objeto de nuestro análisis, así como permitir la aplicación de las correcciones apropiadas en circunstancias en las que las teorías de medio efectivo pueden desviarse notablemente.

Finalmente, nuestra última meta es obtener experimentalmente pruebas de la formación de ondas de superficie no plasmónicas que pueden aparecer en la interfase entre un sustrato anisótropo y un material isótropo dieléctrico. Además, si éste último emite una señal luminiscente fuerte, la excitación de ondas de superficie es factible como resultado del acoplo de la parte evanescente que integra la característica emisión dipolar. Con este propósito, unimos fuerzas con el Prof. Juan P. Martínez Pastor, responsable de la Unidad de Materiales y Dispositivos Optoelectrónicos (UMDO), que también pertenece a la Universidad de Valencia. Su experiencia en la fabricación de sistemas

ópticos multicapa, en particular utilizando materiales semiconductores, será decisiva para la viabilidad de nuestra propuesta.

## 1.7 Publicaciones asociadas a la presente Tesis

Esta Tesis Doctoral puede ser dividida en tres bloques. El primero de ellos está relacionado con técnicas de invisibilidad aplicadas a partículas pequeñas y dio como resultado tres publicaciones en tres revistas internacionales diferentes. El diseño de las metasuperficies y metalentes sería la segunda área, donde el estudiante colaboró en la realización de tres artículos más. Finalmente, el estudiante llevó a cabo algunos experimentos en relación con guías de ondas anisótropas que constituirían el tercer bloque de la presente Tesis.

En la parte introductoria de la Tesis (apartados 1.1 a 1.3) incluimos brevemente conceptos relacionados con la dispersión luminosa en partículas y cómo se puede reducir la señal dispersada en cuerpos pequeños, lo que constituye la principal meta del trabajo presente, como se menciona en el apartado 1.6. Investigamos sobre este tema y diseñamos un mecanismo que consiste en una estructura multicapa cilíndrica que permite la cancelación de la dispersión. En el aparta-

do 4.1 describiremos el procedimiento para conseguir invisibilidad con una nanoestructura multicapa, y presentaremos varios diseños para mejorarla con el fin de aumentar la cancelación de la dispersión. Primero describimos algunas condiciones satisfactorias para hacer una nanocavidad invisible (ver apartado 4.1.2) y cómo optimizar su diseño (ver apartado 4.1.3) con los materiales dados; en nuestro caso, plata y  $\text{TiO}_2$ . A continuación, aplicamos la aproximación de medio efectivo para tratar las nanoestructuras diseñadas como un medio hiperbólico, haciendo posible así una simplificación sustancial del problema y, lo que es más importante, proporcionando esquemas para la reducción de la dispersión en configuraciones más generales (ver apartado 4.1.1). Tres artículos científicos resumen los principales resultados de nuestro estudio.

El primer trabajo, titulado “*Conditions for achieving invisibility of hyperbolic multilayered nanotubes*” (“Condiciones para conseguir invisibilidad en nanotubos multicapa”), fue publicado en la revista *Optics Communications* (factor de impacto 1.588 en 2016 y clasificada 52/92 en la categoría Óptica del JCR). El artículo está anexo a la presente Tesis y es citado como referencia [115]. El trabajo del estudiante se basó principalmente en el análisis de la estructura multicapa diseñada: modelado de la partícula multicapa, estimación

de la permitividad efectiva en el rango visible, investigación del ajuste de la permitividad del nanotubo mediante la modificación del factor de llenado de los constituyentes de la estructura, análisis de la eficiencia de dispersión en el rango de longitudes de onda deseado, y simulación del comportamiento óptico de la partícula cuando los elementos materiales son cambiados de posición y se varía el número de capas dado un cierto grosor de la estructura.

La segunda publicación lleva como título “*Optimization of multilayered nanotubes for maximal scattering cancellation*” (“Optimización de nanotubos multicapa para una máxima cancelación de la dispersión”). Fue publicada en *Optics Express* (factor de impacto 3.307 en 2016 y clasificada 17/92 en la categoría Óptica del JCR). Este trabajo queda adjunto a esta Tesis y se hace referencia a él como [117]. En este artículo el estudiante se inspiró en las soluciones del trabajo anterior e investigó cómo mejorar la estructura para reducir su dispersión para diferentes medios internos y externos. Para ello, simuló la eficiencia de dispersión de la estructura utilizando diferentes permitividades del medio exterior a ella y también varió la permitividad del material cubierto por el cilindro multicapa. El estudiante evaluó analítica y numéricamente el comportamiento óptico del nanotubo cuando la celda unidad periódica se fija en el sentido en el que

las capas interior y exterior están fabricadas con el mismo material, de forma que uno puede ajustar el grosor de dichas capas para aumentar la cancelación del campo dispersado. El estudio fue llevado a cabo en el rango de longitudes de onda del visible, para diferentes factores de llenado y tanto para polarización de la luz incidente TM como TE.

El título del tercer artículo científico del primer bloque de esta Tesis es “*Tunable scattering cancellation of light using anisotropic cylindrical cavities*” (“Cancelación sintonizable de la dispersión de la luz usando cavidades cilíndricas anisótropas”). La revista en la que fue publicado es *Plasmonics* (factor de impacto 2.339 en 2016 y clasificada 114/275 en la categoría Ciencia de Materiales, Multidisciplinario del JCR). Este artículo se encuentra como anexo a la presente Tesis y se cita como la referencia [116]. El trabajo del estudiante para la realización de este artículo fue llevar a cabo el modelado y los cálculos (tanto analíticos como numéricos) de la nanopartícula hiperbólica. Los cálculos se hicieron para un amplio abanico de condiciones; para completar nuestro estudio se variaron parámetros en el sistema como la frecuencia de la luz, los radios interno y externo del nanotubo uniáxico, la permitividad de los medios que rodean la nanocavidad hiperbólica, y la anisotropía del metamaterial empleada para analizar la corteza invisible.

La segunda parte de esta Tesis se centra en el diseño y análisis del comportamiento de metalentes y metasuperficies metal-dieléctricas cuando se usan para controlar el frente de ondas de un haz de luz. En el apartado 2.4 nos centramos en las ventajas existentes cuando se usan estructuras MD multicapa para alterar a voluntad las principales propiedades de la luz, como su dirección de propagación. Es posible, teóricamente, alcanzar una gran localización espacial cercana al límite de difracción con las metasuperficies MD diseñadas, formadas por subestructuras más pequeñas que la longitud de onda, como se describe en los siguientes artículos que están publicados en varias revistas internacionales revisadas.

Los resultados derivados de esta segunda línea de investigación condujeron a la publicación de tres artículos científicos. El primero de ellos se titula “*Accelerating wide-angle converging waves in the near field*” (“Ondas convergentes de gran apertura angular aceleradas en el campo cercano”) y fue publicado en *Journal of Optics* (factor de impacto 1.847 en 2015 y clasificada 36/90 en la categoría Óptica del JCR). El segundo trabajo lleva como título “*Ultrathin high-index metasurfaces for shaping focused beams*” (“Metasuperficies ultrafinas de alto índice para el conformado de haces focalizados”) y se publicó en *Applied Optics* (factor de impacto



1.598 en 2015 y clasificada 45/90). La tercera y última publicación de este bloque se titula “*Metacoatings for wavelength-scale, high-numerical-aperture plano-concave focusing lenses*” (“Meta-recubrimientos para lentes focalizadoras plano-cóncavas de alta apertura numérica y a escala de la longitud de onda”). Se publicó en *Journal of the Optical Society of America B* (factor de impacto 1.843 y clasificada 41/92 en 2016). En todos estos tres casos el estudiante contribuyó en la realización de ciertas simulaciones numéricas utilizando principalmente COMSOL Multiphysics.

Finalmente, en la tercera parte de esta Tesis el estudiante realizó algunos trabajos experimentales con el objetivo de obtener pruebas empíricas de la existencia de ondas superficiales en guías de ondas anisótropas completamente dieléctricas. El trabajo del estudiante en esta tarea consistió en la fabricación de una guía de ondas activa plana sustentada por un material anisótropo; específicamente utilizamos un sustrato de  $\text{TeO}_2$ . Por otra parte, la capa activa está compuesta por perovskita, y la deposición se llevó a cabo mediante el uso de un grupo de varias técnicas comunes, rápidas y baratas, como el *Doctor-blading* y el *spin-coating*. Después del proceso de fabricación, el estudiante caracterizó la muestra preparada (ver apartado 4.3.1). También realizó algunas medidas experimentales (procedimiento descrito en el

apartado 4.3.2), y posteriormente confirmó que los resultados obtenidos concordaban con los calculados a partir de simulaciones numéricas (ver también apartado 4.3.3). En el momento del depósito de la Tesis Doctoral hay un artículo en preparación, en el que se recopilan los resultados principales de nuestro estudio.

# Chapter 2

## Introduction (English)

Governing the flow of light is currently possible with unprecedented control by means of recent progress in micro- and nanofabrication methods [1]. Metamaterials and metasurfaces are designed nanostructures formed by engineered building blocks, also known as meta-atoms, with the ability to manipulate light under a prescribed response. As a result, metamaterials leave open the door to a number of potential applications which were formerly considered unimaginable. One is not necessarily limited to the electromagnetic response of materials found in nature and their chemical compounds. Alternatively, we modify the size and shape of the basic units of a metamaterial, fine-tune the composition and morphology of the optical structure, and gain novel

functionalities. The exceptional properties of photonic metamaterials and devices based on transformation optics, which were conceived by metamaterials, enable a negative index of refraction, imaging with subwavelength resolution, effective light concentrators, and invisibility cloaks. In this Thesis we take a step in this direction and propose new photonic structures that due to their form anisotropy are capable of generating highly localized light distributions, as well as optically inert responses in the far field.

## 2.1 Metamaterials

One of the most profitable human features is the ability of seeing, which involves electromagnetic wave propagation, a phenomenon that is present in our daily life. Waves propagate and also interact with materials. Very exciting effects of the light-matter interaction can be observed, such as iridescent colors on the bodies of some beetles or seashells, or fantastic color patterns on the wings of a butterfly [2, 3]. This happens because of interaction of light with structural periodic distributions on them. It is possible to reproduce that kind of periodic structures in a laboratory by means of dielectric and also plasmonic materials. Plasmonics is of great significance and it is applied

in current nanotechnology [4]. Unique phenomena like subwavelength confinement [5], amplification of evanescent waves [6], extraordinary transmission [7], hyperbolic dispersion in complex metallic composites [8], and sharp resonances in nanoparticles and meta-atoms [9] have caused a tremendous impact. These lead to numerous devices and applications in photonics such as superlenses [10], nanoantennas [11], subwavelength waveguides [12], invisibility-cloaking structures [13], enhanced sensors for chemical detection of biological agents [14], and chiral metamolecules [15] that work in the near-infrared and optical range, color prints with resolutions up to the optical diffraction limit [16], drilled-hole metasurfaces [17] or V-shaped optical antennas [18] for shaping of wave fields by means of resonant nanostructures [19], and light trapping in thin film solar cells [20]. They are all based on the ability to control and manipulate the propagation of the electromagnetic field.

One of our goals is to control the light bending. We see this effect if we take a glass of water and we put a pen in it. Using the appropriate materials, those with suitable electric permittivity ( $\varepsilon$ ) and magnetic permeability ( $\mu$ ) for the case in study, we may control the propagation of the light waves. For this purpose, frequently there are no natural materials available with the required values of  $\varepsilon$  and  $\mu$ . On these

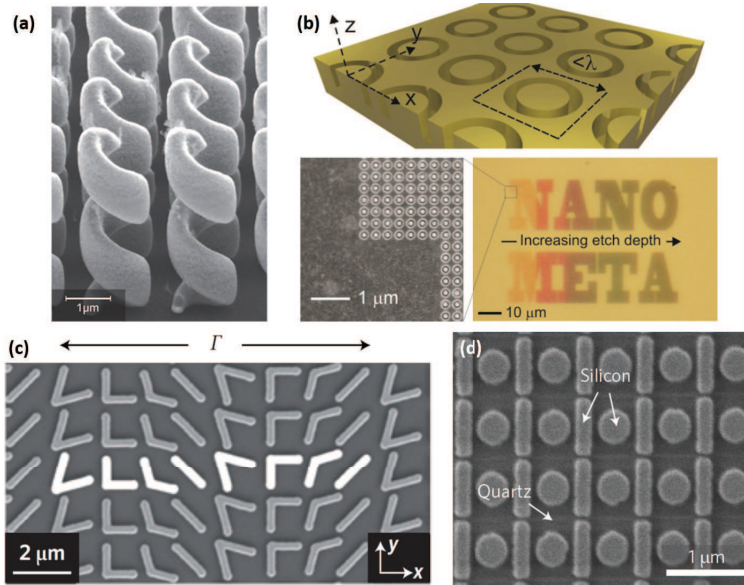


Figure 2.1: (a) Chiral metamaterial fabricated by direct laser writing [15]. (b) Generic intaglio metamaterial array of sub-wavelength single ring meta-molecules inscribed into a metal surface to generate metallic structural color [21]. (c) Scanning electron microscopy image of a metasurface consisting of an array of V-shaped gold optical antennas fabricated on a silicon wafer, where  $\Gamma = 11\mu\text{m}$  [22] (d) A Fano-resonant silicon metasurface showing strong enhancement of third-harmonic generation [23].

cases we have to design artificial materials to let us control the light. Materials combine in a subwavelength structure to achieve the electromagnetic parameters needed to manipulate waves. The combination of these materials gives structures called ‘metamaterials’.

Metamaterials may behave as hyperbolic materials, which present a dispersion relation that supports very high values of the wavenumber.

Hyperbolic materials present an uncommon optical anisotropy [24], a critical feature to achieve subwavelength imaging [25–28] and focusing [28, 29] for example. This kind of metamaterials will be profitable for us to exploit the invisibility phenomenon.

Producing metamaterials in the visible and infrared needs of an extreme miniaturization that imposes severe restrictions in the fabrication processes, allowing the assembly of elementary geometries. Maybe the simplest one is the metal–insulator multilayered nanostructure, which has been theoretically analyzed [30] and fabricated [31] extensively. In the theoretical analysis of subwavelength stratified nanomaterials, an effective medium approach (EMA) is widely employed [32, 33] and exploited for the design of plasmonic devices [34, 35]. However, such an approach was proved to fail when dealing with transverse magnetic (TM) polarized waves [36–38], that is, when the magnetic field is perpendicular to the axis of periodicity of the metal–dielectric (MD) nanostructure. In this case, nonlocal effects arise provided that the width of the metallic layers becomes close and even surpasses the penetration depth of the metal [39]. Bearing in mind that current technologies meet a bound in the fabrication of multilayered nanostructures with smooth metal slabs and gaps thinner than 10 nm [40, 41] and that the penetration depth for a metal like silver (gold) is around

24 nm (31 nm) at  $\lambda = 600$  nm, we may conclude that nonlocal effects are generally taking place in realistic plasmonic arrangements.

One of the most outstanding effects driven by nonlocalities is the existence of an additional extraordinary mode in TM polarization [42–45]. Under certain conditions, a beam will split into two wave packets in an air/metamaterial interface, one of them undergoing positive refraction and the other beam being refracted under negative angles. Together with single refraction displayed for incident transverse electric (TE) polarized, metallodielectric multilayered metamaterials may manifest trirefringence. In other words, three indices of refraction are necessary to typify such exotic behavior. We point out that tailored photonic crystals also exhibit multirefringent properties, nevertheless provided that the structural details of the media (lattice constants) are on the scale of the optical wavelength [46].

In all the studies carried out formerly on trirefringent MD metamaterials, a detailed description of the direction of propagation of the multirefracted beams has been specified. However, the distribution of energy flow that corresponds to each refracted beam is not clear, especially in TM polarization. An accurate evaluation of transmissivity and reflectivity may provide new insights included in nonlocalities.



## 2.2 Cloaking structures

From a different point of view, let us point out that an inhomogeneous refractive index can give us some control of the light path, as happens for instance on gradient-index (GRIN) lenses [47]. To manipulate this refractive index, we need to engineer the permittivity and permeability, which can also be anisotropic. For an anisotropic material light response depends on its polarization [48]. In particular, optical cloaking is achieved by manipulating light propagation, and it became very popular for the researchers after the publication of two seminar papers [49, 50]. They proposed two different cloaking devices which are based on the Transformation Optics Method (TOM). This kind of devices allow incident light to flow bordering the cloaking structure, and keep the same propagation features as there was nothing there [51]. One can introduce some given objects to be hidden inside that structure, so light goes around them and any observer outside of the device sees no perturbation on the light field. Development of these ideas in the form of carpet cloaks and also skin cloaks have been recently demonstrated experimentally (see fig. 2.2).

Taking into account TOM in its original concept, the structure considered commonly exhibits a very high anisotropy. The material parameters will take extreme values at some regions of the cloak, which

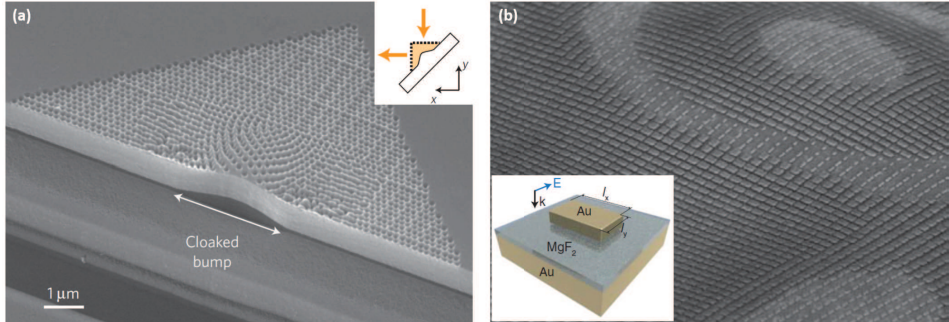


Figure 2.2: (a) Scanning electron microscope image of a fabricated carpet cloak. The carpet cloak design that transforms a mirror with a bump into a virtually flat mirror [52]. (b) A metasurface invisibility skin cloak for a 3D arbitrarily shaped object. Inset: A 3D illustration of a nanoantenna used to build the metasurface [53].

makes impossible the selection of natural materials [54]. In addition, permittivity and permeability should be similar at the outer regions of the structure to satisfy the impedance-matched condition. Fortunately, using metamaterials it is possible to tune the anisotropy of both permeability and permittivity [55]. This is the relation of cloaking with metamaterials: the structure for achieving perfect cloaking is made of metamaterials. The first metamaterials for demonstrating cloaking were split ring resonators [51], probably the most used structures for this purpose [56–58]. Importantly, revolutionary progress in the development of new structures for cloaking has completely transformed the current scenario. Advances on science and industry make

possible the study and fabrication of new and smaller camouflages and invisibility sensors made by metamaterials [59–61]. With these novel devices and techniques, invisibility cloaking keeps attracting the attention of researchers on the whole world.

## 2.3 Scattering cancellation

Although perfect cloaking is a highly studied method to completely suppress the visibility of an object, we count on supplemental ways to at least minimize its electromagnetic perceptibility. An alternate method specially adapted to small particles and coined as scattering cancellation leads to invisibility by reducing to minimum the scattering cross section of a structure which partially can be made of metamaterials [62]. The basic idea consists of turning a particle undetectable by covering it with ultra-thin coatings or metasurfaces, so the scattering of the arrangement is much reduced than the one without the covering nanostructured element [63–66]. Structures like gold-covered silicon nanowires [67] were proposed for reducing light scattering from detectors and increase the optical signal at the same time, as illustrated in fig. 2.3. More recently, atomically thin surface cloaks have been proposed using graphene at THz frequencies [68, 69].

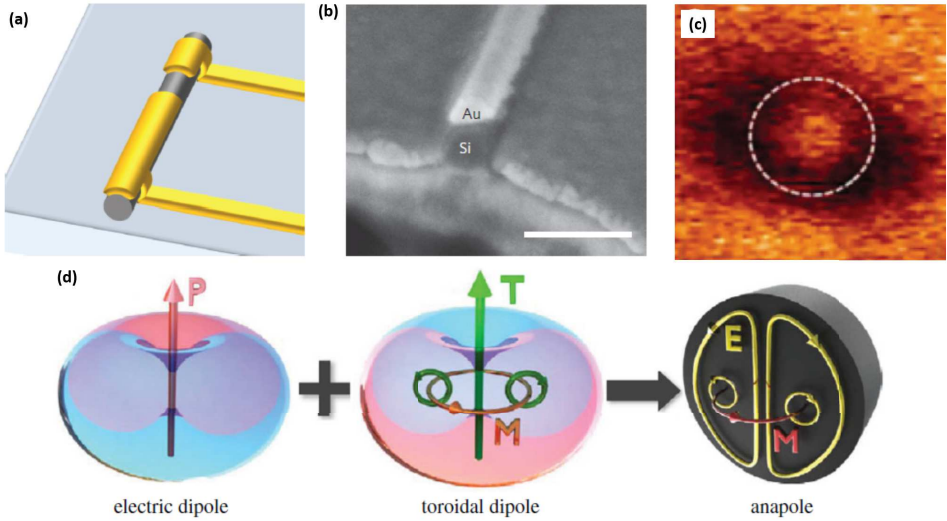


Figure 2.3: (a) Schematic of a gold/silicon nanowire photodetector. (b) SEM image of a 50-nm-diameter silicon nanowire with a 20-nm-thick gold *cover*. Scale bar, 100 nm [67]. (c) The near-field distributions for the anapole modes excited within a silicon nanodisc with plane wave incidence [70]. (d) The destructive interference of an electric dipole (left) and a toroidal dipole (middle) leads to the formation of a non-radiating anapole mode.

The scattering drop in metacoated structures may be attributed to different aspects of the light matter interaction. For instance, the local polarizability of distinct components of a moderately sized object with opposite signs may be canceled out in a proper designed configuration [63, 71–77]. As an example, let us consider a core-shell nanowire of internal (external) permittivity  $\varepsilon_1$  ( $\varepsilon_2$ ) and radius of curvature  $r_1$  ( $r_2$ )

embedded in a region of permittivity  $\varepsilon_3$  exhibits a polarizability [78]

$$\alpha = 4\pi\varepsilon_0 \frac{[(\varepsilon_1 - \varepsilon_2)(\varepsilon_2 + \varepsilon_3)r_1^2 + (\varepsilon_1 + \varepsilon_2)(\varepsilon_2 - \varepsilon_3)r_2^2]}{(\varepsilon_1 - \varepsilon_2)(\varepsilon_2 - \varepsilon_3)r_1^2 + (\varepsilon_1 + \varepsilon_2)(\varepsilon_2 + \varepsilon_3)r_2^2}, \quad (2.1)$$

where  $\varepsilon_0$  is the permittivity in vacuum. Therefore, the polarizability can theoretically vanish for a specific combination of the shell parameters  $r_2$  and  $\varepsilon_2$ . The polarization vector in each of the elementary materials is antiparallel with respect to each other, implying that a dipole moment of opposite phase is induced. The inclusion of epsilon-near-zero shells in the spectral range of interest is of particular interest. It may lead to a significant drop of scattering spectrum of the structure and also create a shielding effect in the boundary space [79]. Focusing on scatterers with cylindrical symmetry along  $z$  axis, composed of dielectric and plasmonic materials, the effects of opposite polarizabilities is mostly observed in  $\text{TM}^z$ -polarized wavefields, whereas Fano resonances, another approach for the cancellation of scattering may be simply used in  $\text{TE}^z$  polarization configurations. Properties of the characteristic lineshape of Fano resonance can be driven for the cancellation of scattering of an engineered scatterer. In the particular case, the emission of electromagnetic waves by the object create the interference between the nonresonant scattering from the particle and scattering by narrow Mie modes [80]. This effect has also

been observed in high-index nanoparticles without additional coating layers [81].

It is worth to mention that scattering of electromagnetic waves by a given subwavelength particle can be described by a multipole decomposition of the electromagnetic field enabling to characterize the scattering intensity by interference of dominant multipole modes. Such multipolar interference effects might involve electric, magnetic and toroidal multipoles leading, for instance, to non-radiating optical anapoles [70], as illustrated in fig. 2.3. This novel mechanism for reducing the scattering efficiency of an object is currently an active area of research, though it remains out of the scope of this Thesis.

A particular kind of invisible nanostructure called our attention, which is based on hyperbolic metamaterials exhibiting an enormous form anisotropy and shaped as wavelength-scale nanotubes [82]. These metal and dielectric layers are designed to allow light to propagate through the structure without distortion of the incident wave, for both TE- and TM-polarized incident light. When the effective permittivity of the hyperbolic nanotube is close to zero in the angular direction, the scattering is reduced significantly, producing invisibility. The original proposal focused on the analysis of how the filling fraction and inner diameter of the nanotube affect the scattering cancellation. These

results are also compared by considering a hyperbolic nanotube instead of a layered one and appreciate that the invisibility of the layered nanotube can be tuned, so it may be used in future nanophotonic devices. In this Thesis we go beyond and study how other parameters as edge effects or inner and outer permittivity alter the scattering of the nanocylinder.

## **2.4 Metalenses and light-concentrator metasurfaces**

We are also concerned on focusing devices based on metasurfaces and metalenses. The operation of a large number of optical devices, such as lenses, prisms, axicons, and spatial light modulators, is based on controlling the wavefront of light by modifying its phase, amplitude and state of polarization. Propagation effects are responsible of the beam shaping carried out by the above-mentioned optical components. In this case, bulk metamaterials would present a problem: they usually are too lossy [85]. An alternative consists of designing ultrathin metamaterials that enable waves pass through with a considerable reduction of losses. Perforated metascreens or engineered nanoresonator-based metasurfaces are currently good choices, as illus-

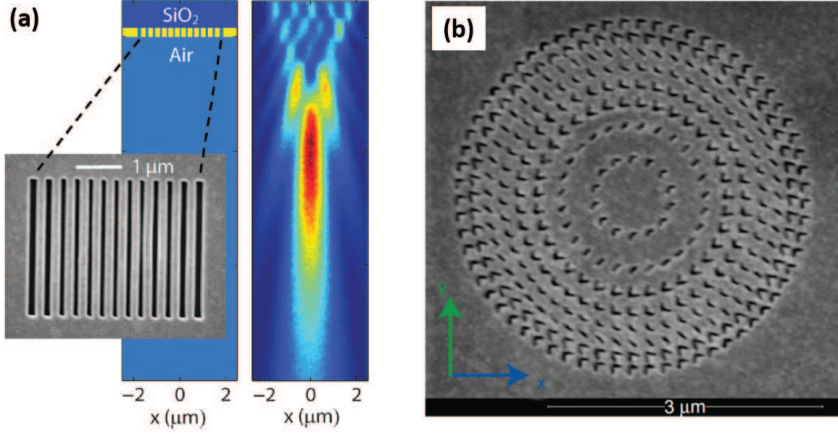


Figure 2.4: (a) Planar lens based on nanoscale slit array in metallic film. The lens consisting of a 400 nm optically thick gold film (yellow) with air slits of different widths (80 to 150 nm) (light blue) milled therein on a fused silica substrate (dark blue) [83]. (b) A SEM image of a planar plasmonic metalens consisting of a concentrically perforated 30-nm-thick gold film, with a focal length of  $2.5 \mu\text{m}$  at an operational wavelength of  $676 \text{ nm}$  [84].

trated in figs. 2.4 and 2.5. Hence, it is possible to control light properties, such as the wave direction and even transform an evanescent wave into a homogeneous one. For instance, a metal-dielectric multilayered metamaterial supports wave propagation at extremely-high effective index of refraction [45]

$$n_{\text{eff}} = \text{Re} \sqrt{\frac{\varepsilon_d \varepsilon_m}{\varepsilon_d f_m + \varepsilon_m (1 - f_m)}} \quad (2.2)$$



where  $\varepsilon_m$  and  $\varepsilon_d$  denote the permittivity of the metal and the dielectric, respectively, with tunable features by simply engineering the metal filling fraction  $f_m$  in the metamaterial. Thus, fields passing through such metal-dielectric metamaterials undergo fast phase variations of the scattered field even taking into account a subwavelength propagation distance. Furthermore, some metasurfaces provide electromagnetic currents to produce a certain electromagnetic field distribution as a response of a known incident electromagnetic wavefront [86,87]. With these metasurfaces, which are the 2D equivalent to bulk metamaterials, one can take an exceptional control of electromagnetic wavefronts, and present the advantage of being composed by subwavelength unit cells with subwavelength thickness too. They permit us to mold the incident wavefront into the desired one, and to control electromagnetic waves, by means of spatial variations introduced in the unit cells [88–92].

It is well known that the spatial resolution is constrained by the diffraction limit of light [95], which has a deep impact in applications such as data storage or far field microscopy [96,97]. Many attempts have been done to achieve this resolution limit, and even surpass it, employing flat metasurfaces [98–100]. Apart of using flat configurations, there are some other designs with non-planar geometries

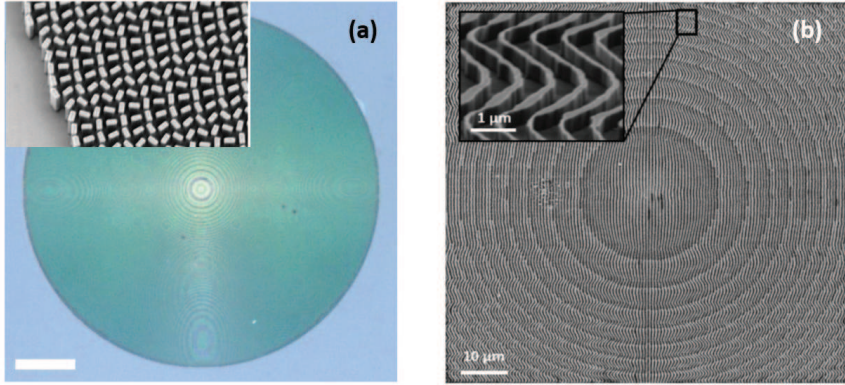


Figure 2.5: (a) Metalens designed at the wavelength of 660 nm, which consists of  $\text{TiO}_2$  nanofins on a glass substrate. Scale bar,  $40 \mu\text{m}$  [93]. (b) Grating lens for  $f = 100 \mu\text{m}$  fabricated with standard silicon microfabrication techniques [94].

that allow a better performance for molding optical waves [101–103]. In particular, high-aperture optical waves can be transformed into diffraction-free non-paraxial beams. These beams also exhibit strong spatial acceleration [104, 105]. Within our research, it was carried out by using MD metamaterials with the same curvature as the focal wave, so we can achieve highly localized accelerating waves. By using the same cylindrical (or spherical using the appropriate design) configuration of the impinging beam we avoid an inadequate beam shaping which may be induced by optical aberrations. It is worth to mention that not only high-index metamaterials but also epsilon-near-zero metacoatings, which can be implemented for instance over

plano-concave transparent substrates, demonstrate an adequate shaping of a plane wave into Bessel wave fields with non-closed trajectories [106, 107].

## 2.5 Optical surface waves in anisotropic substrates

The flat interface separating two different materials contributes significantly in many optical phenomena. An electromagnetic surface wave may travel all along the interface but, on each side of the surface, its amplitude is imperceptible when moving far enough from the interface. The relevance of the concept of electromagnetic surface wave was revealed in 1907 when Zenneck [108] released a theoretical study exploring the possibility of finding guided waves at the interface that separates the atmosphere and the earth or a large body of water. This particular case focused on radio waves, which is a region of the electromagnetic spectrum that is far from the optical regime on which we are interested, but the physical basis of this phenomenon is the same, given the scale invariance of the Maxwell's equations. Furthermore, the surface plasmon polariton (SPP) has reached our days, dominating the current technological scenario in the visible spectrum, thus

allowing significant advances in current nanotechnology such as the creation of bio/chemical sensors, to mention one of the most significant examples [109]. While the interface of a plasmonic material and a polarizable material supports SPPs, other types of surface waves can also be supported by the interface of two distinct polarizable materials.

A particular type of surface wave can be found at the interface of two homogeneous dielectric materials, provided that at least one is anisotropic, even though every component of the permittivity dyadics has a real part that is positive for both materials. Some interest arose from guided waves propagating on the surface separating two dielectric materials after Dyakonov analyzed in 1988 [110] the bound modes appearing at the interface between a uniaxial dielectric material and an isotropic dielectric material. In fact, form birefringence inherent in metamaterials would also enable a precise control of these Dyakonov surface waves (DSWs) [111–114]. One of the most prominent features of the DSW is its obliquity, that is, propagation of the surface wave is always carried out obliquely to the optic axis of the anisotropic material. In this Thesis we also perform a thorough analysis of DSWs taking place along the optic axis of the uniaxial dielectric. Experimental evidences of this phenomenon, that appears with the connivance of the losses of the material, are also provided.

## 2.6 Thesis objectives

The general objective of this Thesis is the design of photonic devices and arrangements based on structures with a high form anisotropy, the latter derived from the convenient combination of dielectric and metallic elements. Among the potential applications that can take advantage of this property of optical anisotropy of metamaterials, in this Thesis we focus on two of them: 1) nanoresonators for applications in optical invisibility, and 2) metalenes and metasurfaces for light focusing. Finally, we also aim to carry out experiments that might confirm the existence of surface waves in anisotropic substrates, in which a natural anisotropic medium,  $\text{TeO}_2$ , has been used. Obviously, the extension of these ideas to meta-substrates with form anisotropy seems immediate.

First, the mechanism of scattering cancellation will be explored in subwavelength particles of simple geometries: infinitely-long multi-layered cylinders are of our interest. Previous studies showed that a drastic reduction of scattering can be driven by the destructive interference of optical signals caused by a convenient combination of metal and dielectric layers. Due to the anisotropic geometry of the nanoresonators under investigation, the electromagnetic dynamics will differ for plane wave illumination assuming either TE or TM polarization.

Controlled morphologies and proper combination of materials can lead us to fine tune the scattering cancellation at different wavelengths. For instance, silver and  $\text{TiO}_2$  are considered as adequate materials for reducing the scattered signal in the visible regime, though application of the Drude model for plasmonic materials will provide more general results. The analytical estimation of the scattering efficiency for a given polarization of the incident light will be performed by using of the Lorenz-Mie method. Since a large number of layers can make the standard procedure rather tedious, a transfer matrix formulation can be developed for the fast estimation of the scattering efficiency [115–117]. Furthermore, Matlab and Mathematica software are extensively used to solve our math problems. Particularly useful is COMSOL Multiphysics, a simulation tool for solving wave electromagnetics problems, which has also been employed all along this Thesis, which is capable of solve numerically the Maxwell's equation and thus provides accurate simulations of the scattering behavior of our nanostructures.

Secondly, we will be faced with the severe geometrical restrictions of flat metalenses to attain extremely high numerical apertures. Our proposals consist of sculpturing a concave surface, by using sub-wavelength metal–dielectric arrays, following the adequate design of the nonplanar metacoating to accomplish our objectives. Achiev-

ing tight focusing of high numerical aperture (NA) electromagnetic waves with an incredible miniaturization of the components is of special significance for us. Thus we might use the basic concept of extremely anisotropy observed in metal-dielectric multilayered metamaterials to engineer gradient-index subwavelength coatings as high-numerical-aperture focusing devices exhibiting high efficiency [118]. Also a given wavefront curvature from a converging wave field can be conveniently modified to increase significantly the numerical aperture of the optical architecture [119]. Furthermore, executing a given beam shaping can be extended to more general localized fields in the nonparaxial regime. In particular, we are interested in transforming wide-angle converging waves into a shape-preserving accelerating beam, specially when the beam-width remains near the diffraction limit [120].

It is important to note that nonlocal effects of highly anisotropic metamaterials can induce significant changes in the photonic behavior estimated with effective medium theories. This type of analysis was carried out prior to admission to the Doctoral Programme in Physics, during the completion of the Master's Degree in Advanced Physics, also in the University of Valencia. In particular, we analyzed a 'bulk' metamaterial made by alternative flat layers of metal and dielectric

which clearly manifests birefringence [121]. Due to the collective excitation of surface plasmon polaritons in the subwavelength metallic layers, one can observe simultaneously two Bloch waves exhibiting a counterpropagating behaviour. Such observations in numerical experiments have helped to design correctly the photonic devices object of our analysis, as well as to allow the application of the appropriate corrections in circumstances where the effective medium theories can deviate notably.

Finally, our ultimate goal is to obtain experimental evidences of the formation of non-plasmonic surface waves that may appear at the interface between an anisotropic substrate and a dielectric isotropic material. If, in addition, the latter exhibits a strong luminescent signal, the excitation of surface waves is feasible as a result of coupling the evanescent part which integrates the characteristic dipolar emission. For that purpose, we join forces with Prof. Juan P. Martínez Pastor, responsible for the Optoelectronic Materials and Devices Unit, also belonging to the University of Valencia. His experience in the fabrication of multilayered optical systems, in particular using semiconductor materials, will be decisive for the viability of our proposal.



## 2.7 Publications associated to the present Thesis

This Ph.D. Thesis may be divided in three blocks. The first one is related with invisibility techniques applied to small particles and gave as a result three publications in three different peer-reviewed international journals. Metasurfaces and metalenses design would be the second area, where the student collaborated in the realization of three more articles. Finally, the student performed some experiments in relation with anisotropic waveguides constituting the third block of the present Thesis.

In the introductory part of this Thesis (sections 2.1 to 2.3) we briefly included concepts related with optical scattering and how to reduce the scattered signal in small bodies, which is the first goal of the present work, as mentioned in section 2.6. We investigated about this topic and we designed a mechanism that consists on a cylindrical multilayer structure that allows scattering cancellation. In section 4.1 we will describe a procedure to achieve invisibility with a multilayered nanostructure, and several designs will be presented to improve it in order to gain scattering cancellation. We first describe some satisfactory conditions to turn the nanocavity invisible (see sec-

tion 4.1.2) and how to optimize its design (see section 4.1.3) with the given materials; in our case silver and  $\text{TiO}_2$ . Next, we will apply an effective-medium approach to treat the engineered nanostructure as a hyperbolic medium, enabling a substantial simplification of the problem and more importantly providing schemes for scattering reduction in more general configurations (see section 4.1.1). Three peer-reviewed scientific articles summarize the main results of our study.

The first work, entitled ‘**Conditions for achieving invisibility of hyperbolic multilayered nanotubes,**’ was published in *Optics Communications* journal (impact factor 1.588 in 2016 and ranked 52/92 in the Optics JCR-category). The paper is annexed in the present Thesis and it is cited as reference [115]. The work of the student relied mostly on the analysis of the designed multilayer structure: modeling the multilayered particle, estimating the effective permittivity in the visible range, investigating the tunability of the nanotube permittivity by modifying the filling factor of the structure constituents, analyzing the scattering efficiency in the desired wavelength range, and simulating the optical behavior of the particle when the material elements changed in position and varying the number of layers given a structure thickness.

The second publication is entitled ‘**Optimization of multilay-**

**ered nanotubes for maximal scattering cancellation.**' It was published in *Optics Express* (impact factor 3.307 in 2016 and ranked 17/92 in the Optics JCR-category). This work is attached to this Thesis and it is referenced to as [117]. In this article the student was inspired in the solutions of the previous work and investigated how to improve the structure to reduce its scattering for different outer and inner media. For that, he simulated the scattering efficiency of the structure for different permittivities of the medium outside of it and also varying the permittivity of the material covered by the multilayered cylinder. The student evaluated analytically and numerically the optical behavior of the nanotube when the periodic unit cell is set in a way that the inner and outer layers are made of the same material, so that one might tune their thickness in order to enhance the cancellation of the scattered field. The study was performed in the visible wavelength range, for different filling factors and for both TM and TE incident light polarizations.

The title of the third scientific article within the first block of this Thesis is '**Tunable scattering cancellation of light using anisotropic cylindrical cavities.**' The journal in which it is published is *Plasmonics* (impact factor 2.339 in 2016 and ranked 114/275 in the Materials Science, Multidisciplinary JCR-category). This paper

is set as an annex of the present Thesis and it is cited as reference [116]. The work of the student for the realization of this article was to perform the modeling and calculations (both analytical and numerical) of the hyperbolic nanoparticle. Calculations were carried out for a wide range of conditions: parameters in the system like the light frequency, the inner and outer radii of the uniaxial nanotube, the permittivity of the media surrounding the hyperbolic nanocavity, and the metamaterial anisotropy employed to analyze the invisible shell were varied to complete our study.

The second part of the Thesis is focused on the design and performance analysis of metal-dielectric metalenses and metasurfaces when they are used to control the light wavefront. In section 2.4 we gave a glimpse of the advantages when using this MD structures to alter at will the main light properties, such as its direction of propagation. It is theoretically possible to reach a high spatial localization near the diffraction limit with the designed subwavelength MD metasurfaces, as it is described in the following papers which are published in diverse peer-reviewed international journals.

The results derived in this second research line led to the publication of three scientific articles. The first of them is titled '**Accelerating wide-angle converging waves in the near field**' and it was pub-

lished in *Journal of Optics* (impact factor 1.847 in 2015 and ranked 36/90 in the Optics JCR-category). The second work is entitled ‘**Ultrathin high-index metasurfaces for shaping focused beams**’ and it was published in *Applied Optics* (impact factor 1.598 in 2015 and ranked 45/90). The third and last publication of this block is entitled ‘**Metacoatings for wavelength-scale, high-numerical-aperture plano–concave focusing lenses.**’ It was published in *Journal of the Optical Society of America B* (impact factor 1.843 and ranked 41/92 in 2016). In all these three cases the student contributed in performing certain numerical simulations, mostly using COMSOL Multiphysics.

Finally, in the third part of this Thesis the student carried out some exploratory experiences with the objective of obtaining experimental evidences of the existence of surface waves in anisotropic all-dielectric waveguides. The work of the student in this task consisted on fabricating a planar active waveguide supported by an anisotropic material; specifically we used a  $\text{TeO}_2$  substrate. Furthermore, the active layer is made of perovskite, and the deposition was performed by using a group of various common, fast and cheap techniques, such as Doctor-blading and spin-coating. After the fabrication process, the student characterized the prepared sample (see section 4.3.1). He also

conducted some experimental measurements (procedure described in section 4.3.2), and subsequently he confirmed that the given results were in agreement with the ones obtained from numerical simulations (see also section 4.3.3). At the moment of the Doctoral Thesis deposit, there is an article in preparation collecting the main results of our study.

# Chapter 3

## Methodology

In this section we describe a number of mathematical procedures, basic theoretical schemes and numerical methods enabling the proper design of metamaterial nanostructures, which exhibit certain interesting optical effects such as scattering cancellation and efficient beam shaping, to mention those that are more relevant in this Thesis. For this purpose, we follow the Mie theory of scattering to evaluate the scattering cross section of cylindrical nanostructures. In particular we focus on multilayered structures, where metals and dielectric materials can be combined. In addition, useful approximations such as the effective medium approach are briefly described, which allows a simplified calculation in our designs. Finally, numerical methods as

the finite element method are succinctly outlined, providing a valuable tool to simulate the optical behavior of complex nanostructures and potentially confirming the validity of our approaches.

### 3.1 Mie theory

In 1908, Gustav Mie wrote a well-known paper focused on light dispersion by spherical particles, motivated by the striking chromatic effects observed in colloidal gold solutions. Nowadays, the interest in Mie's theory covers a much broader spectrum. Note that plane wave scattering by a homogeneous isotropic sphere is commonly referred to as Lorenz-Mie theory [122, 123]. Nonspherical particles can also be treated analytically, though restricted to simple geometries, by using the guidelines of the Lorenz-Mie theory [124]. Here we consider multilayered cylindrical structures, a particular case enabling analytical solutions to the Maxwell's equations [125, 126]. Furthermore, we develop a matrix formalism for the rapid evaluation of the scattering efficiency of our stratified nanotubes.



### 3.1.1 Particles with multilayered coating

The nanoscatterer considered here is a cylindrical shell made of a multilayered nanostructure formed by  $N$  layers. The thickness of the shell is  $T = R_{N+1} - R_1$ , where  $R_{N+1}$  (also denoted by  $R$ ) is the outer radius of the whole structure and  $R_1$  is the inner radius of the cylinder, as shown in fig. 3.1. We will assume that the core of the structure is made of a material with permittivity  $\varepsilon_C$ , and the cylinder is embedded in a medium of dielectric constant  $\varepsilon$ . The permittivity of a given layer  $q$  is then characterized by  $\varepsilon_q$ .

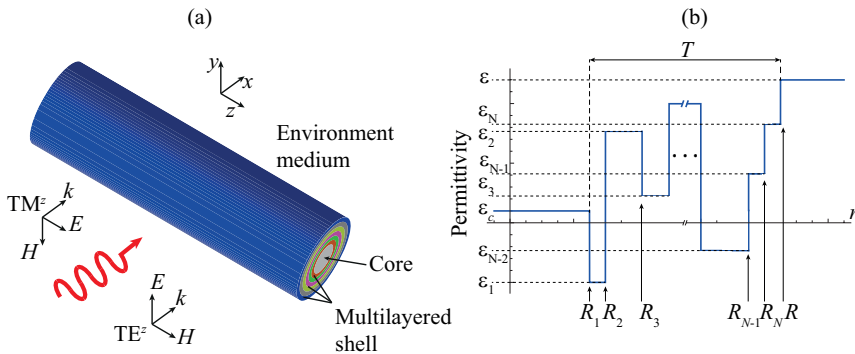


Figure 3.1: (a) Illustration of the multilayered and infinitely-long nanotube. (b) Permittivity of the scatterer as a function of the radial coordinate.

Assuming the incident light is a  $TM^z$  polarized plane wave (for incident  $TE^z$  polarized light the fields would be simply determined by means of the duality principle [127]) which propagates along  $x$  axis

direction, the electric field for the incident light can be written as

$$\mathbf{E}_{in} = \hat{z}E_0 \sum_{n=-\infty}^{+\infty} i^n J_n(kr) \exp(in\phi), \quad (3.1)$$

expressed in function of the radial and azimuthal cylindrical coordinates,  $r$  and  $\phi$  respectively, a constant amplitude  $E_0$ , the Bessel function of first kind and order  $n$ ,  $J_n(\cdot)$ , and the wavenumber  $k = k_0\sqrt{\varepsilon}$ , where  $k_0 = \omega/c$  is the vacuum wavenumber. In addition, the scattered electric field outside the structure ( $r > R$ ) is set as [122]

$$\mathbf{E}_{sca} = -\hat{z}E_0 \sum_{n=-\infty}^{+\infty} a_n i^n H_n^{(1)}(kr) \exp(in\phi), \quad (3.2)$$

where  $H_n^{(1)}(\cdot) = J_n(\cdot) + iY_n(\cdot)$  is the Hankel function of first kind and order  $n$ . The coefficients  $a_n$  of eq. (3.2) must be determined imposing the proper boundary conditions. The total electric field outside the structure is the sum of the incident field given in eq. (3.1) and the scattered one of eq. (3.2),  $\mathbf{E}_{tot} = \mathbf{E}_{in} + \mathbf{E}_{sca}$ .

On the other hand, for the electric field in the layer  $q$  of the stratified shell, we have [122]

$$\mathbf{E}_q = \hat{z}E_0 \sum_{n=-\infty}^{+\infty} i^n [b_{n,q}J_n(k_q r) + c_{n,q}Y_n(k_q r)] \exp(in\phi), \quad (3.3)$$

where  $R_q < r < R_{q+1}$ ,  $q = 1, 2, 3, \dots, N$  is the medium considered, and the wavenumber is  $k_q = k_0\sqrt{\varepsilon_q}$ . The electric field in the core of the nanoscatterer, ( $r < R_1$ ), is set as

$$\mathbf{E}_C = \hat{z}E_0 \sum_{n=-\infty}^{+\infty} i^n d_n J_n(k_C r) \exp(in\phi), \quad (3.4)$$

and the wavenumber is  $k_C = k_0\sqrt{\varepsilon_C}$  in this case. Finally, the scattering coefficients  $a_n$ ,  $b_n$ ,  $c_n$  and  $d_n$  are determined by setting the appropriate boundary conditions.

The above-mentioned conditions are based on the continuity of the  $z$ -component of the electric field and the  $\phi$ -component of the magnetic field,  $H_\phi = (i/\omega)\partial_r E_z$ . These boundary conditions must be accomplished at the environment-multilayer shell interface ( $r = R$ ) and also at all internal interfaces ( $r = R_{q+1}$ , with  $0 < q < N$ ). For the internal interfaces at  $r = R_{q+1}$  the boundary conditions can be expressed in matrix form as [128]

$$D_{n,q}(R_{q+1}) \cdot \begin{bmatrix} b_{n,q} \\ c_{n,q} \end{bmatrix} = D_{n,q+1}(R_{q+1}) \cdot \begin{bmatrix} b_{n,q+1} \\ c_{n,q+1} \end{bmatrix}, \quad (3.5)$$

where

$$D_{n,m}(x) = \begin{bmatrix} J_n(k_m x) & Y_n(k_m x) \\ Z_m^{-1} J'_n(k_m x) & Z_m^{-1} Y'_n(k_m x) \end{bmatrix} \quad (3.6)$$

is called the dynamical matrix. It is given in terms of the reduced impedance, that is  $Z_m = 1/\sqrt{\varepsilon_m}$ , and  $Z_q = 1/\sqrt{\varepsilon_C}$  for the core of the nanocavity ( $m = C$ ). The prime in the Bessel functions  $J_n(x)$  and  $Y_n(x)$  means derivative with respect to the argument  $x$ . In a similar way, for the interface at  $r = R_1$  we have

$$D_{n,1}(R_1) \cdot \begin{bmatrix} d_n \\ 0 \end{bmatrix} = D_{n,2}(R_1) \cdot \begin{bmatrix} b_n \\ c_n \end{bmatrix} \quad (3.7)$$

On the other hand, at the utmost interface  $r = R$  we can apply the proper boundary conditions and we get

$$D_{n,N}(R) \cdot \begin{bmatrix} b_{n,N} \\ c_{n,N} \end{bmatrix} = D_{n,N+1} \cdot \begin{bmatrix} 1 - a_n \\ -i a_n \end{bmatrix}, \quad (3.8)$$

where  $Z_{N+1} = 1/\sqrt{\varepsilon}$  and  $k_{N+1} = k$ .

In particular, we are interested on the fields outside of the nanotube and in its core. In fact, there is a way of evaluating these fields with no need to calculating any field in the intermediate layered medium.

For that purpose, we use the following matrix equation:

$$\begin{bmatrix} d_n \\ 0 \end{bmatrix} = M_n \cdot \begin{bmatrix} 1 - a_n \\ ia_n \end{bmatrix}, \quad (3.9)$$

where the matrix  $M_n$  is calculated as follows:

$$\begin{aligned} M_n &= \begin{bmatrix} M_{n,11} & M_{n,12} \\ M_{n,21} & M_{n,22} \end{bmatrix} = \\ &= [D_{n,C}(R_1)]^{-1} \cdot \left\{ \prod_{q=1}^N D_{n,q}(R_q) \cdot [D_{n,q}(R_{q+1})]^{-1} \right\} \cdot D_{n,N+1}(R). \end{aligned} \quad (3.10)$$

In particular we obtain

$$a_n = \frac{M_{n,21}}{M_{n,21} + iM_{n,22}}. \quad (3.11)$$

In other words, with our matrix formalism we are able to calculate analytically the coefficients  $a_n$  characterizing the scattered field in eq. (3.2). Finally, it is possible to estimate the scattering efficiency as [122]

$$Q_{sca} = \frac{2}{kR} \sum_{n=-\infty}^{+\infty} |a_n|^2. \quad (3.12)$$

## 3.2 The effective medium approach in 1D stratified periodic media

The treatment of electromagnetic wave propagation in a periodic medium has certainly some similarities with the motion of electrons in crystalline solids. Therefore, the formulation based on the Kronig-Penney model that is used in elementary band theory of solids can be appropriately applied to the description of optical radiation in periodic layered media [129]. Next we consider a simple stratified periodic medium consisting of alternating flat layers made of transparent non-magnetic materials. The direction perpendicular to the layers is set by the  $x$  axis. The variation of the permittivity in the unit cell is given by  $\varepsilon_1$ , for  $x_0 < x < x_1$ , and  $\varepsilon_2$ , for  $x_1 < x < x_2$ . In addition,  $\varepsilon(x) = \varepsilon(x + \Lambda)$  holds, where  $w_1 = x_1 - x_0$  ( $w_2 = x_2 - x_1$ ) is the thickness of the layer of permittivity  $\varepsilon_1$  ( $\varepsilon_2$ ) and  $\Lambda = w_1 + w_2$  stands for the period of the structure.

Following the Floquet theorem, the electric field in a periodic medium may be set as  $\mathbf{E}(x + \Lambda) = \mathbf{E}(x) \exp(iK\Lambda)$ , where  $K$  stands for the well-known Bloch wavenumber. Furthermore, the equation  $\cos(K_q\Lambda) = \frac{1}{2}\text{tr}\{M_q\}$  provides the dispersion relation for  $q = \text{TE}$  and  $q = \text{TM}$  modes, written in terms of the trace of the unit cell transla-

tion matrix [2, 129]. Denoting  $K_{TE}$  ( $K_{TM}$ ) the Bloch wavenumber  $K$  associated with the TE (TM) mode, and writing

$$\begin{aligned} \text{tr}\{M_{TE}\} &= 2 \cos(w_1 k_{x1}) \cos(w_2 k_{x2}) \\ &- \frac{(k_{x1}^2 + k_{x2}^2)}{k_{x1} k_{x2}} \sin(w_1 k_{x1}) \sin(w_2 k_{x2}), \end{aligned} \quad (3.13a)$$

$$\begin{aligned} \text{tr}\{M_{TM}\} &= 2 \cos(w_1 k_{x1}) \cos(w_2 k_{x2}) \\ &- \frac{(\varepsilon_2^2 k_{x1}^2 + \varepsilon_1^2 k_{x2}^2)}{\varepsilon_1 \varepsilon_2 k_{x1} k_{x2}} \sin(w_1 k_{x1}) \sin(w_2 k_{x2}), \end{aligned} \quad (3.13b)$$

we find the dispersion equation of a binary periodic medium for each polarization. Also,  $k_{xi} = \sqrt{\varepsilon_i k_0^2 - (k_y^2 + k_z^2)}$  gives the  $x$ -component of the wave vector in each part of the unit cell.

For ultra-thin metallic layers, typically lower than the penetration depth, the dispersion curves resembles ellipses and circumferences for TM and TE modes, respectively. In reference to such point, recent advances in nanofabrication technology open the door for engineering this kind of subwavelength structures [130]. At increasing values of the metal width, however, some deviations are evident giving rise to the so-called nonlocal effects. Neglecting at the moment these effects, for near-infrared and visible wavelengths, nanolayered metal-dielectric compounds enable a simplified description of the medium by using the long-wavelength approximation; note that this also in-

volves an homogenization not only of the structured metamaterial but also of the wave fields [32, 131]. The MD multilayered metamaterial is represented as a uniaxial plasmonic crystal, having its optical axis oriented normally to the layers. Moreover, a relative permittivity tensor  $\underline{\varepsilon} = \varepsilon_{\parallel} (\mathbf{xx}) + \varepsilon_{\perp} (\mathbf{yy} + \mathbf{zz})$ , where [132]

$$\varepsilon_{\parallel} = \frac{\varepsilon_1 \varepsilon_2}{(1-f)\varepsilon_2 + f\varepsilon_1}, \quad (3.14)$$

gives the permittivity along the optical axis, and

$$\varepsilon_{\perp} = (1-f)\varepsilon_1 + f\varepsilon_2 \quad (3.15)$$

provides the permittivity in the transversal direction. The metal rate in a unit cell is given by the filling factor  $f = w_2/(w_1 + w_2)$ . The dispersion equation for TE ( $o$ -) waves is then given by  $k_x^2 + k_y^2 + k_z^2 = \varepsilon_{\perp} k_0^2$ , where  $k_x$  represents the Bloch wavenumber  $K_{TE}$ , and for TM ( $e$ -) waves we have

$$\frac{k_x^2}{\varepsilon_{\perp}} + \frac{k_y^2 + k_z^2}{\varepsilon_{\parallel}} = k_0^2, \quad (3.16)$$

where  $k_x$  represents now the Bloch wavenumber  $K_{TM}$ .



### 3.2.1 Hyperbolic media

As we have discussed above, nanolayered metal-dielectric compounds behave like plasmonic homogeneous crystals. Under certain conditions, the second-rank tensor characterizing the permittivity in the medium include elements of opposite sign, leading to extremely anisotropic metamaterials [133,134]. This class of nanostructured media with hyperbolic dispersion, as seen in eq. (3.16), are proposed for a plethora of practical applications ranging from biosensing to fluorescence engineering [135].

A uniaxially anisotropic medium which can be described by a permittivity tensor with negative  $\varepsilon_{\parallel}$  but positive  $\varepsilon_{\perp}$  is referred as type I hyperbolic medium. In this case, eq. (3.16) leads to a two-sheet hyperboloid [136]. Contrarily, type II hyperbolic media leads to positive  $\varepsilon_{\parallel}$  and negative  $\varepsilon_{\perp}$ , thus eq. (3.16) giving a one-sheet hyperboloid. Importantly, a hyperbolic dispersion allows wave propagation over a broad spatial spectrum, which includes forbidden spectral bands in ordinary isotropic dielectrics [8]. At the optical range, hyperbolic media can be manufactured by using metallic nanowires instead of metal-dielectric multilayers [137].

The system under analysis for numerical purposes consists of a periodic binary medium, where a transparent dielectric medium is

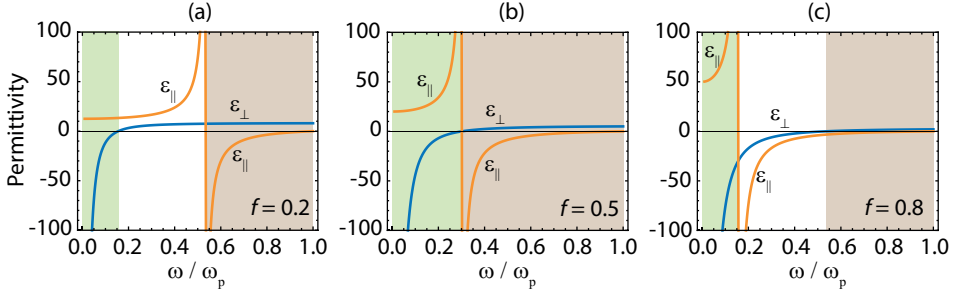


Figure 3.2: Real part of the components  $\varepsilon_{\parallel}$  (orange line) and  $\varepsilon_{\perp}$  of the permittivity tensor for the multilayered metamaterial composed of a plasmonic material, which follows the Drude model and  $\gamma = \omega_P/100$ , and an insulator with  $\varepsilon_I = 10$  [115]. Three different filling factors are considered: (a)  $f = 0.2$ , (b)  $f = 0.5$  and (c)  $f = 0.8$ . Brown shaded regions denote spectral bands where the material exhibits a hyperbolic dispersion of type I; green shaded regions are for hyperbolic dispersion of type II.

referred to as medium 1 which ideally is nondispersive. We take a lossy Drude metal where its permittivity  $\varepsilon_2 = 1 - \omega_P^2/(\omega^2 + i\omega\gamma)$ , and a dielectric medium with permittivity  $\varepsilon_1 = 10$ , varying the filling factor. If necessary, frequencies can be expressed in units of the plasma frequency,  $\omega_P$ . In fig. 3.2 we represent permittivities  $\varepsilon_{\parallel}$  and  $\varepsilon_{\perp}$  of the plasmonic crystals for a wide range of frequencies. For a realistic metamaterial, its dissipative effects are governed by the metal filling factor, thus low values of  $f$  are of great convenience in practice, as plotted in fig. 3.2(a). For low frequencies, propagating  $\text{TE}^x$  modes ( $E_x = 0$ ) cannot exist in the bulk crystal since it behaves like a metal, contrarily to what happens with  $\text{TM}^x$  waves. This is a characteristic

of Type II hyperbolic media. Near the plasma frequency, eq. (3.16) turns to an hyperboloidal shape (Type I hyperbolic medium). Note that the upper limit of this hyperbolic band is determined by the condition  $\varepsilon_{\parallel} = 0$ , occurring precisely at the plasma frequency [45].

### 3.3 Surface bound modes in anisotropic waveguides

Bound modes can arise in all-dielectric multilayered structures. Probably the most known mode of this type is the Bloch surface wave, also known as photonic Tamm state, provided one semi-space is composed of a 1-D photonic crystal [138]. However, dielectric homogeneous media also establish appropriate conditions to sustain surface waves. For instance, Dyakonov surface waves (DSWs) are supported at the interface between an isotropic medium and a birefringent material. Following the original work by Dyakonov, whose English version was reported in 1988 [110], here we consider that the optical axis of a uniaxial medium is set in-plane with respect to the interface. Nevertheless, developments of DSWs proposing alternate materials such as biaxial crystals [139], structurally chiral materials [140], and even structurally-anisotropic multilayered media [141] are still in progress.

### 3.3.1 Dispersion equation of DSWs

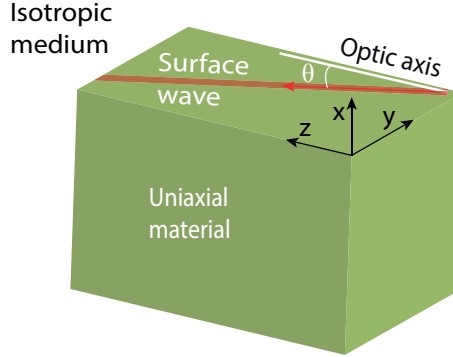


Figure 3.3: Schematic setup supporting DSWs at the plane  $x = 0$ , consisting of a semi-infinite uniaxial material with its optic axis oriented along the  $z$  axis ( $x < 0$ ) and an isotropic substrate ( $x > 0$ ).

Fig. 3.3 shows the optical system under analysis, where we have two semi-infinite media, one of them is isotropic and the second one is birefringent. In particular, the indices “1” and “2” refer to the birefringent material and the isotropic medium, respectively. A comprehensive analysis of this case can be found in [142], and here we will provide the most basic steps. The permittivity of the uniaxial anisotropic medium along its optical axis is set as  $\varepsilon_{z1} = \varepsilon_{\parallel}$ , and the permittivity in the transverse direction is  $\varepsilon_{x1} = \varepsilon_{y1} = \varepsilon_{\perp}$ . From hereon, the permittivity  $\varepsilon_2$  of the isotropic medium in  $x > 0$  will be denoted by  $\varepsilon$ .

We may establish the diffraction equation giving the 2D wave vec-

tor  $\mathbf{k}_D = [0, k_y, k_z]$  of the surface wave propagating in  $x = 0$  analytically. For that purpose, hybrid-polarized surface modes should be considered. In the isotropic medium we consider  $\text{TE}^x$  ( $E_x = 0$ ) and  $\text{TM}^x$  ( $H_x = 0$ ) waves simultaneously, whose wave vectors have identical real components  $k_y$  and  $k_z$  in the plane  $x = 0$ . The electric field in the isotropic medium (also in the birefringent material) may be set as

$$\mathbf{E}_{tot} = \mathbf{E}(x) \exp(ik_y y + ik_z z - i\omega t). \quad (3.17)$$

These fields decay evanescently inside the isotropic medium and in the birefringent material. In the anisotropic medium ( $x < 0$ ) the evanescent electric amplitude can be written as

$$\mathbf{E}(x) = B_{o1} \hat{b}_{o1} \exp(-ik_{o1} x) + B_{e1} \hat{b}_{e1} \exp(-ik_{e1} x), \quad (3.18)$$

where the ordinary and extraordinary waves in the uniaxial medium decay exponentially with rates given by  $\kappa_o = -ik_{o1}$  and  $\kappa_e = -ik_{e1}$ , respectively. Note that  $k_{oi} = \sqrt{\varepsilon_{xi} k_0^2 - (k_y^2 + k_z^2)}$  for the  $o$ -waves, and  $k_{ei} = \sqrt{\varepsilon_{zi} k_0^2 - (k_y^2 + \varepsilon_{zi} k_z^2 / \varepsilon_{xi})}$  for the  $e$ -waves. The vectors  $\hat{b}_{o1}$  and  $\hat{b}_{e1}$  indicate the state of polarization of the  $o$ -wave and the  $e$ -wave, respectively, with constant amplitudes  $B_{o1}$  and  $B_{e1}$ . In the isotropic

medium ( $x > 0$ ) the amplitude of the electric field is

$$\mathbf{E}(x) = A'_{TE2} \hat{a}_{TE2} \exp(ik_{x2}x) + A'_{TM2} \hat{a}_{TM2} \exp(ik_{x2}x), \quad (3.19)$$

where the evanescent decay for TE and TM modes is  $\kappa = -ik_{x2}$ . Now the amplitudes  $A'_{TE2}$  and  $A'_{TM2}$ , and the vectors  $\hat{a}_{TE2}$  and  $\hat{a}_{TM2}$ , are characteristic for the TE and TM modes.

Once we have the amplitudes in both sides of the interface, we apply the boundary conditions at  $x = 0$ , which reduce to

$$\begin{bmatrix} 0 \\ B_{o1} \\ 0 \\ B_{e1} \end{bmatrix} = \mathbf{M}_h \begin{bmatrix} A'_{TE2} \\ 0 \\ A'_{TM2} \\ 0 \end{bmatrix}, \quad (3.20)$$

where the transmission matrix  $\mathbf{M}_h = \mathbf{D}_1^{-1} \cdot \mathbf{D}_2$  establishes a relationship between the amplitudes of *hybrid*-polarized modes. More specif-

ically,

$$\mathbf{D}_i = \begin{bmatrix} k_{oi} & -k_{oi} & k_y k_z & k_y k_z \\ 0 & 0 & k_z^2 - \varepsilon_{xi} k_0^2 & k_z^2 - \varepsilon_{xi} k_0^2 \\ -k_y k_z & -k_y k_z & \varepsilon_{xi} k_0^2 k_{ei} & -\varepsilon_{xi} k_0^2 k_{ei} \\ -k_z^2 + \varepsilon_{xi} k_0^2 & -k_z^2 + \varepsilon_{xi} k_0^2 & 0 & 0 \end{bmatrix} \quad (3.21)$$

applies for the anisotropic medium, and

$$\mathbf{D}_i = \begin{bmatrix} k_z & k_z & -k_y k_{xi} & k_y k_{xi} \\ -k_y & -k_y & -k_z k_{xi} & k_z k_{xi} \\ k_y k_{xi} & -k_y k_{xi} & \varepsilon_i k_0^2 k_z & \varepsilon_i k_0^2 k_z \\ k_z k_{xi} & -k_z k_{xi} & -\varepsilon_i k_0^2 k_y & -\varepsilon_i k_0^2 k_y \end{bmatrix} \quad (3.22)$$

is used for the isotropic medium. Finally, Dyakonov equation is the solution to eq. (3.20), giving

$$k_0^2 k_y^2 \varepsilon_{\perp} (\kappa + \kappa_e) (\varepsilon \kappa_o + \varepsilon_{\perp} \kappa) = \kappa_o k_z^2 (\kappa + \kappa_o) (\varepsilon \kappa_o^2 + \varepsilon_{\perp} \kappa \kappa_e), \quad (3.23)$$

which provides a spectral map of allowed values  $(k_y, k_z)$ . Assuming that  $\varepsilon_{\parallel}$ ,  $\varepsilon_{\perp}$ , and all decay rates are positive, the additional restriction  $\varepsilon_{\perp} < \varepsilon < \varepsilon_{\parallel}$  can be deduced for the existence of surface waves. As a consequence, positive birefringence is mandatory to ensure a station-

ary solution of Maxwell's equations. Importantly, DSWs cannot exist when propagating along the optical axis ( $k_y = 0$ ) and perperdicularly to this ( $k_z = 0$ ).

### 3.3.2 A thin dielectric waveguide on an anisotropic substrate

Let us now assume that a new medium (numbered as “3”) is included in our photonic system. Again, medium “1” is anisotropic and medium “2” is isotropic, the latter having a width  $w_2$ . Bound modes now can be determined using again eq. (3.20), which should be conveniently modified. In particular the column vector  $[A'_{TE2}, 0, A'_{TM2}, 0]$  is now associated with the semi-infinite medium “3” so that we should use  $[A'_{TE3}, 0, A'_{TM3}, 0]$  instead. In addition, the matrix of the stratified optical system is now evaluated as  $\mathbf{M}_h = \mathbf{D}_1^{-1} \cdot \mathbf{D}_2 \cdot \mathbf{P}_2 \cdot \mathbf{D}_2^{-1} \cdot \mathbf{D}_3$ , taking into account the propagation matrix [142]

$$\mathbf{P}_i = \begin{bmatrix} e^{-ik_{xi}w_i} & 0 & 0 & 0 \\ 0 & e^{ik_{xi}w_i} & 0 & 0 \\ 0 & 0 & e^{-ik_{xi}w_i} & 0 \\ 0 & 0 & 0 & e^{ik_{xi}w_i} \end{bmatrix}, \quad (3.24)$$



which is characteristic of the thin dielectric waveguide.

Note that eq. (3.20) provides not only Dyakonov surface waves in interface between the thin isotropic waveguide and the birefringent cladding. This equation also provides any other kind of bound modes, not necessarily coined as surface waves. In particular, guided modes and leaky waves can also be estimated using our matrix formulation.

### 3.4 Finite Element Method (FEM)

Scientific advances and modern technological improvement challenge scientists to carry out high resources' consuming calculations. The applicability of these jobs covers a wide range of scientific areas such as photonics in general but also nuclear applications, aeronautics, water course management or radiofrequency applications. To properly understand the analyzed problems we need mathematical models to simulate the behavior of the system. These models are based on differential and integral equation systems and the FEM has become one of the most frequently used methods for solving them. Although this is a method that requires an intensive use of a computer, it can be employed to solve the majority of these problems. It can be applied in the resolution of projects in one, two or three dimensions even if

the geometry is complex or the considered material is heterogeneous.

In a few cases the problems can be solved analytically, as the examples given in previous subsections, but most of them need a numerical method for resolution. The FEM consists on using a simple approximation of unknown variables, typically based upon different types of discretizations, to transform the differential or integral equations into numerical model equations which are easier to solve. For a detailed description see [143–145]. The first step of this approximation is to replace the continuous system by an equivalent discrete one. To do so we divide the domain into smaller subdomains called finite elements.

The elements are connected with points called nodes, in which we solve the numerical model equations. Solving methods are based on comparison with a test function (fig. 3.4) built from a set of combined basis functions. Assuming the function that we want to model is  $u$ , we can approximate it by

$$u \approx \sum u_i \psi_i, \quad (3.25)$$

where the approximated function can be described with a set of basis functions  $\psi_i$  properly weighted.

In the example shown in fig. 3.4 the basis functions  $\psi_i$  can only have values 1 at their respective nodes or 0 at others. But with the

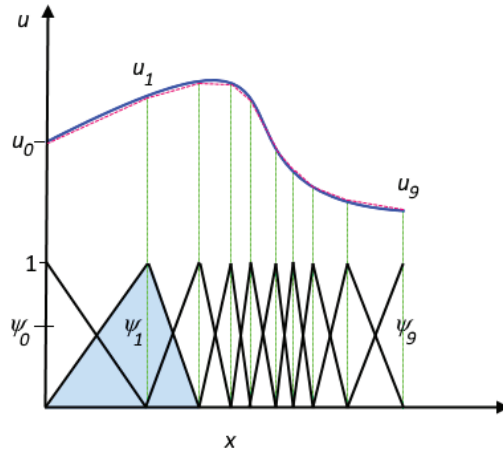


Figure 3.4: Example of 1D resolution process by evaluating a set of basis test functions  $\psi_i$  properly weighted by  $u_i$  [146]. The interval where function  $u$  is defined is discretized in 10 nodes or elements in which the approximated function  $u_j$  is evaluated.

appropriate weight  $u_i$  in each case we can obtain a very approximated solution of the function  $u$ . These weights are calculated with different numerical methods such as direct methods based on LU decomposition or iterative methods, depending on the job, which are not described in this Thesis but can be found in literature [147, 148].

It is easy to observe that we need more points (a finer mesh) for the areas of the domain in which we think that our function is more abrupt. By doing so we will reproduce better the curve or field that we are calculating.

### 3.4.1 Commercial software based on FEM

In our case, we chose a commercial software called COMSOL Multiphysics to model and simulate our photonic structures [146]. The version employed here is v.5.1.0. It allows us to perform the simulations from its graphical user interface or from MatLab software. The first way might be more intuitive since you can graphically model the structure and the program presents a lists of parameters, materials, geometry characteristics and study resolutions visible in every moment. Another advantage of the software is that the user is capable of giving different attributes to any geometry domain at any moment. We can select a different material for each region, set the proper boundary conditions and, if needed, a constraint.

For the simulations which are required we need the module ‘electromagnetic waves, frequency domain.’ After selecting the study for each case we define the parameters to use in the model and build the geometry. With the geometry set and the materials defined we have to mesh our model (fig. 3.5). This mesh is a subdivision of each domain into small finite elements to calculate the electromagnetic fields in each discretized point. As it was mentioned before, we must adjust the mesh by increasing the density points in areas where the electromagnetic field is expected to vary more (in interfaces between two

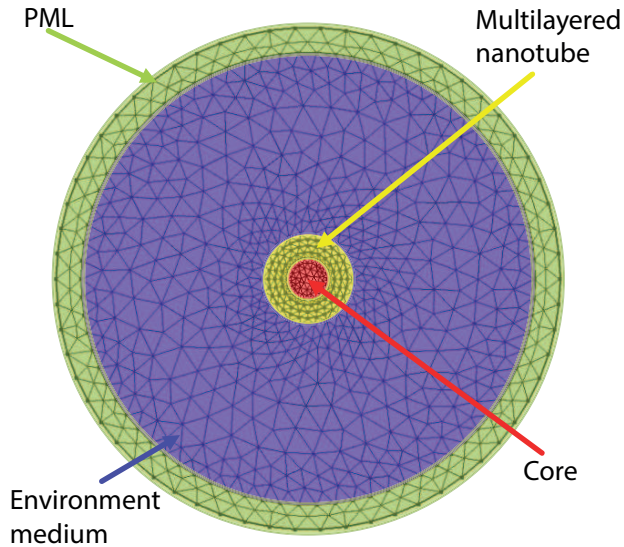


Figure 3.5: Division of each domain into multiple subdomains. Example of a COMSOL image which shows a meshed model of a multilayer nanotube in an environment medium developed for performing some studies of scattering cancellation.

materials with quite different refractive index) and leaving it larger (but never larger than half a wavelength) in areas where we think the variation of the fields is smoother. By doing this we can reach enough accuracy and at the same time we save calculation resources, i.e. the job will be less time consuming but we will have results with high enough precision. In some calculations, like for obtaining the propagation constant associated to a mode traveling in a waveguide, we also need to give the program an appropriate seed which can be estimated

with other methods or we can even try some values from experimental results. In the case of scattering wave fields this is not necessary and the program will provide us all the electric and magnetic fields resulted from the given illumination and the appropriate boundary conditions, typically Perfectly Matched Layers (PMLs).

# Chapter 4

## Results and analysis

In this chapter we gather the main results achieved for this Ph.D. Thesis work. Section 4.1 gives the most important conclusions of the first from the three blocks in which this Thesis consists of. This is focused on the conditions that an anisotropic cylindrical particle must accomplish to make invisibility feasible. Then we clarify how to optimize the structure geometry to improve its scattering cancellation, and we also compare such results with those estimated by means of simplified models based on considering the scatterer having a hyperbolic structure.

In section 4.2 we meet with the second block of the studies performed for the elaboration of this work. We collect the most relevant

results of the numerical simulations which I have performed with the purpose of investigating the shaping of focused beams by using ultrathin high-index metasurfaces and the design conditions that these metasurfaces need to hold. In addition, we explore beamshaping under high NA and the structures employed to achieve this effect. Briefly, we also mention how to exploit metasurfaces for accelerating converging waves in the near field.

Finally, section 4.3 is devoted to explain the experimental part of the work in this Thesis; that consists on the third block of it. Our objective is to find appropriate conditions for the observation of surface waves in all-dielectric materials. We need to mention the experimental techniques employed both in the fabrication and in the characterization processes and we introduce the reader to them. After this, some experimental results are presented and compared with theoretical calculations that prove their validity.

## 4.1 Anisotropic particles

This first section is focused on the capability of multilayered scatterers to become optically undetectable. In particular, an engineered metastructure that consists of a MD multilayered nanotube will con-



duct to invisibility, and a subsequent interpretation of our estimations is given in detail. This nanocavity is characterized by some opto-geometric parameters, such as its thickness including its constituent layers, its metal filling factor, and in general the materials that conform the multilayered nanoparticle. Our study is based on fixing the materials employed and tuning the remaining parameters in addition to the wavelength of the radiation for a complete spectroscopy examination. By analyzing the structure behavior under these changes we are able to estimate the conditions that must be satisfied to enhance the scattering cancellation. Furthermore, with the estimations obtained we proceed to optimize the nanostructure thus dropping the scattering cross section to a minimum and making the nanoparticle undetectable in the far field. We also compare the results with the ones calculated if an effective medium approach is considered.

#### 4.1.1 Invisibility in hyperbolic nanotubes

Let us start by establishing the proper conditions for a multilayered cylindrical nanostructure to become invisible. The structure used in our study is an infinitely long MD multilayered nanotube, shown in fig. 4.1. The stratified shell is periodically arranged in deep-subwavelength units so that the effective medium approach described

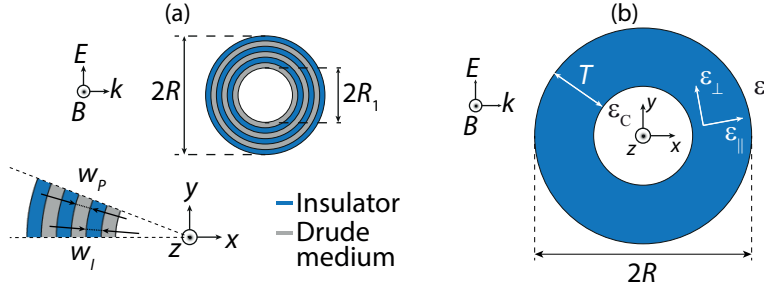


Figure 4.1: (a) Schematics of the multilayered metamaterial establishing a radial form birefringence. (b) Illustration of the anisotropic nanotube under analysis.

in section 3.2 can be employed. The permittivities along the optic axis (OA),  $\epsilon_{\parallel}$ , which is radially directed, and perpendicular to the OA,  $\epsilon_{\perp}$ , constitute the components of the permittivity tensor  $\underline{\epsilon} = \epsilon_{\parallel} \hat{r}\hat{r} + \epsilon_{\perp} \hat{\theta}\hat{\theta} + \epsilon_{\perp} \hat{z}\hat{z}$ . To estimate analytically the scattering efficiency of the anisotropic nanotube, we followed the Lorenz-Mie scattering method given for instance in refs. [149] and [150]; also details are given in one of our recently published manuscripts [115]. For numerical purposes, the multilayered nanotube is composed of a nondispersive insulator with permittivity  $\epsilon_d = 10$  in the frequency range of study and a metal which permittivity follows the Drude model in the spectral range of interest:

$$\epsilon_m = 1 - \frac{\omega_P^2}{\omega^2 + i\omega\gamma}. \quad (4.1)$$

Again,  $\omega_P$  represents the plasma frequency of the plasmonic material and  $\gamma$  is the damping rate.

As shown in fig. 3.2, which was previously discussed in section 3.2.1, when  $\text{Re}(\varepsilon_{\parallel})\text{Re}(\varepsilon_{\perp}) < 0$  is accomplished provided that  $\text{Re}(\varepsilon_{\perp}) > 0$  it corresponds with the so-called hyperbolic regime of type I, whereas  $\text{Re}(\varepsilon_{\perp}) < 0$  denotes a type II hyperbolic medium. For the particular case when both insulator and plasmonic layers have the same width ( $f = 0.5$ ), both a zero of  $\varepsilon_{\perp}$  and a pole of  $\varepsilon_{\parallel}$  occur simultaneously at the frequency  $\omega_P/\sqrt{1 + \varepsilon_d}$ , in addition happening when  $\text{Re}(\varepsilon_m) = -\varepsilon_d$ . Importantly, the hyperbolic regime spans the whole spectrum below plasma frequency in such a case.

In fig. 4.2 we show the scattering efficiency in terms of the material filling factor that corresponds with the Drude medium and considering the latter with a low damping factor  $\gamma = \omega_P/100$ . The numerical evaluation of  $Q_{sca}$  is performed for a  $\text{TE}^z$ -polarized incident light; the case of  $\text{TM}^z$ -polarized waves will be treated in section 4.1.2. We assume the anisotropic cavity immersed in air ( $\varepsilon = \varepsilon_C = 1$ ) and that it is small enough ( $R_1 = T = k_P^{-1}/20$  where  $k_P = \omega_P/c$ ) to excite only the dipole term  $n = 1$ . The symmetric and antisymmetric coupling between the surface charges associated with the cavity and surface polaritons at  $r = R_1$  and  $r = R$  [151, 152] produce two resonances shown

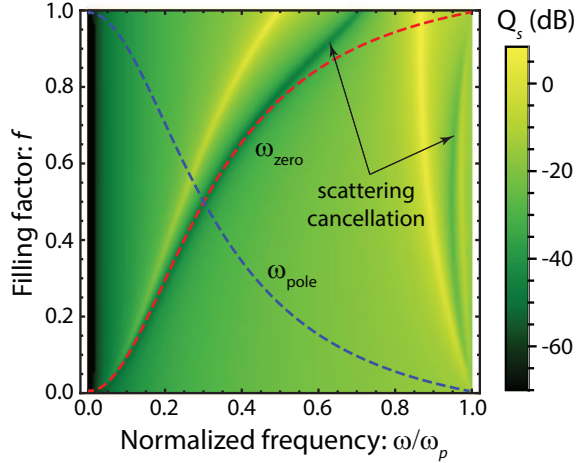


Figure 4.2: Scattering efficiency  $Q_{sca}$  expressed in dB of an anisotropic cavity with  $R_1 = T = k_P^{-1}/20$  immersed in air ( $\varepsilon = \varepsilon_C = 1$ ). The filling factor of the Drude medium varies from 0 to 1, where the damping rate is kept at  $\gamma = \omega_P/100$ . The calculations are performed for a  $TE^z$ -polarized incident light. The zeros of  $\varepsilon_{\perp}$  and the poles of  $\varepsilon_{\parallel}$  are included in red dashed line and blue dashed line, respectively.

in fig. 4.2. Close to the resonance we find a minimum in scattering.

Scattering cancellation is virtually achieved for fundamental frequencies  $\omega_{zero}$  and represented by the red dashed line in fig. 4.2. These frequencies coincide with the condition of  $\varepsilon_{\perp}$  near zero. In principle, we should be able to tune the invisibility frequency just changing the filling factor  $f$ , as suggested by Kim *et al* [82]. However, we find that close to the plasma frequency it is not possible, even considering values of  $f$  close to unity. The invisibility associated with the fundamental peak is observed in this case at an intermediate frequency

between the symmetric and antisymmetric resonances below  $\omega_P$ . In the limit of a filling factor  $f \rightarrow 1$  the invisibility condition is found for a frequency  $\omega = 0.707\omega_P \approx \omega_P/\sqrt{2}$ , coinciding with the surface plasmon frequency. On the other hand, as it is shown in fig. 4.2,  $\omega_{zero}$  approaches the plasma frequency at this limit.

To achieve scattering cancellation near the plasma frequency we should take profit of the second minimum of scattering efficiency located close to  $\omega_P$  as we show in fig. 4.2. For instance, for a filling factor of  $f = 0.5$  there is a first minimum of  $Q_{sca} = 30.7 \cdot 10^{-7}$  at  $\omega = 0.3\omega_P$  and there is also a secondary minimum of  $Q_{sca} = 5.11 \cdot 10^{-5}$  at a frequency  $\omega = 0.9454\omega_P$ . We see that the invisibility for a lower energy provides a better performance than the one found at a higher frequency.

In fig. 4.3 we present the scattering efficiency of different nanocavities with a filling factor  $f = 0.5$  and a damping factor given by  $\gamma = \omega_P/100$ . The ratio of the thickness of the nanocavity to its outermost radius is set constant ( $T/R = 1/2$ ) in all the structures studied. We compare the structure analyzed in fig. 4.2 with those where the inmost radius and tube thickness take the values  $R_1 = T = k_P^{-1}/4$ ,  $R_1 = T = k_P^{-1}/2$  and  $R_1 = T = k_P^{-1}$ . All curves show essentially the same behavior regarding the spectral position of the fundamental

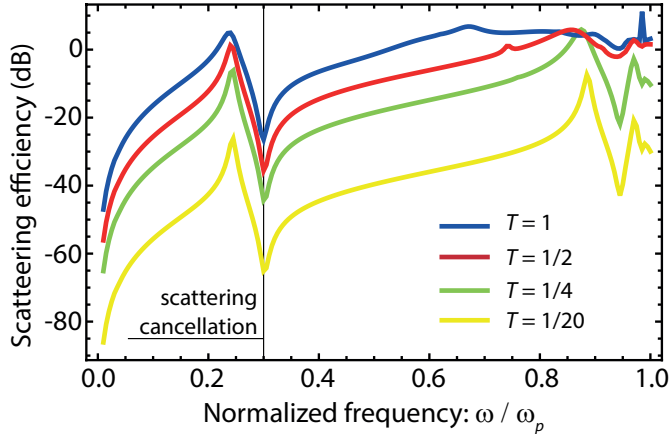


Figure 4.3: Scattering efficiency for nanocavities with different tube thicknesses  $T$  (expressed in units of  $k_P^{-1}$ ) provided  $T/R = 0.5$  is conserved. Again, the considered filling factor is  $f = 0.5$  and the damping factor is  $\gamma = \omega_P/100$ .

resonance and the scattering cancellation at the lowest energy. For instance, the invisibility is found for  $\omega = 0.3 \omega_P$  in all cases with scattering efficiencies of  $Q_{sca} = 3.7 \cdot 10^{-5}$ ,  $2.7 \cdot 10^{-4}$  and  $2.3 \cdot 10^{-3}$ . We realize that the invisibility window is invariant upon the cavity diameter, provided that the modulation is performed in the subwavelength scale. As expected, the scattering efficiency increases in approximately one order of magnitude when the nanotube doubles its size, although it reaches a minimum at the mentioned frequency.

When we focus on the secondary minimum the situation changes abruptly. For the smallest cavities the scattering pattern remains unaltered except for a scaling factor. However, the rise of additional

resonances at increasing sizes manages the contour of the spectrum in the vicinity of the plasma frequency.

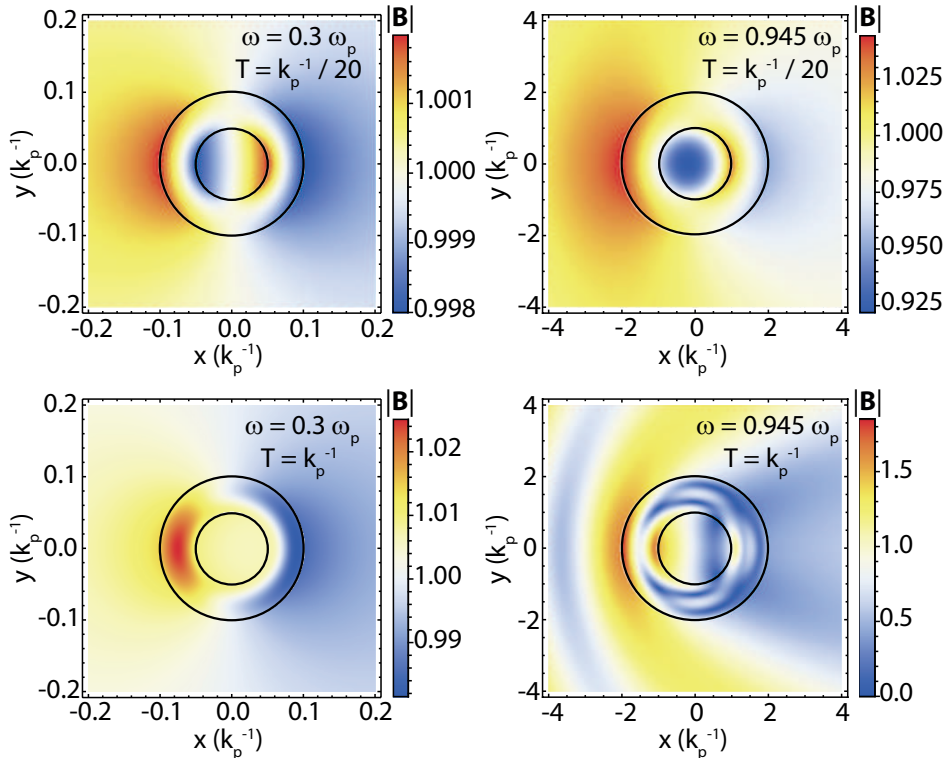


Figure 4.4: Normalized scattering magnetic field  $|\mathbf{B}|/B_0$  for anisotropic cavities characterized by  $R_1 = T = k_p^{-1}/20$  and  $R_1 = T = k_p^{-1}$ , both with  $f = 0.5$ , and for frequencies  $\omega = 0.3\omega_P$  and  $\omega = 0.945\omega_P$ .

In fig. 4.4 we represent the magnetic field near the cylindrical cavities for the frequencies of interest in order to infer further insights. We show  $|\mathbf{B}|/B_0$  for two anisotropic scatterers with  $R_1 = T = k_p^{-1}/20$

and  $R_1 = T = k_P^{-1}$ , with a filling factor  $f = 0.5$  for both of them and at frequencies of minimum scattering  $\omega = 0.3\omega_P$  and  $\omega = 0.945\omega_P$ . For the smallest cavity we find a dominant dipole contribution at both frequencies. Despite the extreme birefringence revealed in the nanocavity, the magnetic fields present a remarkably low contrast inside the nanostructure and nearby. The field distribution along the radial direction at the lowest frequency is antisymmetric inside the anisotropic shell, whereas it becomes symmetric for the highest resonant frequency. This confirms the existence of a symmetric and antisymmetric coupling between the surface charges associated with the cavity and surface polaritons. We find a similar behavior for the biggest nanostructure, but for the first resonant frequency  $\omega = 0.3\omega_P$  only. Because of the non-negligible contribution of high order scattering coefficients the magnetic field distribution for the highest frequency becomes much more intricate. The existence of an invisibility window near  $\omega_P$  is not possible due to this fact.

The spectrum of  $Q_{sca}$  for cylinders of utmost radius  $R = k_P^{-1}/2$  and various values of the aspect ratio  $T/R$ , with a filling factor ranging from 0 to 1, was also analyzed in ref. [115]. For an anisotropic nanocavity with a tiny concentric hole ( $T = 0.9R$ ), we highlight the occurrence of multiple peaks and their associated minima scattering



efficiency. Notably, the fundamental frequency of scattering cancellation continues attached to the condition of  $\varepsilon_{\perp}$  near zero.

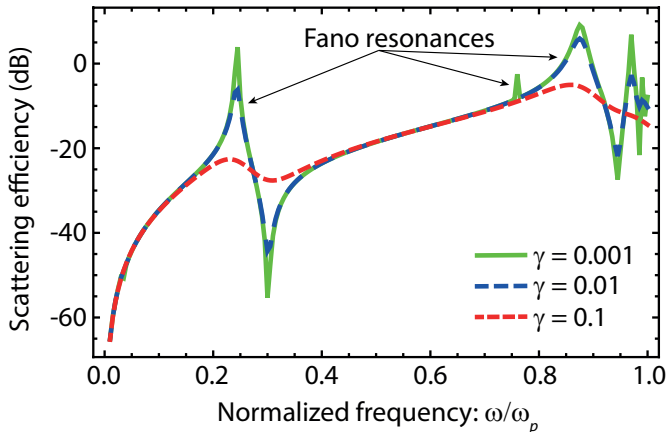


Figure 4.5: Scattering efficiency of a tubular anisotropic metamaterial of equal outermost radius and shell thickness  $R = T = k_P^{-1}/4$  immersed in air and with a filling factor  $f = 0.5$ . The damping rate of the Drude medium varies from  $\gamma = \omega_P/10$  to  $\gamma = \omega_P/1000$ .

We analyze now the influence of losses of the Drude medium. We plot in fig. 4.5 the scattering efficiency of a hollow metamaterial nanocylinder immersed in air, with a filling factor  $f = 0.5$ , outermost radius  $R = k_P^{-1}/2$  and shell thickness  $T = R/2$ . Metamaterials with the lowest damping rate for the Drude medium plotted in fig. 4.5 achieve a minimum of scattering of around one order of magnitude lower than the scattering efficiency obtained for  $\gamma = \omega_P/100$ . If we examine the peaks associated to the fundamental resonance we find

the opposite. Thus, the peak-to-valley contrast increases two orders of magnitude when the damping rate of the Drude medium is reduced in only one order of magnitude. The additional ultra-narrow peaks emerging may be attributed to multipole Mie resonances occurring for higher orders. Nevertheless, this cannot be applied to achieve invisibility in a practical case. On the other hand, when we consider higher losses for the Drude medium we obtain a reduction of several orders of magnitude of the peak-to-valley contrast.

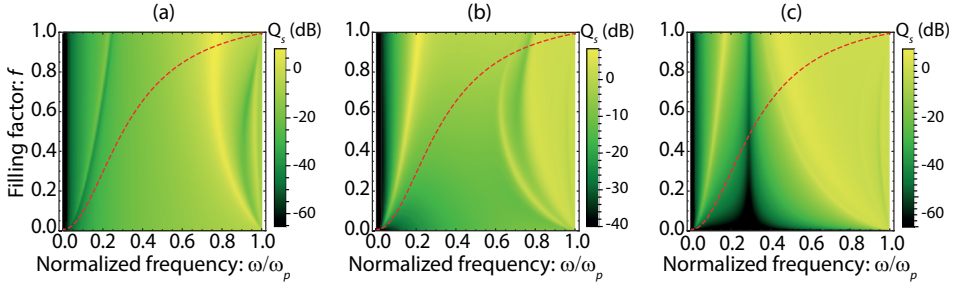


Figure 4.6: Scattering efficiency, expressed in dB, of a cylindrical cavity of utmost radius  $R = k_P^{-1}/2$  and shell thickness  $T = R/2$ . The dielectric constant of the core and environment medium are (a)  $\varepsilon_C = 10$  and  $\varepsilon = 1$ , (b)  $\varepsilon_C = 1$  and  $\varepsilon = 10$ , and (c)  $\varepsilon_C = \varepsilon = 10$ . The red line corresponds to the frequencies  $\omega_{zero}$ .

Until this moment the only discrepancy of scattering cancellation to the rule of  $\varepsilon_{\perp}$  near zero was found for cavities with high filling factor  $f$  of the Drude medium. But this is not the unique exception. We study the influence of both the core and environment medium permittivities on invisibility for a cylindrical cavity of outermost radius

$R = k_P^{-1}/2$ , shell thickness  $T = k_P^{-1}/4$  and a damping factor of  $\gamma = \omega_P/100$  for the Drude material. The filling factor  $f$  will range from 0 to 1. In fig. 4.6(a) we analyze the  $Q_{sca}$  of the tubular cavity immersed in air ( $\varepsilon = 1$ ) and a core permittivity of  $\varepsilon_C = 10$ . It is evident the presence of two resonances associated with the symmetric and antisymmetric excitation of surface polaritons. The loci of the  $Q_{sca}$  minima are shifted with respect to the case in which  $\varepsilon = \varepsilon_C = 1$ . Note that the fundamental frequency of invisibility is substantially displaced from  $\omega_{zero}$  even at low and moderate filling factors.

In fig. 4.6(b) we have the situation in which we exchange dielectric constants, being  $\varepsilon = 10$  and  $\varepsilon_C = 1$ . First of all we identify the fundamental Fano resonance with an enormous spectral gap between its peak and valley frequencies. In addition, the peak-to-valley efficiency contrast is moderate. For a filling factor  $f = 0.5$  the peak is located at  $\omega = 0.153 \omega_P$ , whereas the valley frequency is  $\omega = 0.707 \omega_P$ . This suggests that the reduction of scattering efficiency associated with Fano resonances is practically vanished.

Finally, in fig. 4.6(c) we examine the scattering efficiency when the anisotropic cavity is immersed in a high permittivity medium and has a core with high dielectric constant simultaneously ( $\varepsilon = \varepsilon_C = 10$ ). We find that the fundamental frequency of invisibility remains practically

in the same value for all filling factors. For instance, taking a filling factor of  $f = 0.2$  the invisibility frequency is found at  $\omega = 0.292\omega_P$ ; if we increase  $f$  to 0.8 the frequency of the best scattering reduction is now  $\omega = 0.294\omega_P$ . These results demonstrate an important dependence of the invisibility effect with the permittivities of the core and the environment medium. This conclusion is in disagreement with previous studies in which the condition given by  $\omega_{zero}$  was remarked [82].

### 4.1.2 Non-homogenized cylindrical nanoparticles

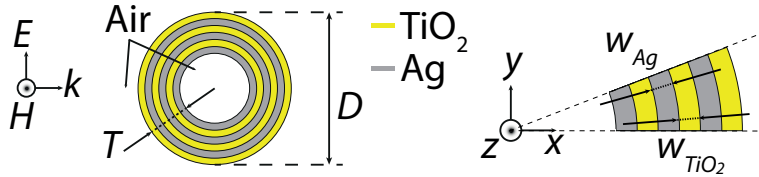


Figure 4.7: Illustration of the nanotube employed in the analysis of invisibility conditions.

Realistic conditions for a cylindrical nanostructure to become invisible can be treated by means of the Lorenz-Mie scattering theory, which is briefly resumed in section 3.1. This is the motivation of our recently published manuscript given in ref. [116]. The structure used here is an infinitely long Ag-TiO<sub>2</sub> multilayered nanotube, presented in fig. 4.7. First it is set with a metal filling factor  $f = 0.5$ , metal

and dielectric widths of  $w_{Ag} = 10$  nm and  $w_{TiO_2} = 10$  nm respectively, and a cylinder diameter of  $D = 220$  nm. As it is shown in this figure, we first assumed  $TE^z$  polarization for the incident light. By using the Lorenz-Mie theory we can estimate the scattering efficiency by means of eq. (3.12). The invisibility conditions are established provided that the scattering coefficients  $a_n$  given in eq. (3.11) approach simultaneously to a near-zero value. In our specific case, we found that eq. (3.12) is accurately estimated with  $|n| < 5$ , which may save computational time.

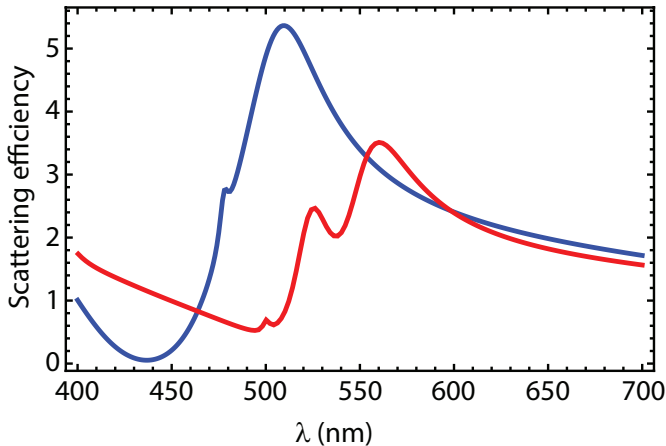


Figure 4.8: Scattering efficiency of a Ag-TiO<sub>2</sub> multilayered nanocylinder composed of 6 layers. The nanotube shell is  $T = 60$  nm, the nanocavity diameter is  $D = 220$  nm and the metal filling factor is  $f = 0.5$ . Blue curve stands for the innermost layer made of Ag and red curve is for a TiO<sub>2</sub> inner layer. Calculations were performed for  $TE^z$ -polarized incident light.

Although the effective medium approach, as described in section 3.2, sets that the cylinder would behave in the same manner if we exchange the order of the materials for the layers in our nanocylinder, it is clear from our results (fig. 4.8) that the calculated scattering efficiency  $Q_{sca}$  exhibits significant discrepancies when the inmost layer is metallic or dielectric. The minimum for the scattering efficiency when the interior layer of the nanocavity is made of silver results  $Q_{sca} = 0.053$  at  $\lambda = 437$  nm, as reported in [82]. However, if the inner layer is made of  $\text{TiO}_2$  the minimum of scattering efficiency is shifted to  $\lambda = 491$  nm and it reaches a value of 0.53, which is an order of magnitude higher than with the former sequence of layers.

The fact that the minimum value of  $Q_{sca}$  varies when exchanging the materials of the layers evidences that the EMA might not be correctly applied in some cases. The deviations of the actual structure as compared with respect to the homogenized nanoparticle based on the effective medium approach are specially notable in the case of setting a metallic outer layer (see fig. 4.11 and discussion below). We analyze the fields in the structure for a wavelength of  $\lambda = 437$  nm, for which the EMA expects invisibility [82]. In fig. 4.9 we show the modulus of the magnetic field  $|\mathbf{H}|$  for the mentioned wavelength provided the incident wave is  $\text{TE}^z$ -polarized. For the case in which titanium dioxide

is the material of the inner layer we find strong variations of the field especially at the rear part of the nanotube. In one hand, this fact reveals a strong deviation from homogenization approaches, and on the other hand, this is critical for making it not useful for invisibility. Finally, when the utmost covering layer is  $\text{TiO}_2$ , one can observe in fig. 4.9(a) that the field amplitude at the center of the nanotube and its neighborhood is, in average, near the amplitude of the remaining field in the environment.

When the number of layers in our nanotube is increased while its thickness ( $T = 60$  nm) and metal filling factor ( $f = 0.5$ ) remain constant, thus reducing metal and dielectric layer widths, the shape of the scattering efficiency curves become more similar, in agreement with the postulates of homogenization, though notable differences still are evident. For the sake of illustration, we calculate  $Q_{sca}$  for a nanocylinder made of 12 metal-dielectric alternating layers. We kept the shell thickness  $T$  and the metal filling factor  $f$  at the same value as for the 6-layers structure and we reduced to one half both the period of the multilayered structure and the layer width. The scattering efficiency of this new nanotube is shown in fig. 4.10.

For this configuration we evaluated again the scattering efficiency by means of the Lorenz-Mie method. When the layer in contact with

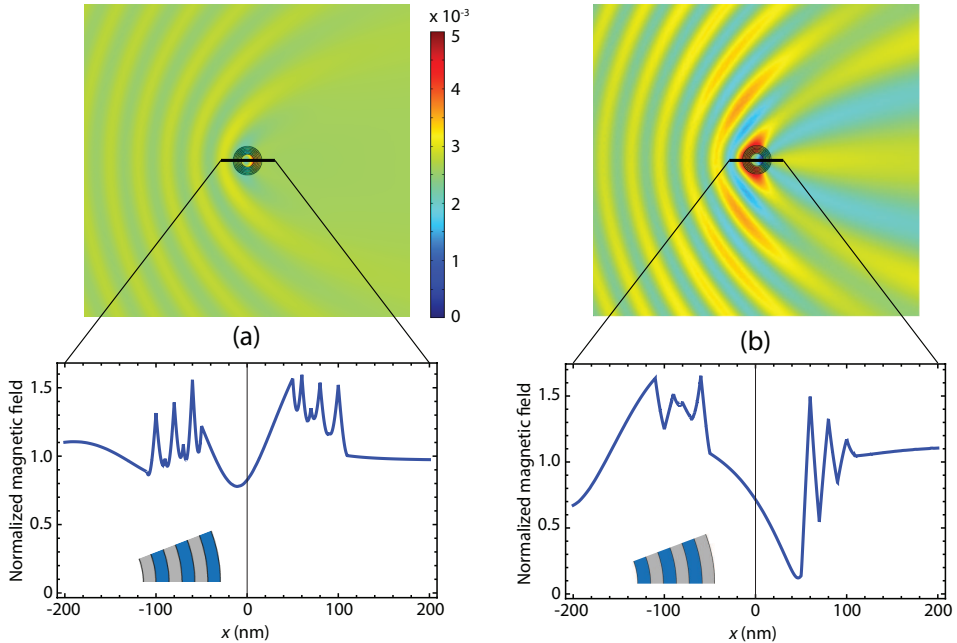


Figure 4.9: Amplitude distribution of normalized magnetic field  $|\mathbf{H}|/|H_0|$  at  $\lambda = 437$  nm for a 6 layer nanocylinder with (a) inner layer made of Ag and (b)  $\text{TiO}_2$  inmost layer.

the core is silver, the minimum value of  $Q_{sca}$  is 0.026 at  $\lambda = 444$  nm. Compared with the one estimated for a 6 layer nanocylinder, the difference is slightly. On the other hand, when the inmost layer is made of titanium dioxide we find a minimum of scattering efficiency of 0.345 at  $\lambda = 477$  nm.

The amplitude of the magnetic field is represented in fig. 4.11, where one can realize of the abrupt changes in the metal-dielectric in-



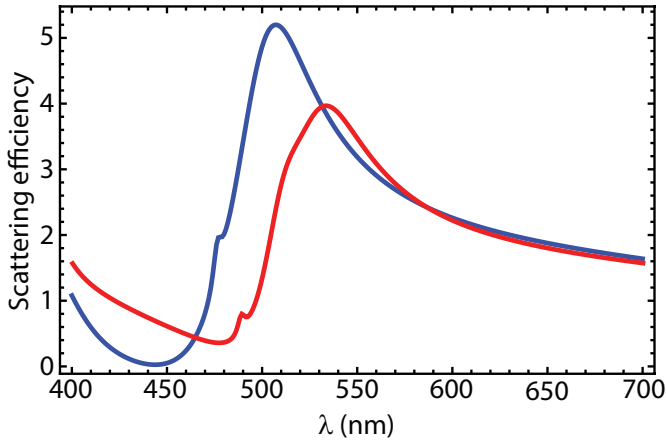


Figure 4.10: Scattering efficiency of a Ag-TiO<sub>2</sub> multilayered nanocylinder composed of 12 layers where shell thickness is  $T = 60$  nm, the nanocavity diameter is  $D = 220$  nm and the metal filling factor is  $f = 0.5$ . Blue curve stands for the innermost layer made of silver and red curve is for a titanium dioxide inner layer.

interfaces, as occurred also for the nanotube with 6 layers. In fig. 4.11(a) we represent the amplitude distribution of the magnetic field for  $\lambda = 444$  nm assuming the material of the innermost layer is Ag. If we calculate the average value it would present a slow variation with reduced dispersion inside the metamaterial. In addition, we find a non-zero minimum of intensity near the origin of coordinates disabling the gain of a shielding effect in the cloaked region. In fig. 4.11(b) it is shown the magnetic field distribution when we consider the interior layer as made of TiO<sub>2</sub>. The mechanism responsible for the increase of scattering efficiency in this configuration seems to be the resonant excitation

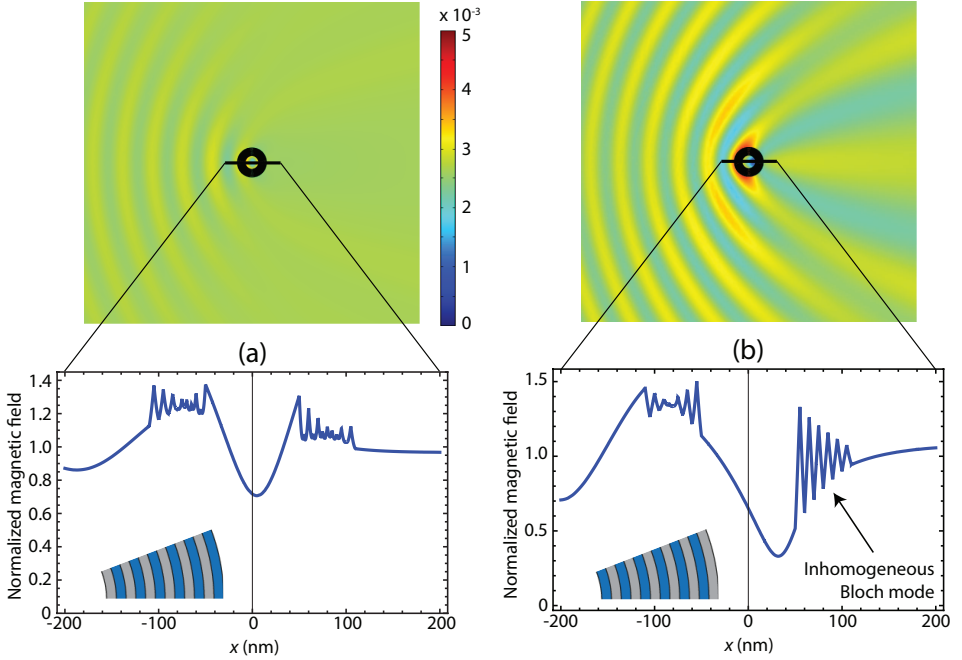


Figure 4.11: Amplitude distribution of normalized magnetic field  $|\mathbf{H}|/|H_0|$  at  $\lambda = 444$  nm for a nanocylinder made of 12 layers where  $T = 60$  nm,  $D = 220$  nm and  $f = 0.5$ . The innermost layer is made of (a) silver and (b) titanium dioxide.

of collective SPPs at the rear part of the structure, which develop an inhomogeneous Bloch wave in the multilayered metamaterial.

After analyzing these two structures, one can conclude that introducing a higher number of layers while maintaining the same shell thickness as well as the same structure diameter and filling factor both the scattering efficiency spectrum and magnetic field pattern, for the Ag and  $\text{TiO}_2$  ending layers, will approach themselves towards the re-

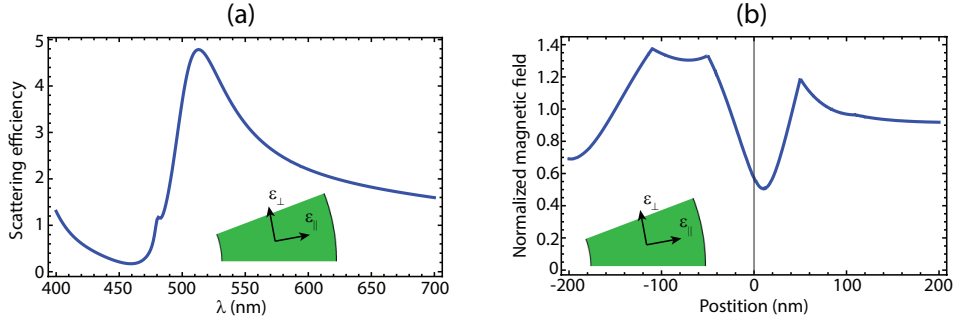


Figure 4.12: (a) Scattering efficiency for a nanocylinder of thickness  $T = 60$  nm and total diameter  $D = 220$  nm, made of a hyperbolic metamaterial. The components of the permittivity tensor for the metamaterial are given by eq. (3.14) and eq. (3.15) where a filling factor  $f = 0.5$  is considered. (b) Normalized magnetic field  $|\mathbf{H}|/H_0$  along the  $x$ -axis at the invisibility wavelength  $\lambda = 459$  nm.

sponse of a purely hyperbolic nanocylinder. Fig. 4.12(a) represents the scattering efficiency  $Q_{sca}$  of a hollow nanocylinder of thickness  $T = 60$  nm and total diameter  $D = 220$  nm composed of a hyperbolic metamaterial with components of permittivity tensor given by eqs. (3.14) and (3.15), considering a filling factor  $f = 0.5$ . The minimum for the scattering efficiency is  $Q_{sca} = 0.172$  found at an invisibility wavelength of  $\lambda = 459$  nm. It is also plotted in fig. 4.12(b) the magnetic field amplitude distribution at the invisibility wavelength ( $\lambda = 459$  nm). There exists a formation of localized surface waves in the two air-hyperbolic metamaterial interfaces whose pattern is closer to the field distribution pictured in fig. 4.11(a), where the material of the inmost layer is silver, than the one exhibited in fig. 4.11(b), where

the inmost layer is made of titanium dioxide.

### 4.1.3 Optimized nanostructure

As we already demonstrated, the number of layers is critical to make the effective medium approach accurate enough to be employed in simplified calculations. However, a high number of layers with such low thickness presents an important technological challenge so it might be a great idea to improve the metamaterial nanocylinder structure instead of introducing more and thinner layers. In this case the EMA should not be employed, characterized by its lack of precision, to a larger extent due to edge effects as discussed in section 4.1.2.

We introduce a new degree of freedom to our analysis of the structure to take advantage of these edge effects which consists on building the unit cell as a layer of one material surrounded by the other one. More details are given in one of our recently published manuscripts [117]. With this arrangement we will have the central metal layer of the unit cell of width  $w_m$  for instance, surrounded by two slices of widths  $m w_d$  and  $(1-m) w_d$  of insulator, where  $m$  is the marginal factor currently introduced which can take values from -1 to +1. A negative value means that the central layer of the unit cell is an insulator instead. Due to the periodicity of the nanostructure, the internal radial

distribution is kept unaltered with a periodicity given by  $\Lambda = w_d + w_m$  and only the marginal layers may change. The width of the inmost marginal layer is given by  $w_{in} = R_2 - R_1$  and the outermost width is  $w_{out} = R_{N+1} - R_N$ . Positive values of  $m$  denote dielectric marginal layers. In this case we define  $w_{in} = (1 - m)w_d$  and  $w_{out} = mw_d$ , providing  $w_d = w_{in} + w_{out}$ , so the extreme value  $m = +1$  stands for a full dielectric outermost layer (full metallic inmost layer) and in  $m = 0$  we consider a full dielectric inmost layer (full metallic outermost layer). For negative values of  $m$  we consider metallic marginal layers. The limit  $m = -1$  would be formally the same situation as for  $m = +1$ , where the outermost layer is metallic and the inmost one is dielectric.

To show the relevance of the introduced new degree of freedom we developed numerical simulations for the multilayered nanotube made of silver and titanium dioxide and composed of  $T/\Lambda = 3$  periods, that is  $N = 7$  layers taking into account the new unit cell composition. The inner radius is  $R_1 = 50$  nm and the shell thickness is  $T = 60$  nm. Metal width and dielectric width are  $w_m = 10$  nm and  $w_d = 10$  nm respectively, so the metal filling factor results  $f = 0.5$ . In fig. 4.13 we plot the scattering efficiency in the visible wavelength range of the previously described nanotube immersed in air ( $\varepsilon = 1$  and  $\varepsilon_C = 1$ ). For a  $\text{TM}^z$ -polarized field we found two local minima in  $Q_{sca}$ , as shown

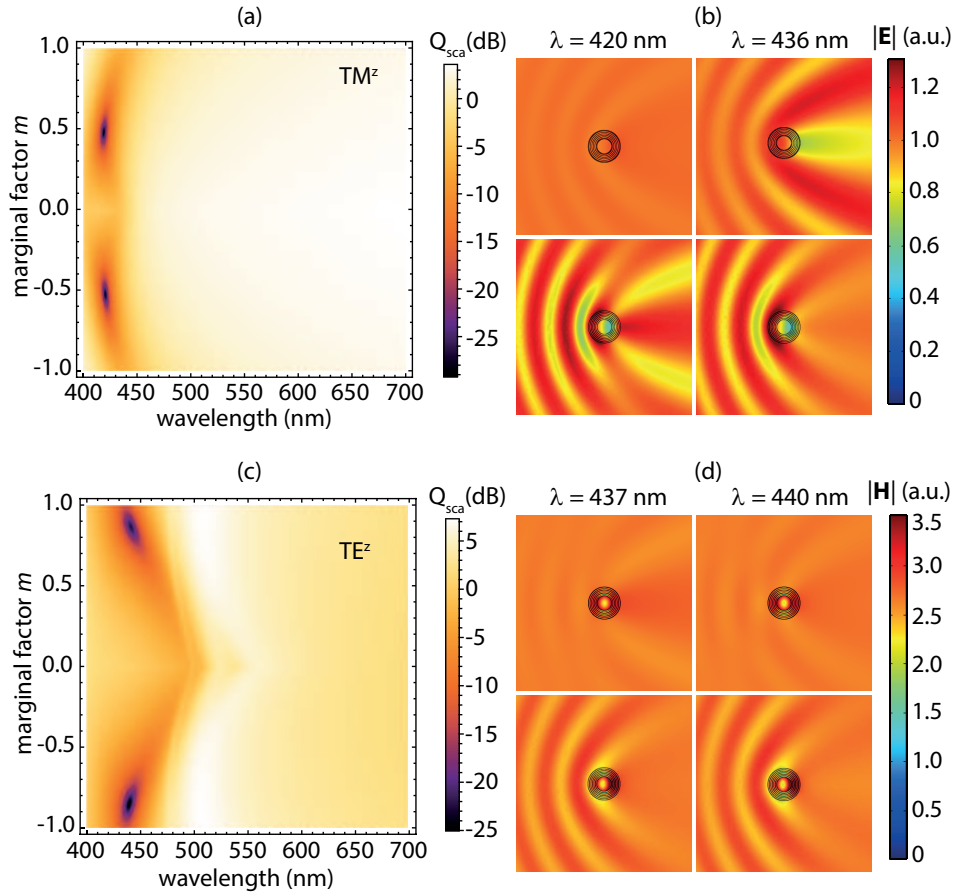


Figure 4.13: Scattering efficiency of a MD multilayered nanotube immersed in air with  $T = 60$  nm,  $R_1 = 50$  nm,  $\Lambda = 20$  nm and  $f = 0.5$  for different values of marginal factor  $m$ . (a)-(b) Incident  $TM^z$ -polarized plane wave. (c)-(d) Incident  $TE^z$ -polarized plane wave. In (b) and (d) we compare the scattered fields of the nanotubes for the optimal marginal configurations here studied (top scatterer) with the nanotubes proposed in [82] (bottom scatterer) for different wavelengths.

in fig. 4.13(a): a first minimum for  $Q_{sca} = 1.40 \cdot 10^{-3}$  at  $\lambda = 421$  nm with  $m = -0.53$ , and a second minimum where  $Q_{sca} = 1.20 \cdot 10^{-3}$  at  $\lambda = 419$  nm for  $m = 0.48$ . In both cases, the marginal factor is close to  $|m| = 0.5$ , which means that marginal layers are about 5 nm thick each. This represents a notorious improvement of two orders of magnitude compared with the case analyzed in [82], which corresponds to the case where  $m = -1$ . We represent in fig. 4.13(b) the comparison of the scattered electric field for the structure with the configuration of  $m = -0.5$  and the one with  $m = -1$  at the invisibility wavelength calculated for our nanocavity ( $\lambda = 420$  nm, where  $Q_{sca} = 2.15 \cdot 10^{-3}$ ) and the one obtained in [82] ( $\lambda = 436$  nm, where  $Q_{sca} = 0.21$ ). In addition, our structure with  $m = -0.5$  has a similar behavior ( $Q_{sca} = 0.27$ ) as the previously proposed nanocavity at its best performance wavelength.

For a  $TE^z$ -polarized incident wave the scattering efficiency varies considerably. In fig. 4.13(c) we show the results of  $Q_{sca}$  for this polarization. We find one minimum for a marginal factor  $m = -0.85$  at  $\lambda = 440$  nm for which  $Q_{sca} = 3.02 \cdot 10^{-3}$  and a second minimum for  $m = 0.86$  at  $\lambda = 442$  nm for which  $Q_{sca} = 5.47 \cdot 10^{-3}$ . Our approach provides a reduction of one order of magnitude for the scattering efficiency compared to the nanocavity reported by Kim *et al*

( $Q_{sca} = 5.30 \cdot 10^{-2}$  at  $\lambda = 437$  nm), as we illustrate in fig. 4.13(d) where we compare the wave fields scattered by those two nanocylinders ( $m = -0.85$  on the top and  $m = -1$  on the bottom).

To understand this significant drop of the scattered signal, we will consider sufficiently narrow slabs ( $\Lambda \ll \lambda$ ) where a radially form birefringence may be established for the metamaterial composed of concentric multilayers. Under this consideration the  $\text{TM}^z$  fields behave like ordinary waves that propagate in a uniaxial crystal with optic axis set along the radial coordinate [129]. The variation of the electric field  $E_z$  is negligible for the waves that propagate through the metallodielectric metamaterial. However, the electric displacement field  $\mathbf{D} = D_z \hat{z}$  experiments critical discontinuities at the metal-dielectric interfaces. Due to the negative value of the real part of  $\varepsilon_m$  the electric displacement field decreases when the metal filling factor grows, even vanishing at the epsilon-near-zero regime. To estimate the  $z$ -component of the effective permittivity of the multilayered metamaterial we may employ

$$\langle \varepsilon_z \rangle = \frac{\int \varepsilon(r) E_z(r, \phi) r dr d\phi}{\int E_z(r, \phi) r dr d\phi} \approx \frac{2}{(R^2 - R_1^2)} \int_{R_1}^R \varepsilon(r) r dr. \quad (4.2)$$

On the other hand,  $\text{TE}^z$ -polarized wave fields propagate like extraordinary waves in the multilayered metamaterial where the average permittivity components  $\langle \varepsilon_\phi \rangle$  (which coincides with  $\langle \varepsilon_z \rangle$ ) and  $\langle \varepsilon_r \rangle$



characterize the radial anisotropy, and the latter takes much higher values than the former. Analyzing eq. (4.2) we find that the average permittivity  $\langle \varepsilon_z \rangle$  depends on the absolute value of the marginal parameter  $m$ . As we see in fig. 4.13(a) and (c) there exists a symmetry for the valleys and peaks with  $|m|$ , so we potentially may establish a correlation of the locations of these peaks and valleys in terms of  $\langle \varepsilon_z \rangle$ .

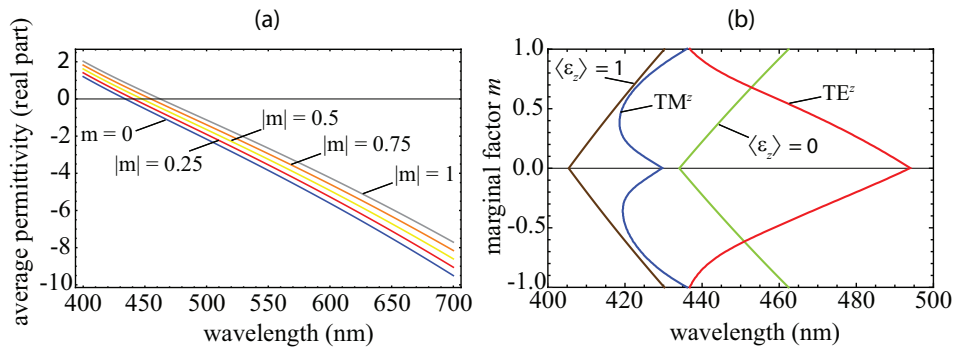


Figure 4.14: (a) Real part of  $\langle \varepsilon_z \rangle$  calculated for an Ag-TiO<sub>2</sub> multilayered nanocylinder with  $R_1 = 50$  nm,  $T = 60$  nm,  $\Lambda = 20$  nm and  $f = 0.5$ . (b) Values of iso-permittivity curves for  $\langle \varepsilon_z \rangle = 0$  and  $\langle \varepsilon_z \rangle = 1$ . Also plotted the  $Q_{sca}$  minima shown in fig. 4.13(a) for  $TM^z$  (blue line) and fig. 4.13(c) for  $TE^z$  (red line).

In fig. 4.14(a) we show the real part of  $\langle \varepsilon_z \rangle$  calculated with eq. (4.2) for an Ag-TiO<sub>2</sub> nanocavity with inmost radius  $R_1 = 50$  nm, shell thickness  $T = 60$  nm, period  $\Lambda = 20$  nm and filling factor  $f = 0.5$  for different marginal factors. We found that  $\langle \varepsilon_z \rangle$  increases with  $|m|$  reaching the highest value for  $|m| = 1$ . The permittivity matching of the core and environment medium with the multilayered structure, given by

the condition  $\text{Re}(\langle \varepsilon_z \rangle) = 1$ , is accomplished at  $\lambda = 405$  nm for  $m = 0$  and shifts to longer wavelengths for higher  $|m|$ , up to  $\lambda = 430$  nm for  $|m| = 1$ . Such permittivity matching is behind the invisibility effect that occurs when we illuminate the structure with a  $\text{TM}^z$ -polarized plane wave, for moderate and high  $|m|$  values, as we see in fig. 4.14(b). For the optimal case in which  $m = 0.5$ ,  $\text{Re}(\langle \varepsilon_z \rangle) = 1$  is achieved for  $\lambda = 417$  nm, quite close to the minimum shown in fig. 4.13(a) at  $\lambda = 419$  nm. Nevertheless, the EMA presents some remarkable limitations. For low  $|m|$  we find notorious deviations of the condition  $\text{Re}(\langle \varepsilon_z \rangle) = 1$  and the loci of minima of scattering efficiency. Moreover, the extraordinary reduction of  $Q_{sca}$  for marginal factors around  $|m| = 0.5$  cannot be predicted by the EMA.

For  $\text{TE}^z$ -polarized fields the differences are even more abrupt. The minima given in fig. 4.13(c) for the scattering efficiency are blue-shifted along with higher values of  $|m|$ , advancing to the opposite direction to the one predicted by any iso-permittivity curve with invariant  $\langle \varepsilon_\phi \rangle$  ( $=\langle \varepsilon_z \rangle$ ). The validity of the effective medium approach is then questionable to describe the invisibility effect treated here. Particularly, for the minimum found at  $\lambda = 440$  nm for  $m = -0.85$  the effective permittivity is  $\text{Re}(\langle \varepsilon_\phi \rangle) = 0.437$ , far from unity. Especially under  $\text{TE}^z$  polarization the nonlocalities inherent in MD nanostruc-

tures lead to edge effects that seem to be the causal agent of the anomalous behavior of the long-wavelength approximation, as we previously pointed out in section 4.1.2.

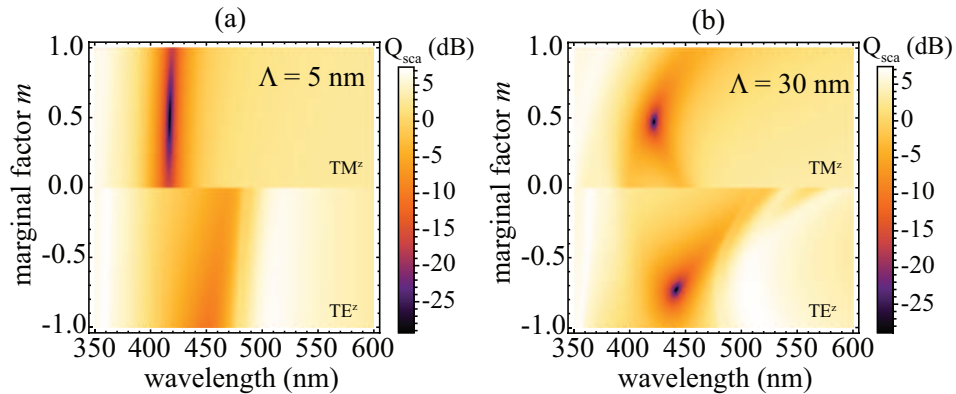


Figure 4.15: Scattering efficiency of an Ag-TiO<sub>2</sub> multilayered nanocavity with  $R_1 = 50$  nm,  $T = 60$  nm and  $f = 0.5$ . Marginal factor  $m$  and period length  $\Lambda$  parameters are varied. (a)  $\Lambda = 5$  nm ( $N = 25$  layers), and (b)  $\Lambda = 30$  nm ( $N = 5$ ).

To obtain further and revelatory conclusions we evaluated the scattering efficiency of our designed nanotube of  $T = 60$  nm,  $R_1 = 50$  nm and  $f = 0.5$  for different number of periods. The results of this analysis are pictured in fig. 4.15 where we can appreciate the greater importance of the marginal factor  $m$  for larger periods, making inappropriate the use of EMA in these situations. For the smallest period ( $\Lambda = 5$  nm) the marginal factor has a limited influence on the scattering spectrum. In this case we find for  $\text{TM}^z$  polarization a minimum of scattering effi-

ciency of  $Q_{sca} = 1.17 \cdot 10^{-3}$  at  $\lambda = 417$  nm. For  $TE^z$ -polarized incident light the minimum value increases in nearly two orders of magnitude reaching  $Q_{sca} = 8.99 \cdot 10^{-2}$  at  $\lambda = 451$  nm. Note that this configuration presents a technological challenge due to the high number of layers and their thin width (2.5 nm each layer). Also, the long-wavelength approximation is valid in this case as it might be expected, and the nanocylinder might be considered as a radially-anisotropic medium.

Now if we take a look at the other extreme for which  $\Lambda = 30$  nm the minima for the scattering efficiency are of the same order for both polarizations. In the case of  $TM^z$ -polarized fields the minimum of  $Q_{sca} = 1.43 \cdot 10^{-3}$  is found at  $\lambda = 422$  nm and for  $m = 0.48$ , whereas for  $TE^z$ -polarized wave fields the minimum of scattering efficiency is  $Q_{sca} = 1.28 \cdot 10^{-3}$  at  $\lambda = 441$  nm for  $m = -0.72$ . In addition, this latter configuration presents certain practical advantages such as the reduced number of layers and the thickness of them (5 layers of 15 nm thick each, except for the margin layers). We will consider from now on a multilayered nanocylinder with a period of  $\Lambda = 30$  nm due to its genuine invisibility performance and its convenience for a fabrication process.

Using the new arrangement for the nanocavity we now study the behavior of our structure under variation of both core and environment

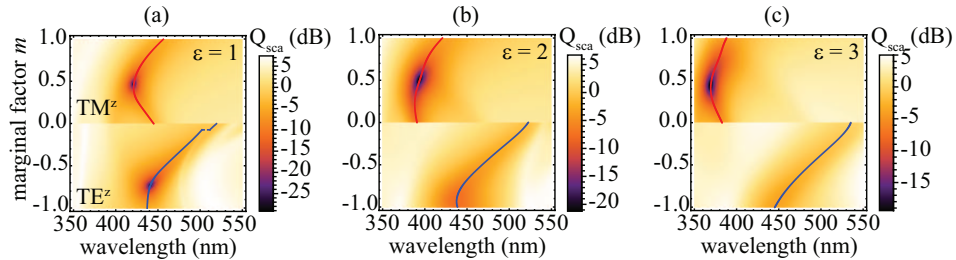


Figure 4.16: Scattering efficiency of an Ag-TiO<sub>2</sub> multilayered nanotube with  $R_1 = 50$  nm,  $T = 60$  nm,  $\Lambda = 30$  nm and  $f = 0.5$  for different marginal factors  $m$ . The core and environment medium permittivities are set as (a)  $\varepsilon = \varepsilon_C = 1$ , (b)  $\varepsilon = \varepsilon_C = 2$  and (c)  $\varepsilon = \varepsilon_C = 3$ . The solid lines indicate the minimum of  $Q_{sca}$  for each value of  $m$  for TM<sup>z</sup> polarization (red line) and TE<sup>z</sup> polarization (blue line).

permittivities. For simplicity we will assume  $\varepsilon$  and  $\varepsilon_C$  to be the same. Fig. 4.16 illustrates the minimum of scattering efficiency for different marginal factors and with various core and environment medium permittivities. For TM<sup>z</sup> incident light polarization the scattering efficiency experiments again a dramatic drop but at lower wavelengths when both permittivities increase. The index matching condition to find now the minimum of  $Q_{sca}$  should be reestablished as  $\text{Re}(\langle \varepsilon_z \rangle) = \varepsilon$  which is in agreement with the shift undergone by the invisibility wavelength. We point out that the optimal geometrical configuration in found for a value of marginal factor  $|m|$  near 0.5 in all cases.

Considering TE<sup>z</sup>-polarized wave fields a dramatical increase of scattering efficiency is observed. The minimum of  $Q_{sca}$  remains approximately in the same spectral band, slightly shifting to longer

wavelengths for higher-index media. However, scattering efficiency increases several orders of magnitude with permittivity. The minimum scattering efficiency for the higher permittivity considered in this analysis  $\varepsilon = 3$  is  $Q_{sca} = 0.435$ , found at  $\lambda = 449$  nm for a marginal factor of  $m = -0.935$ . The wavelengths at which the minima of  $Q_{sca}$  are located for this polarization seem to be essentially determined by the optogeometrical characteristics of the nanocylinder, so the core and environment medium permittivity changes do not affect its location significantly. Nevertheless, for extremely high values of permittivities this may not remain valid and significant variations may be found [115], as seen in section 4.1. This confirms the resonant behavior of the invisibility effect for the structure found for  $TE^z$ -polarized incident fields, differently from what is observed for  $TM^z$ -polarized wave fields.

In fig. 4.17 we study the scattering efficiency of nanocylinders with inmost radius  $R_1 = 50$  nm, shell thickness  $T = 60$  nm and multilayer period  $\Lambda = 30$  nm for different metal filling factors  $f = w_m/\Lambda$ . We show the minimum of  $Q_{sca}$  for the best marginal factor configuration at each metal filling factor analyzed. We set a permittivity of unity for both core and environment medium in this study. The wavelength for which the best invisibility performance occurs decreases around 200

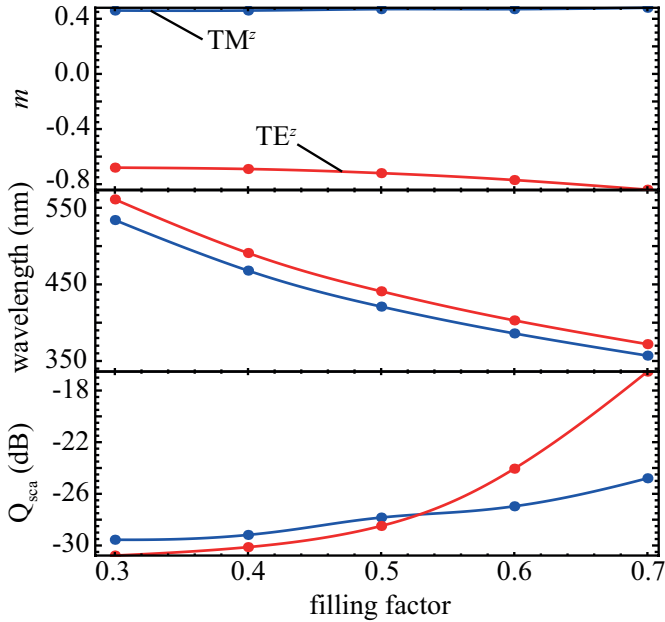


Figure 4.17: Optimal marginal factor  $m$  for invisible nanotubes with  $R_1 = 50$  nm,  $T = 60$  nm,  $\Lambda = 30$  nm and different metal filling factor  $f$ . Blue line stands for  $\text{TM}^z$ -polarized incident light and red line refers to  $\text{TE}^z$  polarization. The minimum of scattering efficiency  $Q_{sca}$  at such optimal configuration is also shown and the wavelength  $\lambda$  for which it is achieved.

nm, for both polarizations concurrently, when the metal filling factor  $f$  varies from 0.3 to 0.7. This suggests a way of tuning the invisibility spectral band of the multilayered nanotube [82]. For  $\text{TM}^z$  scattered wave fields this optimization leads to nanocylinders with marginal factors of modulus close to 0.5, which provide scattering efficiencies below -25 dB for a filling factor range between 0.3 and 0.7. In the case

of  $TE^z$ -polarized fields the scattering efficiency is partially reduced, at least for lower values of  $f$ . This happens for nanocavities where the inmost silver layer is considerably wider than the outermost one, that is for marginal factors  $m$  near -0.8. However, for high filling factors we appreciate that  $Q_{sca}$  cannot decrease the limit of -20 dB. This should not have a critical impact in the tunability of the invisible spectral band unless we need it for ultrasensitive applications.

To conclude, as the size of the nanocavity might be essential concerning the applicability of the EMA in  $TM^z$ -polarized fields, and more critically the resonant behavior of the nanotube for  $TE^z$ -polarized wave fields, we studied the scattering efficiency of Ag-TiO<sub>2</sub> multilayered nanocylinders of shell thickness  $T = 60$  nm, with different inner radii and immersed in air. In the case of incident  $TM^z$ -polarized waves it can be shown a minimal alteration for a range of inmost radius from  $R_1 = 50$  nm to  $R_1 = 200$  nm. These limited deviations are attributed to the reduced dependence of  $\varepsilon_z$  with the inmost radius  $R_1$ . On the other hand, for  $TE^z$ -polarized scattered fields,  $Q_{sca}$  pattern is significantly modified. The minimum in scattering efficiency increases two orders from  $Q_{sca} = 1.41 \cdot 10^{-3}$  for  $R_1 = 50$  nm to  $Q_{sca} = 0.135$  for  $R_1 = 100$  nm. For this polarization, the ability of our structures for canceling the scattering wave field in the optical wavelength range de-



cays progressively when inmost radius  $R_1$  grows. This is certainly due to the existence of multiple localized resonances.

## 4.2 Anisotropic metasurfaces

In this section we focus on the second block of the present Thesis. We analyze the results obtained from the simulations of metal-dielectric metasurfaces to perform beamshaping and summarize the design conditions to achieve the desired behavior. We first study the shaping of focused beams to improve their numerical aperture and their spot width. Secondly, we examine the possibility of improving the previous behavior by introducing a second MD metasurface. Then we explain the modifications of the MD structure to accelerate converging waves in the near field.

### 4.2.1 Ultrathin high-index metasurfaces for shaping focused beams

The structure used in the simulations was a cylindrical MD multilayered metasurface. It consists on alternating gold and silicon layers of different filling factors and unit cell periods to introduce a dephase that permits to control light and increase the NA of the incident con-

verging beam. It is characterized by a thickness much lower than the wavelength and the multilayer arrangement is radially distributed. Also, the distribution has to compensate the optical path in excess  $L(\theta)$ , so we use different periods of the multilayer to adjust it. For an ideal case in which the path in excess is corrected in a continuous way we should use  $N \rightarrow \infty$  steps of the refractive index. In practical terms this is not possible and we must use a finite number of steps. When one simulates the performance of the arrangement with different number of steps it can be found that  $N = 4$  steps are enough to provide a decent field distribution at the exit of the metasurface, as it is shown in fig. 4.18.

In the case of using  $N = 2$  steps of  $\pi$  radians each we obtain sidelobes that affect the resulted field distribution, but for  $N = 4$  the field pattern is much more similar to the one simulated assuming a continuous variation of the refraction index  $n(\theta) = n(0) - L(\theta)d$ , where  $d$  is the thickness of the metasurface ( $d \ll \lambda$ ). For dephases of  $\pi/2$  radians ( $N = 4$  steps) the multilayer is divided in periods  $\Lambda_i$  which, together with the metal width  $w_i$ , define the metal filling factor  $f_i = w_i/\Lambda_i$ . In fig. 4.19 it is illustrated a scheme of the arrangement of the MD multilayer to produce a variation of two units ( $n_i = n_{i-1} + 2$ ) for the effective index of refraction ( $n_0 = 3.69$  for the bulk silicon layer)

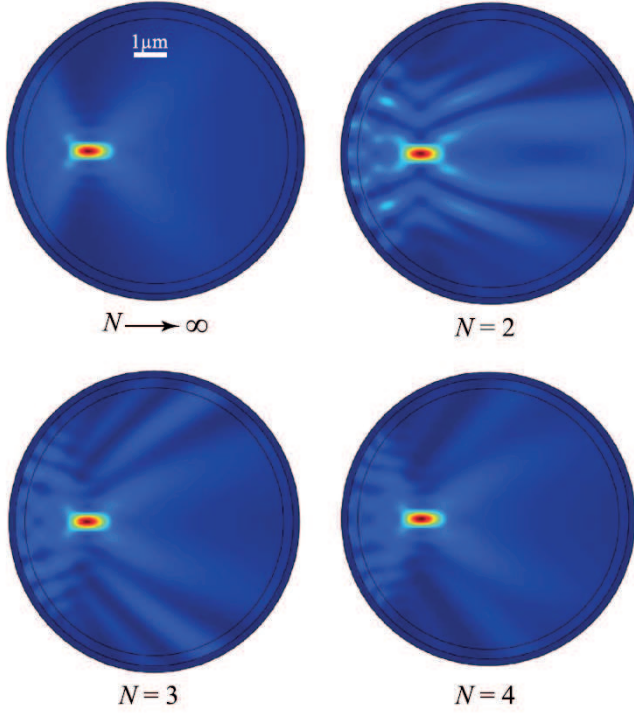


Figure 4.18: Intensity distribution  $|H(\mathbf{r})|^2$  of focal waves with its phase modulated by  $N$  steps of  $N/2\pi$  radians.

by changing both the period and the metal filling factor to obtain the desired sequence, which is characterized by  $f = 0, 0.37, 0.49$ , and  $0.54$ .

In views of a practical case the geometrical parameters chosen for the structure were  $(w_1, \Lambda_1) = (9, 24)$  nm,  $(w_2, \Lambda_2) = (15, 30)$  nm and  $(w_3, \Lambda_3) = (20, 35)$  nm, that have filling factors of  $f = 0, 0.38, 0.50$  and  $0.57$  which are in good agreement with the previous estimation.

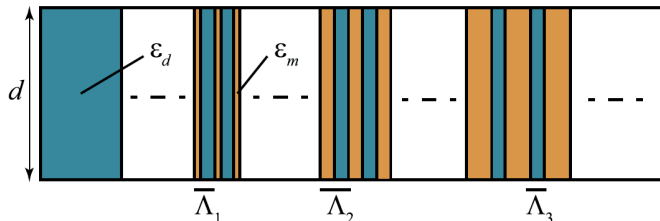


Figure 4.19: Illustration of the basic arrangement of a flat metasurface with a bulk dielectric and  $N - 1 = 3$  metallic gratings. By controlling the metal filling factor  $f_i$  it is possible to produce a phase shift of  $\pi/2$  radians.

These metamaterials, together with silicon, were arranged to form an ultrathin curved metasurface of  $4 \mu\text{m}$  inner radius and a thickness of  $d = 100 \text{ nm}$ . Apart from non-negligible sidelobes a super-resolved focal spot with reduced full width at half maximum (FWHM) in both directions is achieved. Concretely, the on-axis FWHM is reduced from  $2.4 \mu\text{m}$  to  $1.2 \mu\text{m}$ , as it is shown in fig. 4.20.

If the incident light is  $\text{TE}^z$ -polarized the behavior differs notably, presenting a strong blurring of the focal spot. This occurs because the waves propagating in each metallic grating behave like ordinary waves in an effective uniaxial crystal.

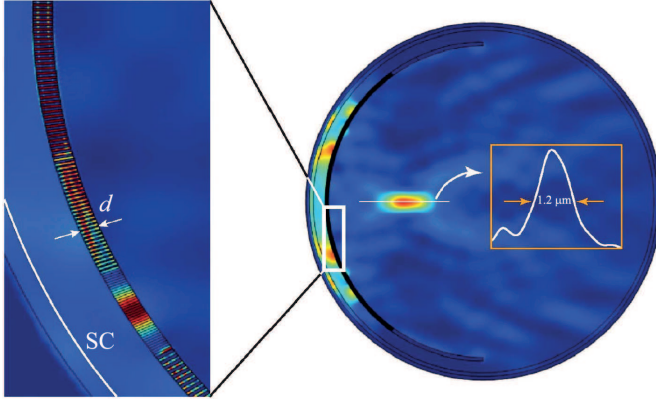


Figure 4.20: Intensity  $|H(\mathbf{r})|^2$  in the focal region of the converging field shaped by the Au-Si curved metasurface. A cylindrical surface current (SC) with super-Gaussian apodization ( $\Omega = 45^\circ$ ) is employed for excitation. The inset on the left shows the composition of the layers in detail. In the inset on the right the intensity in the focal region is depicted.

### 4.2.2 Beamshaping under high numerical aperture

Continuing with the idea of focusing a wave field by means of MD metasurfaces, we designed a solution for the case in which the impinging light is a plane wave and it impinges to a plano-concave pure dielectric lens immersed in air. For an index of the lens  $n > 1$ , as occurs in natural dielectric materials, it will present a divergent behavior. Therefore, to achieve focusing the effective index of the lens must be lower than unity. This is possible by using metamaterials.

In the special case in which  $n = 0$  the focusing will be performed at the center of the curvature of the concave surface of the lens, as illustrated in fig. 4.21(b). To achieve an increased numerical aperture a metamaterial with negative index must be used (fig. 4.21(c)). In this case, Ohmic losses present an inconvenient at the infrared and visible range. Our approach consists on a dielectric plano-concave thick lens coated by graded-index ultrathin metasurfaces (fig. 4.21(d)). The metacoatings are set to compensate the divergence of the dielectric lens and transform the incident field into a cylindrical wave with center at the focusing point  $F'$ . The first metasurface converts the incident plane wave into a cylindrical one centered at  $C$ , and the metacoating set at the curved surface increases the focusing power as explained in section 4.2.1. This configuration takes the advantage of a high reduction of losses with respect to considering a metamaterial lens.

Both metacoatings used here are composed of four types of zones. One of them is bulk silicon and the other three are constituted by metal-dielectric subwavelength gratings, enabling the introduction of controlled phase shifts of multiples of  $\pi/2$  radians. The thickness of the metasurfaces is considered as  $d = 100$  nm with slits of dielectric widths  $w_d = 15$  nm which are arranged in arrays of periods  $\Lambda_1 = 24$  nm,  $\Lambda_2 = 30$  nm and  $\Lambda_3 = 38$  nm. The phase shift introduced

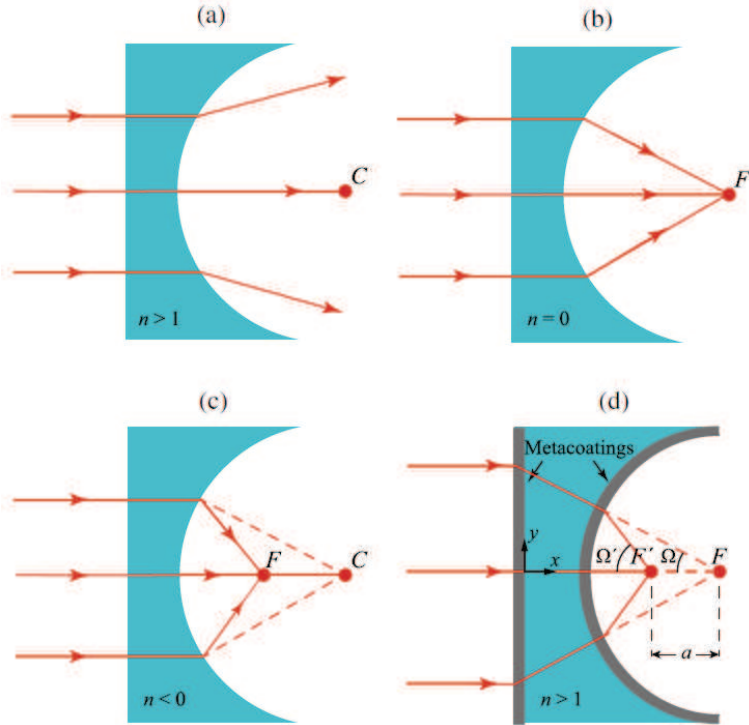


Figure 4.21: Scheme of the focusing action of a plano-concave lens (a) with an index of refraction greater than unity (divergent), (b) made of an epsilon-near-zero metamaterial (focusing at the center of curvature), (c) made of a metamaterial with negative index (increased numerical aperture), and (d) made of a dielectric ( $n > 1$ ) with metacoatings set at the entrance and the exit surfaces of the lens. For the latter the numerical aperture is again increased leading to a focus closer to the curved surface.

by the metasurfaces is symmetric with respect to the center of each metacoating, exhibiting a mirror symmetry with respect to  $y = 0$ .

In fig. 4.22 we compare the focusing effect for a  $\text{TM}^z$ -polarized

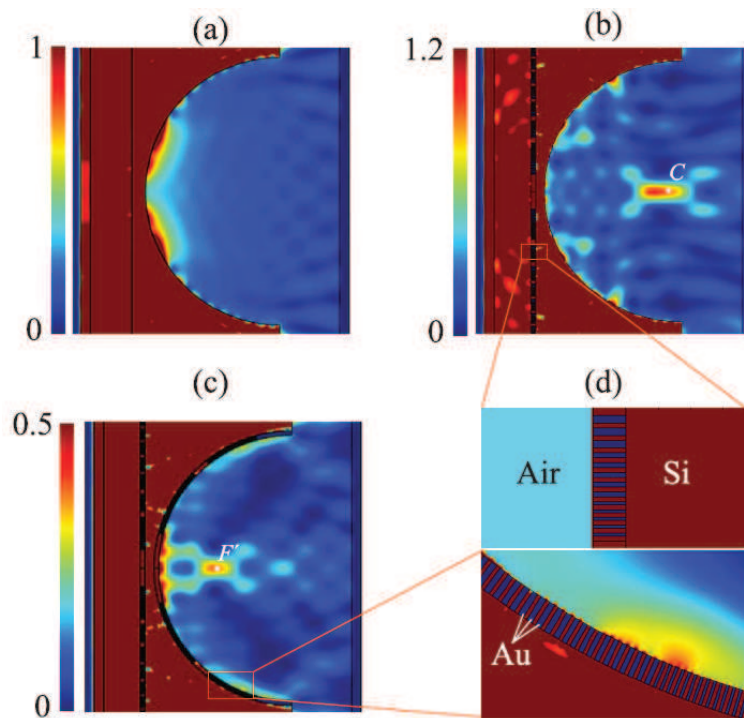


Figure 4.22: Intensity of the magnetic field for an impinging  $TM^z$ -polarized plane wave with  $\lambda = 800$  nm over a silicon plano-concave lens of radius  $R = 3 \mu\text{m}$  and vertex distance of 200 nm. (a) Lens with no metacoatings. (b) One metacoating is set at the flat surface of the lens. (c) Lens with coupled metacoatings on both flat and curved surfaces. (d) Close-up view of the gold nanoslit arrays set on the flat (top) and curved (bottom) surfaces of the lens.

plane wave impinging onto a silicon plano-concave lens coated with the designed metasurfaces with the cases in which only the flat meta-coating is set and the one considering the Si lens alone. The silicon lens has a radius of  $R = 3 \mu\text{m}$  and a vertex distance of 200 nm. The



illuminating wavelength is  $\lambda = 800$  nm. In fig. 4.22(a) we appreciate the divergent behavior of the silicon lens when no metacoating is set, in agreement with fig. 4.21(a). When the flat metacoating is set at the flat surface of the lens we find a beam focusing on the center of the curvature of the lens (fig. 4.22(b)), as previously described in fig. 4.21(b). Finally, in fig. 4.22(c) it is shown that for the structure engineered with both metacoatings set at the flat and curved metasurfaces of the silicon lens a focal shift of  $a = 1.5 \mu\text{m}$  with respect to the case of considering only the flat metacoating is obtained, thus presenting a super-resolved focal spot. In particular, the FWHM of the magnetic field intensity decreases from  $1.12 \mu\text{m}$  for the case presented in fig. 4.22(b) to  $0.84 \mu\text{m}$  for the designed structure analyzed in fig. 4.22(c).

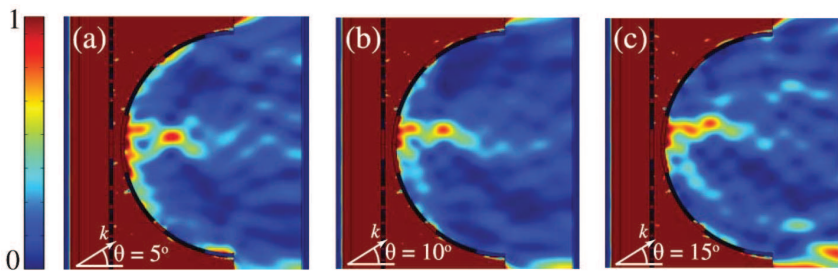


Figure 4.23: Field intensity of focal waves produced by incident tilted  $\text{TM}^z$ -polarized plane waves. Tilt angles are (a)  $\theta = 5^\circ$ , (b)  $\theta = 10^\circ$  and (c)  $\theta = 15^\circ$  measured with respect to the optical axis  $y = 0$ .

Under oblique incident  $\text{TM}^z$ -polarized waves the engineered structure also presents a favorable performance. In fig. 4.23 it is shown the behavior of the structure under three different tilted angles of the incident illumination. In these cases the spot is not focused on  $F'$  but it is laterally displaced. Both the lateral and on-axis resolutions are practically unaltered due to the essentially conserved beam shape with respect to the previous studied case.

### 4.2.3 Accelerating converging waves in the near field

The lateral deviations presented above can also be achieved accelerating a focal incident wave. Lets assume a cylindrical metasurface impinged by a  $\text{TM}^z$ -polarized focal wave. In agreement with the diffraction theory of Debye the scattered field can be expressed in terms of the apodization function  $A(\theta)$  which takes into account the truncation of the converging field passing the metasurface, and a phase only term  $\exp(iw(\theta))$  where  $w(\theta)$  denotes deviations of the wavefront of the converging field from the reference cylinder:

$$H_{sca}(\theta) = A(\theta) \exp(iw(\theta)). \quad (4.3)$$

The deviation  $w(\theta)$  will be induced by the metasurface to shape an aberration-free cylindrical wave. On the other hand, the apodization function used will be a super-Gaussian function given by

$$A(\theta) = A_0 \exp(-(\theta/\Omega)^6), \quad (4.4)$$

to reduce edge effects, where  $\Omega$  is the semi-aperture angle. For  $w(\theta)$  a series expansion around  $\theta = 0$  is considered, thus setting  $w(\theta) = m\theta$  provided we neglected defocusing and higher order terms of the expansion and also a constant term which will not contribute significantly. The parameter  $m$  will govern the curvilinear trajectory around the focus of the original wave and the radius of the caustic curve will be  $r_m = |m|/k$ , being  $k = \omega/c$  the wavenumber.

In fig. 4.24 it is shown the simulations of the magnetic field distribution  $|H(\mathbf{r})|^2$  for different semi-apertures  $\Omega$  and normalized radii  $m$ . Illuminating wavelength is  $\lambda = 632.8$  nm. As expected, the parameter  $m$  determines the distance from the geometrical focus  $F$  and the radius of curvature increases with it. On the other hand, we see that the length of the accelerated beam trajectory is proportional to the semi-aperture  $\Omega$ .

The structure proposed by us for the molding of an incident converging wave into an accelerating beam is based on metal-dielectric

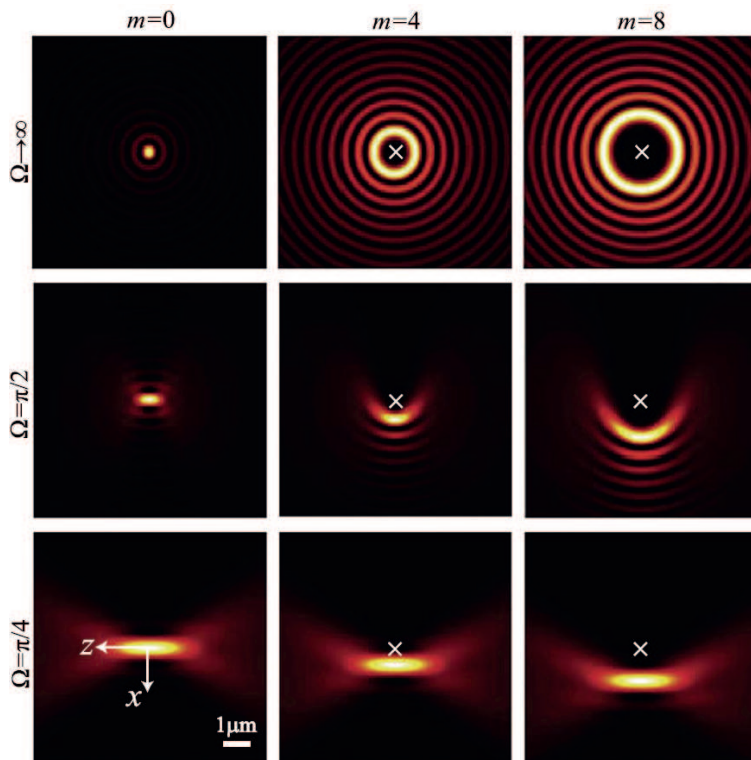


Figure 4.24: Magnetic field intensity  $|H(\mathbf{r})|^2$  simulated for different semi-apertures  $\Omega$  and normalized radii  $m$ . The white crosses indicate the focal point of the original converging beam.

multilayer stacks with a circular pattern. This arrangement may be considered as an inhomogeneous uniaxial metamaterial with permittivities given by eqs. (3.14) and (3.15) as explained in section 3.2. The permittivities of the metal and dielectric constituents are  $\epsilon_m = -10.77$ , which corresponds to the real part of the dielectric constant

for the gold at  $\lambda = 632.8$  nm, and  $\varepsilon_d = 1$ , respectively.

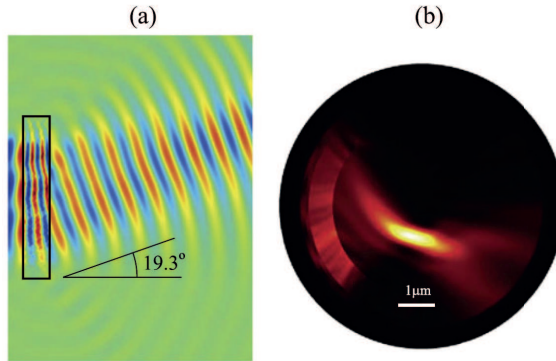


Figure 4.25: (a) Real part of the magnetic field distribution for a plane wave scattered by the proposed inhomogeneous anisotropic metamaterial in a planar configuration. (b) Energy density for the metamaterial in an annular configuration with inner radius  $R = 2.4415 \mu\text{m}$ .

In fig. 4.25(a) we show the behavior of the proposed MD metamaterial with a planar configuration of thickness  $d = 660$  nm under the impinge of a collimated  $\text{TM}^z$ -polarized beam. The normally incident wave field experiments an angular deviation  $\phi' \approx 19^\circ$ . Fig. 4.25(b) presents a circular arrangement which has more interest for us. We will focus on this arrangement from now on. It is represented in fig. 4.25(b) the time-averaged energy density of the accelerated wave field. The incident wavelength is again  $\lambda = 632.8$  nm. The arrangement of the cylindrical metamaterial is designed to convert a cylindrical incident wave into an accelerating beam of order  $m = 8$ . The radius at the

exit surface is estimated as  $R = 2.4415 \mu\text{m}$  provided the slab thickness is  $d = 660 \text{ nm}$ . The resultant beam is in good agreement with the prediction of fig. 4.24.

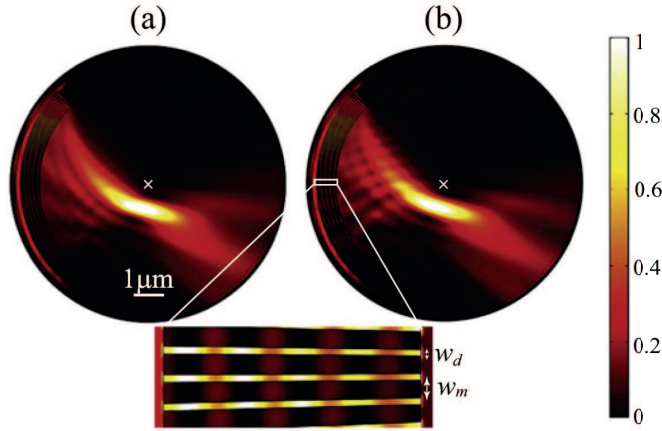


Figure 4.26: Time-averaged energy density of accelerating beams at  $\lambda = 632.8 \text{ nm}$ . The focal waves are accelerated by a concentric graded grating made of gold which width is  $w_m = 25 \text{ nm}$  at the exit surface. The dielectric widths range from 5 to 78 nm (a) continuously and (b) with steps higher than 1 nm.

To introduce the dephase needed to accelerate focal waves the thickness of the films composing the circular metamaterial must be subwavelength. In fact, for the metal it must be lower than its penetration depth, which is typically a few tens of nanometers in the optical range. Taking into account losses, the permittivity for gold is  $\varepsilon_m = -10.77 - 0.79i$  at  $\lambda = 632.8 \text{ nm}$ . We consider a converging super-Gaussian beam with semi-aperture  $\Omega = 2\pi/7$  impinging on the

outermost radius of the metamaterial and propagating inside the MD metamaterial for a distance of  $d = 660$  nm (fig. 4.26). The MD interfaces of the metamaterial are concentric to the focal point of the incident beam, which is represented by a white X mark in the figure.

In fig. 4.26(a) it is shown the time-averaged energy density of the spatially-accelerated beam after being transformed by the subwavelength engineered metamaterial. Comparing the results obtained with fig. 4.25(b) one can verify that they are in good agreement. In practical terms we are constrained to design the metamaterial with integer values in nanometers for the dielectric width  $w_d$  (at the exit surface). The result of this is presented in fig. 4.26(b), where artificial ripples are evident close to the metamaterial. However, the main lobe of the accelerated wave is kept almost unaltered.

As one may expect, the behavior of the metamaterial will change when varying its thickness  $d$ . In fig. 4.27 we appreciate that for different values of  $d$ . It is important to note that the value of the radius  $r_m = |m|/k$  of the accelerating beam must be shorter than the radius of the metamaterial at its exit surface. In the considered situations this means that the thickness  $d$  must be shorter  $2.95 \mu\text{m}$  to avoid total internal reflection at the exit surface of the metamaterial as occurs at fig. 4.27(a).

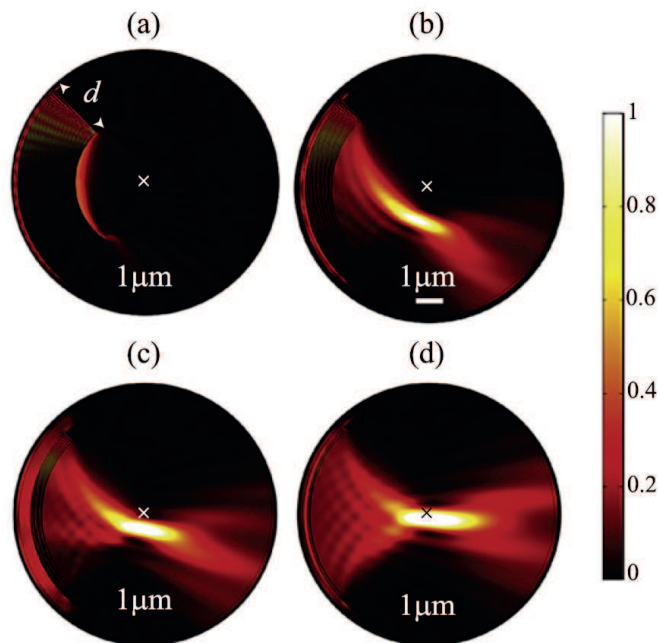


Figure 4.27: Accelerating beams resultant of engineered metamaterials with different thickness: (a)  $d = 3.0 \mu\text{m}$ , (b)  $d = 1.0 \mu\text{m}$ , (c)  $d = 0.4 \mu\text{m}$  and (d)  $d = 0.1 \mu\text{m}$ .

### 4.3 Anisotropic waveguides

As mentioned above, the last part of this Thesis is devoted to the experimental observation of surface waves propagating at the interface of a uniaxial medium and an isotropic material. In this section we will first briefly examine the experimental fabrication and characterization of anisotropic waveguides which serve as support for the surface waves. After that, we will describe the experimental measurements evidencing



the existence of surface waves. Finally, numerical calculations are performed to corroborate our assumptions.

### 4.3.1 Fabrication techniques

The experimental sample fabrication is inspired in a method proposed by the Materials and Optoelectronic Devices Group also in the University of Valencia. It consists in depositing a solution that contains the active mineral, here we used hybrid halide perovskite, set over an anisotropic glass substrate (we choose  $\text{TeO}_2$ ). After the solution deposition, doctor blade can be used to spread the liquid uniformly all along the substrate surface. Subsequently, the solvent is evaporated by heating the sample. As a result, we have the mineral deposited over the substrate. It is convenient to rapidly characterize the roughness and thickness of the deposited mineral, and to cover the sample by using poly(methyl methacrylate), in order to prevent the perovskite being in contact with air and thus to degrade.

#### 4.3.1.1 Deposition process

The process of fabrication begins when we receive the solution of perovskite. The preparation of the solution was performed by some members of our group, not detailed here since it is out of the scope

of this Thesis. Once arrived to the solution concentration which is required, we prepare the substrate by removing any dust particles; after that we deposit a drop of the solution on it. We found out that depositing a tiny drop of toluene over the perovskite-based drop improves the surface roughness of the sample after the baking process. The concentration of the perovskite solution is one of the factors involved in the resultant thickness of the perovskite layer, observing thicker layers for higher concentrations. In our particular case, for a deposition of 20  $\mu\text{l}$  of a 5% concentration of perovskite we obtain a thickness about 4  $\mu\text{m}$ . With a deposition of 20  $\mu\text{l}$  of a 10% concentration the width changes to 8  $\mu\text{m}$ . Next we transfer the sample to the doctor blade setup to spread the liquid over the whole substrate.

#### 4.3.1.2 Doctor blade and baking process

Doctor blade is a technique which permits us spreading many substances over solid substrates [153–155]. The device we used is shown in fig. 4.28. It consists of a blade mounted perpendicularly to the surface where one leaves the substrate. We let the blade moving parallel to the substrate at a certain height, which is fixed by the user. Occasionally, it is employed to remove the excess of substance deposited on the top of the substrate. Mainly, our purpose is simply to spread the

perovskite solution over the whole substrate surface. As mentioned above, the thickness of the perovskite layer will depend on the mineral concentration of the solution, but also the volume of it applied, the blade gap above the substrate and the blading speed [154]. Some advantages of this method are the possibility of a large area deposition and the reduced fabrication time. We point out that an accurate control of the spreading is provided by adjusting the blade height which offers a highly efficient utilization of the mineral solution.

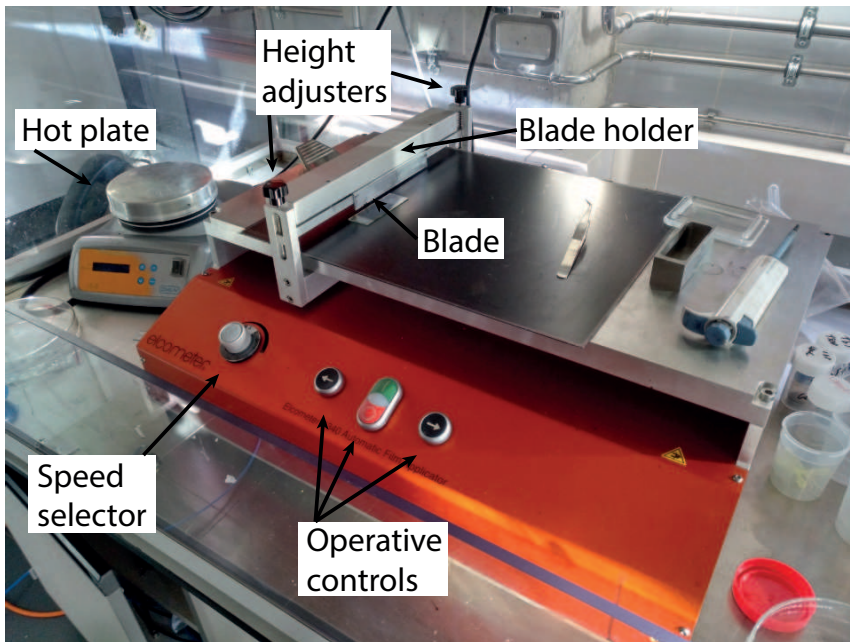


Figure 4.28: Doctor blade device for film application. Next to the doctor blade a hot plate is shown.

The substrate surface on which we deposited the perovskite solution has a squared shape with  $10\text{ mm} \times 10\text{ mm}$  area. The thickness of the  $\text{TeO}_2$  crystal was 1 mm. Once the substrate is set on the doctor blade device, we adjust its height by using a couple of black screws on the top of the blade holder (fig. 4.28). When we drop the solution (concentration 10%) and the toluene over it, next we pass the blade over the surface to spread the liquid mixture [154]. After that, we take the sample carefully and put it on the hot plate, which is previously preheated to 100 degrees Celsius. We leave the sample baking for an hour to ensure all the solvent is evaporated. After this time, we have the perovskite deposited over the  $\text{TeO}_2$  anisotropic substrate. Next we proceed to characterize the fabricated structure.

#### 4.3.1.3 Sample characterization

In this step we use the spectrometer shown in fig. 4.29 to measure the transmissivity and reflectivity of the sample, and the profilometer shown in fig. 4.30 to measure both the depth and the surface roughness of the perovskite layer.

Our spectrometer is designed in a way allowing to measure both transmissivity and reflectivity of thin films. The light source provides a wide range of wavelengths, from UV to visible, and the optical signal

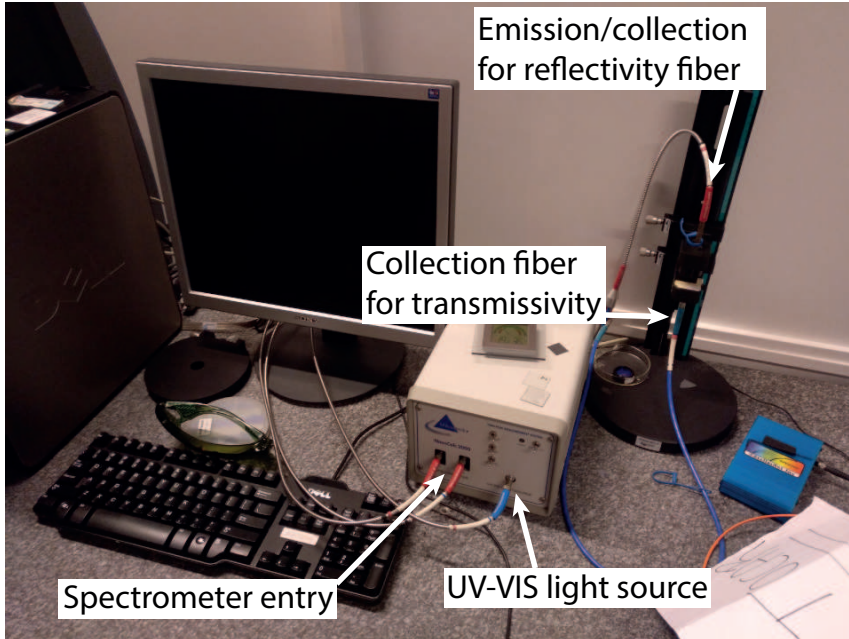


Figure 4.29: Mikropack NanoCalc 2000 spectrometer for transmissivity and reflectivity measurements.

is collected and analyzed by the Mikropack NanoCalc 2000 device. A personalized program which is installed in a connected computer lets choosing to collect light from the top or from the bottom of the sample, depending on if we need to measure reflectivity or transmissivity of the sample, respectively, assuming illumination is launched from the top of the configuration, as shown in fig. 4.29. It is important to mention that this is a non-invasive process, and the sample is maintained unaltered during these measurements.

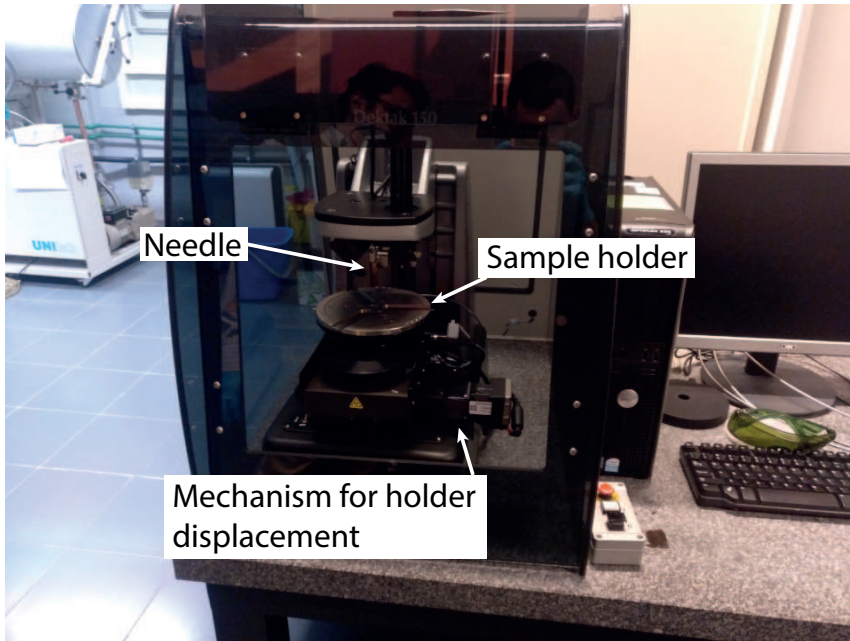


Figure 4.30: Veeco Dektak 150 Surface Profilometer used for surface characterization and width estimation of the deposited layer.

Note that we need to scratch the sample in order to characterize the thickness of the deposited layer. To that end, we perform such tiny scratch in a representative area, that is an area close to a border of the substrate with enough mineral deposited on it but which will not interfere with subsequent measurements. In other words, assuming that the sample is uniformly covered with perovskite, we will scratch it close to a corner of the sample in such a way that the rest of the border remains wide enough to be used in following measurements.

The scratch penetrates to the top of the substrate in a way to prevent substrate damage. This allows a precise measurement of the thickness of the perovskite layer.

The contact profilometer Dektak 150 Surface Profiler, from Veeco, which we used is shown in fig. 4.30. It consists of a stylus with a well-defined tip and a detector that acquires the deviation of the needle from its original position. Based on the out-of-plane deviation of the needle, the device registers the profile of the layer surface. Vertical resolution is about  $2\text{ nm}$ . To shift horizontally the sample in order to characterize its surface profile, a piezoelectric is used for each of the two plane axes. To control the profilometer and collect the data, we use the computer shown in fig. 4.30 and a commercial software also given with Dektak.

Both the surface roughness and the thickness of the perovskite layer deposited on the anisotropic substrate can be measured at the same time. However, it is convenient to perform some other measurements of the surface roughness on different areas to ensure the validity of our results. We put the sample on the profilometer plate and activate it to lower the needle. We must be sure that the needle falls on a proper region of the surface, at least close to the one that we pretend to characterize. After that, we proceed to the profile registration by

means of the required software. Provided that we are by an area where there is no scratch, we can only measure the roughness of the film surface. On the other hand, setting the needle where our previous mark is will allow us to estimate the thickness of the mineral layer.

After full characterization is completed, it is important to prevent degrade the sample in contact with air and humidity, as we mentioned before. Therefore, we will cover the sample with a very thin layer of poly(methyl methacrylate) (PMMA).

#### 4.3.1.4 Spin-coating

To cover the prepared sample with PMMA we use a common and simple technique coined as spin-coating [155–158]. It consists basically in depositing a drop of a material dispersed or diluted in a solution (PMMA in our case) on the sample and spinning it to cover the whole surface with a thin film of the desired material. In fig. 4.31 we show our spin-coating device, together with a hot plate to bake the samples after deposition and spinning.

To protect our sample, we put it on the spinning sample holder. First of all, we have to make sure that the vacuum which holds the sample on the device while it spins is well done. Otherwise, the sample might fly out probably breaking it up. After setting the sample



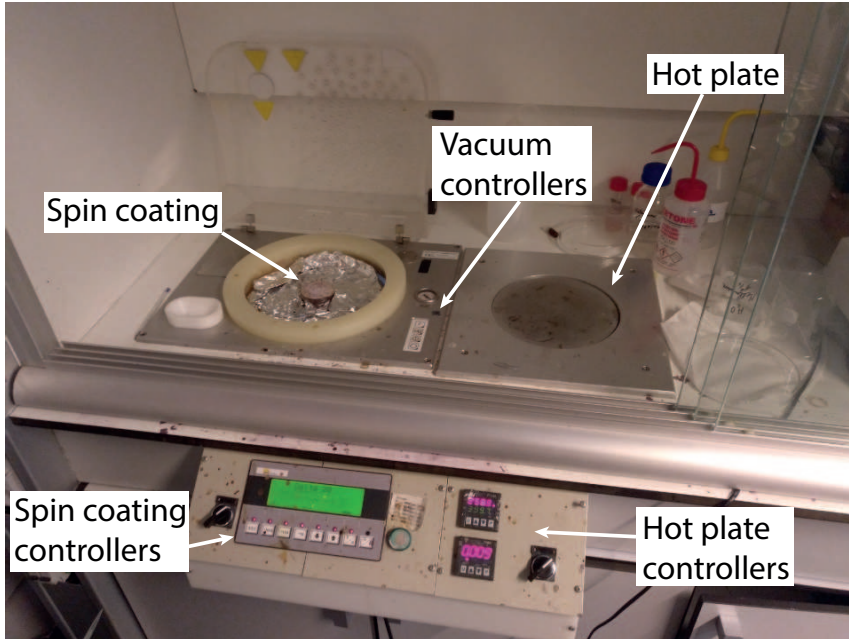


Figure 4.31: Spinning mechanism on the left of the image, protected with aluminum foil to reduce dirt accumulation on the device when it spins. A hot plate can also be seen on the right.

correctly with the vacuum we deposit  $10 \mu\text{l}$  of a PMMA solution with 1% concentration on the center of the perovskite layer. Note that we control the final thickness of the layer by modifying the rotation velocity and the solvent concentration. Once the spinning velocity is set at 2000 revolutions per second, we activate the device and wait for 30 seconds until the solution is spread on the entire surface. Immediately after completing the spinning we bake the sample again at  $80^\circ\text{C}$  and

150°C during two minutes at each temperature [156]. The first baking will evaporate the PMMA solvent completely, and the second baking is made under a higher temperature for glass transition (around 105°C) for its polymerization. The resultant thickness of the PMMA cover is estimated as 50 nm. It is worth to mention that although the active layer is protected, it is convenient to perform any remaining sample processing, measurements and analysis as soon as possible to minimize any residual degradation of the sample.

### 4.3.2 Experimental results

Once the multilayered sample is fabricated, it is still necessary to prepare it conveniently for our specific experimental setup. First we polish the output surface from which we will collect the scattered field from bound waves propagating all along the sample. This process is made by an initial smoothing with a set of three abrasive papers, specifically with 600, 800 and 1200 grains per square centimeter. Next we use several polishing pastes categorized by their grain size, starting with a grain of 15  $\mu\text{m}$  and finishing with one of 1/4  $\mu\text{m}$ .

After polishing the output surface of the sample, we take it to the experimental setup illustrated in fig. 4.32. The sample is illuminated from above by using a fiber tip, impinging normally to the PMMA flat

film. Finally, light interacts with the active medium, that is the hybrid halide perovskite, activating a photoluminescence (PL) effect. The photo-physical and semiconducting properties of hybrid halide perovskites are based on recombination processes of photo-excited charge carriers, which lead to a high efficient radiative recombination [159]. As a result, the PL signal exhibits a longer wavelength than the light previously absorbed by the sample.

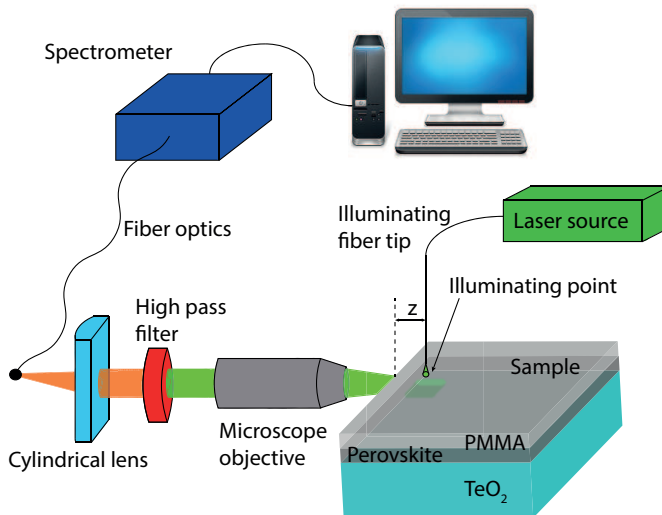


Figure 4.32: Schematics of experimental setup used to detect guiding surface modes in anisotropic waveguides.

The optical fiber is positioned perpendicularly and close to the mineral in order to maximize light-matter interaction in the active

layer. The light source is a Nd:Yag laser emitting at a wavelength  $\lambda = 532$  nm (second harmonic signal). Perovskite absorbs this radiation efficiently, inducing a broadband PL emission centered at a wavelength  $\sim 780$  nm. A key point is that the PL signal will generate bound modes in the anisotropic waveguide by near-field coupling, including waves tightly confined in the perovskite layer and surface waves localized on the perovskite-TeO<sub>2</sub> interface. Guided waves then travel along the multilayered photonic structure for a given distance, so that we may collect them at the output edge, which is the one that we polished in advance. Collection of light is performed with a 20x microscope objective which focuses it into a second optical fiber to be channeled and analyzed into a HR4000 Ocean Optics spectrograph. To remove the component of scattered light produced on the PMMA surface, which is directly given by the laser, we use a filter to be set between our sample and the spectrometer input fiber, right behind the microscope objective. Finally, with the appropriate software, we are able to manage the input data, that is the light intensity emerging from the anisotropic waveguide, within a wide range of wavelengths.

Our objective is to characterize the inherent losses of surface and bound modes excited by the photoluminescence of the perovskite. They represent a modal signature in the detected signal. For that

purpose, we proceed in the following way. First we displace the optical fiber tip along the PMMA flat surface from the output edge towards the center of the sample. The spatial coordinate  $z$  determines the distance from the tip position to the output edge, as shown in fig. 4.32. For a given value of  $z$ , we measure the collected light intensity. We expect to determine the modal attenuation in the anisotropic waveguide by monitoring the output intensity versus  $z$ , thus revealing the propagation characteristic of the dominant bound mode propagating along a specific direction. The existence of a few dominant bound modes can also be treated appropriately. The set of points captured in the spectrometer can be adjusted to a double exponential decay function in the form

$$\Psi = A_1 \cdot \exp(-\alpha_1 \cdot z) + A_2 \cdot \exp(-\alpha_2 \cdot z), \quad (4.5)$$

where  $A_1$  and  $A_2$  are constant amplitudes which depend on the maximum collected intensity, and  $\alpha_1$  and  $\alpha_2$  are the decay parameters. Specifically,  $\alpha_1$  provides the imaginary part of the effective refractive index of the propagating mode as

$$n''_{eff} = \frac{\alpha_1 \cdot \lambda}{4\pi}. \quad (4.6)$$

Note that the captured data, for each position of the illumination tip, can be analyzed with a specific software tool by representing both the power spectrum and also the integrated intensity within a desired wavelength range. When we represent the spectrum of the collected intensity for a given displacement  $z$ , such set of points can be adjusted to a Gaussian function (not shown here) with a given peak center and standard deviation. Furthermore, we might appreciate any spectral shift by analyzing the centroid of this Gaussian function.

To investigate the anisotropic response of the waveguide, we measure the output signal of bound waves propagating along the optic axis of the  $\text{TeO}_2$ , and also its perpendicular direction. Oblique propagation is not determined due to evident experimental difficulties in preparing the output edge. The integrated intensity measured in both directions, as a function of the position  $z$  of the fiber tip, and the central peak of the spectrum at each value of  $z$ , are shown in figs. 4.33 and 4.34.

From the results given in figs. 4.33 and 4.34 we can deduce that losses are lower for the coupled light propagating along a perpendicular direction of the optic axis. In particular,  $\alpha_1 = 0.1$  ( $n''_{eff} = 0.006$ ) for waves propagating along the optic axis ( $A_1 = 1$ ,  $A_2 = 0.015$  and  $\alpha_2 = 0.001$  for the fit as explained in eq. (4.5)), and  $\alpha_1 = 0.06$  ( $n''_{eff} =$

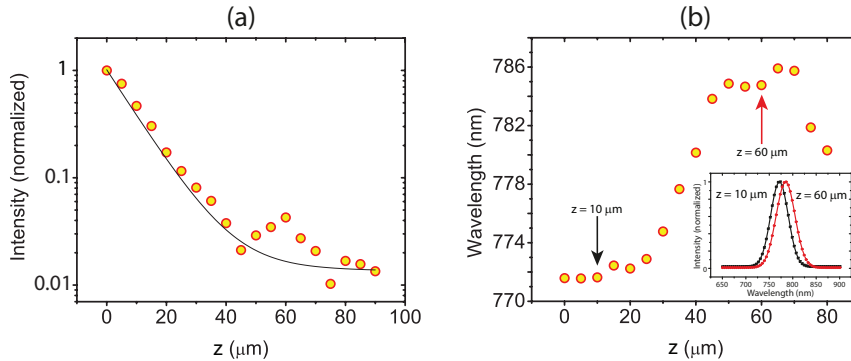


Figure 4.33: Output intensity (a) and spectral shift (b) of waves propagating in the multilayered structure, in a direction parallel to the  $\text{TeO}_2$  optic axis. In (a) we also include the intensity fitted to eq. (4.5). Inset in (b) shows the power spectra of the detected signal when the fiber is located at  $z = 10 \mu\text{m}$  (solid black line) and at  $z = 60 \mu\text{m}$  (solid red line).

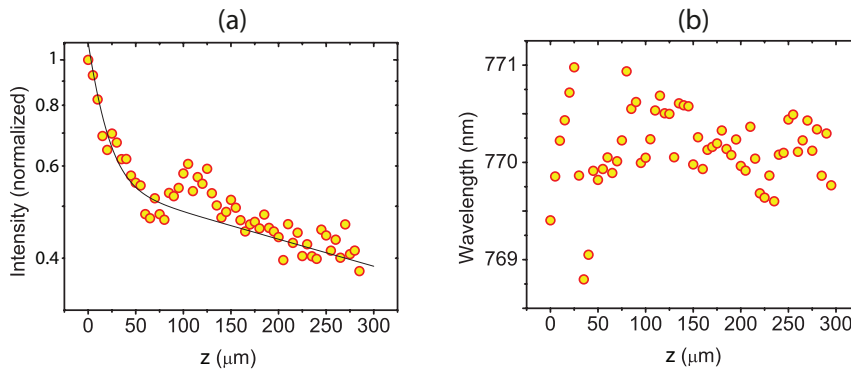


Figure 4.34: The same as in fig. 4.33 but waves propagate in a direction perpendicular to the  $\text{TeO}_2$  optic axis.

0.004) for waves propagating perpendicularly ( $A_1 = 0.65$ ,  $A_2 = 0.45$  and  $\alpha_2 = 0.0015$  for the fit as explained in eq. (4.5)). Regarding the

spectral shift analyzed in the output signal, a red shift induced at higher  $z$  is evident when guided light propagates along the optic axis, as shown in fig. 4.33(b). For the measurements performed by collecting the light that is guided in the structure, traveling perpendicularly to the optic axis, shown in fig. 4.34(b), we find almost no spectral displacement. The spectral shift found for light collection parallel to the optic axis is related to a stronger absorption of the perovskite at lower wavelengths [160], as shown in fig. 4.35, which causes an increasing redshift at longer propagation distance  $z$ . On the other hand, when we collect the guided light propagating perpendicular to the optic axis the tail of the surface bound mode penetrates less into the perovskite layer making the spectral shift negligible.

From the estimated imaginary part of the complex refractive index at both perpendicular directions of propagation, we infer that the modal confinement in the lossy material (perovskite) differs substantially for these directions. In fact, we will numerically demonstrate that the governing wave mode propagating perpendicular to the optic axis of the substrate is a surface wave, in opposition to the mode guided in the perovskite when propagation is directed along the optic axis. Specifically, this surface bound mode propagates along the interface between the perovskite and the  $\text{TeO}_2$ . The numerical sim-



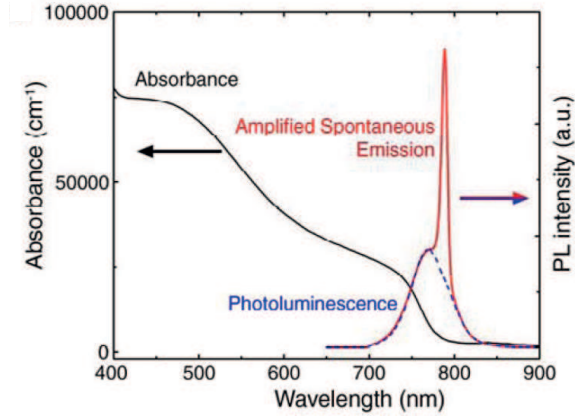


Figure 4.35: Absorbance, photoluminescence and amplified spontaneous emission curves for perovskite [160], the latter not of interest here. Note a greater absorbance at lower wavelengths and the PL peak centered at 780 nm.

ulations are performed by using the FEM-based commercial software which was previously described in section 3.4. We also used Wolfram Mathematica to calculate the wave modes by means of the transfer matrix theory (see section 3.3), corroborating our previous results.

### 4.3.3 Theoretical results

To confirm our experimental results we performed some numerical simulations based on FEM, as we briefly explained in section 3.4. In particular, we used the commercial available software COMSOL Multiphysics to model our multilayered waveguide and to obtain the effective refractive index and the fields in the structure. Also, we performed

some simulations by using the transfer matrix theory, as described in section 3.3. The latter problem can be numerically solved to obtain the effective refractive index  $n_{eff}$ , which is a complex number. For these calculations we employed the Wolfram Mathematica software. Note that both numerical procedures will provide the decay in intensity when bound and surface waves propagate along the optic axis of the substrate and perpendicularly to it. In all cases, we use a wavelength  $\lambda = 780$  nm, a dielectric constant  $\varepsilon = 5.47 - 0.23i$  ( $n = 2.34 - 0.05i$ ) for the perovskite [160], and  $\varepsilon_{\parallel} = 5.692$  and  $\varepsilon_{\perp} = 5.003$  for TeO<sub>2</sub> [161]. Note that  $\varepsilon_{\perp} < \text{Re}(\varepsilon) < \varepsilon_{\parallel}$ , which is commonly required for the existence of DSWs [110].

First, we numerically determined a minimum width of perovskite needed to sustain DSWs in its boundary with the substrate. With less than 7 micrometers we found no propagating surface waves. As a result, we considered a layer width of  $8 \mu\text{m}$  in our simulations. Our samples were fabricated in agreement with this restriction, using a perovskite layer of  $8 \mu\text{m}$  (approximately) and a PMMA layer of 50 nm, the latter disregarded in our numerical simulations.

In fig. 4.36 and fig. 4.37 we show two different modal fields simulated with FEM when the wave fields propagate perpendicular to the optic axis. We specifically choose confined modes with decaying fields

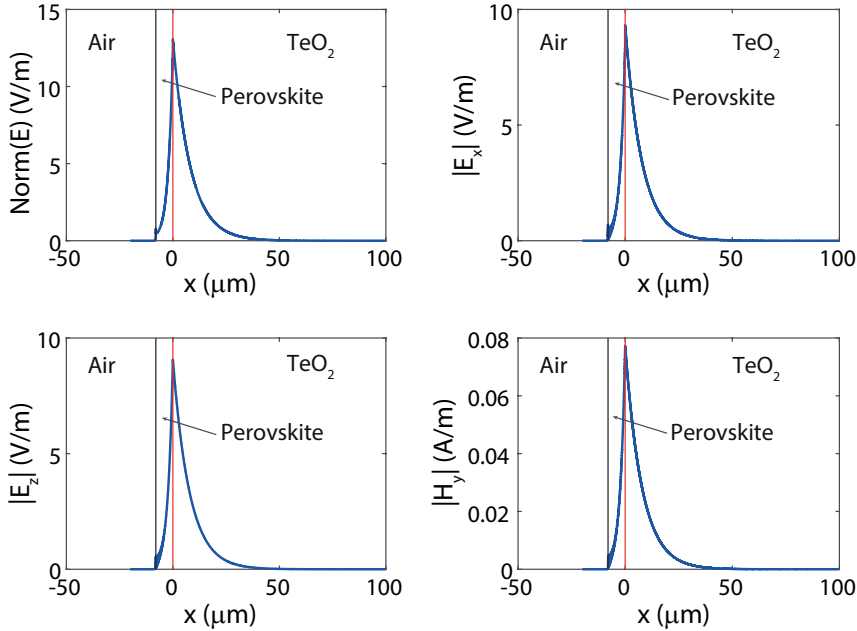


Figure 4.36: Fields for a propagating surface wave in the interface between the perovskite layer and the  $\text{TeO}_2$  substrate. The components of the EM field not shown are zero. Propagation perpendicular to the optic axis.

when moving far from the active layer, also exhibiting the lowest losses. The latter condition implies that the selected field will dominate the intensity distribution of the excited waves, by near-field coupling, after propagating a certain distance. In fig. 4.36 we show all the components of the chosen electromagnetic field, which clearly represent a surface wave in the isotropic-anisotropic surface. Furthermore, this surface mode has a propagation constant  $\beta = 1.6290 - 0.0143i$  and it exhibits

$TE^y$  polarization (propagation is set along the  $z$  axis). It is important to note that in a lossless multilayered structure, we cannot find DSWs propagating neither perpendicular nor parallel to the optic axis of the uniaxial medium. As a consequence, the existence of such confined wave field is directly related to the presence of the lossy perovskite.

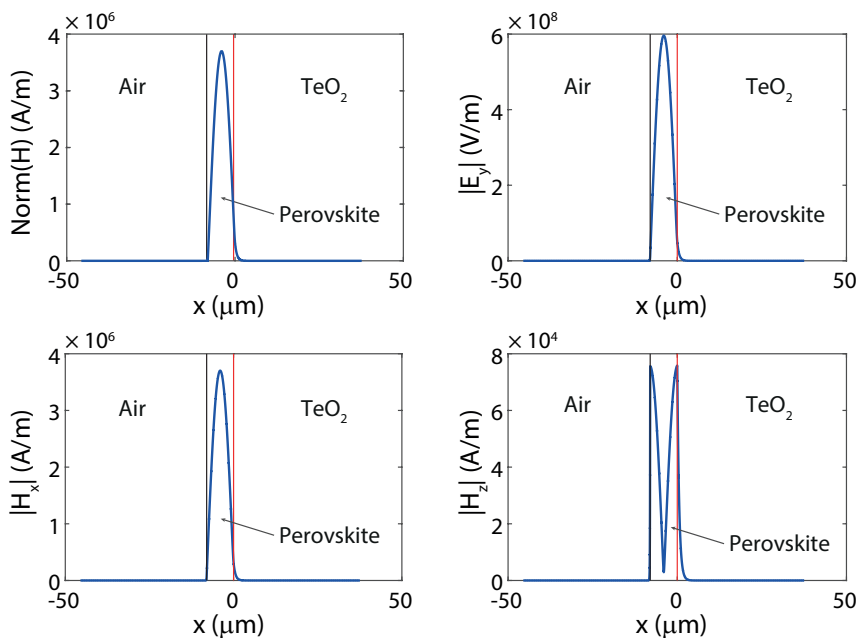


Figure 4.37: Fields for the guided mode in the perovskite layer. The field components not shown are zero. Propagation perpendicular to the optic axis.

In addition to this surface wave we find other types of modes. One example is the fundamental mode of the perovskite waveguide under  $TM^y$  polarization, shown in fig. 4.37. The main difference that we

take profit of to distinguish perovskite modes from the propagating surface wave in which we are interested in is focused on the modal losses. When we estimate the effective index we appreciate a larger imaginary part for the mode in the perovskite. This means that the mode in the mineral has greater losses. Specifically, the fundamental guided mode traveling in the perovskite layer presents a propagation constant  $\beta = 2.3395 - 0.0500i$ . Note that this value is essentially the same found for a plane wave propagation in bulk perovskite, and its intensity decays notably stronger than that found for the surface wave. We point out that complementary  $TE^y$ -polarized guided modes can be found, not shown in the figures, exhibiting practically the same propagation constant.

When we calculate the modes propagating parallel to the optic axis, we numerically find that there is no surface bound modes in this direction. On the other hand, guided modes in the perovskite layer still remain. For the fundamental mode, we observe practically the same effective refractive index than that calculated for propagation along the perpendicular orientation. Therefore, we conclude that the waveguide presents a clear anisotropic response, where a surface mode is found only in one principal direction. This is consistent with the experimental results given in section 4.3.2.



# Chapter 5

## Conclusions

In this Ph.D. Thesis we have proposed the use of anisotropic materials and metamaterials for various technological applications, from invisibility and wave field bending to surface light guiding. In this chapter we will sum up the main results and conclusions of the studies performed along this work. We will differentiate the three blocks that give form to this Thesis and we will focus on the results obtained in each of them.

In the first block of this Thesis we first studied a cylindrical cavity formed by a radially anisotropic medium established by the form birefringence of a metamaterial composed of a periodic distribution of subwavelength concentric multilayers. For this subwavelength struc-

ture we analyzed the scattering efficiency and we observed two resonances which correspond to the symmetric and antisymmetric modes of surface polaritons. By the side of each resonant peak, at a slightly higher frequency, we found a minimum in scattering efficiency that can be attributed to Fano shapes. When the nanocavity is immersed in air the fundamental frequency at which we find a minimum for scattering is the one at which the metamaterial permittivity  $\varepsilon_{\perp}$  takes values near zero. With this in mind, by balancing the composition of the metamaterial shell, we might tune the invisibility frequency up to the plasma frequency of the Drude medium. Unfortunately, for filling factors close to unity this approach is not valid because the nanotube behaves like a low-birefringent plasmonic cavity. For high filling factors we should use the secondary dip in the scattering spectrum to obtain invisibility. When the cavity size increases, in the order of the wavelength, additional resonances emerge governing the contour of the scattering spectrum and vanishing the invisibility effect. For different values of the shell thickness-utmost radius ratio  $T/R$  the main invisibility frequencies remain practically unaltered. The case of a cylinder with a very small concentric hole is of special relevance due to the appearance of multiple peaks and their associated minima of scattering, which reveals an accumulation of excited Fano resonance. Also,



when the permittivity constant of both the core and the environment medium is modified, we found severe discrepancies to the rule of  $\varepsilon_{\perp}$  near zero. For instance, for a high dielectric constant in both media, the fundamental invisibility frequency is practically fixed for the whole range of filling factors. The results obtained demonstrate that the invisibility regime completely depends on the permittivities of the core and environment medium.

Secondly, we analyzed the conditions to achieve invisibility with the use of realistic metal-dielectric metamaterials. We investigated numerically the scattering efficiency of a MD multilayered nanotube composed of Ag and  $\text{TiO}_2$  with special emphasis in the invisibility region. We demonstrated that when the dielectric layer is set in contact with the core of the nanocylinder the invisibility of the hyperbolic nanotube is cleared away, even for layers of a few nanometers. In this case plasmonic-Bloch resonances are found on the wave fields localized at the rear part of the structure. Furthermore, the effective medium theory gives inaccurate estimations of the characterization of the nanostructure, although such effect is weaker if the width of the nanolayers is lower than 5 nanometers.

Finally, we proposed a new degree of freedom in the design of the multilayered nanotube in which we include a marginal factor. This

feature allows us to improve the invisibility achieved by such metamaterials with the additional advantage of tunability in a broad spectral band. The achieved reduction of the scattering efficiency of these structures of nearly two orders of magnitude in comparison with previous studies also based on radially-periodic arrangements is consequence of the inherent nonlocal effects of metallodielectric nanostructures. Invisibility of our Ag-TiO<sub>2</sub> nanotube is mainly attributed to scattering cancellation for TM<sup>z</sup>-polarized incident plane waves and to a Fano-type isolated resonance in the case of TE<sup>z</sup>-polarized incident fields. The resonant behavior of the nanotube under TE<sup>z</sup> polarization made it to reduce the maximal efficiency to changes in external environment, diameter of the nanocylinder and the period of the multilayered shell. We can adjust the nanocavity response to present a significant reduction of scattering efficiency for both polarizations although the response of the cylindrical cavity is very selective under polarization. Moreover, we set the Lorenz-Mie scattering coefficients in terms of a transfer matrix formalism that enables a fast evaluation of the scattering efficiency of the multilayered nanocylinder.

In the second block of this Thesis we continue describing the use of MD metasurfaces for beamshaping and focusing applications. In this case the structures are designed with the interfaces in a concen-

tric way instead of the layers. As it is described in section 4.2.1 the use of curved ultrahigh-refraction-index MD metasurfaces enables a high-NA beam shaping. With these structures it is possible to control the dephase of the transmitted  $TM^z$ -polarized wave field, modifying the curvature of the exit wavefront, to obtain an increased NA which demonstrates an exceptional super-resolution effect on axis. Furthermore, assuming the impinging field is a plane wave we can achieve a similar behavior by setting two MD metasurfaces on the faces of a dielectric plano-concave lens (section 4.2.2). It is demonstrated that the use of a planar MD metasurface on the plane face of the lens together with the curved metacoating on the concave face allows tightly focusing of light in the interior of the hollow opening and even its lateral shift by controlling the tilt angle of the incident plane wave. The use of such ultrathin metacoatings offers a considerable reduction of Ohmic losses and efficient coupling to exterior radiation. Our design of a curved MD multilayered metamaterial also enables the acceleration of focal converging waves around their geometrical focus. With a controlled variation of the metal width in the multilayer it is possible to induce a selective dephase at different parts of the incident wave to obtain such accelerating beams. In particular, the arrangement explained in section 4.2.3 enables the introduction of a certain dephase on the con-

verging incident beam to transform it into an accelerating Bessel beam with order  $m = 8$  at a wavelength  $\lambda = 632.8$  nm. On the other hand, a metamaterial thickness too high will enable total internal reflection at the exit surface of the structure. From the technological point of view, the fabrication of these MD metamaterials should not be a problem since the silver and silica deposition by e-beam evaporation is a practicable procedure.

Finally, in the third and last part of this Thesis we performed some experiments supported by numerical simulations. We were able to fabricate an anisotropic surface waveguide made of an active mineral (perovskite) and an anisotropic substrate ( $\text{TeO}_2$ ). I was able to employ different experimental devices and procedures to fabricate the waveguiding structure, as doctor blade and spin coating, among other interesting techniques for sample characterization. After studying the structure we deduced lower losses for the light collected perpendicular to the optic axis, and higher when the analysis is performed in the parallel direction with respect to the optic axis. When compared this results with the simulations, it is revealed a surface bound mode propagating along perpendicular direction with respect to the optic axis but not in the parallel one. This fact explains the lower losses in the perpendicular direction. This propagating surface bound mode is

found only in one direction because of the anisotropic nature of the substrate material.



# Bibliography

- [1] A. V. Kildishev, A. Boltasseva, and V. M. Shalaev, “Planar photonics with metasurfaces,” *Science* **339**, 1232009 (2013).
- [2] P. Yeh and A. Yariv, “Optical waves in crystals,” A Wiley Interscience Publication, John Wiley & Sons (1984).
- [3] H. Tada, S. E. Mann, I. N. Miaoulis, and P. Y. Wong, “Effects of a butterfly scale microstructure on the iridescent color observed at different angles,” *Appl. Opt.* **37**, 1579–1584 (1998).
- [4] E. Ozbay, “Plasmonics: merging photonics and electronics at nanoscale dimensions,” *Science* **311**, 189–193 (2006).
- [5] J. Schuller, E. Barnard, W. Cai, Y. C. Jun, J. S. White, and M. L. Brongersma, “Plasmonics for extreme light concentration and manipulation,” *Nat. Mater.* **9**, 193–204 (2010).

- [6] J. B. Pendry, “Negative refraction makes a perfect lens,” *Phys. Rev. Lett.* **85**, 3966–3969 (2000).
- [7] T. W. Ebbesen, H. J. Lezec, H. F. Ghaemi, T. Thio, and P. A. Wolf, “Extraordinary optical transmission through sub-wavelength hole arrays,” *Nature (London)* **391**, 667–669 (1998).
- [8] A. Poddubny, I. Iorsh, P. Belov, and Y. Kivshar, “Hyperbolic metamaterials,” *Nat. Photonics* **7**, 948–957 (2013).
- [9] E. Hutter and J. H. Fendler, “Exploitation of localized surface plasmon resonance,” *Adv. Mater.* **16**, 1685–1706 (2004).
- [10] I. I. Smolyaninov, Y.-J. Hung, and C. C. Davis, “Magnifying superlens in the visible frequency range,” *Science* **315**, 1699–1701 (2007).
- [11] L. Novotny and N. van Hulst, “Antennas for light,” *Nat. Photonics* **5**, 83–90 (2011).
- [12] S. I. Bozhevolnyi, V. S. Volkov, E. Devaux, J.-Y. Laluet, and T. W. Ebbesen, “Channel plasmon subwavelength waveguide components including interferometers and ring resonators,” *Nature* **440**, 508–511 (2006).



- [13] T. Ergin, N. Stenger, P. Brenner, J. B. Pendry, and M. Wegener, “Three-dimensional invisibility cloak at optical wavelengths,” *Science* **328**, 337–339 (2010).
- [14] S. Lal, S. Link, and N. J. Halas, “Nano-optics from sensing to waveguiding,” *Nat. Photonics* **1**, 641–648 (2007).
- [15] J. K. Gansel, M. Thiel, M. S. Rill, M. Decker, K. Bade, V. Saile, G. von Freymann, S. Linden, and M. Wegener, “Gold helix photonic metamaterial as broadband circular polarizer,” *Science* **325**, 1513–1515 (2009).
- [16] K. Kumar, H. Duan, R. S. Hegde, S. C. W. Koh, J. N. Wei, and J. K. W. Yang, “Printing colour at the optical diffraction limit,” *Nat. Nanotechnol.* **7**, 557–561 (2012).
- [17] F. J. Garcia-Vidal, L. Martín-Moreno, and J. B. Pendry, “Surface with holes in them: new plasmonic metamaterials,” *J. Opt. A* **7**, S97–S101 (2005).
- [18] N. Yu and F. Capasso, “Flat optics with designer metasurfaces,” *Nat. Mater.* **13**, 139–150 (2014).
- [19] F. Aieta, P. Genevet, M. A. Kats, N. Yu, R. Blanchard, Z. Gaburro, and F. Capasso, “Aberration-free ultrathin flat

- lenses and axicons at telecom wavelengths based on plasmonic metasurfaces,” *Nano Lett.* **12**, 4932–4936 (2012).
- [20] H. A. Atwater and A. Polman, “Plasmonics for improved photovoltaic devices,” *Nat. Mater.* **9**, 205–213 (2010).
- [21] J. Zhang, J.-Y. Ou, N. Papasimakis, Y. Chen, K. F. MacDonald, and N. I. Zheludev, “Continuous metal plasmonic frequency selective surfaces,” *Opt. Express* **19**, 23279–23285 (2011).
- [22] N. Yu, P. Genevet, F. Aieta, M. A. Kats, R. Blanchard, G. Aoust, J.-P. Tetienne, Z. Gaburro, and F. Capasso, “Flat optics: Controlling wavefronts with optical antenna metasurfaces,” *IEEE J. Sel. Top. Quantum Electron.* **19**, 4700423–4700423 (2013).
- [23] M. R. Shcherbakov, D. N. Neshev, B. Hopkins, A. S. Shorokhov, I. Staude, E. V. Melik-Gaykazyan, M. Decker, A. A. Ezhov, A. E. Miroshnichenko, I. Brener *et al.*, “Enhanced third-harmonic generation in silicon nanoparticles driven by magnetic response,” *Nano Lett.* **14**, 6488–6492 (2014).

- [24] D. R. Smith and D. Schurig, “Electromagnetic wave propagation in media with indefinite permittivity and permeability tensors,” *Phys. Rev. Lett.* **90**, 077405 (2003).
- [25] Z. Jacob, L. V. Alekseyev, and E. Narimanov, “Optical hyperlens: far-field imaging beyond the diffraction limit,” *Opt. Express* **14**, 8247–8256 (2006).
- [26] Z. Liu, H. Lee, Y. Xiong, C. Sun, and X. Zhang, “Far-field optical hyperlens magnifying sub-diffraction-limited objects,” *Science* **315**, 1686 (2007).
- [27] J. Rho, Z. Ye, Y. Xiong, X. Yin, Z. Liu, H. Choi, G. Bartal, and X. Zhang, “Spherical hyperlens for two-dimensional sub-diffractive imaging at visible frequencies,” *Nat. Commun.* **1**, 143 (2010).
- [28] D. Lu and Z. Liu, “Hyperlenses and metalenses for far-field super-resolution imaging,” *Nat. Commun.* **3**, 1205 (2012).
- [29] S. Ishii, A. V. Kildishev, E. Narimanov, V. M. Shalaev, and V. P. Drachev, “Sub-wavelength interference pattern from volume plasmon polaritons in a hyperbolic medium,” *Laser Photonics Rev.* **7**, 265–271 (2013).

- [30] A. A. Orlov, S. V. Zhukovsky, I. V. Iorsh, and P. A. Belov, “Controlling light with plasmonic multilayers,” *Phot. Nanostr. Fund. Appl.* **12**, 213–230 (2014).
- [31] D. Lu, J. J. Kan, E. E. Fullerton, and Z. Liu, “Enhancing spontaneous emission rates of molecules using nanopatterned multilayer hyperbolic metamaterials,” *Nat. Nanotechnol.* **9**, 48–53 (2014).
- [32] A. Yariv and P. Yeh, “Electromagnetic propagation in periodic stratified media. II. Birefringence, phase matching, and x-ray lasers,” *J. Opt. Soc. Am.* **67**, 438–448 (1977).
- [33] D. R. Smith and J. B. Pendry, “Homogenization of metamaterials by field averaging,” *J. Opt. Soc. Am. B* **23**, 391–403 (2006).
- [34] P. A. Belov and Y. Hao, “Subwavelength imaging at optical frequencies using a transmission device formed by a periodic layered metal-dielectric structure operating in the canalization regime,” *Phys. Rev. B* **73**, 113110 (2006).
- [35] S. M. Vuković, J. J. Miret, C. J. Zapata-Rodríguez, and Z. Jakšić, “Oblique surface waves at an interface of metal-

- dielectric superlattice and isotropic dielectric,” *Phys. Scr.* **T149**, 014041 (2012).
- [36] J. Elser, V. A. Podolskiy, I. Salakhutdinov, and I. Avrutsky, “Nonlocal effects in effective-medium response of nanolayered metamaterials,” *Appl. Phys. Lett.* **90**, 191109 (2007).
- [37] A. Orlov, I. Iorsh, P. Belov, and Y. Kivshar, “Complex band structure of nanostructured metal-dielectric metamaterials,” *Opt. Express* **21**, 1593–1598 (2013).
- [38] R.-L. Chern, D. Han, Z. Zhang, and C. T. Chan, “Additional waves in the graphene layered medium,” *Opt. Express* **22**, 31677–31690 (2014).
- [39] E. Popov and S. Enoch, “Mystery of the double limit in homogenization of finitely or perfectly conducting periodic structures,” *Opt. Lett.* **32**, 3441–3443 (2007).
- [40] H. Im, K. C. Bantz, N. C. Lindquist, C. L. Haynes, and S.-H. Oh, “Vertically oriented sub-10-nm plasmonic nanogap arrays,” *Nano Lett.* **10**, 2231–2236 (2010).

- [41] W. Chen, M. D. Thoreson, S. Ishii, A. V. Kildishev, and V. M. Shalaev, “Ultra-thin ultra-smooth and low-loss silver films on a germanium wetting layer,” *Opt. Express* **18**, 5124–5134 (2010).
- [42] L. Shen, T.-J. Yang, and Y.-F. Chau, “50/50 beam splitter using a one-dimensional metal photonic crystal with parabolalike dispersion,” *Appl. Phys. Lett.* **90**, 251909 (2007).
- [43] A. A. Orlov, P. M. Voroshilov, P. A. Belov, and Y. S. Kivshar, “Engineered optical nonlocality in nanostructured metamaterials,” *Phys. Rev. B* **84**, 045424 (2011).
- [44] G. Castaldi, V. Galdi, A. Alu, and N. Engheta, “Nonlocal Transformation Optics,” *Phys. Rev. Lett.* **108**, 045122 (2012).
- [45] C. J. Zapata-Rodríguez, D. Pastor, J. J. Miret, and S. Vuković, “Uniaxial epsilon-near-zero metamaterials: from superlensing to double refraction,” *J. Nanophoton.* **8**, 083895 (2014).
- [46] M. Netti, A. Harris, J. Baumberg, D. Whittaker, M. Charlton, M. Zoorob, and G. Parker, “Optical birefringence in photonic crystal waveguides,” *Phys. Rev. Lett.* **86**, 1526 (2001).
- [47] D. Smith, J. Mock, A. Starr, and D. Schurig, “Gradient index metamaterials,” *Phys. Rev. E* **71**, 036609 (2005).

- [48] Y. Zhao and A. Alù, “Manipulating light polarization with ultrathin plasmonic metasurfaces,” *Phys. Rev. B* **84**, 205428 (2011).
- [49] J. B. Pendry, D. Schurig, and D. R. Smith, “Controlling electromagnetic fields,” *Science* **312**, 1780–1782 (2006).
- [50] U. Leonhardt, “Optical conformal mapping,” *Science* **312**, 1777–1780 (2006).
- [51] D. Schurig, J. Mock, B. Justice, S. A. Cummer, J. B. Pendry, A. Starr, and D. Smith, “Metamaterial electromagnetic cloak at microwave frequencies,” *Science* **314**, 977–980 (2006).
- [52] J. Valentine, J. Li, T. Zentgraf, G. Bartal, and X. Zhang, “An optical cloak made of dielectrics,” *Nat. Mater.* **8**, 568 (2009).
- [53] X. Ni, Z. J. Wong, M. Mrejen, Y. Wang, and X. Zhang, “An ultrathin invisibility skin cloak for visible light,” *Science* **349**, 1310–1314 (2015).
- [54] W. Cai, U. K. Chettiar, A. V. Kildishev, and V. M. Shalaev, “Optical cloaking with metamaterials,” *Nat. Photonics* **1**, 224–227 (2007).
- [55] H. Chen, C. T. Chan, and P. Sheng, “Transformation optics and metamaterials,” *Nat. Mater.* **9**, 387 (2010).

- [56] B. Kanté, A. de Lustrac, J.-M. Lourtioz, and S. N. Burokur, “Infrared cloaking based on the electric response of split ring resonators,” *Opt. Express* **16**, 9191–9198 (2008).
- [57] J. Han, A. Lakhtakia, and C.-W. Qiu, “Terahertz metamaterials with semiconductor split-ring resonators for magnetostatic tunability,” *Opt. Express* **16**, 14390–14396 (2008).
- [58] L. Kang, Q. Zhao, H. Zhao, and J. Zhou, “Magnetically tunable negative permeability metamaterial composed by split ring resonators and ferrite rods,” *Opt. Express* **16**, 8825–8834 (2008).
- [59] B. Edwards, A. Alu, M. G. Silveirinha, and N. Engheta, “Experimental verification of plasmonic cloaking at microwave frequencies with metamaterials,” *Phys. Rev. Lett.* **103**, 153901 (2009).
- [60] M. Gharghi, C. Gladden, T. Zentgraf, Y. Liu, X. Yin, J. Valentine, and X. Zhang, “A carpet cloak for visible light,” *Nano Lett.* **11**, 2825–2828 (2011).
- [61] N. Landy and D. R. Smith, “A full-parameter unidirectional metamaterial cloak for microwaves,” *Nat. Mater.* **12**, 25 (2013).



- [62] P.-Y. Chen, J. Soric, and A. Alù, “Invisibility and cloaking based on scattering cancellation,” *Adv. Mater.* **24**, OP281–OP304 (2012).
- [63] A. Alu and N. Engheta, “Achieving transparency with plasmonic and metamaterial coatings,” *Phys. Rev. E* **72**, 016623 (2005).
- [64] S. Tricarico, F. Bilotti, and L. Vegni, “Scattering cancellation by metamaterial cylindrical multilayers,” *J. Eur. Opt. Soc, Rapid Publ.* **4**, 09021 (2009).
- [65] A. Monti, A. Alù, A. Toscano, and F. Bilotti, “Optical invisibility through metasurfaces made of plasmonic nanoparticles,” *J. Appl. Phys.* **117**, 123103 (2015).
- [66] J. C. Soric, A. Monti, A. Toscano, F. Bilotti, and A. Alù, “Multi-band and wideband bilayer mantle cloaks,” *IEEE Trans. Antennas Propag.* **63**, 3235–3240 (2015).
- [67] P. Fan, U. K. Chettiar, L. Cao, F. Afshinmanesh, N. Engheta, and M. L. Brongersma, “An invisible metal–semiconductor photodetector,” *Nat. Photonics* **6**, 380 (2012).
- [68] P.-Y. Chen and A. Alù, “Atomically thin surface cloak using graphene monolayers,” *ACS Nano* **5**, 5855–5863 (2011).

- [69] M. Naserpour, C. J. Zapata-Rodríguez, S. M. Vuković, H. Pashaeiadi, and M. R. Belić, “Tunable invisibility cloaking by using isolated graphene-coated nanowires and dimers,” *Sci. Rep.* **7**, 12186 (2017).
- [70] A. E. Miroshnichenko, A. B. Evlyukhin, Y. F. Yu, R. M. Bakker, A. Chipouline, A. I. Kuznetsov, B. Luk’yanchuk, B. N. Chichkov, and Y. S. Kivshar, “Nonradiating anapole modes in dielectric nanoparticles,” *Nat. Commun.* **6**, 8069 (2015).
- [71] A. Alù and N. Engheta, “Cloaking a sensor,” *Phys. Rev. Lett.* **102**, 233901 (2009).
- [72] A. Alù and N. Engheta, “Cloaked near-field scanning optical microscope tip for noninvasive near-field imaging,” *Phys. Rev. Lett.* **105**, 263906 (2010).
- [73] F. Bilotti, F. Pierini, and L. Vegni, “Employment of metamaterial cloaks to enhance the resolution of near-field scanning optical microscopy systems based on aperture tips,” *Metamaterials* **5**, 119–124 (2011).

- [74] F. Bilotti, S. Tricarico, F. Pierini, and L. Vegni, “Cloaking apertureless near-field scanning optical microscopy tips,” *Opt. Lett.* **36**, 211–213 (2011).
- [75] L. V. Alekseyev, E. E. Narimanov, T. Tumkur, H. Li, Y. A. Barnakov, and M. A. Noginov, “Uniaxial epsilon-near-zero metamaterial for angular filtering and polarization control,” *Appl. Phys. Lett.* **97**, 131107 (2010).
- [76] J. Gao, L. Sun, H. Deng, C. J. Mathai, S. Gangopadhyay, and X. Yang, “Experimental realization of epsilon-near-zero metamaterial slabs with metal-dielectric multilayers,” *Appl. Phys. Lett.* **103**, 051111 (2013).
- [77] R. Maas, J. Parsons, N. Engheta, and A. Polman, “Experimental realization of an epsilon-near-zero metamaterial at visible wavelengths,” *Nat. Photonics* **7**, 907–912 (2013).
- [78] J. Zhu, “Theoretical study of the light scattering from gold nanotubes: Effects of wall thickness,” *Mater. Sci. Eng. A* **454**, 685–689 (2007).

- [79] D. S. Filonov, A. P. Slobozhanyuk, P. A. Belov, and Y. S. Kivshar, “Double-shell metamaterial coatings for plasmonic cloaking,” *Phys. Status Solidi RRL* **6**, 46–48 (2012).
- [80] T. J. Arruda, A. S. Martinez, and F. A. Pinheiro, “Tunable multiple Fano resonances in magnetic single-layered core-shell particles,” *Phys. Rev. A* **92**, 023835 (2015).
- [81] M. V. Rybin, D. S. Filonov, P. A. Belov, Y. S. Kivshar, and M. F. Limonov, “Switching from visibility to invisibility via Fano resonances: Theory and experiment,” *Sci. Rep.* **5**, 8774 (2015).
- [82] K.-H. Kim, Y.-S. No, S. Chang, J.-H. Choi, and H.-G. Park, “Invisible hyperbolic metamaterial nanotube at visible frequency,” *Sci. Rep.* **5**, 16027 (2015).
- [83] L. Verslegers, P. B. Catrysse, Z. Yu, J. S. White, E. S. Barnard, M. L. Brongersma, and S. Fan, “Planar lenses based on nanoscale slit arrays in a metallic film,” *Nano Lett.* **9**, 235–238 (2009).
- [84] X. Ni, S. Ishii, A. V. Kildishev, and V. M. Shalaev, “Ultra-thin, planar, Babinet-inverted plasmonic metalenses,” *Light Sci. Appl.* **2**, e72 (2013).

- [85] C. J. Zapata-Rodríguez, D. Pastor, L. E. Martínez, and J. J. Miret, “Left-handed metamaterial coatings for subwavelength-resolution imaging,” *J. Opt. Soc. Am. A* **29**, 1992–1998 (2012).
- [86] E. F. Kuester, M. A. Mohamed, M. Piket-May, and C. L. Holloway, “Averaged transition conditions for electromagnetic fields at a metafilm,” *IEEE Trans. Antennas Propag.* **51**, 2641–2651 (2003).
- [87] C. L. Holloway, M. A. Mohamed, E. F. Kuester, and A. Dienstfrey, “Reflection and transmission properties of a metafilm: With an application to a controllable surface composed of resonant particles,” *IEEE Trans. Electromagn. Compat.* **47**, 853–865 (2005).
- [88] Y. Zhao, X.-X. Liu, and A. Alù, “Recent advances on optical metasurfaces,” *J. Opt.* **16**, 123001 (2014).
- [89] M. Selvanayagam and G. V. Eleftheriades, “Discontinuous electromagnetic fields using orthogonal electric and magnetic currents for wavefront manipulation,” *Opt. Express* **21**, 14409–14429 (2013).

- [90] C. L. Holloway, E. F. Kuester, J. A. Gordon, J. O'Hara, J. Booth, and D. R. Smith, "An overview of the theory and applications of metasurfaces: The two-dimensional equivalents of metamaterials," *IEEE Antennas Propag. Mag.* **54**, 10–35 (2012).
- [91] D. L. Sounas, T. Koderer, and C. Caloz, "Electromagnetic modeling of a magnetless nonreciprocal gyrotropic metasurface," *IEEE Trans. Antennas Propag.* **61**, 221–231 (2013).
- [92] C. Pfeiffer, C. Zhang, V. Ray, L. J. Guo, and A. Grbic, "High performance bianisotropic metasurfaces: asymmetric transmission of light," *Phys. Rev. Lett.* **113**, 023902 (2014).
- [93] M. Khorasaninejad, W. T. Chen, R. C. Devlin, J. Oh, A. Y. Zhu, and F. Capasso, "Metalenses at visible wavelengths: Diffraction-limited focusing and subwavelength resolution imaging," *Science* **352**, 1190–1194 (2016).
- [94] A. B. Klemm, D. Stellinga, E. R. Martins, L. Lewis, G. Huyet, L. O'Faolain, and T. F. Krauss, "Experimental high numerical aperture focusing with high contrast gratings," *Opt. Lett.* **38**, 3410–3413 (2013).

- [95] M. Born and E. Wolf, *Principles of Optics Seventh (expanded) edition* (Cambridge University Press, 1999).
- [96] A. Toriumi, S. Kawata, and M. Gu, “Reflection confocal microscope readout system for three-dimensional photochromic optical data storage,” *Opt. Lett.* **23**, 1924–1926 (1998).
- [97] C. J. R. Sheppard and A. Choudhury, “Annular pupils, radial polarization, and superresolution,” *Appl. Opt.* **43**, 4322–4327 (2004).
- [98] X. Zhang and Z. Liu, “Superlenses to overcome the diffraction limit,” *Nat. Mater.* **7**, 435–441 (2008).
- [99] P. Wróbel, J. Pniewski, T. J. Antosiewicz, and T. Szoplik, “Focusing radially polarized light by a concentrically corrugated silver film without a hole,” *Phys. Rev. Lett.* **102**, 183902 (2009).
- [100] C. J. Zapata-Rodríguez, D. Pastor, M. T. Caballero, and J. J. Miret, “Diffraction-managed superlensing using plasmonic lattices,” *Opt. Commun.* **285**, 3358–3362 (2012).
- [101] L. Yin, V. K. Vlasko-Vlasov, J. Pearson, J. M. Hiller, J. Hua, U. Welp, D. E. Brown, and C. W. Kimball, “Subwavelength

- focusing and guiding of surface plasmons,” *Nano Lett.* **5**, 1399–1402 (2005).
- [102] Y. A. Barnakov, N. Kiriya, P. Black, H. Li, A. V. Yakim, L. Gu, M. Mayy, E. E. Narimanov, and M. A. Noginov, “Toward curvilinear metamaterials based on silver-filled alumina templates,” *Opt. Mater. Express* **1**, 1061–1064 (2011).
- [103] G. Wu, J. Chen, R. Zhang, J. Xiao, and Q. Gong, “Highly efficient nanofocusing in a single step-like microslit,” *Opt. Lett.* **38**, 3776–3779 (2013).
- [104] M. Naserpour, C. J. Zapata-Rodríguez, A. Zakery, and J. J. Miret, “Highly localized accelerating beams using nano-scale metallic gratings,” *Opt. Commun.* **334**, 79–84 (2015).
- [105] M. Naserpour, C. J. Zapata-Rodríguez, A. Zakery, and J. J. Miret, “Light capsules shaped by curvilinear meta-surfaces,” *Appl. Phys. B* **120**, 551–556 (2015).
- [106] C. J. Zapata-Rodríguez and M. Naserpour, “Nonparaxial shape-preserving Airy beams with Bessel signature,” *Opt. Lett.* **39**, 2507–2510 (2014).



- [107] M. Naserpour, C. J. Zapata-Rodríguez, and M. Hashemi, “Plano-concave microlenses with epsilon-near-zero surface-relief coatings for efficient shaping of nonparaxial optical beams,” *Opt. Laser Technol.* **98**, 152–157 (2018).
- [108] J. Zenneck, “Über die Fortpflanzung ebener elektromagnetischer wellen längs einer ebenen Leiterfläche und ihre Beziehung zur drahtlosen Telegraphie,” *Ann. Phys. Lpz.* **23**, 846–866 (1907).
- [109] S. A. Maier, *Plasmonics: Fundamentals and Applications* (Springer, New York, 2007).
- [110] M. I. D’yakonov, “New type of electromagnetic wave propagating at an interface,” *Sov. Phys. JETP* **67**, 714–716 (1988).
- [111] J. J. Miret, C. J. Zapata-Rodríguez, Z. Jakšić, S. M. Vuković, and M. R. Belić, “Substantial enlargement of angular existence range for Dyakonov-like surface waves at semi-infinite metal-dielectric superlattice,” *J. Nanophoton.* **6**, 063525 (2012).
- [112] C. J. Zapata-Rodríguez, J. J. Miret, J. A. Sorni, and S. Vuković, “Propagation of dyakonon wave-packets at the boundary of metal-dielectric lattices,” *IEEE J. Sel. Top. Quantum Electron.* **19**, 4601408 (2013).

- [113] C. J. Zapata-Rodríguez, J. J. Miret, S. Vuković, and M. R. Belić, “Engineered surface waves in hyperbolic metamaterials,” *Opt. Express* **21**, 19113–19127 (2013).
- [114] J. A. Sorni, M. Naserpour, C. J. Zapata-Rodríguez, and J. J. Miret, “Dyakonov surface waves in lossy metamaterials,” *Opt. Commun.* **355**, 251–255 (2015).
- [115] C. Díaz-Aviñó, M. Naserpour, and C. J. Zapata-Rodríguez, “Tunable scattering cancellation of light using anisotropic cylindrical cavities,” *Plasmonics* **12**, 675–683 (2017).
- [116] C. Díaz-Aviñó, M. Naserpour, and C. J. Zapata-Rodríguez, “Conditions for achieving invisibility of hyperbolic multilayered nanotubes,” *Opt. Commun.* **381**, 234–239 (2016).
- [117] C. Díaz-Aviñó, M. Naserpour, and C. J. Zapata-Rodríguez, “Optimization of multilayered nanotubes for maximal scattering cancellation,” *Opt. Express* **24**, 18184–18196 (2016).
- [118] M. Naserpour, C. J. Zapata-Rodríguez, C. Díaz-Aviñó, M. Hashemi, and J. J. Miret, “Ultrathin high-index metasurfaces for shaping focused beams,” *Appl. Opt.* **54**, 7586–7591 (2015).

- [119] M. Naserpour, C. J. Zapata-Rodríguez, C. Díaz-Aviñó, and M. Hashemi, “Metacoatings for wavelength-scale, high-numerical-aperture plano–concave focusing lenses,” *J. Opt. Soc. Am. B* **33**, 2120–2128 (2016).
- [120] M. Naserpour, C. J. Zapata-Rodríguez, A. Zakery, C. Díaz-Aviñó, and J. J. Miret, “Accelerating wide-angle converging waves in the near field,” *J. Opt.* **17**, 015602 (2015).
- [121] C. Díaz-Aviñó, D. Pastor, C. J. Zapata-Rodríguez, M. Naserpour, R. Kotyński, and J. J. Miret, “Some considerations on the transmissivity of birefringent metamaterials,” *J. Opt. Soc. Am. B* **33**, 116–125 (2016).
- [122] C. F. Bohren and D. R. Huffman, *Absorption and scattering of light by small particles* (Wiley, 1998).
- [123] W. Hergert and T. Wriedt, *The Mie theory: basics and applications*, vol. 169 (Springer, 2012).
- [124] M. I. Mishchenko, J. W. Hovenier, and L. D. Travis, *Light scattering by nonspherical particles: theory, measurements, and applications* (Academic press, 1999).

- [125] H. E. Bussey and J. H. Richmond, “Scattering by a lossy dielectric circular cylindrical multilayer, numerical values,” *IEEE Trans. Antennas Propag.* **23**, 723–725 (1975).
- [126] G. A. Shah, “Scattering of plane electromagnetic waves by infinite concentric circular cylinders at oblique incidence,” *Mon. Not. R. Astron. Soc.* **148**, 93–102 (1970).
- [127] C. A. Balanis, *Advanced engineering electromagnetics* (Wiley, New York, 1989).
- [128] A. Helaly, E. A. Soliman, and A. A. Megahed, “Electromagnetic waves scattering by nonuniform plasma cylinder,” *IEE Proc-Microw. Antennas Propag.* **144**, 61–66 (1997).
- [129] P. Yeh, *Optical waves in layered media* (Wiley, New York, 1988).
- [130] X. Yang, J. Yao, J. Rho, X. Yin, and X. Zhang, “Experimental realization of three-dimensional indefinite cavities at the nanoscale with anomalous scaling laws,” *Nat. Photonics* **6**, 450 (2012).
- [131] S. M. Vukovic, I. V. Shadrivov, and Y. S. Kivshar, “Surface Bloch waves in metamaterial and metal-dielectric superlattices,” *Appl. Phys. Lett.* **95**, 041902 (2009).

- [132] S. M. Rytov, “Electromagnetic properties of a finely stratified medium,” *Sov. Phys. JETP* **2**, 466–475 (1956).
- [133] D. R. Smith, D. Schurig, M. Rosenbluth, and S. Schultz, “Limitations on subdiffraction imaging with a negative refractive index slab,” *Appl. Phys. Lett.* **82**, 1506–1508 (2003).
- [134] I. I. Smolyaninov, E. Hwang, and E. Narimanov, “Hyperbolic metamaterial interfaces: Hawking radiation from Rindler horizons and spacetime signature transitions,” *Phys. Rev. B* **85**, 235122 (2012).
- [135] Y. Guo, W. Newman, C. L. Cortes, and Z. Jacob, “Applications of hyperbolic metamaterial substrates,” *Advances in OptoElectronics* **2012**, ID 452502 (2012).
- [136] C. L. Cortes, W. Newman, S. Molesky, and Z. Jacob, “Quantum nanophotonics using hyperbolic metamaterials,” *J. Opt.* **14**, 063001 (2012).
- [137] L. Ferrari, C. Wu, D. Lepage, X. Zhang, and Z. Liu, “Hyperbolic metamaterials and their applications,” *Prog. Quant. Electron.* **40**, 1–40 (2015).

- [138] P. Yeh, A. Yariv, and A. Y. Cho, “Optical surface waves in periodic layered media,” *Appl. Phys. Lett.* **32**, 104–105 (1978).
- [139] D. B. Walker, E. N. Glytsis, and T. K. Gaylord, “Surface mode at isotropic-uniaxial and isotropic-biaxial interfaces,” *J. Opt. Soc. Am. A* **15**, 248–260 (1998).
- [140] J. Gao, A. Lakhtakia, and M. Lei, “Dyakonov-Tamm waves guided by the interface between two structurally chiral materials that differ only in handedness,” *Phys. Rev. A* **81**, 013801 (2010).
- [141] A. G. Ardakani, M. Naserpour, and C. J. Zapata-Rodríguez, “Dyakonov-like surface waves in the THz regime,” *Photon. Nanostruct.: Fundam. Appl.* **20**, 1–6 (2016).
- [142] C. J. Zapata-Rodríguez, S. Vuković, J. J. Miret, M. Naserpour, and M. R. Belić, “Dyakonov surface waves: anisotropy-enabling confinement on the edge,” in “Surface waves - New trends and developments,” (InTech, 2018).
- [143] K.-J. Bathe, *Finite element method* (Wiley Online Library, 2008).

- [144] G. Dhatt, E. Lefrançois, and G. Touzot, *Finite element method* (John Wiley & Sons, 2012).
- [145] J. N. Reddy, *An introduction to the finite element method* (McGraw-Hill, 1993).
- [146] <https://www.comsol.com/multiphysics/finite-element-method>.
- [147] M. Heath, *Scientific Computing: An Introductory Survey* (McGraw-Hill, 2005).
- [148] D. Pepper and J. Heinrich, *The Finite Element Method: Basic Concepts and Applications with MATLAB, MAPLE, and COM-SOL, Third Edition* (CRC Press, 2017).
- [149] H. L. Chen and L. Gao, “Anomalous electromagnetic scattering from radially anisotropic nanowires,” *Phys. Rev. A* **86**, 033825 (2012).
- [150] H. L. Chen and L. Gao, “Tunability of the unconventional Fano resonances in coated nanowires with radial anisotropy,” *Opt. Express* **21**, 23619–23630 (2013).
- [151] J. Zhu, “Local environment dependent linewidth of plasmon absorption in gold nanoshell: Effects of local field polarization,” *Appl. Phys. Lett.* **92**, 241919 (2008).

- [152] L. Nickelson and J. Bucinkas, “Microwave power absorbed by and scattered from a multilayered zero-index anisotropic metamaterial-semiconductor cylinder,” *Appl Phys. A* **109**, 883–889 (2012).
- [153] J. C. Williams, “Doctor-blade process,” in “*Treatise on Materials Science & Technology*, vol. 9,” (Elsevier, 1976), pp. 173–198.
- [154] A. Maulu, P. J. Rodríguez-Cantó, J. Navarro-Arenas, R. Abarques, J. F. Sánchez-Royo, R. García-Calzada, and J. P. M. Pastor, “Strongly-coupled PbS QD solids by doctor blading for IR photodetection,” *RSC Adv.* **6**, 80201–80212 (2016).
- [155] Y.-H. Chang, S.-R. Tseng, C.-Y. Chen, H.-F. Meng, E.-C. Chen, S.-F. Horng, and C.-S. Hsu, “Polymer solar cell by blade coating,” *Org. Electron.* **10**, 741–746 (2009).
- [156] M. Signoretto, N. Zink-Lorre, J. P. Martínez-Pastor, E. Font-Sanchis, V. S. Chirvony, Á. Sastre-Santos, F. Fernández-Lázaro, and I. Suárez, “Purcell-enhancement of the radiative PL decay in perylenediimides by coupling with silver nanoparticles into waveguide modes,” *Appl. Phys. Lett.* **111**, 081102 (2017).



- [157] T. T. Ngo, I. Suarez, R. S. Sanchez, J. P. Martinez-Pastor, and I. Mora-Sero, “Single step deposition of an interacting layer of a perovskite matrix with embedded quantum dots,” *Nanoscale* **8**, 14379–14383 (2016).
- [158] S. Coe-Sullivan, J. S. Steckel, W.-K. Woo, M. G. Bawendi, and V. Bulović, “Large-area ordered quantum-dot monolayers via phase separation during spin-casting,” *Adv. Funct. Mater.* **15**, 1117–1124 (2005).
- [159] J. M. Richter, M. Abdi-Jalebi, A. Sadhanala, M. Tabachnyk, J. P. Rivett, L. M. Pazos-Outón, K. C. Gödel, M. Price, F. Deschler, and R. H. Friend, “Enhancing photoluminescence yields in lead halide perovskites by photon recycling and light out-coupling,” *Nat. Commun.* **7**, 13941 (2016).
- [160] G. Xing, N. Mathews, S. S. Lim, N. Yantara, X. Liu, D. Sabba, M. Grätzel, S. Mhaisalkar, and T. C. Sum, “Low-temperature solution-processed wavelength-tunable perovskites for lasing,” *Nat. Mater.* **13**, 476 (2014).
- [161] N. Uchida, “Optical properties of single-crystal paratellurite ( $\text{TeO}_2$ ),” *Phys. Rev. B* **4**, 3736 (1971).



# Publications annex



1<sup>st</sup> Publication:

**Tunable Scattering Cancellation of Light  
Using Anisotropic Cylindrical Cavities**

**Authors:** Carlos Díaz-Aviñó, Mahin Naserpour and Carlos J.  
Zapata-Rodríguez

Published in **Plasmonics**, volume 12, pages 675-683, year 2017.

# Tunable Scattering Cancellation of Light Using Anisotropic Cylindrical Cavities

Carlos Díaz-Aviño<sup>1</sup> · Mahin Naserpour<sup>1,2</sup> · Carlos J. Zapata-Rodríguez<sup>1</sup>

Received: 13 April 2016 / Accepted: 14 June 2016 / Published online: 15 July 2016  
© Springer Science+Business Media New York 2016

**Abstract** Engineered core-shell cylinders are good candidates for applications in invisibility and cloaking. In particular, hyperbolic nanotubes demonstrate tunable ultra-low scattering cross section in the visible spectral range. In this work, we investigate the limits of validity of the condition for invisibility, which was shown to rely on reaching an epsilon near zero in one of the components of the effective permittivity tensor of the anisotropic metamaterial cavity. For incident light polarized perpendicularly to the scatterer axis, critical deviations are found in low-birefringent arrangements and also with high-index cores. We suggest that the ability of anisotropic metalodielectric nanocavities to dramatically reduce the scattered light is associated with a multiple Fano-resonance phenomenon. We extensively explore such resonant effect to identify tunable windows of invisibility.

**Keywords** Anisotropic metamaterial · Invisibility · Plasmonics

## Introduction

Cloaking and invisibility are optical techniques with considerable advances recently due to the advent of metamaterials.

Designs for cloaking where a shadow region prevents the light-matter interaction with a tailored target placed therein are largely based on transformation optics [1–3] providing extensive theoretical studies and physical analysis without drawing on numerical simulations [4, 5]. On the other hand, invisibility relies on the scattering cancellation of a given object by using for instance a metallic coating and even complex nanostructured coverings [6, 7]; the negative polarizability of the carpet layer might severely drop the scattering cross section of the particle making it undetectable [8]. The first experimental realization was performed in the microwave spectral range by using an array of metallic fins, immersed in a high-permittivity environment, thus creating a metamaterial cloaking shell [9]. Of particular interest results the inclusion of shells made of materials with a permittivity near zero in the spectral range of interest, which may lead to a significant drop of the scattering spectrum and, in addition, create a shielding effect in the bounded space [10].

The development of multilayered plasmonic coatings and metasurfaces integrates the current state of the art in the engineering of devices for applications in invisibility and cloaking [11–13]. The possibility to experimentally realize a structured nanoparticle which is invisible in the optical range remains a challenge, and designs using experimental data can be conveniently considered [14]. A recent proposal proving a critical reduction of the scattering cross section consists of alternating metallic and dielectric coatings which are arranged in a periodic radial distribution, thus shaping an anisotropic-nanostructured hyperbolic shell [15, 16]. For the purpose of simplifying the description of the stratified metamaterial and the application of the analytical Lorenz-Mie scattering method [17, 18], a long-wavelength approximation is used thus enabling an adequate interpretation of the resulting spectra under some circumstances [19]. A key

---

✉ Carlos J. Zapata-Rodríguez  
carlos.zapata@uv.es

<sup>1</sup> Department of Optics and Optometry and Vision Science, University of Valencia, Dr. Moliner 50, Burjassot 46100, Spain

<sup>2</sup> Department of Physics, College of Science, Shiraz University, Shiraz 71454, Iran

issue is that the permittivity tensor describing the nanotube reaches near zero values of one of its components in the vicinities of the invisibility regime.

In this study, we analyze in detail the validity of such an approach and we extend their results to achieve a higher tunability degree concerning the invisibility spectral windows. For that purpose, we first evaluate the scattering cross section for different configurations of a nanostructured infinitely-long shell and for different core and environment media in order to verify the existence of a minimum in the epsilon-near-zero regime. For the sake of generality, we assume a Drude free-electron theory for the characterization of the material with negative permittivity [20], and we employ the effective medium theory to describe the form anisotropy of the hollow cylinder. Furthermore, we establish a matrix-transfer formulation with applications in multilayered radially anisotropic media, which presents some similarities to developments previously implemented in stratified plane metamaterials [21]. We demonstrate that in the narrow band with epsilon-near-zero cylinders, the invisibility of the particle becomes a reality provided that the core and environment medium are not polarizable, and that the Drude medium composing the shell has a moderate and low filling factor. Additional higher-energy bands of scattering reduction are found for large particles with applications in invisibility. The ability of anisotropic metalodielectric nanocavities to dramatically reduce the scattered light is also discussed in terms of the Fano-resonance phenomenon.

### The Lorenz-Mie Scattering Coefficients

We consider a cylindrical shell formed by a radially anisotropic nanostructure. The optical arrangement is illustrated in Fig. 1a. The permittivities along the optic axis (OA),  $\epsilon_{\parallel}$ , which is radially directed, and perpendicular to the OA,  $\epsilon_{\perp}$ , constitute the components of the permittivity tensor  $\underline{\epsilon} = \epsilon_{\parallel}\hat{r}\hat{r} + \epsilon_{\perp}\hat{\theta}\hat{\theta} + \epsilon_{\perp}\hat{z}\hat{z}$ . In principle, these permittivities may be complex valued, thus taking into account losses in the metamaterial, and their real part may take a positive, a negative, and even a near zero value. In our numerical

simulations, we considered an anisotropic tube of utmost radius  $R$  with a shell thickness given by  $T < R$ . In this study, we examined tubes with a core material with permittivity  $\epsilon_C$  and immersed in an environment medium of permittivity  $\epsilon$ .

To estimate analytically the scattering efficiency of the anisotropic nanotube, we followed the Lorenz-Mie scattering method given for instance in Refs. [22] and [23]. First we assumed that the nanotube is illuminated by a TE<sup>z</sup>-polarized plane wave propagating along the  $x$  axis, as illustrated in Fig. 1a. The magnetic field of the incident plane wave may be set as

$$\mathbf{B}^i = \hat{z}B_0 \exp(ikx), \tag{1}$$

where  $B_0$  is a constant amplitude,  $k = k_0\sqrt{\epsilon}$  and  $k_0 = \omega/c$  is the wavenumber in the vacuum. In this case, the scattered magnetic field in the environment medium,  $r > R$ , may be set as [18]

$$\mathbf{B}^s = \hat{z}B_0 \sum_{n=-\infty}^{+\infty} a_n i^n H_n^{(1)}(kr) \exp(in\phi), \tag{2}$$

where  $r$  and  $\phi$  are the radial and azimuthal cylindrical coordinates, respectively, and  $H_n^{(1)}$  is the Hankel function of the first kind and order  $n$ . The total magnetic field in the environment medium is simply  $\mathbf{B}^{(tot)} = \mathbf{B}^i + \mathbf{B}^s$ .

In the anisotropic shell (medium 2),  $R_1 < r < R$ , where  $R_1 = R - T$ , the magnetic field may be set as [22]

$$\mathbf{B}^{(2)} = \hat{z}B_0 \sum_{n=-\infty}^{+\infty} i^n [b_n J_{n'}(k_2 r) + c_n Y_{n'}(k_2 r)] \exp(in\phi), \tag{3}$$

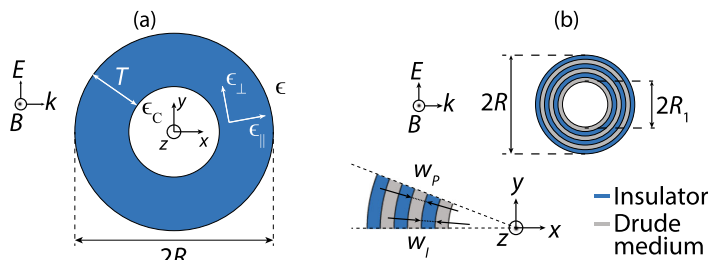
where  $J_{n'}$  and  $Y_{n'}$  are the Bessel functions of the first and second kind, respectively, both of the order  $n'$  given by

$$n' = \sqrt{\frac{\epsilon_{\perp}}{\epsilon_{\parallel}}} n, \tag{4}$$

and the wavenumber  $k_2 = k_0\sqrt{\epsilon_{\perp}}$ . Finally, the magnetic field in the core of the anisotropic tube, which corresponds to the medium 1 ( $r < R_1$ ), is expressed as

$$\mathbf{B}^{(1)} = \hat{z}B_0 \sum_{n=-\infty}^{+\infty} i^n d_n J_n(k_1 r) \exp(in\phi), \tag{5}$$

**Fig. 1** **a** Illustration of the anisotropic infinitely-long cavity. **b** Coaxial multilayered metamaterial establishing a radial-form birefringence



where the wavenumber  $k_1 = k_0\sqrt{\epsilon_C}$ .

The Lorenz-Mie scattering coefficients  $a_n, b_n, c_n,$  and  $d_n,$  are determined by means of the proper boundary conditions, that is, continuity of the  $z$ -component of the magnetic field and the  $\phi$ -component of the electric field, established at the environment-anisotropic medium interface given at  $r = R$  and at the core-anisotropic medium interface set at  $r = R_1$ . In particular, the boundary conditions applied at  $r = R_1$  may be set in matrix form as

$$D_{n,1}^Y(R_1) \cdot \begin{bmatrix} d_n \\ 0 \end{bmatrix} = D_{n',2}^Y(R_1) \cdot \begin{bmatrix} b_n \\ c_n \end{bmatrix}, \tag{6}$$

where the matrix

$$D_{n,m}^Y(x) = \begin{bmatrix} J_n(k_mx) & Y_n(k_mx) \\ Z_n J_n'(k_mx) & Z_m Y_n'(k_mx) \end{bmatrix} \tag{7}$$

is given in terms of the reduced impedance  $Z_1 = 1/\sqrt{\epsilon_C}$  and  $Z_2 = 1/\sqrt{\epsilon_\perp}$  for the media  $m = 1$  and  $m = 2,$  respectively. Here, the prime appearing in  $J_n'(\alpha)$  and  $Y_n'(\alpha)$  denotes derivative with respect to the variable  $\alpha.$  By applying the boundary conditions at  $r = R,$  we may write

$$D_n^H(R) \cdot \begin{bmatrix} 1 \\ a_n \end{bmatrix} = D_{n',2}^Y(R) \cdot \begin{bmatrix} b_n \\ c_n \end{bmatrix}, \tag{8}$$

where

$$D_n^H(R) = \begin{bmatrix} J_n(kR) & H_n^{(1)}(kR) \\ Z J_n'(kR) & Z H^{(1)'}(kR) \end{bmatrix}, \tag{9}$$

where  $Z = 1/\sqrt{\epsilon_C}.$

Finally, we may estimate the fields in the core space and outside the nanotube without calculating the fields in the anisotropic medium by means of the following matrix equation:

$$\begin{bmatrix} 1 \\ a_n \end{bmatrix} = M_n \cdot \begin{bmatrix} d_n \\ 0 \end{bmatrix}, \tag{10}$$

where the matrix

$$M_n = \begin{bmatrix} M_{n,11} & M_{n,12} \\ M_{n,21} & M_{n,22} \end{bmatrix} \tag{11}$$

$$= \left[ D_n^H(R) \right]^{-1} \cdot D_{n',2}^Y(R) \cdot \left[ D_{n',2}^Y(R_1) \right]^{-1} \cdot D_{n,1}^Y(R_1).$$

By using this transfer matrix formalism, it is possible to evaluate analytically the scattering coefficients

$$a_n = \frac{M_{n,21}}{M_{n,11}}, \tag{12}$$

which provide an exact estimation of the scattering efficiency as

$$Q_s = \frac{2}{kR} \sum_{n=-\infty}^{+\infty} |a_n|^2. \tag{13}$$

The nanotube resonances are determined by the poles of the coefficients  $a_n,$  that is for the zeros of  $M_{n,11}.$  On the other

hand, the invisibility condition is established provided that the scattering coefficients  $a_n$  (or alternatively  $M_{n,21}$ ) arrive simultaneously to a value near zero.

### Metamaterial with form Birefringence

From a practical point of view, a radially anisotropic medium may be established by the proper form birefringence of a metamaterial composed of concentric multilayers as illustrated in Fig. 1b [24, 25]. Here, two materials with permittivity of opposite sign were used for the stratified medium in order to substantially increase the form birefringence [26]. A plasmonic nanofilm of width  $w_P$  is set by the side of an insulator layer of width  $w_1,$  thus forming the unit cell of a periodic distribution along the radial coordinate. In our numerical simulations, we considered a nanostructured tube of utmost radius  $R$  and composed of a number of subwavelength layers giving a total shell thickness  $T.$  The permittivity of the plasmonic material, given by

$$\epsilon_P(\omega) = 1 - \frac{\omega_p^2}{\omega^2 + i\omega\gamma}, \tag{14}$$

follows the Drude model within the spectral range of interest [27]. In the previous equation,  $\omega_p$  represents the plasma frequency and  $\gamma$  stands for the damping rate. The real part of  $\epsilon_P(\omega)$  is negative provided that  $\omega^2 < \omega_p^2 - \gamma^2,$  the latter condition approaching  $\omega < \omega_p$  for a low-loss plasmonic material. For simplicity, we will consider a nondispersive permittivity  $\epsilon_1 = 10$  for the insulator in the frequency range under study.

For our structured metamaterial with a deeply subwavelength period, the medium may be considered as a uniaxial crystal within the limits of the long-wavelength approximation [28, 29]. In fact, a satisfactory approach can be implemented in practice with a multilayered tube including real metals and just only three periods [15, 16, 30]. The optic axis of the metamaterial is set along the direction of periodicity; in our particular case, the OA is oriented along the radial axis. The effective anisotropic medium is then optically characterized by a local permittivity tensor  $\underline{\epsilon}$  of component [28]

$$\epsilon_{\parallel}(\omega) = \frac{\epsilon_1 \epsilon_P(\omega)}{f \epsilon_1 + (1 - f) \epsilon_P(\omega)}, \tag{15}$$

along the OA, and

$$\epsilon_{\perp}(\omega) = f \epsilon_P(\omega) + (1 - f) \epsilon_1, \tag{16}$$

in the perpendicular direction. In the previous equations, the filling factor of the Drude medium in the metamaterial is given by

$$f = \frac{w_P}{w_P + w_1}, \tag{17}$$



which represents the unique geometrical parameter determining the effective permittivities  $\epsilon_{\parallel}$  and  $\epsilon_{\perp}$  of the metamaterial, regardless the internal one-dimensional distribution of the materials involved in the unit cell.

In Fig. 2, we represent the real values of  $\epsilon_{\parallel}$  and  $\epsilon_{\perp}$  of a metamaterial composed of a Drude medium and an insulator of permittivity  $\epsilon_1 = 10$ , evaluated within a range of frequencies near  $\omega_p$  and below, considering different values of the filling factor  $f$ . We observe that the real part of  $\epsilon_{\perp}$  is near zero around a frequency

$$\omega_{\text{zero}} = \frac{\sqrt{(\omega_p^2 - \gamma^2) f - \gamma^2(1 - f)\epsilon_1}}{\sqrt{\epsilon_1 - f(\epsilon_1 - 1)}}, \tag{18}$$

whereas the real part of  $\epsilon_{\parallel}$  is near a pole around

$$\omega_{\text{pole}} = \omega_p \frac{\sqrt{1 - f}}{\sqrt{f(\epsilon_1 - 1) + 1}}, \tag{19}$$

the latter being valid when  $\gamma \ll \omega_p$ . The hyperbolic regime is determined by the condition  $\text{Re}(\epsilon_{\parallel})\text{Re}(\epsilon_{\perp}) < 0$ , indicated as shaded regions in Fig. 2. The choice  $\text{Re}(\epsilon_{\perp}) > 0$  corresponds to the so-called type I hyperbolic metamaterials, whereas the choice  $\text{Re}(\epsilon_{\perp}) < 0$  denotes a type II hyperbolic medium [31]. Note that when  $f = 1/2$ , corresponding to the case that the plasmonic and insulator layers have the same width, both a zero of  $\epsilon_{\perp}$  and a pole of  $\epsilon_{\parallel}$  occurs simultaneously at a frequency  $\omega_p/\sqrt{1 + \epsilon_1}$ , in addition happening when  $\text{Re}(\epsilon_p) = -\epsilon_1$ . In this case, the hyperbolic regime spans the whole spectrum below the plasma frequency. Let us point out that the extraordinary dispersion features of hyperbolic and epsilon-near-zero metamaterials have inspired us in a plethora of novel applications such as subwavelength imaging [32, 33], surface-wave engineering [34, 35], and double refraction [19, 36], to mention a few.

### Results and Discussion

In Fig. 3, we represent the scattering efficiency  $Q_s$  in dB as derived from Eq. 13 and calculated by means of the transfer matrix method described above, that is assuming a TE<sup>z</sup>-polarized incident light. The scattering spectrum is evaluated in terms of the  $\epsilon$ -negative material filling factor  $f$ , assuming a low-loss Drude medium with  $\gamma = \omega_p/100$ . The anisotropic cavity is immersed in air, where  $\epsilon = \epsilon_C = 1$ , and it is small enough ( $R_1 = T = k_p^{-1}/20$ , where  $k_p = \omega_p/c$ ) to excite only the dipole term  $n = 1$  of the series given in Eq. 13. We observe two resonances corresponding to the symmetric and antisymmetric coupling between the surface charges associated with the cavity and surface polaritons at  $r = R_1$  and  $r = R$  [37, 38]. By the side of each resonance peak, a minimum in scattering at a slightly higher frequency is found. This effect has also been found in solid high-index cylinders and wires, which is attributed to the existence of Fano resonances [39] where, contrarily to what is commonly assumed, a single scattering coefficient can manifest the interference of two different resonant signals. When the index mismatch with the environment medium is significantly high, one of these resonances arises within a narrow band where a Fano-type lineshape is developed. In our case, we presume that it also happens as a result of the extreme anisotropy of the scatterer. It is worth to mention that the asymmetric resonant response observed in the efficiency spectrum can be categorized in a more general context concerning the coupling of a discrete state with a continuum [40], which was first described by Fano in the context of quantum mechanical systems [41]. Since its pioneering theoretical treatment, Fano resonances have been evidenced in many other frameworks such as in the absorption of a heterogeneous dimer composed of a gold and a silver nanoparticle due to the near-field coupling between the silver surface-plasmon-resonance and the gold interband transitions [42], in plasmonic lattices where the long-living

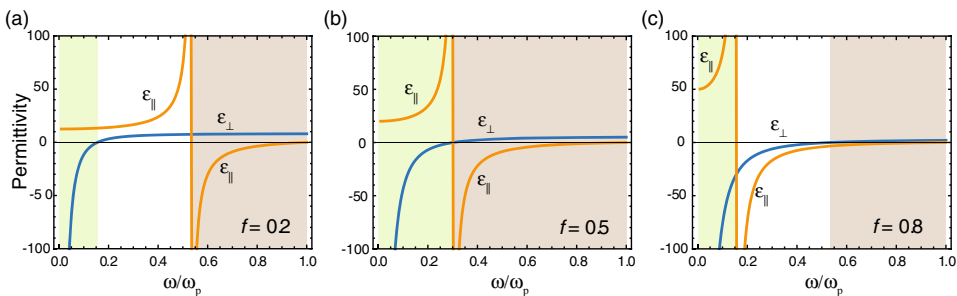


**Fig. 2** Real part of the components  $\epsilon_{\parallel}$  (orange line) and  $\epsilon_{\perp}$  (blue line) of the permittivity tensor for the metamaterial composed of a Drude medium with  $\gamma = \omega_p/100$  and an insulator of permittivity  $\epsilon_1 = 10$ , assuming different filling factors: **a**  $f = 0.2$ , **b**  $f = 0.5$ , and **c**

$f = 0.8$ . The shaded regions denote spectral bands where the metamaterial exhibits a hyperbolic dispersion of the type I (shaded in mauve) and the type II (shaded in green)

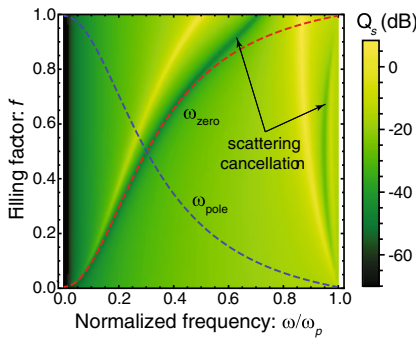


**Fig. 3** Scattering efficiency  $Q_s$ , expressed in dB, of an anisotropic cavity of equal inmost radius and thickness  $R_1 = T = k_p^{-1}/20$ , immersed in air ( $\epsilon = \epsilon_1 = 1$ ). The filling factor of the Drude medium varies from 0 to 1, considering a fixed damping rate  $\gamma = \omega_p/100$ . The calculations are performed for TE<sup>z</sup>-polarized incident light. The red dashed line corresponds to frequencies  $\omega_{zero}$  which are solutions to the Eq. 18, whereas the blue dashed line denotes frequencies  $\omega_{pole}$  given in Eq. 19

subradiant mode overlaps the spectrally broad superradiant mode [43], and the symmetry-breaking trapped-mode resonances in planar metamaterials [44].

Note that the set of *fundamental* frequencies where the scattering cancellation is shown at the lowest energy, is set virtually over the curve  $\omega_{zero}$  given in Eq. 18, coinciding with a metamaterial permittivity  $\epsilon_{\perp}$  near zero. We point out that such outcome has been previously reported by Kim et al in Ref. [15]. Since  $\epsilon_{\perp}$  spans the whole spectrum below  $\omega_p$  by balancing the composition of the Drude medium, in principle we might tune the invisibility frequency by simply changing the value of  $f$  from 0 to 1.

However, such a procedure cannot be followed for invisibility bands near the plasma frequency, even considering values of the filling factor  $f$  close to unity. Kim’s approach is not valid for filling factors  $f$  close to unity, where the tubular particle behaves like a low-birefringent plasmonic cavity. In this case, the scattering cancellation associated with the fundamental peak is observed at an intermediate frequency between the symmetric and antisymmetric resonances found below  $\omega_p$ ; in particular, the invisibility frequency is found at  $\omega = 0.707\omega_p$  in the limit  $f \rightarrow 1$ . On the other hand,  $\omega_{zero}$  approaches the plasma frequency of the Drude medium in such a limit.

Importantly, proper conditions for invisibility are found at higher energies provided that the filling factor  $f$  takes moderate values. Specifically, such scattering cancellation may be observed in the vicinities of the plasma frequency  $\omega_p$ . From Fig. 2, it is clear that, in order to achieve a scattering cancellation near  $\omega_p$ , a second minimum of  $Q_s$  which is located close to the plasma frequency might be also exploited. For instance, at  $f = 1/2$ , we find the first

minimum in the scattering efficiency,  $Q_s = 3.07 \times 10^{-7}$ , at the fundamental frequency  $\omega = 0.3\omega_p$ , and a secondary minimum  $Q_s = 5.11 \times 10^{-5}$  located at a frequency  $\omega = 0.945\omega_p$ . Here, we conclude that invisibility at the lowest energy provides a better performance than the reduction in scattering found near the plasma frequency.

In Fig. 4, we show the scattering efficiency of anisotropic cavities of a higher size. In particular, we set a filling factor  $f = 1/2$ , and compare the case analyzed in Fig. 3 with those where the inmost radius and the tube thickness take the values  $R_1 = T = k_p^{-1}/4$ ,  $R_1 = T = k_p^{-1}/2$  and  $R_1 = T = k_p^{-1}$ . Regarding the spectral position of the fundamental resonance and the lowest-energy cancellation of scattering, all curves show essentially the same behavior. For instance, the invisibility frequency is found at  $\omega = 0.3\omega_p$  in all cases with valley efficiencies given by  $Q_s = 3.7 \times 10^{-5}$ ,  $2.7 \times 10^{-4}$ , and  $2.3 \times 10^{-3}$ , as long as the tubular particle increases in size. As a consequence, the invisibility window is invariant upon the cavity diameter, provided that the modulation is performed in the subwavelength scale. As expected, although the scattering efficiency reaches a minimum at the mentioned frequency, such efficiency grows approximately one order of magnitude when the tube doubles in size.

On the other hand, the situation changes dramatically when analyzing the scattering spectrum near the secondary minimum. The pattern of the scattering efficiency is maintained unaltered for the smallest cavities, except for a scaling factor. However, the onset of additional resonances at increasing sizes (in the order of the current wavelength) governs the contour of the spectrum in the vicinity of the plasma frequency. Since the minima of the high-order Fano resonances, which in nature present a lower depth than

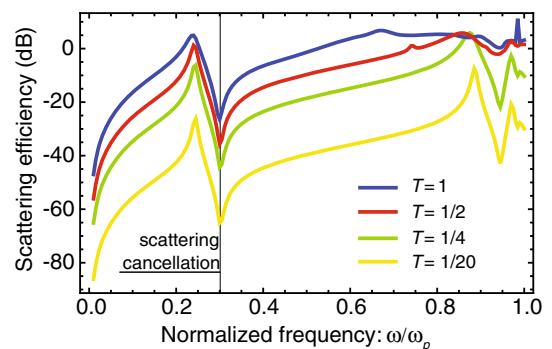


**Fig. 4** Scattering efficiency of metamaterial cavities immersed in air, where the aspect ratio  $T/R = 1/2$  is conserved. The tube thickness  $T$  is expressed in units of  $k_p^{-1}$ . The anisotropic metamaterial is again characterized by a filling factor of the Drude medium set as  $f = 1/2$ , where the damping rate is  $\gamma = \omega_p/100$

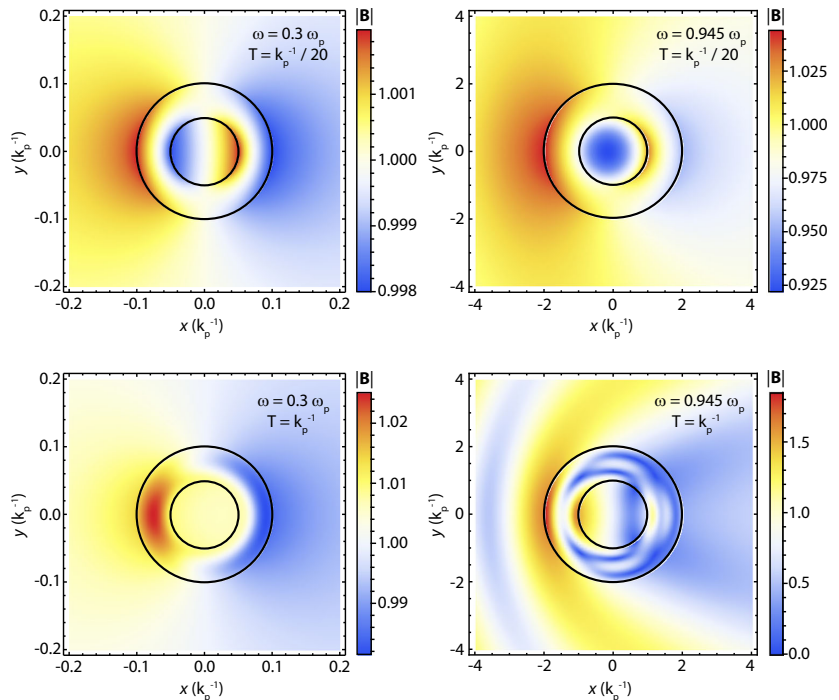
the fundamental resonance, overlap with the peaks of the neighbors thus vanishing the invisibility effect.

Further insights are inferred by representing the magnetic field near the cylindrical cavities for the frequencies of interest. In Fig. 5, we represent  $|\mathbf{B}|$  for an anisotropic scatterer of  $R_1 = T = k_p^{-1}/20$  and filling factor  $f = 1/2$  at frequencies of minimum scattering  $\omega = 0.3\omega_p$  and  $\omega = 0.945\omega_p$ . In both cases, it is evidenced the dominant dipolar contribution of the scattered field. In spite of the extreme birefringence manifested in the nanostructure, the magnetic fields present remarkably low contrast inside the nanotube and nearby. For the lowest frequency, the field distribution is antisymmetric along the radial direction inside the anisotropic shell; however, it becomes symmetric for the highest resonant frequency, thus confirming the existence of a symmetric and antisymmetric coupling between the surface charges associated with the cavity and surface polaritons. Increasing the size of the scatterer up to  $R_1 = T = k_p^{-1}$  leads to an analogous behavior only at  $\omega = 0.3\omega_p$ . Near the plasma frequency, the field distribution becomes much more complex due to the non-negligible contribution of high-order scattering coefficients. For instance, we estimate  $|a_0| = 0.97$ ,  $|a_1| = 0.10$ , and  $|a_2| = 0.14$  as the leading terms at  $\omega = 0.945\omega_p$ . This fact certainly impedes the existence of an invisibility window near  $\omega_p$ .

The spectrum of the scattering efficiency with respect to the filling factor  $f$  of the metamaterial, for cylinders of radius  $R = k_p^{-1}/2$  and different geometrical configurations, i.e., various values of the aspect ratio  $T/R$ , is depicted in Fig. 6. First, we analyzed the response of an anisotropic cavity with a very narrow shell. In Fig. 6a, we represent the scattering efficiency when  $T = R/10$ . The position of the two polaritonic resonances are clearly displaced with respect to the cases shown above. In particular, the secondary peak is located in the very-close neighborhood of the plasma frequency. The latter has a dramatic consequence: the secondary frequency associated with scattering cancellation drops out of sight, limiting the tunability of the invisibility effect. Notably, the main invisibility frequency remains practically unaltered, approaching  $\omega_{\text{zero}}$  at low and moderate filling factors.

Examining the case where  $T = 0.9R$ , which suggests a cylinder with a very small concentric hole, we obtained the scattering efficiency depicted in Fig. 6b. The main feature of the derived pattern is the occurrence of multiple peaks and their associated minima in efficiency, indicating an accumulation of excited Fano resonances [39]. Nevertheless, the fundamental frequency of invisibility again continues attached to the condition of  $\epsilon_{\perp}$  near zero.

**Fig. 5** Scattered magnetic field  $|\mathbf{B}|$  (normalized to  $B_0$ ) for anisotropic cavities of  $R_1 = T = k_p^{-1}/20$  and  $R_1 = T = k_p^{-1}$ , both with a filling factor  $f = 1/2$ , at invisibility frequencies  $\omega = 0.3\omega_p$  and  $\omega = 0.945\omega_p$



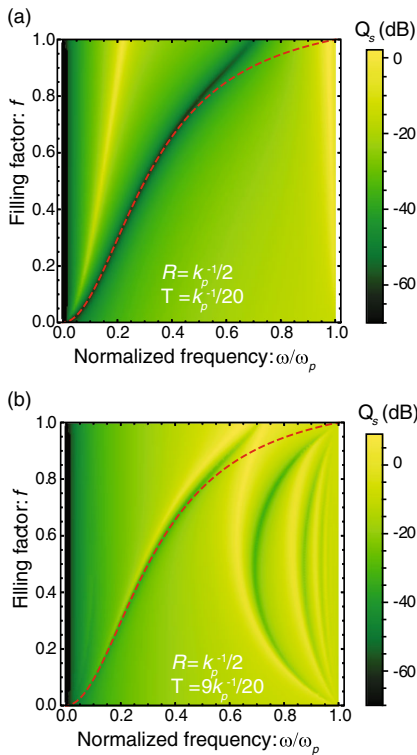


**Fig. 6** Scattering spectrum of a tubular cavity immersed in air ( $\epsilon = \epsilon_1 = 1$ ) with utmost radius  $R = k_p^{-1}/2$ , when the thickness of the shell is **a**  $T = 0.1R$ , and **b**  $T = 0.9R$ . The red dashed line indicates the frequency  $\omega_{\text{zero}}$  given in Eq. 18

The influence of losses in the Drude medium are analyzed in the following. In Fig. 7, we represent the scattering efficiency of a hollow metamaterial cylinder immersed in

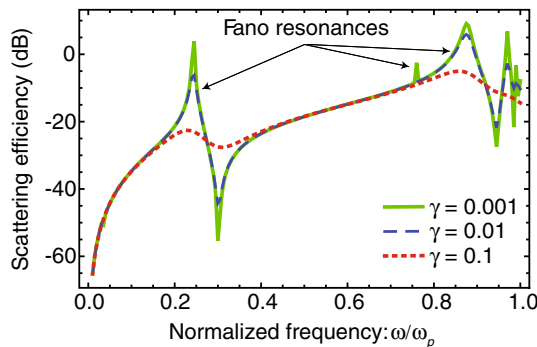


**Fig. 7** Scattering efficiency of a tubular anisotropic metamaterial ( $f = 1/2$ ) of equal radius and thickness,  $R = T = k_p^{-1}/4$ , immersed in air. The damping rate of the Drude medium varies from  $\gamma = 1/10$ , expressed in units of  $\omega_p$ , and  $\gamma = 1/1000$

air and with dimensions given by  $R = k_p^{-1}/2$  and  $T = R/2$ . Again, the filling factor is  $f = 1/2$ . We observe that metamaterials including an ultra low-loss Drude medium, like that assuming  $\gamma = \omega_p/1000$  and analyzed in Fig. 7, gives a minimum in scattering which represents approximately one order of magnitude lower than that obtained for a damping rate of  $\gamma = \omega_p/100$ . The inverse occurs when examining the peaks corresponding to the fundamental resonance. As a consequence, the peak-to-valley contrast increases two orders of magnitude for a decrement of only one order of magnitude in the damping rate of the Drude medium. Regimes for ultra-cancellation of scattering are inevitably related with strong Fano resonances observed in low-loss Drude media. Also note that additional ultra-narrow peaks emerge, which may be attributed to multipole Mie resonances occurring for high orders  $n > 1$ . However, this cannot be applied to achieve an invisibility effect in practice.

On the other hand, considering higher losses of the Drude medium, the minimum and maximum of scattering efficiency associated with the fundamental Fano resonance may reduce their contrast in several orders of magnitude. This is illustrated in Fig. 7 by evaluating the scattering efficiency of an anisotropic metamaterial including a Drude medium with  $\gamma = \omega_p/10$ . This critical issue is of relevance since the electrons in the Drude medium experience a significant reduction of their effective mean free path in realistic multilayered anisotropic metamaterials; note that electron scattering in ultrathin layers results in the loss of electron phase coherence leading to a higher damping rate [37]. Finally, the drop of peak-to-valley contrast may be also observed in higher energy Fano resonances.

Heretofore, the only discrepancy to the rule of  $\epsilon_{\perp}$  near zero, enabling to find the principal Fano resonance with associated scattering cancellation, was found with cavity metamaterials of a high filling factor  $f$ . However, that is not certainly unique. As an illustration, we examine the effects of the dielectric constant in the core ( $\epsilon_C$ ) and in the environment medium ( $\epsilon$ ). In particular, we evaluated the scattering efficiency of a cylindrical cavity of radius  $R = k_p^{-1}/2$  and shell thickness  $T = k_p^{-1}/4$ . Again, a fixed damping rate  $\gamma = \omega_p/100$  is considered. In Fig. 8a, we plot  $Q_s$  for cylinders of different filling factors  $f$  immersed in air and having a high permittivity core of  $\epsilon_C = 10$ . Two resonances associated with the excitation of symmetric and antisymmetric surface polaritons, showing a peak-to-valley spectral pattern, govern again the scattering efficiency of the core-shell cylinder. The loci of the maxima are clearly shifted with respect to the case of a hollow cavity with  $\epsilon_C = 1$ . Remarkably, the fundamental frequency of invisibility undergoes a substantial departure from  $\omega_{\text{zero}}$  even at low and moderate filling factors.

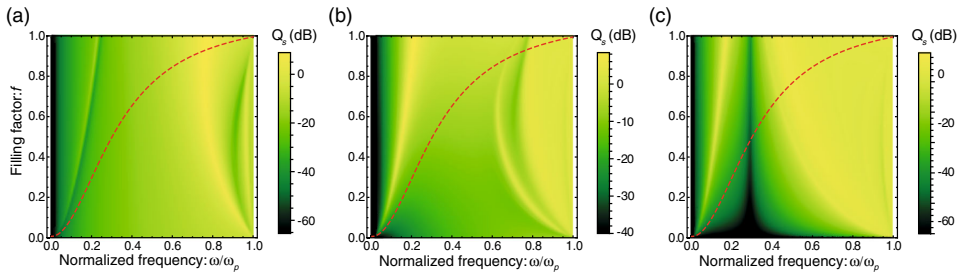


**Fig. 8** Scattering efficiency, expressed in dB, of a cylindrical cavity of radius  $R = k_p^{-1}/2$  and thickness  $T = R/2$ , when varying the dielectric constant of the core and environment medium: **a**  $\epsilon_C = 10$  and  $\epsilon = 1$ ,

**b**  $\epsilon_C = 1$  and  $\epsilon = 10$ , and **c**  $\epsilon_C = 10$  and  $\epsilon = 10$ . The red dashed line corresponds to frequencies  $\omega_{\text{zero}}$  which are solutions to the Eq. 18

In the reversed scene, where the environment medium presents a high permittivity, for instance  $\epsilon = 10$  as shown in Fig. 8b, and the core is filled with air, the behavior in scattering changes completely. Firstly, we identify the fundamental Fano resonance with an enormous spectral gap between its peak frequency and the first valley frequency, where the peak-to-valley efficiency has a moderate contrast. When the filling factor  $f = 1/2$ , the main peak is found at  $\omega = 0.153\omega_p$ , whereas the first valley is located at  $\omega = 0.707\omega_p$ . This fact suggests that the reduction of  $Q_s$  associated with the fundamental Fano resonance is deleted in practical terms, enabling to observe exclusively minima of higher order resonances in the scattering spectrum. In this sense, additional resonances covering the spectrum below  $\omega_p$  may be found. We conclude that the effect of invisibility is basically erased from this picture.

Finally, we analyzed the scattering efficiency of the anisotropic cavity for a high dielectric constant of the core and environment medium, simultaneously. In Fig. 8c, we represent  $Q_s$  when  $\epsilon_C = \epsilon = 10$ . Importantly, the fundamental frequency of invisibility is set practically in the same value for the whole range of filling factors. For instance, the scattering cancellation is produced at  $\omega = 292\omega_p$  when the filling factor is  $f = 0.2$ ; increasing such a factor to  $f = 0.8$ , the frequency corresponding to the valley of lowest energy is found at  $\omega = 0.294\omega_p$ . These results demonstrate that the invisibility regime dramatically depends on the permittivities of the core and environment medium, a conclusion that might be in disagreement with previous studies which remarked the importance of the condition given by  $\omega_{\text{zero}}$  [15].

## Conclusions

In summary, we investigated the scattering efficiency of cylindrical cavities formed by a radially anisotropic nanostructure, when the illumination is carried out by a  $\text{TE}^z$  plane

wave. A radially anisotropic medium was established by the form birefringence of a metamaterial composed of periodic distribution of subwavelength concentric multilayers. The Lorenz-Mie scattering coefficients are determined by means of the proper boundary conditions, which we set in terms of a transfer matrix formalism.

For subwavelength cavities, we observe two resonances corresponding to modal symmetric and antisymmetric surface polaritons. By the side of each resonance peak, a minimum in scattering at a slightly higher frequency is found, which can be attributed to Fano shapes. For scatterers immersed in air, the fundamental frequency where the scattering cancellation is shown at the lowest energy makes the metamaterial permittivity  $\epsilon_{\perp}$  takes values near zero. Thus, by balancing the composition of the metamaterial, we might tune the invisibility frequency up to the plasma frequency of the constituting Drude medium. Unfortunately, such approach is not valid for high filling factors close to unity, where the tubular particle behaves like a low-birefringent plasmonic cavity. In these cases, the secondary dip in the scattering spectrum might efficiently be used to obtain an invisibility effect.

The onset of additional resonances at increasing cavity sizes, in the order of the current wavelength, governs the contour of the scattering spectrum thus vanishing the invisibility effect. The main invisibility frequency remains practically unaltered of various values of the aspect ratio  $T/R$ . In particular, examining the case which suggests a cylinder with a very small concentric hole, we obtained the occurrence of multiple peaks and their associated minima in efficiency, indicating an accumulation of excited Fano resonances.

Finally, severe discrepancies to the rule of  $\epsilon_{\perp}$  near zero, enabling to find the principal Fano resonance with associated scattering cancellation, were found by modifying the dielectric constant in the core and in the environment medium, even at low and moderate filling factors. For instance, for a high dielectric constant of the core

and environment medium, the fundamental frequency of invisibility is set practically fixed for the whole range of filling factors. These results demonstrate that the invisibility regime dramatically depends on the permittivities of the core and environment medium.

**Acknowledgments** This work was supported by the Spanish Ministry of Economy and Competitiveness (MINECO) (TEC2014-53727-C2-1-R).

## References

- Leonhardt U (2006) *Science* 312:1777
- Pendry JB, Schurig D, Smith DR (2006) *Science* 312:1780
- Cai W, Chettiar UK, Kildishev AV, Shalaev VM (2007) *Nat Photon* 1:224
- Forouzbafard MR, Farzad MH (2015) *Plasmonics* 10:1345
- Yu GX, Cao R, Luo M (2015) *Optik* 126:1990
- Alù A, Rainwater D, Kerkhoff A (2010) *New J Phys* 12:103028
- Ni Y, Gao L, Qiu CW (2010) *Plasmonics* 5:251
- Alu A, Engheta N (2005) *Phys Rev E* 72:016623
- Edwards B, Alu A, Silveirinha MG, Engheta N (2009) *Phys Rev Lett* 103:153901
- Filonov DS, Slobozhanyuk AP, Belov PA, Kivshar YS (2012) *Phys Status Solidi RRL* 6:46
- Alu A, Engheta N (2008) *Phys Rev Lett* 100:113901
- Tricarico S, Bilotti F, Vegni L, Eur J (2009) *Opt Soc, Rapid Publ* 4:09021
- Chen PY, Soric J, Alu A (2012) *Adv Mater* 24:OP281
- Mirzaei A, Miroshnichenko AE, Shadrivov IV, Kivshar YS (2015) *Sci Rep* 5:9574
- Kim KH, No YS, Chang S, Choi JH, Park HG (2015) *Sci Rep* 5:16027. doi:10.1038/srep16027
- Díaz-Aviñó C, Naserpour M, Zapata-Rodríguez CJ (2016). arXiv:1605.00030
- Bussey HE, Richmond JH (1975) *IEEE Trans Antennas Propag* 23:723
- Bohren CF, Huffman DR (1998) *Absorption and scattering of light by small particles*. Wiley
- Díaz-Aviñó C, Pastor D, Zapata-Rodríguez CJ, Naserpour M, Kutyński R, Miret JJ (2016) *J Opt Soc Am B* 33:116
- Johnson PB, Christy RW (1972) *Phys Rev B* 6(12):4370
- Yeh P, Yariv A, Hong CS, *Opt J* (1977) *Soc Am* 67:423
- Chen HL, Gao L (2012) *Phys Rev A* 86:033825
- Chen HL, Gao L (2013) *Opt Express* 21:23619
- Torrent D, Sánchez-Dehesa J (2009) *Phys Rev Lett* 103:064301
- Kettunen H, Wallén H, Sihvola A (2015) *Photonics* 2:509
- Kidwai O, Zhukovsky SV, Sipe JE (2012) *Phys Rev A* 85:053842
- Maier SA (2007) *Plasmonics: fundamentals and applications*. Springer, New York
- Yeh P (1988) *Optical waves in layered media*. Wiley, New York
- Elser J, Podolskiy VA, Salakhutdinov I, Avrutsky I (2007) *Appl Phys Lett* 90:191109
- Díaz-Aviñó C, Naserpour M, Zapata-Rodríguez CJ (2016) arXiv:1603.08317. doi:10.1016/j.optcom.2016.06.081
- Ferrari L, Wu C, Lepage D, Zhang X, Liu Z (2015) *Prog Quant Electron* 40:1
- Zapata-Rodríguez CJ, Pastor D, Camps V, Caballero MT, Miret JJ (2011) *J Nanophoton* 5:051807
- Zapata-Rodríguez CJ, Pastor D, Caballero MT, Miret JJ (2012) *Opt Commun* 285:3358
- Miret JJ, Zapata-Rodríguez CJ (2010) *J Opt Soc Am B* 27(7):1435
- Zapata-Rodríguez CJ, Miret JJ, Vuković S, Belić MR (2013) *Opt Express* 21:19113
- Zapata-Rodríguez CJ, Pastor D, Miret JJ, Vuković S (2014) *J Nanophoton* 8:083895
- Zhu J (2008) *Appl Phys Lett* 92:241919
- Nickelson L, Bucinskas J (2012) *Appl Phys A* 109:883
- Rybin MV, Filonov DS, Belov PA, Kivshar YS, Limonov MF (2015) *Sci Rep* 5:8774
- Lukyanchuk B, Zheludev NI, Maier SA, Halas NJ, Nordlander P, Giessen H, Chong CT (2010) *Nat Mater* 9:707
- Fano U (1961) *Phys Rev* 124:1866
- Bachelier G, Russier-Antoine I, Benichou E, Jonin C, Fatti ND, Vallée F, Brevet PF (2008) *Phys Rev Lett* 101:197401
- Christ A, Ekinci Y, Solak HH, Gippius NA, Tikhodeev SG, Martin OJF (2007) *Phys Rev B* 76(R):201405
- Fedotov VA, Rose M, Prosvirnin SL, Papasimakis N, Zheludev NI (2007) *Phys Rev Lett* 99:147401

2<sup>nd</sup> Publication:  
**Conditions for Achieving Invisibility of  
Hyperbolic Multilayered Nanotubes**

**Authors:** Carlos Díaz-Aviñó, Mahin Naserpour and Carlos J.  
Zapata-Rodríguez

Published in **Optics Communications**, volume 381, pages 234-239,  
year 2016.



# Conditions for achieving invisibility of hyperbolic multilayered nanotubes



Carlos Díaz-Aviñó, Mahin Naserpour, Carlos J. Zapata-Rodríguez \*

Department of Optics, University of Valencia, Dr. Moliner 50, Burjassot 46100, Spain

## ARTICLE INFO

### Article history:

Received 17 May 2016  
Received in revised form  
26 June 2016  
Accepted 28 June 2016

### Keywords:

Hyperbolic metamaterial  
Invisibility  
Plasmonics

## ABSTRACT

Highly anisotropic plasmonic nanotubes exhibit a dramatic drop of the scattering cross section in the transition regime from hyperbolic to elliptic dispersion. The characterization of a realistic multilayered metamaterial is typically carried out by means of an effective medium approach providing average components of the permittivity tensor and wave fields. Here, the edge effects of the metal-dielectric stratified nanotube for different combinations were thoroughly analyzed. We show how the boundary layers, which in principle remain fully irrelevant in the estimation of the effective permittivity of the nanotube, however play a critical role in the resonant scattering spectra and the near field patterns. A remarkable enhancement of the scattered wave field is unexpectedly experienced at the frequencies of interest when a dielectric layer is chosen to be in contact with the cavity core.

© 2016 Elsevier B.V. All rights reserved.

## 1. Introduction

Metamaterials with unprecedented optical properties have been recently proposed by several groups for applications in cloaking and invisibility. A vast majority of cloaking nanostructures are engineered in the basis of transformation optics principles [1–3] enabling analytical expressions of the electromagnetic fields and metamaterial properties [4–6]. An original concept suggested by Alu and Engheta has also attracted great attention which relies on the use of metamaterial (or metal) coatings to severely drop the scattering efficiency of an object by means of a nonresonant scattering-cancellation approach [7]. The strategy of such scattering cancellation takes advantage of the local negative polarizability of metamaterials, and its experimental realization was first demonstrated at microwave frequencies by using an array of metallic fins which are embedded in a high-permittivity environment to generate a metamaterial cloaking shell [8].

Novel extensions of the previous concepts have more recently made the scene, which are based on the use of double-shell and multilayered plasmonic coatings [9,10]. For instance, using plasmonic shells with an epsilon-near-zero material enables to reduce substantially the scattering losses and simultaneously providing the shielding of the cloaked region [11,12]. As an alternative, a nanotube consisting of a periodic distribution of metal and dielectric alternating layers, where the stratified metamaterial was

described as a radial-anisotropic hyperbolic medium, has recently demonstrated narrow-band ultra-low scattering [13]. The invisibility spectral band occurs when one of the components of the effective permittivity tensor is near zero. The effective medium theory was adopted to efficiently reproduce the results provided by the analytical Lorenz-Mie scattering method [14,15].

Here, we study in detail the edge effects of the stratified hyperbolic nanotube employed in Ref. [13] for different combinations, that is, when the layer in contact with the environment medium is either the metal or the nonconducting material. We demonstrated that boundary effects play a relevant role in the resulting scattering efficiency of the nanotube, potentially clearing away the characteristic invisibility of the nanotube and boosting additional plasmonic resonances in the visible. Explicitly, when silver is set as the constituent material of the outermost layer, unexpectedly, a significant enhancement of the scattered signal is observed. As a consequence, the effective medium theory enabling a simplified model for the optical characterization of the nanoparticle may apparently lead to fallacious estimations even for metamaterials composed of subwavelength layers with a few-nanometers width.

## 2. The hyperbolic multilayered nanotube

Let us consider a cylindrical shell formed by a multilayered nanostructure as illustrated in Fig. 1. Following Ref. [13], silver and titanium dioxide was used for the stratified medium. A silver nanofilm of width  $w_{Ag}$  is set by the side of a  $TiO_2$  layer of width  $w_{TiO_2}$ ,

\* Corresponding author.

E-mail address: [carlos.zapata@uv.es](mailto:carlos.zapata@uv.es) (C.J. Zapata-Rodríguez).



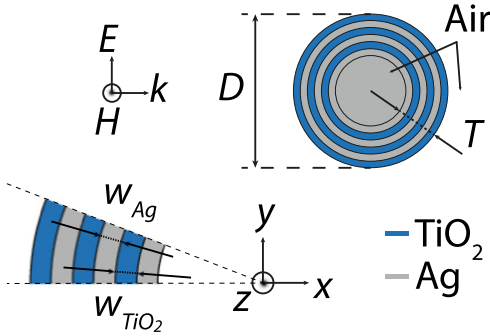


Fig. 1. Illustration of the multilayered nanotube.

thus forming the unit cell of periodic distribution along the radial coordinate. In our numerical simulations we considered a nanostructured tube of outermost diameter  $D$  and composed of six layers, giving a total shell thickness of  $T = 3(w_{Ag} + w_{TiO_2})$ . The relative permittivities of silver and  $TiO_2$  within the visible range of frequencies may be approximated by [13]

$$\epsilon_{Ag}(\lambda) = 3.691 - \frac{9.152^2}{(1.24/\lambda)^2 + i0.021(1.24/\lambda)}, \tag{1}$$

and

$$\epsilon_{TiO_2}(\lambda) = 5.193 + \frac{0.244}{\lambda^2 - 0.0803}, \tag{2}$$

respectively. In the previous equations, the working wavelength  $\lambda$  is set in micrometers. In this study we examined hollow cylinders immersed in air.

Within a long-wavelength approach, the multilayered metamaterial may be considered as a uniaxial medium whose optic axis is set along the direction of periodicity, that is the radial axis in our particular case. The effective anisotropic medium is then optically characterized by a local permittivity tensor  $\epsilon$  of component [16]

$$\epsilon_{||} = \frac{\epsilon_{Ag}\epsilon_{TiO_2}}{f\epsilon_{TiO_2}} + (1-f)\epsilon_{Ag}, \tag{3}$$

along the optic axis, and

$$\epsilon_{\perp} = f\epsilon_{Ag} + (1-f)\epsilon_{TiO_2}, \tag{4}$$

in the perpendicular direction. In the previous equations, the metal filling factor

$$f = \frac{w_{Ag}}{w_{Ag} + w_{TiO_2}}, \tag{5}$$

represents the unique geometrical parameter determining the effective permittivities of the metamaterial, regardless the internal one-dimensional distribution of the materials involved in the unit cell.

In Fig. 2 we represent the real values of  $\epsilon_{||}$  and  $\epsilon_{\perp}$  within the visible range of frequencies, for different values of the metal filling factor. We observe that the real part of  $\epsilon_{\perp}$  is near zero around a filling factor  $f_z = \epsilon_{TiO_2}/(\epsilon_{TiO_2} - \text{Re}(\epsilon_{Ag}))$ , whereas the real part of  $\epsilon_{||}$  is near a pole around a filling factor  $f_p = \text{Re}(\epsilon_{Ag})/(\text{Re}(\epsilon_{Ag}) - \epsilon_{TiO_2})$ . The hyperbolic regime is determined by the condition  $\text{Re}(\epsilon_{||})\text{Re}(\epsilon_{\perp}) < 0$ , indicated as shaded regions in Fig. 2. The choice  $\text{Re}(\epsilon_{\perp}) > 0$  corresponds to the so-called Type I hyperbolic metamaterials, whereas the choice  $\text{Re}(\epsilon_{\perp}) < 0$  denotes a Type II hyperbolic medium [17]. Note that when  $\text{Re}(\epsilon_{Ag}) = -\epsilon_{TiO_2}$  occurring at a wavelength  $\lambda = 448$  nm, both  $f_z$  and  $f_p$  coincide at a value 0.5, denoting

that the silver layers and the  $TiO_2$  layers have the same width. In this case, the hyperbolic regime spans the whole spectrum. Let us point out that the extraordinary dispersion features of hyperbolic and epsilon-near-zero metamaterials have inspired us in a plethora of applications such as subwavelength imaging [18,19], surface-wave engineering [20,21], and double refraction [22,23], to mention a few.

### 3. Results and discussion

To estimate analytically the scattering efficiency of the multilayered Ag- $TiO_2$  nanotube we followed the Lorenz-Mie scattering method [14]. Note that the axis of the cylindrical cavity is oriented along the z-axis. First we assumed that the nanotube is illuminated by a  $TE^z$ -polarized plane wave propagating along the x-axis, as illustrated in Fig. 1. The magnetic field of the incident plane wave may be set as

$$\mathbf{H}^i = \hat{z}H_0\exp(ikx), \tag{6}$$

where  $H_0$  is a constant amplitude and  $k = 2\pi/\lambda$  is the wavenumber in air. In this case, the scattered magnetic field may be set as

$$\mathbf{H}^s = \hat{z}H_0 \sum_{n=-\infty}^{+\infty} a_n i^n H_n^{(1)}(kr)\exp(in\phi), \tag{7}$$

where  $r$  and  $\phi$  are the radial and azimuthal cylindrical coordinates, respectively, and  $H_n^{(1)}$  is the Hankel function of the first kind and order  $n$ . By using the Lorenz-Mie theory [15], it is possible to evaluate analytically the scattering coefficients  $a_n$ , which provide the estimation of the scattering efficiency as

$$Q_s = \frac{4}{kD} \sum_{n=-\infty}^{+\infty} |a_n|^2. \tag{8}$$

Plasmonic resonances are determined by the poles of the coefficients  $a_n$ . On the other hand, the invisibility condition is established provided that the scattering coefficients  $a_n$  arrive simultaneously to a value near zero.

In Fig. 3 we show the scattering efficiency of our Ag- $TiO_2$  nanotube calculated with Eq. (8), provided that the hyperbolic metamaterial has a metal filling factor  $f=0.5$  and that the hollow particle is illuminated by a  $TE^z$  polarized plane wave. In the numerical simulations we set a layer width  $w_{Ag}$  and  $w_{TiO_2}$  of 10 nm and a cylinder diameter of  $D=220$  nm. Eq. (8) is accurately estimated by using a finite number of scattering coefficients satisfying  $|n| < 5$ . As illustrated in Fig. 3, the calculated  $Q_s$  exhibits significant discrepancies when the inmost layer is either Ag or  $TiO_2$ , despite  $\epsilon_{||}$  and  $\epsilon_{\perp}$  remain the same in both cases. When the interior layer is made of silver, the scattering efficiency of the nanostructure reaches a minimum of 0.053 at  $\lambda = 437$  nm, as reported in Ref. [13], where  $\text{Re}(\epsilon_{\perp}) = 0.34$  and  $\text{Re}(\epsilon_{||}) = -143$ . In addition, a high peak of  $Q_s=5.36$  is found at  $\lambda = 510$  nm, where  $\text{Re}(\epsilon_{\perp}) = -1.96$  and  $\text{Re}(\epsilon_{||}) = 35$ . However, the number of resonant peaks increases if titanium dioxide is set in the inmost layer. In this case, the highest peak is located at a wavelength of 560 nm where the scattering efficiency yields 3.50, and a secondary strong peak is found at  $\lambda = 525$  nm ( $Q_s=2.46$ ). In addition, its minimum in scattering efficiency is shifted at  $\lambda = 491$  nm where importantly it reaches a value of 0.53. We point out that such minimum in scattering efficiency, which is far of being associated with invisibility, is one order of magnitude higher than that estimated previously for an Ag inmost coating. Finally, a dissimilar behavior in scattering is also manifested for  $TM^z$ -polarized incident light (not shown in Fig. 3).

In order to provide a physical insight of such a behavior, we

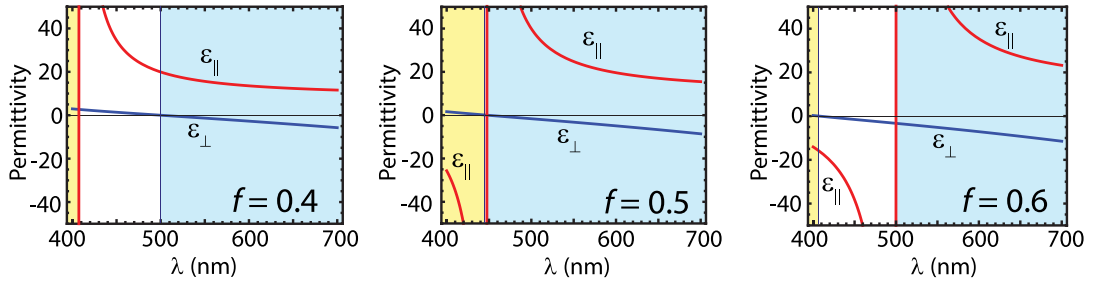


**Fig. 2.** Real part of the components  $\epsilon_{||}$  (red line) and  $\epsilon_{\perp}$  (blue line) of the permittivity tensor in the visible regime for different metal filling factors. The shaded regions denote spectral bands where the metamaterial exhibits a hyperbolic dispersion of the Type I (shaded in yellow) and the Type II (shaded in blue). (For interpretation of the references to color in this figure caption, the reader is referred to the web version of this paper.)

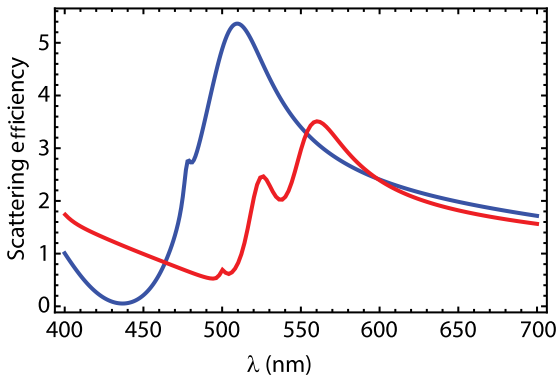


**Fig. 3.** Scattering efficiency ( $Q_s$ ) of a hollow metamaterial cylinder composed of 6 layers, where the nanotube thickness is  $T=60$  nm, its diameter is  $D=220$  nm, and the silver filling factor is  $f=0.5$ . The inmost layer is made of either silver (blue line) or titanium dioxide (red line). The calculations are performed in the visible spectral range for  $TE^z$ -polarized incident light. (For interpretation of the references to color in this figure caption, the reader is referred to the web version of this paper.)

analytically calculated the electromagnetic fields inside the nanotube and in the air core and in the environment medium. In Fig. 4 we represent the modulus of the magnetic field,  $|\mathbf{H}|$ , at the invisibility wavelength  $\lambda = 437$  nm for different geometric configurations, calculated by means of the Lorenz–Mie scattering method, provided that the incident wave field is  $TE^z$  polarized. When silver is set in the inmost layer of the hyperbolic metamaterial, we observe a moderate enhancement of the field at three different Ag–TiO<sub>2</sub> interfaces, as shown in Fig. 4(a), which corresponds to a collective excitation of surface plasmon polaritons (SPPs). It is clear that the field exhibits strong irregularities derived from nonlocal effects in the multilayered metal–dielectric nanostructure [24]. Though such phenomenon severely puts into question the validity of the effective medium approach followed in Ref. [13], the deviations from an average field inside the hyperbolic nanotube are moderate in this case. Analyzing the case that titanium dioxide is placed in contact with the interior medium, however, we observe even abrupt variations of the field especially at the rear part of the nanotube (in the semi-space  $x > 0$ ), as shown in Fig. 4(b). Furthermore, now the field distribution is clearly asymmetric with respect to the origin of coordinates, leaving a strong backscattered signal.

Finally, we observe from Fig. 4 that the field amplitude at the center of the nanotube and in its neighborhood is, in average, near the field remaining in the environment medium rather than zero. This fact evidences that the shielding effect that commonly is recognized in epsilon-near-zero core–shell nanocylinders [12]

cannot be reproduced in our hyperbolic metamaterial nanotube when the light impinges under  $TE^z$  polarization.

The following analyzes the effects of increasing the number of layers in our nanotube maintaining the thickness  $T=60$  nm and the metal filling factor  $f=0.5$  of the shell, implying that the layer width  $w_{Ag}$  and  $w_{TiO_2}$  of the metamaterial is reduced. Considering 12 alternating layers of silver and titanium dioxide, the layer width (and the period of the multilayered nanostructure) is reduced to one half with respect to the cases analyzed above and illustrated in Figs. 3 and 4. The scattering efficiency of such additional nanotube is shown in Fig. 5, considering the examples where the inmost layer is either Ag or TiO<sub>2</sub>; the efficiency  $Q_s$  is again evaluated by means of the Lorenz–Mie scattering method. When the layer in contact with the core is silver, we find a minimum of  $Q_s$  equal to 0.026 at a wavelength  $\lambda = 444$  nm, representing an exiguous variation in comparison with the hyperbolic nanotube of 6 layers. In addition, the maximum of scattering efficiency reaches a value of 5.20 at  $\lambda = 507$  nm. If now we consider a nanotube with the interior layer made of TiO<sub>2</sub>, its scattering efficiency at the invisibility wavelength  $\lambda = 444$  nm reaches a value of 0.671, representing a factor of 25 with respect to the case previously analyzed. In fact, the minimum of the scattering efficiency is 0.345, which is found at  $\lambda = 477$  nm. The overall shape of  $Q_s$ , however, becomes relatively similar in both cases.

The profile of the magnetic field at the new invisibility wavelength  $\lambda = 444$  nm again exhibits abrupt changes at the metal–dielectric interfaces, as shown in Fig. 6(a) for a nanotube with inmost layer made of Ag, but the envelope enabling the estimation of an average value presents a slow variation inside the metamaterial. Moreover, a minimum of intensity is found near the origin of coordinates, however such intensity is far of zero disabling the gain of a shielding effect. In Fig. 6(b) we represent the magnetic field of the nanotube at the invisibility wavelength of  $\lambda = 444$  nm, considering a nanotube of interior layer made of TiO<sub>2</sub>. The resonant excitation of collective SPPs at the rear part of the nanocylinder, developing a chief (inhomogeneous) Bloch wave in the multilayered metamaterial [25], seems to be responsible of the significant increase in the scattering efficiency and subsequently the predominant visibility of the nanotube. Now this is clear that the appearance of a predominant radially evanescent Bloch wave also occurs for a 6-layer nanostructure, as shown in Fig. 4(b).

Obviously, by including a higher number of layers and, at the same time, maintaining the thickness  $T$  of the nanotube and the filling factor  $f$  of the metamaterial, both the scattering efficiency spectrum and the field pattern will continuously approach for the Ag and TiO<sub>2</sub> ending layers, leading to the response of a purely hyperbolic nanotube [13]. Fig. 7(a) shows the scattering efficiency  $Q_s$  of a hollow nanocylinder of thickness  $T=60$  nm and total diameter  $D=220$  nm, which is composed of a hyperbolic

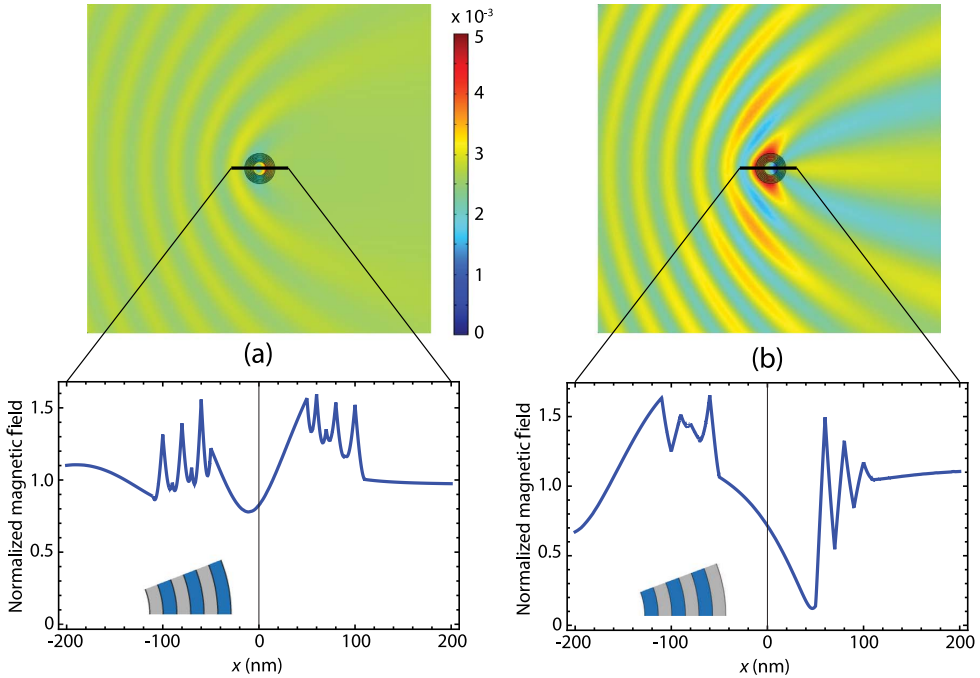


Fig. 4. Amplitude distribution of the normalized magnetic field  $|H|/|H_0|$  at the invisibility wavelength  $\lambda = 437$  nm and different arrangements of the metamaterial; the inmost layer is made of (a) Ag and (b)  $\text{TiO}_2$ .

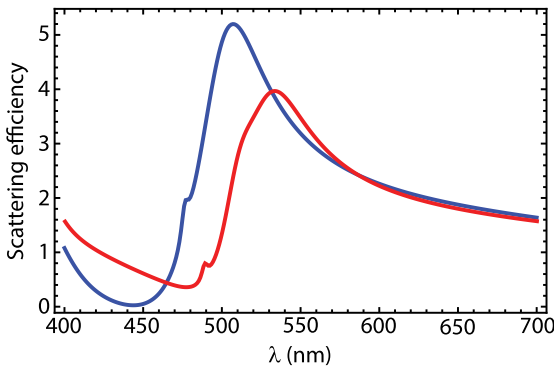


Fig. 5. Scattering efficiency of a hollow metamaterial cylinder composed of 12 layers, where  $T=60$  nm,  $D=220$  nm, and  $f=0.5$ . The interior layer is made of either titanium dioxide (red line) or silver (blue line). (For interpretation of the references to color in this figure caption, the reader is referred to the web version of this paper.)

metamaterial with components of its permittivity tensor as given by Eqs. (3) and (4), considering that the filling factor  $f=0.5$ . The calculations were carried out by using the Lorenz–Mie scattering method described in Refs. [26–28]. The minimum efficiency ( $Q_s=0.172$ ) is found at  $\lambda = 459$  nm establishing the invisibility wavelength, where  $\text{Re}(\epsilon_1) = -0.36$  and  $\text{Re}(\epsilon_0) = 151$ . The main efficiency peak reaching 4.76 is localized at  $\lambda = 513$  nm. The field distribution in the nanotube is also plotted in Fig. 7(b) at the invisibility wavelength  $\lambda = 459$  nm. We observe the formation of surface waves in the two air–hyperbolic metamaterial interfaces. In average, this field pattern is closer to the field distribution shown in Fig. 6(a) for an Ag inmost layer than that exhibited for a

nanostuctured tube of Ag ending coating depicted in Fig. 6(b). At the rear part of the nanotube, the field oscillations inside the multilayered metamaterial become stronger near the core; however, a surface wave at the metamaterial–core interface is only produced when a silver layer remains in contact with the core, as shown in Fig. 6(a) but not in Fig. 6(b).

#### 4. Conclusions

In summary, we investigated numerically the scattering efficiency, with emphasis in the invisibility regime, of multilayered Ag– $\text{TiO}_2$  nanotubes with configurations of a different ending layer. We demonstrated that when the nonconducting layer remains in contact with the core of the hollow cylinder, the characteristic invisibility of the hyperbolic nanotube is cleared away, even considering elementary layers of a few nanometers. In this case there is an additional boosting of plasmonic–Bloch resonances markedly observed on the wave fields localized at the rear part of the multilayered nanocylinder. Furthermore, the effective medium theory enabling a simplified model for the optical characterization of the nanoparticle will lead to fallacious estimations. Such effect becomes weaker for metamaterials composed of subwavelength layers with less-than-5-nanometers width.

#### Acknowledgments

This work was supported by the Spanish Ministry of Economy and Competitiveness (MINECO) (TEC2014-53727-C2-1-R).

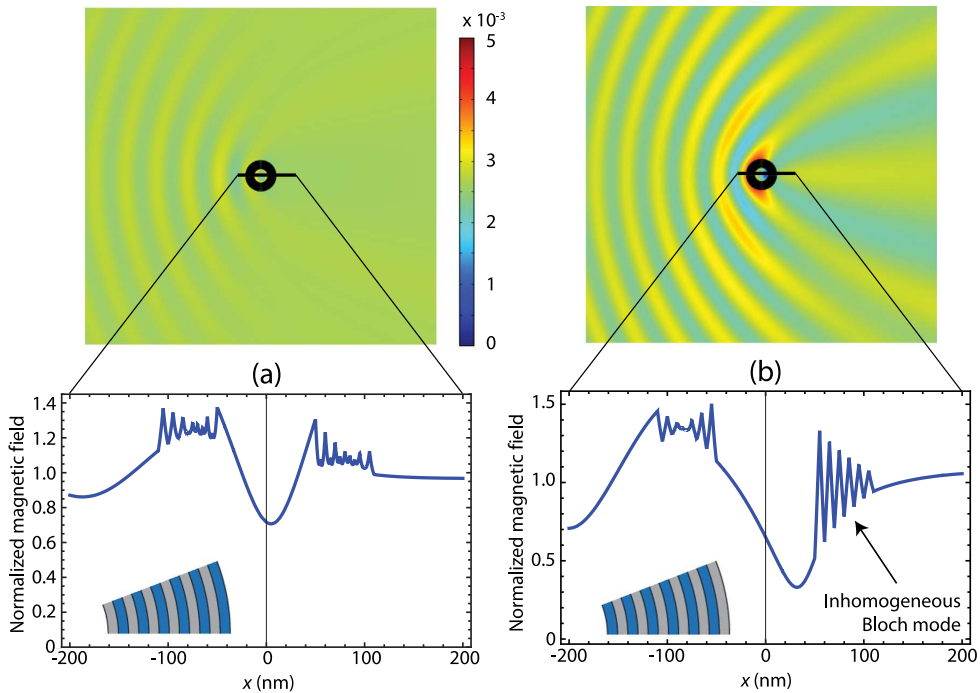


**Fig. 6.** Amplitude distribution of the normalized magnetic field  $|H||/|H_0|$  at the invisibility wavelength  $\lambda = 444$  nm and different arrangements of the metamaterial, where  $T=60$  nm,  $D=220$  nm, and  $f=0.5$ . The interior layer is made of (a) silver and (b) titanium dioxide.

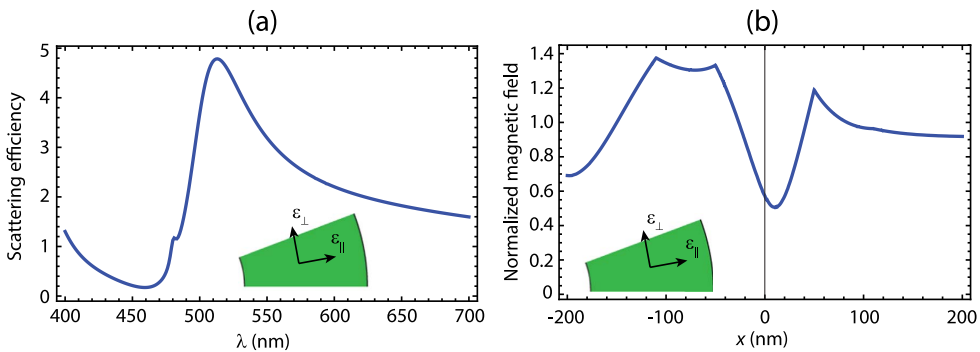


**Fig. 7.** (a) Scattering efficiency of a hollow cylinder of thickness  $T=60$  nm and total diameter  $D=220$  nm, composed of a hyperbolic metamaterial with components of its permittivity tensor is given by Eqs. (3) and (4), where  $f=0.5$ . (b) Normalized magnetic field  $|H||/|H_0|$  along the  $x$ -axis at the invisibility wavelength  $\lambda = 459$  nm.

## References

- [1] U. Leonhardt, Optical conformal mapping, *Science* 312 (2006) 1777–1780.
- [2] J.B. Pendry, D. Schurig, D.R. Smith, Controlling electromagnetic fields, *Science* 312 (2006) 1780–1782.
- [3] W. Cai, U.K. Chettiar, A.V. Kildishev, V.M. Shalaev, Optical cloaking with metamaterials, *Nat. Photon.* 1 (2007) 224–227.
- [4] M.R. Forouzeshefard, M.H. Farzad, Electromagnetic wave propagation through two coaxial transformation-based cylindrical media, *Plasmonics* 10 (2015) 1345–1357.
- [5] G.X. Yu, R. Cao, M. Luo, The property of energy flow velocity in the cloak shell, *Optik* 126 (2015) 1990–1993.
- [6] A. Rajput, K.V. Srivastava, Design of thin simplified cloak with finite and small dynamic range constitutive tensors, *Appl. Phys. A* 122 (2016) 230.
- [7] A. Alu, N. Engheta, Achieving transparency with plasmonic and metamaterial coatings, *Phys. Rev. E* 72 (2005) 016623.
- [8] B. Edwards, A. Alu, M.G. Silveirinha, N. Engheta, Experimental verification of plasmonic cloaking at microwave frequencies with metamaterials, *Phys. Rev. Lett.* 103 (2009) 153901.
- [9] S. Tricarico, F. Bilotti, L. Vegni, Scattering cancellation by metamaterial cylindrical multilayers, *J. Eur. Opt. Soc., Rapid Publ.* 4 (2009) 09021.
- [10] X. Zhou, Y. Chen, Y. Zhou, Z. Luo, The effect of coordinate transformation function on scattering characteristics of cylindrical cloaks with a quantity of discrete layers, *Opt. Commun.* 364 (2016) 67–71.
- [11] A. Alu, N. Engheta, Multifrequency optical invisibility cloak with layered plasmonic shells, *Phys. Rev. Lett.* 100 (2008) 113901.
- [12] D.S. Filonov, A.P. Slobozhanyuk, P.A. Belov, Y.S. Kivshar, Double-shell metamaterial coatings for plasmonic cloaking, *Phys. Status Solidi RRL* 6 (2012) 46–48.
- [13] K.-H. Kim, Y.-S. No, S. Chang, J.-H. Choi, H.-G. Park, Invisible hyperbolic metamaterial nanotube at visible frequency, *Sci. Rep.* 5 (2015) 16027, <http://dx.doi.org/10.1038/srep16027>.
- [14] H.E. Bussey, J.H. Richmond, Scattering by a lossy dielectric circular cylindrical multilayer, numerical values, *IEEE Trans. Antennas Propag.* 23 (1975) 723–725.
- [15] C.F. Bohren, D.R. Huffman, *Absorption and Scattering of Light by Small Particles*, Wiley, 1998.
- [16] P. Yeh, *Optical Waves in Layered Media*, Wiley, New York, 1988.
- [17] L. Ferrari, C. Wu, D. Lepage, X. Zhang, Z. Liu, Hyperbolic metamaterials and

- their applications, *Prog. Quant. Electron.* 40 (2015) 1–40.
- [18] C.J. Zapata-Rodríguez, D. Pastor, V. Camps, M.T. Caballero, J.J. Miret, Three-dimensional point spread function of multilayered flat lenses and its application to extreme subwavelength resolution, *J. Nanophoton.* 5 (2011) 051807.
- [19] C.J. Zapata-Rodríguez, D. Pastor, M.T. Caballero, J.J. Miret, Diffraction-managed superlensing using plasmonic lattices, *Opt. Commun.* 285 (2012) 3358–3362.
- [20] J.J. Miret, C.J. Zapata-Rodríguez, Diffraction-free propagation of subwavelength light beams in layered media, *J. Opt. Soc. Am. B* 27 (7) (2010) 1435–1445.
- [21] C.J. Zapata-Rodríguez, J.J. Miret, S. Vuković, M.R. Belić, Engineered surface waves in hyperbolic metamaterials, *Opt. Express* 21 (2013) 19113–19127.
- [22] C.J. Zapata-Rodríguez, D. Pastor, J.J. Miret, S. Vuković, Uniaxial epsilon-near-zero metamaterials from superlensing to double refraction, *J. Nanophoton.* 8 (2014) 083895.
- [23] C. Díaz-Aviñó, D. Pastor, C.J. Zapata-Rodríguez, M. Naserpour, R. Kotyński, J. Miret, Some considerations on the transmissivity of birefringent metamaterials, *J. Opt. Soc. Am. B* 33 (2016) 116–125.
- [24] J. Elser, V.A. Podolskiy, I. Salakhutdinov, I. Avrutsky, Nonlocal effects in effective-medium response of nanolayered metamaterials, *Appl. Phys. Lett.* 90 (2007) 191109.
- [25] D. Torrent, J. Sánchez-Dehesa, Radial wave crystals radially periodic structures from anisotropic metamaterials for engineering acoustic or electromagnetic waves, *Phys. Rev. Lett.* 103 (2009) 064301.
- [26] H.L. Chen, L. Gao, Anomalous electromagnetic scattering from radially anisotropic nanowires, *Phys. Rev. A* 86 (2012) 033825.
- [27] H.L. Chen, L. Gao, Tunability of the unconventional Fano resonances in coated nanowires with radial anisotropy, *Opt. Express* 21 (2013) 23619–23630.
- [28] H.L. Chen, L. Gao, Anomalous optical forces on radially anisotropic nanowires, *Appl. Phys. A* 121 (2015) 1053–1056.



3<sup>rd</sup> Publication:  
**Optimization of Multilayered Nanotubes  
for Maximal Scattering Cancellation**

**Authors:** Carlos Díaz-Aviñó, Mahin Naserpour and Carlos J.  
Zapata-Rodríguez

Published in **Optics Express**, volume 24, pages 18184-18196, year  
2016.

# Optimization of multilayered nanotubes for maximal scattering cancellation

CARLOS DÍAZ-AVIÑÓ,<sup>1</sup> MAHIN NASERPOUR,<sup>1,2</sup> AND CARLOS J. ZAPATA-RODRÍGUEZ<sup>1,\*</sup>

<sup>1</sup>Department of Optics and Optometry and Vision Science, University of Valencia, Dr. Moliner 50, Burjassot 46100, Spain

<sup>2</sup>Department of Physics, College of Science, Shiraz University, Shiraz 71454, Iran

\*carlos.zapata@uv.es

**Abstract:** An optimization for multilayered nanotubes that minimizes the scattering efficiency for a given polarization is derived. The cylindrical nanocavities have a radially periodic distribution, and the marginal layers that play a crucial role particularly in the presence of nonlocalities are disposed to reduce the scattering efficiency up to two orders of magnitude in comparison with previous proposals. The predominant causes leading to such invisibility effect are critically discussed.

© 2016 Optical Society of America

**OCIS codes:** (290.5839) Scattering, invisibility; (240.6680) Surface plasmons; (260.2065) Effective medium theory.

## References and links

- U. Leonhardt, "Optical conformal mapping," *Science* **312**, 1777–1780 (2006).
- J. B. Pendry, D. Schurig, and D. R. Smith, "Controlling electromagnetic fields," *Science* **312**, 1780–1782 (2006).
- W. Cai, U. K. Chettiar, A. V. Kildishev, and V. M. Shalaev, "Optical cloaking with metamaterials," *Nat. Photonics* **1**, 224–227 (2007).
- A. Alu and N. Engheta, "Achieving transparency with plasmonic and metamaterial coatings," *Phys. Rev. E* **72**, 016623 (2005).
- B. Edwards, A. Alu, M. G. Silveirinha, and N. Engheta, "Experimental verification of plasmonic cloaking at microwave frequencies with metamaterials," *Phys. Rev. Lett.* **103**, 153901 (2009).
- S. Tricarico, F. Bilotti, and L. Vegni, "Scattering cancellation by metamaterial cylindrical multilayers," *J. Eur. Opt. Soc. Rapid Publ.* **4**, 09021 (2009).
- D. S. Filonov, A. P. Slobozhanyuk, P. A. Belov, and Y. S. Kivshar, "Double-shell metamaterial coatings for plasmonic cloaking," *Phys. Status Solidi RRL* **6**, 46–48 (2012).
- P.-Y. Chen, J. Soric, and A. Alù, "Invisibility and cloaking based on scattering cancellation," *Adv. Mater.* **24**, OP281 (2012).
- A. Monti, A. Alù, A. Toscano, and F. Bilotti, "Optical invisibility through metasurfaces made of plasmonic nanoparticles," *J. Appl. Phys.* **117**, 123103 (2015).
- J. C. Soric, A. Monti, A. Toscano, F. Bilotti, and A. Alù, "Multiband and wideband bilayer mantle cloaks," *IEEE Trans. Antennas Propag.* **63**, 3235–3240 (2015).
- T. J. Aruda, A. S. Martinez, and F. A. Pinheiro, "Tunable multiple Fano resonances in magnetic single-layered core-shell particles," *Phys. Rev. A* **92**, 023835 (2015).
- M. V. Rybin, D. S. Filonov, P. A. Belov, Y. S. Kivshar, and M. F. Limonov, "Switching from visibility to invisibility via Fano resonances: Theory and experiment," *Sci. Rep.* **5**, 8774 (2015).
- K.-H. Kim, Y.-S. No, S. Chang, J.-H. Choi, and H.-G. Park, "Invisible hyperbolic metamaterial nanotube at visible frequency," *Sci. Rep.* **5**, 16027 (2015).
- L. Ferrari, C. Wu, D. Lepage, X. Zhang, and Z. Liu, "Hyperbolic metamaterials and their applications," *Prog. Quant. Electron.* **40**, 1–40 (2015).
- C. Díaz-Aviñó, M. Naserpour, and C. J. Zapata-Rodríguez, "Conditions for achieving invisibility of hyperbolic multilayered nanotubes," *Opt. Commun.* **381**, 234–239 (2016).
- C. F. Bohren and D. R. Huffman, *Absorption and Scattering of Light by Small Particles* (Wiley, 1998).
- P. Yeh, A. Yariv, and C.-S. Hong, "Electromagnetic propagation in periodic stratified media. I. general theory," *J. Opt. Soc. Am.* **67**, 423–438 (1977).
- H. E. Bussey and J. H. Richmond, "Scattering by a lossy dielectric circular cylindrical multilayer, numerical values," *IEEE Trans. Antennas Propag.* **23**, 723–725 (1975).
- G. A. Shah, "Scattering of plane electromagnetic waves by infinite concentric circular cylinders at oblique incidence," *Mon. Not. R. Astron. Soc.* **148**, 93–102 (1970).
- C. A. Balanis, *Advanced Engineering Electromagnetics* (Wiley, 1989).



21. A. Helaly, E. A. Soliman, and A. A. Megahed, "Electromagnetic waves scattering by nonuniform plasma cylinder," *IEEE Proc-Microw. Antennas Propag.* **144**, 61–66 (1997).
22. E. Shamonina, V. A. Kalinin, K. H. Ringhofer, and L. Solymar, "Imaging, compression and Poynting vector streamlines with negative permittivity materials," *Electron. Lett.* **37**, 1243–1244 (2001).
23. S. Feng, M. Elson, and P. Overfelt, "Transparent photonic band in metalodielectric nanostructures," *Phys. Rev. B* **72**, 085117 (2005).
24. C. J. Zapata-Rodríguez, D. Pastor, M. T. Caballero, and J. J. Miret, "Diffraction-managed superlensing using plasmonic lattices," *Opt. Commun.* **285**, 3358–3362 (2012).
25. D. Torrent and J. Sánchez-Dehesa, "Radial wave crystals: radially periodic structures from anisotropic metamaterials for engineering acoustic or electromagnetic waves," *Phys. Rev. Lett.* **103**, 064301 (2009).
26. H. Kettunen, H. Wallén, and A. Sihvola, "Tailoring effective media by Mie resonances of radially-anisotropic cylinders," *Photonics* **2**, 509–526 (2015).
27. P. Yeh, *Optical Waves in Layered Media* (Wiley, 1988).
28. S. A. Ramakrishna, J. B. Pendry, M. C. K. Wiltshire, and W. J. Stewart, "Imaging the near field," *J. Mod. Opt.* **50**, 1419–1430 (2003).
29. D. E. Aspnes, "Plasmonics and effective medium theory," in *Ellipsometry at the Nanoscale*, M. Losurdo and K. Hingerl, eds. (Springer, 2013), pp. 203–224.
30. C. Díaz-Aviñó, M. Naserpour, and C. J. Zapata-Rodríguez, "Tunable scattering cancellation of light using anisotropic cylindrical cavities," *Plasmonics*, to be published (2016).
31. J. Elser, V. A. Podolskiy, I. Salakhutdinov, and I. Avrutsky, "Nonlocal effects in effective-medium response of nanolayered metamaterials," *Appl. Phys. Lett.* **90**, 191109 (2007).
32. H. L. Chen and L. Gao, "Anomalous electromagnetic scattering from radially anisotropic nanowires," *Phys. Rev. A* **86**, 033825 (2012).
33. J. Wang, T. Zhan, G. Huang, P. K. Chu, and Y. Mei, "Optical microcavities with tubular geometry: properties and applications," *Laser Photonics Rev.* **8**, 521–547 (2014).

## 1. Introduction

The rapid theoretical and experimental advancement in nanomaterials during the last two decades has enabled to engineer multifunctional devices for the control of light with unprecedented proficiency. For instance, some schemes which are mostly based on transformation optics allow the isolation of a region from interaction with an external light that, in addition, remains unperturbed far from the shadowed space [1–3]. Consequently, an outside observer cannot detect any target placed inside the cloak by means of an electromagnetic wave field. However, such cloaking devices are commonly subject to stringent conditions like the need of materials with exotic electromagnetic parameters reducing their applicability to specific frequencies. Alternatively we may turn a nanoparticle to be *invisible* by integrating some nanostructured element like ultrathin coatings and metasurfaces in such a way that scattering of the arrangement is much reduced in comparison with the bare object [4–10]. In this case, light indeed interacts with the nanocomposite, but scattering from different elements interferes destructively to almost cancel the total scattered signal.

The origin of such scattering drop, thus reducing dramatically the overall visibility of the scatterer, may be attributed to different aspects of the light-matter interaction. For instance, the local polarizability of distinct components of a moderately sized object with opposite signs may be canceled out in a proper designed configuration [4–6]. The polarization vector in the elementary materials is anti-parallel with respect to each other, implying that a dipole moment of opposite phase is induced. Another approach for the cancellation of scattering from an engineered scatterer is based on the properties of the characteristic lineshape of the Fano resonance, where the emission of electromagnetic waves by the object create the interference between the nonresonant scattering from the particle and scattering by narrow Mie modes [11]. This effect has also been observed in high-index nanoparticles without additional coating layers [12]. Of particular interest follows the inclusion of epsilon-near-zero shells in the spectral range of interest, which may lead to a significant drop of the scattering spectrum and, in addition, create a shielding effect in the bounded space [7]. For scatterers with cylindrical symmetry (along the  $z$  axis) and composed of dielectric and plasmonic materials, the effect of opposite

polarizabilities is mostly observed in  $TM^z$ -polarized wave fields, whereas Fano resonances may be simply utilized in  $TE^z$  polarization configurations.

Recently, a multilayered metallodielectric nanotube with radially-periodic structure has been proposed, which presents a tunable spectral band with significant reduction of its scattering efficiency [13]. Such scattering cancellation is produced simultaneously for both polarizations and occurs when one of the components of the permittivity tensor characterizing the effective anisotropy of the metamaterial approaches zero, that is near the boundary of the hyperbolic regime [14]. Particularly for  $TE^z$ -polarized fields, a large birefringence of the nanoshell enables a self-guiding effect along the radial direction that is applied to validate the observed scattering reduction.

In this work we extend the previous idea of employing radially-periodic metal-dielectric nanotubes to optimize the scattering cancellation of the nanocavity. For that purpose, we introduce a new degree of freedom that concerns the marginal layers set by the side of the core and the environment medium, the latter playing a critical role primarily in the presence of metamaterial nonlocalities [15]. We also present a critical discussion on the predominant causes leading to such invisibility effect. The estimation of our results is performed using the full-wave Lorenz-Mie method [16], and a matrix formulation is developed in order to further simplify the evaluation of the scattering efficiency, which presents some similarities to the transfer matrix formalism previously implemented in stratified plane metamaterials [17]. In fact, the later formulation might be applied to any complex multilayered cylindrical scatterer composed of homogeneous and isotropic materials.

## 2. The transfer matrix formulation

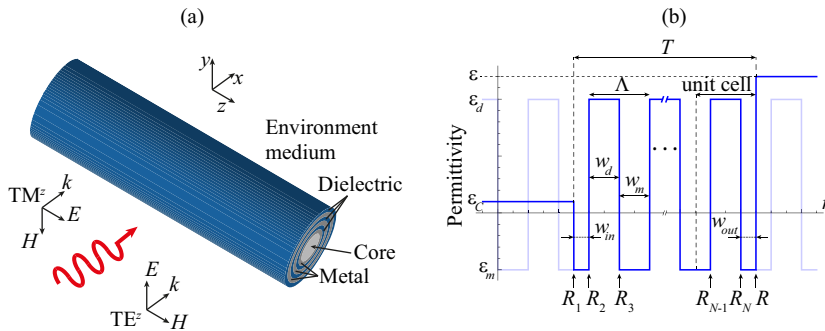


Fig. 1. (a) Illustration of the coaxial multilayered metamaterial forming the infinitely-long nanotube. (b) Permittivity function of our scatterer with radially periodic variation,  $\epsilon(r) = \epsilon(r + \Lambda)$ , and designer marginal layers.

Let us consider a cylindrical shell formed by a multilayered metal-dielectric nanostructure, as illustrated in Fig. 1. The nanotube, which has a radius  $R (= R_{N+1})$ , is composed of  $N$  layers with a shell thickness given by  $T = R_{N+1} - R_1 < R$ . The relative permittivities of the metal  $\epsilon_m$  and the dielectric  $\epsilon_d$  determine the permittivity distribution of the metamaterial along the radial direction,  $\epsilon(r)$ . In this study we consider a periodic distribution,  $\epsilon(r) = \epsilon(r + \Lambda)$  within the nanotube, where the period  $\Lambda = w_m + w_d$  includes the width of the metal and the width of the dielectric. In particular, the permittivity  $\epsilon_m$  is complex valued, thus taking into account losses in the metal. Here we examined nanotubes with a core material of permittivity  $\epsilon_c$  and immersed in an environment medium of dielectric constant  $\epsilon$ .

To estimate analytically the scattering efficiency of the multilayered nanocavity, we followed the Lorenz-Mie scattering method given in detail for instance in Refs. [18, 19]. Following previously well-established algebraic treatments of plane multilayered photonic structures [17], here we propose a transfer-matrix formalism enabling a fast evaluation of the scattering (and potentially extinction) cross section of an infinitely-long cylindrical scatterer composed of a large number of layers.

In this section we assume that the nanotube is illuminated by a  $\text{TM}^z$  plane wave propagating along the  $x$  axis, as illustrated in Fig. 1. Let us point out that the case of  $\text{TE}^z$  incident wave fields might be simply determined by means of the duality principle [20]. The electric field of the incident plane wave may be set as

$$\mathbf{E}_{in} = \hat{z}E_0 \exp(ikx) = \hat{z}E_0 \sum_{n=-\infty}^{+\infty} i^n J_n(kr) \exp(in\phi), \quad (1)$$

where  $r$  and  $\phi$  are the radial and azimuthal cylindrical coordinates, respectively,  $E_0$  is a constant amplitude,  $J_n(\cdot)$  is the Bessel function of the first kind and order  $n$ ,  $k = k_0\sqrt{\epsilon}$  and  $k_0 = \omega/c$  is the wavenumber in the vacuum. In Eq. (1) we used the Jacobi-Anger expansion of a plane wave in a series of cylindrical waves. The scattered electric field in the environment medium,  $r > R$ , may be set as [16]

$$\mathbf{E}_{sca} = -\hat{z}E_0 \sum_{n=-\infty}^{+\infty} a_n i^n H_n^{(1)}(kr) \exp(in\phi), \quad (2)$$

where  $H_n^{(1)}(\cdot) = J_n(\cdot) + iY_n(\cdot)$  is the Hankel function of the first kind and order  $n$ , and the coefficients  $a_n$  must be determined. The total electric field in the environment medium is simply  $\mathbf{E}_{tot} = \mathbf{E}_{in} + \mathbf{E}_{sca}$ . In a given layer of the nanostructured shell (medium  $q$ ),  $R_q < r < R_{q+1}$ , where  $q = \{1, 2, \dots, N\}$ , the electric field may be expressed analytically as [16]

$$\mathbf{E}_q = \hat{z}E_0 \sum_{n=-\infty}^{+\infty} i^n [b_{n,q} J_n(k_q r) + c_{n,q} Y_n(k_q r)] \exp(in\phi), \quad (3)$$

where the wavenumber  $k_q = k_0\sqrt{\epsilon_d}$  for a dielectric layer, and  $k_q = k_0\sqrt{\epsilon_m}$  for a metallic layer. Finally, the electric field in the core of the multilayered tube ( $r < R_1$ ) is expressed as

$$\mathbf{E}_C = \hat{z}E_0 \sum_{n=-\infty}^{+\infty} i^n d_n J_n(k_C r) \exp(in\phi), \quad (4)$$

where the wavenumber  $k_C = k_0\sqrt{\epsilon_C}$ .

The Lorenz-Mie scattering coefficients  $a_n$ ,  $b_{n,q}$ ,  $c_{n,q}$ , and  $d_n$ , are determined by means of the proper boundary conditions, that is, continuity of (the  $z$ -component of) the electric field and the  $\phi$ -component of the magnetic field,  $H_\phi = (i/\omega)\partial_r E_z$ , established at the environment-multilayered medium interface given at  $r = R$  and at internal interfaces set at  $r = R_1$  (boundary with the core) and  $r = R_{q+1}$  ( $q < N$ ). In particular, the boundary conditions applied at  $r = R_{q+1}$  may be set in matrix form as [21]

$$D_{n,q}(R_{q+1}) \cdot \begin{bmatrix} b_{n,q} \\ c_{n,q} \end{bmatrix} = D_{n,q+1}(R_{q+1}) \cdot \begin{bmatrix} b_{n,q+1} \\ c_{n,q+1} \end{bmatrix}, \quad (5)$$

where the *dynamical* matrix

$$D_{n,m}(x) = \begin{bmatrix} J_n(k_m x) & Y_n(k_m x) \\ Z_m^{-1} J_n'(k_m x) & Z_m^{-1} Y_n'(k_m x) \end{bmatrix} \quad (6)$$

is given in terms of the reduced impedance  $Z_q = 1/\sqrt{\epsilon_m}$  ( $Z_q = 1/\sqrt{\epsilon_d}$ ) for the metallic (dielectric)  $m = q$  layer, and  $Z_C = 1/\sqrt{\epsilon_C}$  for the core,  $m = C$ . Here the prime appearing in  $J'_n(\alpha)$  and  $Y'_n(\alpha)$  denotes derivative with respect to the variable  $\alpha$ . Note that  $D_{n,m}$  is a real-valued matrix provided that the permittivity of the medium  $m$  is also real. By applying the boundary conditions at  $r = R$  we may write

$$D_{n,N}(R) \cdot \begin{bmatrix} b_{n,N} \\ c_{n,N} \end{bmatrix} = D_{n,N+1}(R) \cdot \begin{bmatrix} 1 - a_n \\ -ia_n \end{bmatrix}, \quad (7)$$

where, in this case, we set  $Z_{N+1} = 1/\sqrt{\epsilon}$  and  $k_{N+1} = k$ .

Importantly, we may estimate the fields in the core space and outside the nanotube without calculating the fields in the anisotropic medium by means of the following matrix equation:

$$\begin{bmatrix} d_n \\ 0 \end{bmatrix} = M_n \cdot \begin{bmatrix} 1 - a_n \\ -ia_n \end{bmatrix}, \quad (8)$$

where the matrix

$$\begin{aligned} M_n &= \begin{bmatrix} M_{n,11} & M_{n,12} \\ M_{n,21} & M_{n,22} \end{bmatrix} \\ &= [D_{n,C}(R_1)]^{-1} \cdot \left\{ \prod_{q=1}^N D_{n,q}(R_q) \cdot [D_{n,q}(R_{q+1})]^{-1} \right\} \cdot D_{n,N+1}(R). \end{aligned} \quad (9)$$

By using this transfer matrix formalism, it is possible to evaluate analytically the scattering coefficient

$$a_n = \frac{M_{n,21}}{M_{n,21} + iM_{n,22}}, \quad (10)$$

which provide the estimation of the scattering efficiency as [16]

$$Q_{sca} = \frac{2}{kR} \sum_{n=-\infty}^{+\infty} |a_n|^2. \quad (11)$$

The invisibility condition is established provided that the scattering coefficients  $a_n$  (or alternatively  $M_{n,21}/M_{n,22}$ ) arrive simultaneously to a value near zero.

### 3. Optimization procedure

In this study we propose a multilayered metal-dielectric nanotube following a periodic distribution along the radial coordinate. The basic arrangement consisting of alternating metallic and dielectric layers of widths  $w_m$  and  $w_d$ , respectively, was recently introduced by Kim *et al* in Ref. [13]. As a new degree of freedom, we utilize a unit cell within which one of the layers may be surrounded by a second material, and consequently its associated layer must be split into two as illustrated in Fig. 1(b). Due to the periodicity of the nanostructure, the internal radial distribution remains unaltered displaying a cycle length  $\Lambda = w_m + w_d$ , and only the marginal layers may change. We point out that the marginal layers within a stratified plane nanostructure demonstrate a key role for instance in superlensing [22–24]. Finally, the integer  $T/\Lambda$  provides the number of periods found in the nanotube.

In order to characterize the inmost marginal layer of width  $w_{in} = R_2 - R_1$  and the outermost marginal layer of width  $w_{out} = R_{N+1} - R_N$ , we define the factor  $m$  ranging from -1 to +1. Positive values of  $m$  stands for dielectric layers set on the interior and exterior sides of the nanotube. In this case, by writing  $w_{in} = (1 - m)w_d$  and  $w_{out} = mw_d$ , providing  $w_{in} + w_{out} = w_d$ , we also include the extreme value  $m = +1$  taking into account a full dielectric outermost layer and

$m = 0$  referring to a full dielectric inmost layer. Following an equivalent rule,  $m < 0$  is applied to metallic marginal layers, where  $w_{in} = -mw_m$  and  $w_{out} = (1+m)w_m$ . In the limit  $m = -1$  we consider a full metallic inmost layer, formally the same case accounted for  $m = +1$ .

In the next numerical simulations we will consider nanotube shells with  $T/\Lambda = 3$  periods, that is a total number  $N = 7$  layers provided that  $0 < |m| < 1$ . We examine silver and TiO<sub>2</sub> layers, which permittivities may be analytically approximated within the visible range of frequencies by

$$\epsilon_m(\lambda) = 3.691 - \frac{9.152^2}{(1.24/\lambda)^2 + i0.021(1.24/\lambda)}, \quad (12)$$

and

$$\epsilon_d(\lambda) = 5.193 + \frac{0.244}{\lambda^2 - 0.0803}, \quad (13)$$

respectively [13]. In the previous equations, the working wavelength  $\lambda$  is set in micrometers.

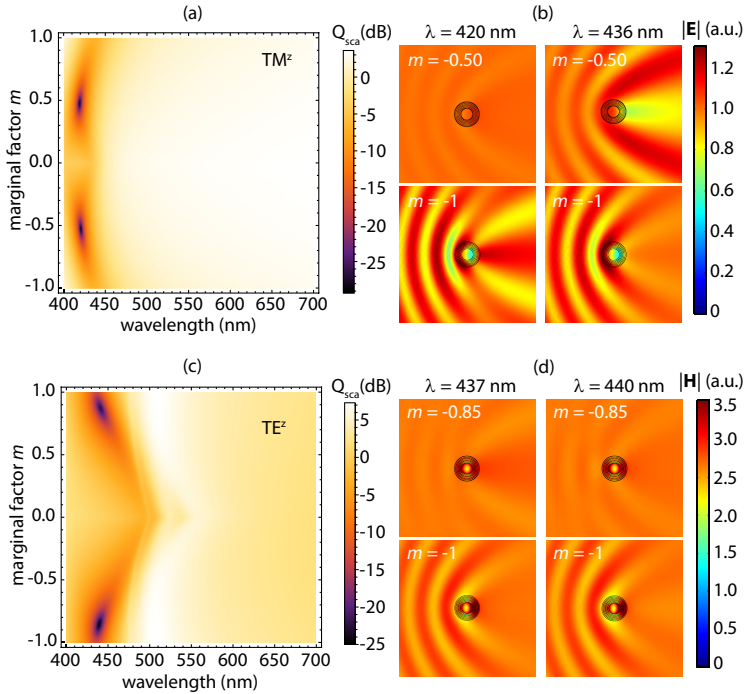


Fig. 2. Scattering efficiency  $Q_{sca}$  of a periodic Ag-TiO<sub>2</sub> nanotube immersed in air with inmost radius  $R_1 = 50$  nm, thickness  $T = 60$  nm, period  $\Lambda = 20$  nm, and metal filling fraction  $f = 0.5$ , when varying the marginal parameter  $m$ . The incident plane wave is: (a)-(b) TM<sup>z</sup> polarized, and (c)-(d) TE<sup>z</sup> polarized. In (b) and (d) we compare the scattered wave fields of the nanocavities under optimal marginal configurations here analyzed (top scatterer) with the nanotubes proposed in [13] (bottom scatterer) for different wavelengths.

For the sake of illustration, in Fig. 2 we plot the efficiency spectrum  $Q_{sca}$ , for wavelengths in the visible, of a nanotube which inmost radius is  $R_1 = 50$  nm and thickness  $T = 60$  nm. The

scattering efficiency is evaluated using Eq. (11) and the transfer-matrix formulation developed above. For TE<sup>z</sup>-polarized wave fields, the dynamical matrices given in Eq. (6) should include the transformation  $Z_m^{-1} \rightarrow Z_m$  in agreement with the duality principle [20]. We initially assume a metallic layer width of  $w_m = 10$  nm and also a dielectric of width  $w_d$  equal to 10 nm, so the metal filling fraction  $f = w_m/(w_m + w_d)$  yields 0.5. The nanotube is immersed in air, where  $\epsilon_C = 1$  and also  $\epsilon = 1$ . For TM<sup>z</sup> polarized wave fields, two local minima in the scattering efficiency are found, as shown in Fig. 2(a): a first minimum  $Q_{sca} = 1.40 \times 10^{-3}$  for the marginal factor  $m = -0.53$  at  $\lambda = 421$  nm, in which case the inmost and outermost silver layers approximately have a width of 5 nm each one, and a second minimum  $Q_{sca} = 1.20 \times 10^{-3}$  for  $m = 0.48$  at  $\lambda = 419$  nm, where the inmost and outermost layers are made of titanium dioxide and also have a thickness of around 5 nm. This represents a substantial improvement of two orders of magnitude with respect to the case  $m = -1$  analyzed in Ref. [13], where the minimum in efficiency  $Q_{sca} = 0.21$  is found at  $\lambda = 436$  nm. Fig. 2(b) shows the electric field scattered by two nanocavities, one with  $m = -0.5$  and the other one with  $m = -1$ , at the wavelengths of interest. It is demonstrated that our nanocavity with half-width marginal layers exhibits an extraordinary effect of invisibility ( $Q_{sca} = 2.15 \times 10^{-3}$ ) at the designer wavelength of  $\lambda = 420$  nm, and in addition has a similar behavior ( $Q_{sca} = 0.27$ ) compared with the previously proposed nanotube at its best performance wavelength given at  $\lambda = 436$  nm.

In the case that the incident field is a TE<sup>z</sup>-polarized plane wave, the resultant scattering efficiency of the nanotubes varies considerably as shown in Fig. 2(c). It is worth noting the nearly symmetric response of  $Q_{sca}$  with respect to the sign of the factor  $m$ , providing an analogous spectrum when the marginal layers are made of either TiO<sub>2</sub> or silver, independently of the modal polarization under consideration. Now the minima are found for a marginal factor  $m = -0.85$  at  $\lambda = 440$  nm, where  $Q_{sca} = 3.02 \times 10^{-3}$ , and for  $m = 0.86$  giving  $Q_{sca} = 5.47 \times 10^{-3}$  at  $\lambda = 442$  nm. Note that Kim *et al* reported a scattering cancellation effect giving  $Q_{sca} = 5.30 \times 10^{-2}$  at  $\lambda = 437$  nm, when we take into account 6 layers and the inmost layer is made of silver ( $m = -1$ ). Again, our approach provides a remarkable decrease in scattering efficiency, as illustrated in Fig. 2(d) comparing the wave fields scattered by those two nanocylinders ( $m = -0.85$  on the top and  $m = -1$  on the bottom) set together.

#### 4. Discussion

The interpretation of such significant reduction in scattering may be carried out, at least partially, in terms of the effective medium theory. For sufficiently narrow slabs ( $\Lambda \ll \lambda$ ), a radially form birefringence may be established for the metamaterial composed of concentric multilayers [25, 26]. In this case, TM<sup>z</sup>-polarized fields behave like ordinary waves propagating in a uniaxial crystal with optic axis set along the radial coordinate [27]. Waves propagate through the metallodielectric metamaterial with negligible variation of the electric field  $E_z$ , a fact that in addition is in agreement with the electrostatic limit. However, the electric displacement  $\mathbf{D} = D_z \hat{z}$  undergoes critical discontinuities at the metal-dielectric interfaces. In average,  $D_z$  decreases when the metal filling fraction grows, even vanishing in the so-called epsilon-near-zero regime, due to the negative value of the real part of  $\epsilon_m$  [28]. The  $z$ -component of the effective permittivity of the layered metamaterial may be estimated accordingly as

$$\langle \epsilon_z \rangle = \frac{\int \epsilon(r) E_z(r, \phi) r dr d\phi}{\int E_z(r, \phi) r dr d\phi} \approx \frac{2}{(R^2 - R_1^2)} \int_{R_1}^R \epsilon(r) r dr. \quad (14)$$

The definition of the weight averaged  $\epsilon(r)$  is intuitive, and refined analyses may be found elsewhere [29]. On the other hand, TE<sup>z</sup>-polarized fields propagate inside the multilayered metamaterial in the same manner as extraordinary waves, where the radial anisotropy is characterized by an average permittivity of components  $\langle \epsilon_\phi \rangle$  (that coincides with  $\langle \epsilon_z \rangle$ ) and  $\langle \epsilon_r \rangle$ , the latter taking much higher values than the former [13].

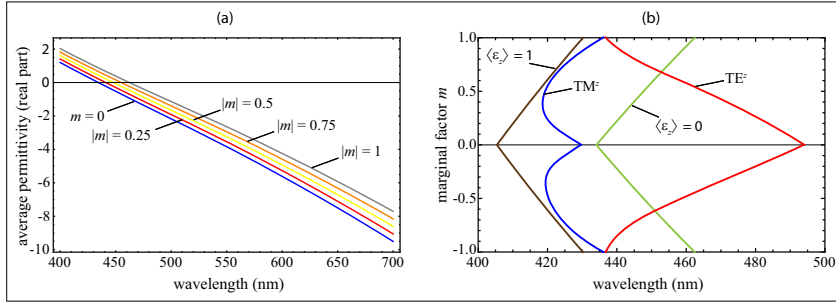


Fig. 3. (a) Real part of the average permittivity  $\langle \epsilon_z \rangle$  defined in Eq. (14) for an Ag-TiO<sub>2</sub> multilayered nanocavity with inmost radius  $R_1 = 50$  nm, thickness  $T = 60$  nm, period  $\Lambda = 20$  nm, and metal filling fraction  $f = 0.5$ . The values of the iso-permittivity curves  $\langle \epsilon_z \rangle = 0$  and  $\langle \epsilon_z \rangle = 1$  are represented in (b) together with the minima in scattering efficiency found in Fig. 2(a) for TM<sup>z</sup> (blue solid line) and Fig. 2(c) for TE<sup>z</sup> (red solid line).

Equation (14) yields exactly the well-known expression  $\epsilon_{\perp} = f\epsilon_m + (1-f)\epsilon_d$ , associated with the component along the perpendicular direction of the optic axis of the permittivity tensor  $\underline{\epsilon}$ , in a Cartesian coordinate system, of a form-birefringent metamaterial [27], only in the particular case that  $m = \pm 1/2$ , that is for half-width marginal layers. Otherwise, the average permittivity  $\langle \epsilon_z \rangle$  critically depends on the inmost radius  $R_1$  and the marginal parameter  $m$ ; only when the shell is sufficiently narrow,  $T \ll R$ , enabling the limit  $R_1 \rightarrow R$ , the average permittivity reduces to  $\langle \epsilon_z \rangle \rightarrow \epsilon_{\perp}$  in all cases. On the other hand, further symmetries may be found when the definition of the average permittivity given in Eq. (14) is applied to a metal-dielectric periodic nanocavity. In particular,  $\langle \epsilon_z \rangle$  depends on the absolute value of the marginal parameter  $m$ . Since the scattering spectra shown in Figs. 2(a) and 2(c) also exhibit such a symmetry, we potentially may establish a correlation of the location of spectral peaks and valleys in terms of the average permittivity.

In Fig. 3(a) we plot the real part of the average permittivity  $\langle \epsilon_z \rangle$  evaluated in an Ag-TiO<sub>2</sub> cylindrical cavity with inmost radius  $R_1 = 50$  nm, thickness  $T = 60$  nm, period  $\Lambda = 20$  nm, metal filling fraction  $f = 0.5$ , and varying marginal factor  $m$ . The average permittivity increases for higher  $|m|$  and reaches its maximum value at  $|m| = 1$  for the whole spectral range. For instance, the condition  $\text{Re}\langle \epsilon_z \rangle = 1$ , where the average permittivity of the multilayered nanotube matches the permittivity of the core and the environment medium, is attained at  $\lambda = 405$  nm for  $m = 0$  and shifts to longer wavelengths for different marginal factors up to  $\lambda = 430$  nm for  $|m| = 1$ . As illustrated in Fig. 3(b), such permittivity matching is behind the invisibility effect observed when the incident plane wave is TM<sup>z</sup> polarized, at least for moderate (and high)  $|m|$  for which  $Q_{sca}$  presents its minima in efficiency. In the near-optimal case where  $m = 0.5$ ,  $\text{Re}\langle \epsilon_z \rangle = 1$  is attained at  $\lambda = 417$  nm, very close to the dip shown in Fig. 2(a) at  $\lambda = 419$  nm. However, the effective medium approximation evidences remarkable limitations. For instance, there exists critical deviations of the condition  $\text{Re}\langle \epsilon_z \rangle = 1$  and the loci of minima in  $Q_{sca}$  for low  $|m|$ . More importantly, it cannot predict the extraordinary scattering reduction for marginal factors around  $|m| = 0.5$ , in comparison with other configurations.

The scene is even more intricate for scattered fields under TE<sup>z</sup> polarization. The minima of the spectral scattering are blue-shifted along with higher values of  $|m|$ , just advancing to the opposite direction with respect to any iso-permittivity curve with invariant  $\langle \epsilon_{\phi} \rangle (= \langle \epsilon_z \rangle)$ . Such severe deviations then put into question the validity of the effective medium theory as an appropriate approach to describe the invisibility effect observed here. Specifically at the

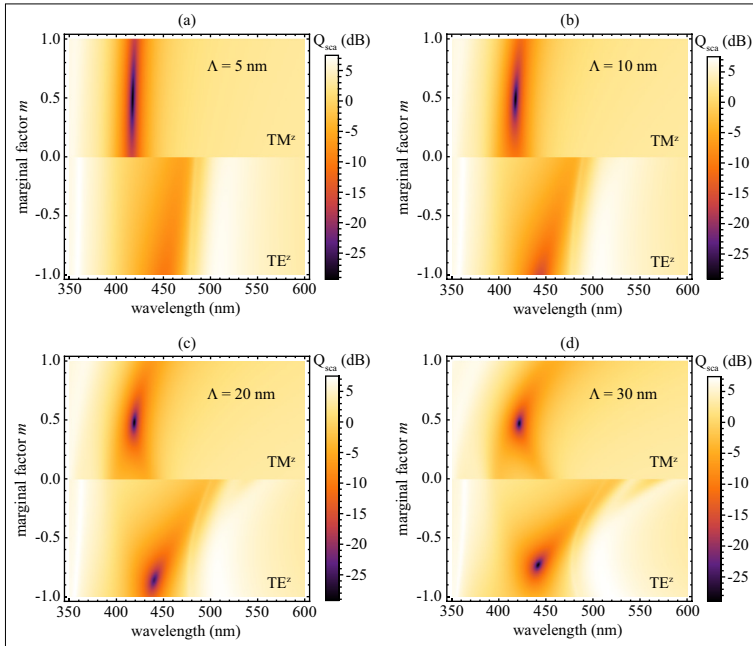


Fig. 4. Scattering efficiency of an Ag-TiO<sub>2</sub> nanotube with  $R_1 = 50$  nm,  $T = 60$  nm,  $f = 0.5$ , and varying marginal factor  $m$ , considering a period  $\Lambda$  of (a) 5 nm ( $N = 25$  layers), (b) 10 nm ( $N = 13$ ), (c) 20 nm ( $N = 7$ ) and (c) 30 nm ( $N = 5$ ). Profiting from the symmetric response of  $Q_{sca}$  on the sign of  $m$ , we represent the scattering spectrum for TM<sup>z</sup>-polarized waves at  $m > 0$  and for TE<sup>z</sup>-polarized fields at negative marginal factors.

minimum  $Q_{sca} = -25.2$  dB found at  $\lambda = 440$  nm for  $m = -0.85$ , the effective permittivity rises to  $\text{Re}\langle\epsilon_\phi\rangle = 0.437$ . In practical terms, we might affirm that the invisibility regime is established for marginal factors in the range  $0.7 \leq |m| \leq 1$  occurring in the spectral band that satisfies  $0 \leq \text{Re}\langle\epsilon_\phi\rangle \leq 1$ .

Let us point out that, in one side, the existence of a peak near the scattering minimum in every spectra for this specific polarization suggests the occurrence of an isolated Fano resonance [30]. As a consequence of the resonant mechanism of invisibility, it is expected a dramatic impact on external factors such as the permittivity of the core and the environment medium, and also structural aspects such as scale and internal architecture of the nanocavity. On the other hand, nonlocalities that are inherent in metal-dielectric nanostructures, specially under TE<sup>z</sup> polarization [31], lead for instance to edge effects that seems to be behind an anomalous behavior out of the long-wavelength approximation, as highlighted in Ref. [15].

We may obtain further and revelatory conclusions by evaluating the scattering efficiency of our Ag-TiO<sub>2</sub> nanotube of  $T = 60$  nm for different number of periods. In Fig. 4 we graphically represent the spectrum of  $Q_{sca}$  for nanotubes with  $T/\Lambda = 2, 3, 6$  and 12 periods. For the smallest period,  $\Lambda = 5$  nm, the marginal factor  $m$  has a limited influence on the scattering spectrum. For TM<sup>z</sup>-polarized wave fields, the minimum of scattering efficiency reaches  $Q_{sca} = 1.17 \times 10^{-3}$  at  $\lambda = 417$  nm. On the other hand, the scattering efficiency rises significantly when the



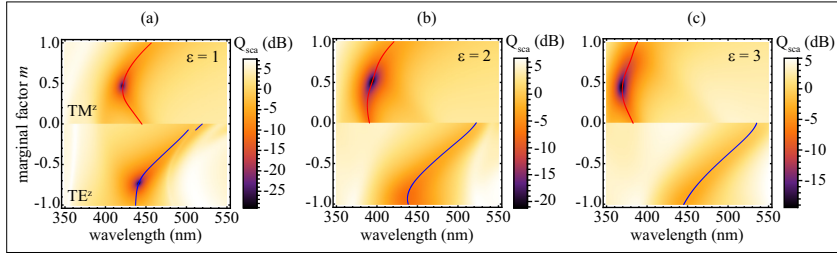


Fig. 5. Scattering efficiency of an Ag-TiO<sub>2</sub> nanotube with  $R_1 = 50$  nm,  $T = 60$  nm,  $\Lambda = 30$  nm,  $f = 0.5$ , and varying marginal factor  $m$ . The core and environment medium have a permittivity: (a)  $\epsilon_C = \epsilon = 1$ , (b)  $\epsilon_C = \epsilon = 2$ , and (c)  $\epsilon_C = \epsilon = 3$ . The red and blue solid lines indicate the wavelengths at which  $Q_{sca}$  reaches a minimum for nanotubes of different  $m$  when incident light is TM<sup>z</sup> and TE<sup>z</sup> polarized, respectively.

polarization of the incident plane wave is TE<sup>z</sup>, for which a minimum value of  $Q_{sca} = 8.99 \times 10^{-2}$  at  $\lambda = 451$  nm, representing a difference of nearly two orders of magnitude. Note that such nanostructure embodies a technological challenge since it takes into account a large number of Ag and TiO<sub>2</sub> layers, each one with a layer width of 2.5 nm. As might be expected, the long-wavelength approximation is valid in this case, and the nanotube might be considered as a radially-anisotropic medium. For instance, provided that the calculations were carried out by using the Lorenz-Mie scattering method for radially-anisotropic cylinders [30,32], considering a TE<sup>z</sup> incident plane wave, the minimum efficiency yields  $Q_{sca} = 0.172$  which is found at  $\lambda = 459$  nm, in which case  $\text{Re}(\epsilon_{\perp}) = -0.36$  and  $\text{Re}(\epsilon_{\parallel}) = 151$  [13,15].

When the period increases to  $\Lambda = 10$  nm, the impact of the marginal factor is evident as a direct result of nonlocal effects. In this case, the minimum efficiency for TM<sup>z</sup>-polarized fields,  $Q_{sca} = 1.22 \times 10^{-3}$ , is attained at  $\lambda = 417$  nm (for  $m = 0.5$ ), manifesting a negligible variation in comparison with the previous case. For TE<sup>z</sup> polarization, the invisibility effect clearly improves in the limiting marginal factor  $m = -1$ , for which minimum scattering efficiency  $Q_{sca} = 2.60 \times 10^{-2}$  got at  $\lambda = 443$  nm. On the other extreme, when the period  $\Lambda = 30$  nm, the minima in scattering efficiency are of the same order for both polarizations. For TM<sup>z</sup>-polarized fields we have a minimum  $Q_{sca} = 1.43 \times 10^{-3}$  at  $\lambda = 422$  nm and  $m = 0.48$ , whereas for TE<sup>z</sup> polarization the minimum  $Q_{sca} = 1.28 \times 10^{-3}$  is found at  $\lambda = 441$  nm for  $m = -0.72$ , providing a good performance in the first case and the best invisibility behavior in the latter. In addition, this sort of nanotube with the longest period manifests certain advantages from the practical point of view, such as the reduced number of layers (only 5) with widths of 15 nm except for the margins. As a consequence, from now on we consider Ag-TiO<sub>2</sub> nanotubes of a period  $\Lambda = 30$  nm. We point out that stratified nanotubes with a period higher than  $\Lambda = 5$  nm cannot be treated as a mono-layered hyperbolic nanocavity where Mie scattering theory for anisotropic shell objects should be accurate [13,30], and consequently the more elaborated matrix formalism given above is apparently unavoidable.

The influence of cores and environment media with different permittivities is examined in Fig. 5, for the same Ag-TiO<sub>2</sub> nanotube described above. For brevity we analyzed the case where the dielectric constants  $\epsilon_C$  and  $\epsilon$  have the same value, since dissimilar permittivities may lead to a loss of the invisibility effect [13]. For TM<sup>z</sup>-polarized incident light, a dramatic drop in the scattering efficiency is again observed but at lower wavelengths when the permittivity  $\epsilon$  (and  $\epsilon_C$ ) increases. In fact, to find the minimum of  $Q_{sca}$ , the index matching condition may be established as  $\text{Re}(\epsilon_z) = \epsilon$  in agreement with the shift undergone by the invisibility wavelength at every marginal factor, that is an extremely accurate approach for moderate and high  $|m|$ .

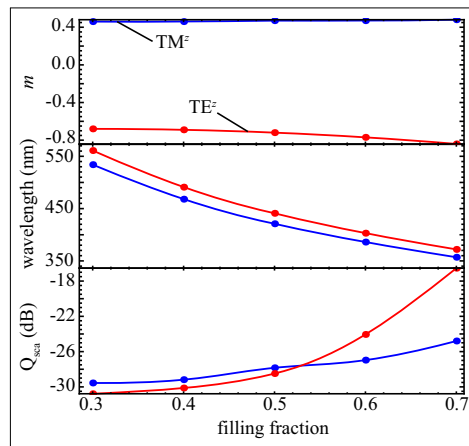


Fig. 6. Optimal marginal factor  $m$  for invisible nanotubes with  $R_1 = 50$  nm,  $T = 60$  nm,  $\Lambda = 30$  nm, and different metal filling fraction  $f$ . The blue solid line corresponds to nanotubes oriented along the electric field of the incident plane wave, whereas the red solid line refers to TE<sup>z</sup>-polarized scattered fields. We also indicate the minimum scattering efficiency  $Q_{sca}$  reached for such optimal configuration, expressed in dB, and the wavelength  $\lambda$  for which the latter is achieved.

The lower difference between the permittivity of the dielectric part of the metamaterial and that of the external material,  $\epsilon_d$  and  $\epsilon$  respectively, requires of a metal with a permittivity also approaching  $\epsilon$  which occurs closer to the plasma frequency [4]. Importantly, the optimal geometrical configuration is found for a marginal factor  $|m|$  around 0.5 in all cases. As an example, a minimum of  $Q_{sca} = 1.14 \times 10^{-2}$  is found at  $\lambda = 370$  nm for  $m = 0.441$  when the permittivity of the environment medium is set as  $\epsilon = 3$ .

On the other hand, the scattering efficiency dramatically increases for TE<sup>z</sup>-polarized wave fields. The loci of minima in  $Q_{sca}$  practically remain in the same spectral band, slightly shifted to longer wavelengths at higher-index core and environment medium, demonstrating a high robustness under changes in the permittivity  $\epsilon$ . However, their efficiencies increase several orders of magnitude. Taking  $\epsilon = 3$  for instance,  $Q_{sca} = 0.435$  is the minimum efficiency which is found at  $\lambda = 449$  nm and  $m = -0.935$ . The wavelengths where minima of  $Q_{sca}$  are located for TE<sup>z</sup>-polarized fields seem to be essentially determined by the optogeometrical characteristics of the nanocavity thus being barely unaltered under changes in the environment; however, this is not longer valid for exceptionally-higher values of the index of refraction and significant deviations might be found [30]. This confirms the resonant behavior of the invisibility effect sustained in TE<sup>z</sup>-polarized wave fields, differently from what occurs for scattered TM<sup>z</sup>-polarized waves

In Fig. 6 we consider nanotubes of different metal filling fractions  $f = w_m/\Lambda$ , but maintaining a nanostructure of period  $\Lambda = 30$  nm; again the inmost radius  $R_1 = 50$  nm and the nanotube thickness  $T = 60$  nm, but the marginal factor  $m$  is varied to minimize the scattering efficiency. A permittivity of unity is set for the core and environment medium in the estimation of  $Q_{sca}$ . The invisibility wavelength in the optimal configuration decreases 200 nm approximately, for both polarizations concurrently, when  $f$  varies between 0.3 and 0.7. This fact suggests a means of tuning the invisibility spectral band of the multilayered scatterers [13]. For TM<sup>z</sup>-polarized scattered fields, the undertaken optimization leads to nanocylinders with marginal factors of

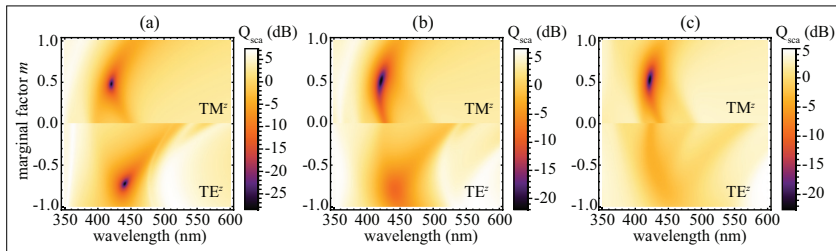


Fig. 7. The same as in Fig. 4(d), but the inmost radius  $R_1$  takes values: (a) 50 nm, (b) 100 nm, and (c) 200 nm.

modulus around 0.5, which provide scattering efficiencies below -25 dB in the range between  $f = 0.3$  and 0.7. On the other hand, the scattering efficiency is reduced to some extent when the incident plane wave is  $TE^z$  polarized, at least for the lowest values of  $f$ . This most favorable arrangement happens for nanostructures where the inmost silver layer is considerably wider than the outer layer giving marginal factors  $m$  neighboring -0.8. However,  $Q_{sca}$  cannot decrease and even reach the limit of -20 dB for the top range of filling fractions, which in principle has no critical impact in the tunability of the invisibility spectral band of the nanotubes expect maybe in ultrasensitive applications.

The size of the metallodielectric nanocavity might be essential concerning the applicability of the effective medium approximation in  $TM^z$ -polarized wave fields, and more critically the resonant behavior of the nanotube for  $TE^z$  polarization. In Fig. 7 we plot the scattering efficiency of Ag-TiO<sub>2</sub> multilayered nanoshells with different radii immersed in air. We maintain the scatterer thickness  $T = 60$  nm, period  $\Lambda = 30$  nm, metal filling fraction  $f = 0.5$ , and we change the marginal factor  $m$  in order to find the configuration with optimal scattering cancellation. For  $TM^z$  polarized fields, the plots remain practically unaltered for inmost radius ranging from  $R_1 = 50$  nm up to  $R_1 = 200$  nm. Limited deviations are attributed to the reduced dependence of  $\langle \epsilon_z \rangle$  on  $R_1$  in spite of the considerable difference in size of the cylindrical scatterers. Considering now scattered fields under  $TE^z$  polarization, the efficiency pattern is modified significantly. The minimum in scattering efficiency changes from  $Q_{sca} = 1.41 \times 10^{-3}$  for  $R_1 = 50$  nm as discussed above, increasing to  $Q_{sca} = 0.135$  for  $R_1 = 100$  nm that is found at  $\lambda = 443$  nm when  $m = -0.80$ , and reaching  $Q_{sca} = 0.446$  for  $R_1 = 200$  nm (at  $\lambda = 426$  nm and  $m = -0.43$ ). For this specific polarization, the capacity of the nanotubes for canceling the scattered wave field, within the spectral band of interest, decays progressively when the radius  $R_1$  grows certainly due to the existence of multiple localized resonances that are associated with whispering-gallery modes. On the other hand, note that for radius  $R_1$  in the micro-scale, such optical microcavities with whispering-gallery modes have stimulated multifunctional applications to optofluidic devices such as microlasers and bio/chemical sensors [33].

## 5. Conclusions

The study carried out here shows the route for the optimal utilization of the marginal layers in metal-dielectric multilayered nanotubes as invisible conducting scatterers within a tunable spectral band. We utilize the inherent nonlocal effects of metallodielectric nanostructures in support of a drastic reduction of the scattered signal of the designer cylindrical nanocavity. Our approach leads to a drop of the nanoparticle scattering efficiency that may reach up to two orders of magnitude in comparison with previous proposals also based on radially-periodic arrangements. The remarkable invisibility of our Ag-TiO<sub>2</sub> nanotube is largely ascribed to scatte-

ring cancellation for  $TM^z$ -polarized incident plane waves and a Fano-type isolated resonance for  $TE^z$ -polarized fields. The resonant behavior of the nanotubes in  $TE^z$  polarization configurations made it reducing the maximal efficiency to changes in the external environment, diameter of the nanoparticle and even the period of the metamaterial. Although the cylindrical cavity has a polarization-selective response, it can be adjusted to present a significant reduction of the scattering efficiency simultaneously for both polarizations. Furthermore, it is reasonable to conceive a refined approach enabling the ultimate minimization of the scattered signal for the  $TE^z$  and  $TM^z$  polarization concurrently. Importantly, the Lorenz-Mie scattering coefficients are set in terms of a transfer matrix formalism leading to the fast evaluation of the scattering efficiency of the multilayered nanocavity. We believe that the use of invisible conducting nanocavities for invisible electrodes and waveguides presents a promising strategy toward next-generation optofluidic and sensing.

### Acknowledgments

This work was supported by the Spanish Ministry of Economy and Competitiveness (MINECO) (TEC2014-53727-C2-1-R)

4<sup>th</sup> Publication:  
**Ultrathin High-Index Metasurfaces for  
Shaping Focused Beams**

**Authors:** Mahin Naserpour, Carlos J. Zapata-Rodríguez, Carlos  
Díaz-Aviñó, Mahdieh Hashemi and Juan J. Miret

Published in **Applied Optics**, volume 54, pages 7586-7591, year  
2015.

# Ultrathin high-index metasurfaces for shaping focused beams

MAHIN NASERPOUR,<sup>1,2</sup> CARLOS J. ZAPATA-RODRÍGUEZ,<sup>1,\*</sup> CARLOS DÍAZ-AVIÑÓ,<sup>1</sup>  
MAHDIEH HASHEMI,<sup>3</sup> AND JUAN J. MIRET<sup>4</sup>

<sup>1</sup>Department of Optics and Optometry and Vision Science, University of Valencia, Dr. Moliner 50, Burjassot 46100, Spain

<sup>2</sup>Department of Physics, College of Sciences, Shiraz University, Shiraz 71946-84795, Iran

<sup>3</sup>Department of Physics, College of Science, Fasa University, Fasa 7461781189, Iran

<sup>4</sup>Department of Optics, Pharmacology and Anatomy, University of Alicante, P.O. Box 99, Alicante, Spain

\*Corresponding author: carlos.zapata@uv.es

Received 25 May 2015; revised 27 July 2015; accepted 3 August 2015; posted 4 August 2015 (Doc. ID 241518); published 25 August 2015

The volume size of a converging wave, which plays a relevant role in image resolution, is governed by the wavelength of the radiation and the numerical aperture (NA) of the wavefront. We designed an ultrathin ( $\lambda/8$  width) curved metasurface that is able to transform a focused field into a high-NA optical architecture, thus boosting the transverse and (mainly) on-axis resolution. The elements of the metasurface are metal-insulator subwavelength gratings exhibiting extreme anisotropy with ultrahigh index of refraction for TM polarization. Our results can be applied to nanolithography and optical microscopy. © 2015 Optical Society of America

**OCIS codes:** (050.6624) Subwavelength structures; (240.6680) Surface plasmons; (350.5730) Resolution.

<http://dx.doi.org/10.1364/AO.54.007586>

## 1. INTRODUCTION

The wave nature of light imposes a fundamental constraint on the attainable spatial resolution known as the diffraction limit of light [1]. Importantly, the diffraction limit has a deep impact in far-field microscopy and data storage [2,3]. According to the Rayleigh criterion, this diffraction limit is of the order of half of the wavelength for a high numerical aperture (NA). For moderate and low NAs, the transverse resolution is directly governed by the inverse of the NA of the focusing arrangement, whereas the on-axis resolution is determined by the inverse squared of its value.

Massive efforts have been carried out in order to reach and even surpass such a limit of diffraction. Gain in the spatial resolution can be achieved by introducing diffraction filters, which tune the complex-valued pattern of the converging beam in the far field, thus molding its focal distribution [4]. A plethora of alternate ways can be found in the literature, such as structuring light used in confocal (also 4Pi-confocal) scanning microscopy [5,6], by employing stimulated emission to inhibit the fluorescence process in the outer regions of the excitation point-spread function [7], two-photon excitations, and multiphoton implementations [8], to mention a few. The use of metamaterials and metasurfaces has also come on to super-resolution since they may actively control the wave direction and even transform the evanescent nature of waves into homogeneous propagating signals [9–12].

In this work, we propose an ultrathin metasurface to efficiently modify the wavefront curvature of a given converging field. In this way, we alter the focal waves by simply increasing the NA of the optical architecture. For that purpose, the beam shaping is carried out near the focal region, thus enhancing the super-resolving effect. The elements of the metasurface will be semi-transparent metal-insulator (MI) gratings with subwavelength features exhibiting an effective high index of refraction. A simple cylindrical arrangement consisting of four of these elements with incremental dephases of  $\pi/2$  radians will satisfactorily serve our aim.

## 2. THEORY AND METHODS

Let us first consider a monochromatic converging wave field of semi-angular aperture  $\Omega$  that is focused to a point  $F$ . Without loss of generality, we will consider cylindrical waves propagating in the  $x$ - $z$  plane for which the physical problem is symmetric with respect to  $y$  axis; in addition, the magnetic field will be expressed as  $\mathbf{H} = H(x, z) \exp(-i\omega t) \hat{\mathbf{y}}$ , where  $\hat{\mathbf{y}}$  stands for the unitary vector pointing along  $y$  axis. As illustrated in Figs. 1(a) and 1(b), we place an ultrathin metasurface, in such a way that it is concentric to the wavefront of the incident converging beam at the point  $F$ . The metasurface will reshape the cylindrical wavefront of the incident beam by increasing its curvature. At the exit of the metasurface, the field is focused to a

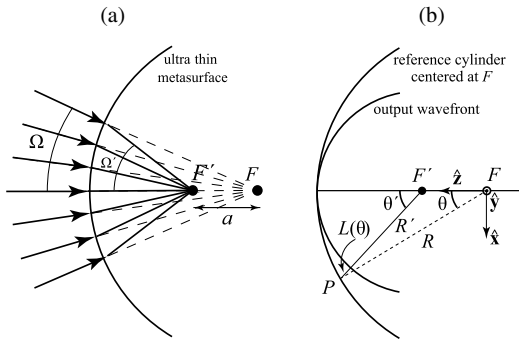


**Fig. 1.** (a) Geometrical interpretation of the beam shaping using optical rays. The focal point  $F$  of a given converging beam of semi-aperture angle  $\Omega$  will be refocused by passing through an ultrathin curved metasurface. (b) Schematic diagram of the converging-wave configuration and illustration of notation. The origin of the coordinate system is placed at the geometrical focus  $F$ , which is the center of the reference cylinder with radius  $R$ . The shaped emerging wave propagates in the  $x$ - $z$  plane and deviates from the reference cylinder by  $L(\theta)$ .

point  $F'$  that is shifted a distance  $a$  toward this ultrathin optical element. Reshaping the wavefront of the incident converging wave leads to an increment in the NA at the exit curved surface of the metamaterial. Induced by the metasurface, the semi-angular aperture of the converging wave field is increased from  $\Omega$  to  $\Omega'$ . Provided that the radius of the metasurface is  $R > 0$  and  $a > 0$  stands for the focal shift induced by the metasurface, we infer that

$$\frac{a}{\sin(\Omega' - \Omega)} = \frac{R}{\sin(\Omega')}, \quad (1)$$

where  $\sin(\Omega')$  is the NA (in free space) of the transmitted wavefront of radius  $R' = R - a$  as shown in Fig. 1(b). In Fig. 2, we present the increased NA  $\sin(\Omega')$  of a given converging wavefront of NA evaluated by  $\sin(\Omega)$ , which is molded by a

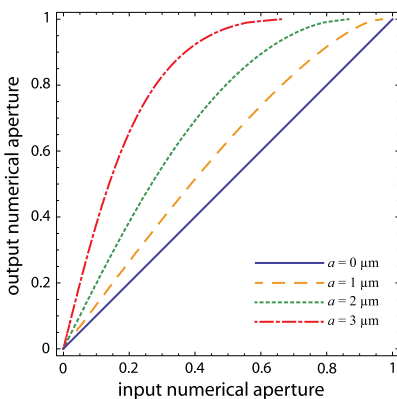


**Fig. 2.** Variation of the output NA,  $\sin(\Omega')$ , versus the input NA,  $\sin(\Omega)$ , for a metasurface of radius  $R = 4 \mu\text{m}$  and different values of the focal shift parameter  $a$ .

metasurface of radius  $R = 4 \mu\text{m}$ . For instance, if the incident wave field originally has an NA of 0.71 (that is,  $\Omega = 45^\circ$ ), then we may reach the highest emerging NA,  $\sin(\Omega') = 1$ , by simply shifting the focal point to a distance of  $a = 2.83 \mu\text{m}$ .

Finally, we may infer that the distance from a given point  $P$  of the reference cylinder, where the ultrathin metasurface is placed, to the wavefront of the emerging wave field of radius  $R'$ , as measured along an optic ray traveling from  $P$  to  $F'$ , is given by

$$L(\theta) = -(R - a) + \sqrt{R^2 + a^2 - 2aR \cos \theta}, \quad (2)$$

where  $\theta$  is the azimuthal angle as measured with respect to  $z$  axis. The optical path in excess,  $L(\theta)$ , must be compensated by a metasurface of amplitude transmittance

$$T(\theta) = \exp[-ikL(\theta)], \quad (3)$$

introducing a dephase, where  $k = 2\pi/\lambda$  is the wavenumber.

According to Debye diffraction theory, the wave field in the focal region can be estimated by means of the following diffraction integral [13,14]:

$$H(\mathbf{r}) = \sqrt{\frac{kR}{2\pi i}} \exp(ikR) \int_{-\pi}^{\pi} H_s(\theta) \exp[-ik(\hat{\mathbf{q}} \cdot \mathbf{r})] d\theta, \quad (4)$$

where the integral is evaluated over the cylindrical wavefront. In Eq. (4),  $\mathbf{r} = (z, x)$  with center at focus and  $H_s$  is the scattered magnetic field as measured over the cylindrical wavefront. Finally,  $\hat{\mathbf{q}} = (\cos \theta, \sin \theta)$  is a unit vector pointing from the focal point in the direction of a given point on the curved wavefront. The field amplitude,  $H_s(\theta)$ , which modulates the cylindrical wavefront of the converging beam, will be expressed by means of a real and positive term taking into account the truncation of the converging field.

We will consider a super-Gaussian apodization function that has the role of an aperture but minimizes edge effects and is given by

$$H_s(\theta) = H_s(0) \exp[-(\theta/\Omega)^6], \quad (5)$$

where  $\Omega$  represents the semi-aperture angle, which in addition determines the NA of the cylindrical wavefront. In Figs. 3(a)–3(c), we present the field intensity  $|H(\mathbf{r})|^2$  derived from the Debye diffraction Eq. (4) for different NAs. Let us note that the field intensity is independent of the wavefront radius; however, it is clearly modified by the NA of the optical arrangement. Importantly, the intensity distribution is mirror-symmetric with respect to  $x$  and  $z$  axes, thus neglecting asymmetric spatial effects caused when the metasurface approaches the focal region [15], as we will see below. Nevertheless, Eq. (4) serves as an accurate estimation of the limit of resolution both transversally to the direction of propagation and on axis. In Fig. 3(d), we plot the full width at half-maximum (FWHM) of the central peak for different values of the wavefront NA, as measured along  $x$  and  $z$  axes. The on-axis resolution, which varies as the inverse square of the NA, is further improved than the transverse resolution, which is inversely proportional to the NA of the cylindrical wavefront.

Finally, we point out that the electric field is kept in the  $x$ - $z$  plane for TM polarization. In high-NA arrangements, in addition, its on-axis component cannot be neglected in the focal region, resulting from applying the equation

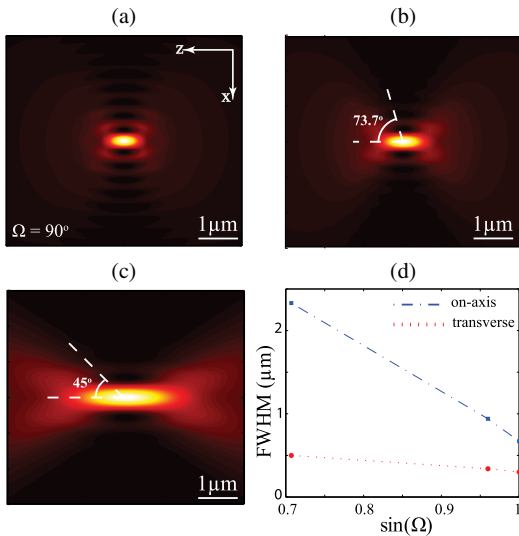


**Fig. 3.** Intensity pattern of the magnetic field derived from Eq. (4) at  $\lambda = 800\ \text{nm}$  for different semi-aperture angles: (a)  $\Omega = 90.0^\circ$ , (b)  $\Omega = 73.7^\circ$ , and (c)  $\Omega = 45.0^\circ$ . (d) FWHM of the central peak as measured along  $x$  axis (dotted line) and  $z$  axis (dashed–dotted line).

$$E_z(\mathbf{r}) = (i/\omega\epsilon_0)\partial H(x, z)/\partial x, \quad (6)$$

where  $\epsilon_0$  is the permittivity of vacuum. The confinement of the magnetic field at the wavelength scale along the transverse direction leads to mean terms of the order of  $k$  when applying the differential operator  $\partial/\partial x$ . As a consequence of the vectorial nature of light, the transverse electric field  $E_x$  and the component  $E_z$  given in the previous equation can be alike in average. For axisymmetric field distributions, as we take into account here, a phase singularity of  $E_z$  will be found on axis, which may produce a deterioration of the transverse resolution [16].

### 3. RESULTS AND DISCUSSION

Let us demonstrate numerically that by patterning a phase distribution  $\exp[-ikL(\theta)]$  along a given converging beam, where the optical path in excess,  $L$ , is given in Eq. (2), we may produce a controlled focal shift. For that purpose, we use COMSOL Multiphysics, which is a finite-element analysis software environment for modeling and simulation of any electromagnetic system. By introducing a cylindrical surface current (SC) of radius  $R = 4\ \mu\text{m}$ , which in addition is apodized by a super-Gaussian distribution with semi-aperture angle  $\Omega$ , we may create a focused field around its center of curvature with an NA of 0.71 ( $\Omega = 45^\circ$ ), as shown in Fig. 4(a). This is in agreement with the Debye diffraction formulation, as shown in Fig. 3(c). The effect of the metasurface is simulated by including an additional phase distribution like that given in Eq. (3). In Fig. 4(b), we show the focal field of the shaped converging wave, provided that the focal shift parameter  $a = 2\ \mu\text{m}$ . We observe that the molded wave field is shifted accordingly, and that the intensity distribution is essentially

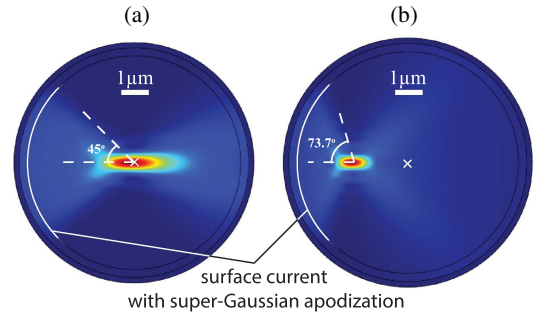


**Fig. 4.** Intensity distribution  $|H(\mathbf{r})|^2$  corresponding to a monochromatic converging wave, which is apodized at points placed at a distance  $R = 4\ \mu\text{m}$  from the focus (in our model we used an SC) with (a) a super-Gaussian distribution of semi-aperture angle  $\Omega = 45^\circ$  and (b) an additional phase modulation with a prescribed parameter  $a = 2\ \mu\text{m}$ . The working wavelength is  $\lambda = 800\ \text{nm}$ . The centered white cross represents the origin of coordinates.

that of a cylindrical converging field of a semi-aperture angle of  $\Omega' = 73.7^\circ$ , as illustrated in Fig. 3(b).

The cylindrical metasurface of amplitude transmittance  $T(\theta)$  can be formed by an inhomogeneous transparent material of refractive index  $n(\theta) = n(0) - L(\theta)/d$ , provided that  $d$  is the width of such an ultrathin layer. However, current nanotechnology presents certain limitations for the fabrication of phase-only nanoplates following a continuous variation of the refractive index  $n$  [17]. Then it is more appropriate to design a nanostructure that shapes the phase of the impinging converging field by discrete ranges. In Fig. 5, we show the result of

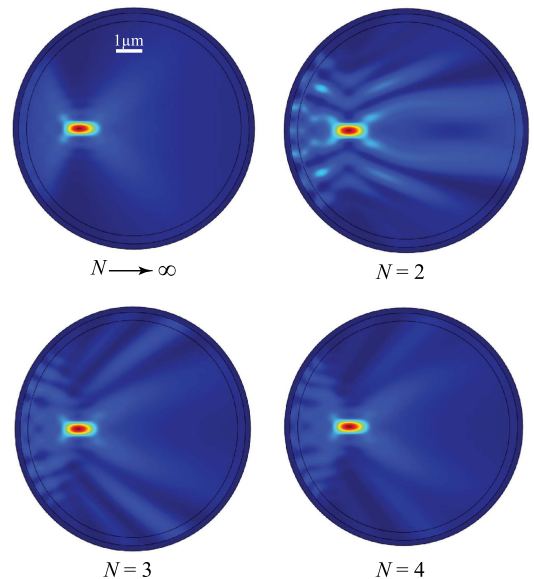


**Fig. 5.** Intensity distribution  $|H(\mathbf{r})|^2$  of focal waves modulated by a piecewise phase-only function  $\exp[-ikL(\theta)]$  of different number  $N$  of steps.



modulating the phase by  $N$  steps of  $2\pi/N$  radians. For instance,  $N = 2$  denotes a modulation of the phase in two types of zones by introducing phase shifts of  $\pi$  radians, leading to an effective focal shift with an increased NA, although exhibiting significant sidelobes. Provided that  $N = 4$ , which is carried out using four elements with different refractive indices, the resultant wave field is certainly interchangeable to the optimized design ( $N \rightarrow \infty$ ), as illustrated in Fig. 5.

For the design of the ultrathin metasurface, where  $d \ll \lambda$ , we will utilize  $N$  types of (meta)materials exhibiting indices of refraction of  $n_i = n_0 + i\lambda/(Nd)$ , where  $i$  is an integer ranging from 0 to  $N - 1$  and  $n_0$  is an arbitrary value for the index of refraction. This procedure requires sharp tunability and a broad range of refractive indices, which has been used elsewhere [18]. An extremely high index of refraction can be obtained by using MI metamaterials, including metallic nanospheres [19] and nanolayers [20]. In our case, we consider gold nanogratings of adjustable metal filling factors  $f_i = w_i/\Lambda_i$ , where  $w_i$  is the width of the Au layer and  $\Lambda_i$  is the period of the grating (see Fig. 6). Specifically, we assume that  $w_0 = 0$  so that  $n_0$  refers to the refractive index of the bulk insulator. Assuming that propagation is carried out along the MI layers, the optical path gained by the transmitted field is  $n_i d$ , where

$$n_i = \text{Re} \sqrt{\frac{\epsilon_d \epsilon_m}{\epsilon_d f_i + \epsilon_m (1 - f_i)}} \quad (7)$$

is the “extraordinary” refractive index of the effective uniaxial nanostructure [21], and  $\epsilon_m$  and  $\epsilon_d$  are the permittivities of the metal and insulator (we chose silicon) hosting the gold nanolayers, respectively. At  $\lambda = 800$  nm, we considered  $\epsilon_m = -23.36 + i0.77$  for gold [22] and  $\epsilon_d = 13.64$  for silicon. Assuming a discrete number of  $\pi/2$  dephases ( $N = 4$ ) and a metasurface width of  $d = 100$  nm, we may infer that a sequence of  $f = 0, 0.37, 0.49$ , and  $0.54$  provides changes of two units ( $n_0 = 3.69$ ) in the effective index of refraction,  $n_i - n_{i-1} = 2$ , as required.

A more accurate design may be performed by using the procedure given in Ref. [18], which is based on Floquet theory. In this case, we solved the Bloch equation for TM-polarized modes propagating with zero Bloch pseudomomentum in order to obtain the effective index for each Au-grating configuration. In Fig. 7, we show the index of refraction obtained from Eq. (7) based on the long-wavelength approximation (LWA) and that estimated from the Bloch equation for an Au–Si nanostructure assuming that the width of the silicon layer is kept fixed as

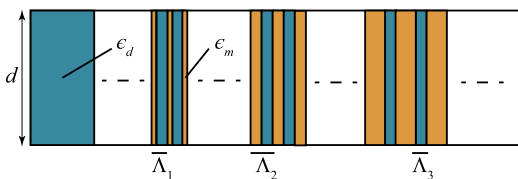


**Fig. 6.** Scheme of the preformed flat metasurface showing a basic arrangement of a bulk insulator and  $N - 1 = 3$  metallic gratings. Neighboring elementary gratings of periods  $\Lambda_i$  and  $\Lambda_{i+1}$  will induce a dephase of  $\pi/2$  radians. For the sake of clarity, we show the basic nanostructured arrangement in a planar geometry.

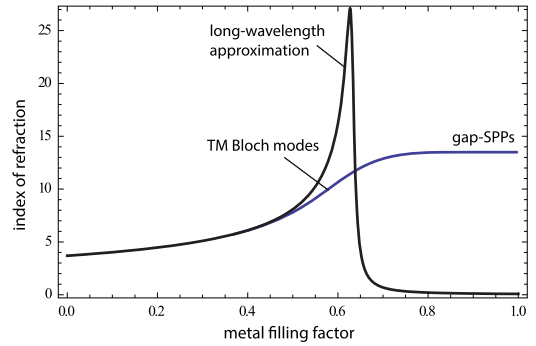


**Fig. 7.** Effective index of refraction of the Au–Si nanostructure based on the LWA (black solid line), that is, Eq. (7), and also evaluated by means of the Bloch equation (blue solid line) assuming that the width of the silicon layer is 15 nm.

15 nm. The Bloch approach deviates from the LWA if the widths of the Au layers reach and surpass the penetration depth of the metal [23]. The origin of this nonlocal effect in MI sub-wavelength gratings lies in a strong variation of the fields on the scale of a single layer [24]. In addition, homogenization of the MI nanostructure precludes the existence of gap surface plasmon polariton modes for large metal filling factors; there we may consider that the thin Si layer is sandwiched between two Au surfaces (with metal extending indefinitely on both sides of the layer) [25]. We found three periodic Au–Si compounds with prescribed effective indices of refraction, which are characterized by the following geometrical parameters:  $(w_1, \Lambda_1) = (9, 24)$  nm,  $(w_2, \Lambda_2) = (15, 30)$  nm, and  $(w_3, \Lambda_3) = (20, 35)$  nm; again  $n_0 = 3.69$  takes into account bulk silicon as a reference material. Note that the sequence of Au filling factors,  $f = 0, 0.38, 0.50$ , and  $0.57$ , is in good agreement with the estimation given above based on the LWA.

Next we apply the three designed metamaterials of effective refractive indices of  $n_i = n_{i-1} + 2$  (approximately, where  $i = 1, 2, 3$ ) and silicon to arrange an ultrathin curved metasurface of  $4 \mu\text{m}$  inner radius and a width of  $d = 100$  nm. The assembly of Au–Si multilayers is engineered to create a phase modulation over the impinging converging wave following the function  $\exp[-ikL(\theta)]$ , sampled for  $N = 4$  steps, in the way we have illustrated in Fig. 5. A modulation in transmissivity also occurs due to successive reflections and refractions in the entrance and exit sides of the metasurface, and to a lesser extent due to metal losses. For instance, the modulus of the transmission factor  $T$  for pure Si gives 0.93, whereas for the subwavelength gratings it reaches 0.33, 0.61, and 0.13, set in order of increasing metal filling factor. The intensity  $|H(\mathbf{r})|^2$  of the molded focal wave is calculated using COMSOL Multiphysics, as shown in Fig. 8. Apart from some non-negligible sidelobes, we achieve a super-resolved focal spot with reduced FWHM both laterally and on axis. Specifically, the on-axis FWHM decreases to  $1.2 \mu\text{m}$ , taking into account that the unshaped converging field produces a central peak with a  $2.4 \mu\text{m}$  on-axis FWHM. Ultimately, we point out that in the optimal case of applying nonabsorbing materials of refractive

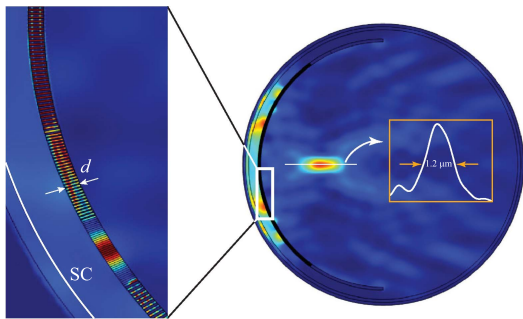


**Fig. 8.** Numerical simulation based on the finite-element method of the intensity  $|H(\mathbf{r})|^2$  in the focal region of the converging field shaped by the Au–Si curved metasurface. Excitation is performed by a cylindrical SC with super-Gaussian apodization ( $\Omega = 45^\circ$ ), in the same way as shown in Fig. 4(a). The inset on the left shows the composition of layers in detail; the on-axis intensity in the focal region is depicted in the inset on the right.

indices  $n_i$ , an increase of 26% in the in-focus intensity is achievable.

The behavior of our curved metasurface differs substantially if the incident focused beam is transverse-electric (TE)-polarized, that is, provided the electric field may be expressed as  $\mathbf{E} = E(x, z) \exp(-i\omega t) \hat{\mathbf{y}}$ . Figure 9(a) shows the intensity  $|E(\mathbf{r})|^2$  of the scattered field, which evidences a strong blurring of the focal spot. In this case, the wave field propagating in each metallic grating behaves like ordinary waves (*o* waves) in an effective uniaxial crystal of transverse (with respect to the optic axis) dielectric constant [26]

$$\epsilon_{\perp i} = f_i \epsilon_m + (1 - f_i) \epsilon_d. \quad (8)$$

Note that the circular symmetry of the nanostructure leads to an inhomogeneous distribution of the optic axis, which in addition is set perpendicular to the propagation direction of the impinging wave field. In Fig. 9(b), we represent the modal indices of TE Bloch waves propagating along the MI layers, indicating high agreement with the LWA. The modal indices in the gratings of metal widths ( $w_1, w_2, w_3$ ) are (0.365, 0.087, 0.079) respectively, much lower than the refraction index of silicon. In practical terms, the phase distribution at the exit

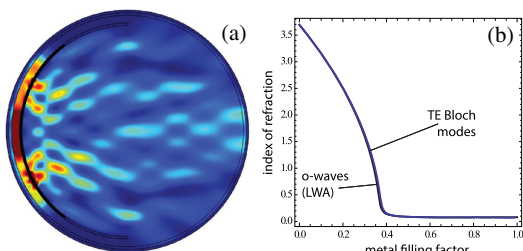


**Fig. 9.** (a) Intensity  $|E(\mathbf{r})|^2$  of the scattered field for TE polarization. (b) Effective indices for TE-polarized waves propagating through MI lattices of different Au filling factors. The index of refraction derived from the LWA is included.

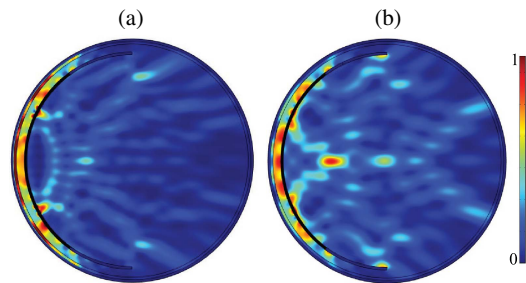


**Fig. 10.** Normalized intensity  $|H(\mathbf{r})|^2$  in the focal region of TM-polarized converging fields of wavelengths (a)  $\lambda = 700$  nm and (b)  $\lambda = 900$  nm shaped by the engineered Au–Si curved metasurface.

surface is binary instead of quaternary. Moreover, increasing the metal filling factor leads to a notable decrease of the transmitted intensity, attributed to the fact that in these cases the MI lattice behaves like an opaque metal. As a result, the MI metasurface causes a serious disturbance of the complex amplitude, leading to a divergent scattered field. We point out that the examination of the polarization dependence has been carried out previously in closely related works [27].

Finally, we analyze the behavior of the engineered metasurface for TM-polarized waves with wavelengths in the vicinity of  $\lambda = 800$  nm. For decreasing wavelengths, the field transmitted through the multigrating device has an averaged lower intensity, which is mainly caused by interband absorption in gold. Such reduced transmissivity is illustrated in Fig. 10(a) for  $\lambda = 700$  nm where Au permittivity is set as  $\epsilon_m = -15.78 + i0.66$  [22]. In these cases, metallic materials with lower loss like silver can be used, instead [28]. In addition, some spurious spots appear off axis and a ring-shaped caustic curve is evident, which are induced by a major departure from the designed phase-only term  $T(\theta)$  given in Eq. (3). On the other hand, higher wavelengths reveal a more solid resistance to the rise of aberration-driven sidelobes in the focal region, as shown in Fig. 10(b) for  $\lambda = 900$  nm. In the latter case, the size of the spot set at  $F'$  yields  $0.99 \mu\text{m}$  on axis. It is noteworthy that the metasurface cannot fully remove the diffracted field of the incident converging field at the focal point  $F$ .

#### 4. CONCLUSIONS

We have designed a curved metasurface for high-NA beam shaping. By using ultrahigh-refraction-index MI gratings, we have a controlled dephase of the TM-polarized transmitted wave field, modifying the curvature of the exit wavefront. The resultant increased NA demonstrates a limited gain in the transverse resolution and an exceptional super-resolution effect on axis. Finally, from a technological point of view, it is important to emphasize that the fabrication of the grating-based configuration does not present limitations since the silver and silica layer deposition by e-beam evaporation is a practicable procedure. In relation to the curved shape of the metamaterial, in addition, we point out that analogous schemes with experimental evidence have been reported elsewhere [29,30]. Our

results may be of relevance in optical microscopy and nanolithography.

**Funding.** Spanish Ministry of Economy and Competitiveness (MEC) (TEC2013-50416-EXP).

## REFERENCES

- M. Born and E. Wolf, *Principles of Optics*, 7th (expanded) ed. (Cambridge University, 1999).
- A. Toriumi, S. Kawata, and M. Gu, "Reflection confocal microscope readout system for three-dimensional photochromic optical data storage," *Opt. Lett.* **23**, 1924–1926 (1998).
- C. J. R. Sheppard and A. Choudhury, "Annular pupils, radial polarization, and superresolution," *Appl. Opt.* **43**, 4322–4327 (2004).
- M. Martínez-Corral, P. Andrés, C. J. Zapata-Rodríguez, and M. Kowalczyk, "Three-dimensional superresolution by annular binary filters," *Opt. Commun.* **165**, 267–278 (1999).
- M. Minsky, "Memoir on inventing the confocal scanning microscope," *Scanning* **10**, 128–138 (1988).
- S. Hell and E. H. K. Stelzer, "Properties of a 4Pi confocal fluorescence microscope," *J. Opt. Soc. Am. A* **9**, 2159–2166 (1992).
- S. W. Hell and J. Wichmann, "Breaking the diffraction resolution limit by stimulated emission: stimulated-emission-depletion fluorescence microscopy," *Opt. Lett.* **19**, 780–782 (1994).
- A. Diaspro, P. Bianchini, G. Vicidomini, M. Faretta, P. Ramoino, and C. Usai, "Multi-photon excitation microscopy," *Biomed. Eng. Online* **5**, 36 (2006).
- X. Zhang and Z. Liu, "Superlenses to overcome the diffraction limit," *Nat. Mater.* **7**, 435–441 (2008).
- P. Wróbel, J. Pniewski, T. J. Antosiewicz, and T. Szoplík, "Focusing radially polarized light by a concentrically corrugated silver film without a hole," *Phys. Rev. Lett.* **102**, 183902 (2009).
- C. J. Zapata-Rodríguez, D. Pastor, M. T. Caballero, and J. J. Miret, "Diffraction-managed superlensing using plasmonic lattices," *Opt. Commun.* **285**, 3358–3362 (2012).
- F. Aieta, P. Genevet, M. A. Kats, N. Yu, R. Blanchard, Z. Gaburro, and F. Capasso, "Aberration-free ultrathin flat lenses and axicons at telecom wavelengths based on plasmonic metasurfaces," *Nano Lett.* **12**, 4932–4936 (2012).
- T. D. Visser and S. H. Wiersma, "Diffraction of converging electromagnetic waves," *J. Opt. Soc. Am. A* **9**, 2034–2047 (1992).
- C. J. Zapata-Rodríguez, "Debye representation of dispersive focused waves," *J. Opt. Soc. Am. A* **24**, 675–686 (2007).
- C. J. Zapata-Rodríguez, P. Andrés, M. Martínez-Corral, and L. Muñoz-Escrivá, "Gaussian imaging transformation for the paraxial Debye formulation of the focal region in a low-Fresnel-number optical system," *J. Opt. Soc. Am. A* **17**, 1185–1191 (2000).
- K. S. Youngworth and T. G. Brown, "Focusing of high numerical aperture cylindrical-vector beams," *Opt. Express* **7**, 77–87 (2000).
- H. Im, K. C. Bantz, N. C. Lindquist, C. L. Haynes, and S.-H. Oh, "Vertically oriented sub-10-nm plasmonic nanogap arrays," *Nano Lett.* **10**, 2231–2236 (2010).
- M. Naserpour, C. J. Zapata-Rodríguez, A. Zakery, and J. J. Miret, "Highly localized accelerating beams using nano-scale metallic gratings," *Opt. Commun.* **334**, 79–84 (2015).
- J. Christensen and F. J. García de Abajo, "Slow plasmonic slab waveguide as a superlens for visible light," *Phys. Rev. B* **82**, 161103 (2010).
- J. T. Shen, P. B. Catrysse, and S. Fan, "Mechanism for designing metallic metamaterials with a high index of refraction," *Phys. Rev. Lett.* **94**, 197401 (2005).
- P. Yeh, *Optical Waves in Layered Media* (Wiley, 1988).
- S. Babar and J. H. Weaver, "Optical constants of Cu, Ag, and Au revisited," *Appl. Opt.* **54**, 477–481 (2015).
- E. Popov and S. Enoch, "Mystery of the double limit in homogenization of finitely or perfectly conducting periodic structures," *Opt. Lett.* **32**, 3441–3443 (2007).
- J. Elser, V. A. Podolskiy, I. Salakhutdinov, and I. Avrutsky, "Nonlocal effects in effective-medium response of nanolayered metamaterials," *Appl. Phys. Lett.* **90**, 191109 (2007).
- S. I. Bozhevolnyi, *Plasmonic Nanoguides and Circuits* (Pan Stanford, 2009).
- A. Yariv and P. Yeh, "Electromagnetic propagation in periodic stratified media. II. Birefringence, phase matching, and x-ray lasers," *J. Opt. Soc. Am.* **67**, 438–448 (1977).
- S. Ishii, A. V. Kildishev, V. M. Shalaev, K.-P. Chen, and V. P. Drachev, "Metal nanoslit lenses with polarization-selective design," *Opt. Lett.* **36**, 451–453 (2011).
- M. Naserpour, C. J. Zapata-Rodríguez, A. Zakery, C. Díaz-Aviñó, and J. J. Miret, "Accelerating wide-angle converging waves in the near field," *J. Opt.* **17**, 015602 (2015).
- I. I. Smolyaninov, Y.-J. Hung, and C. C. Davis, "Magnifying superlens in the visible frequency range," *Science* **315**, 1699–1701 (2007).
- J. Rho, Z. Ye, Y. Xiong, X. Yin, Z. Liu, H. Choi, G. Bartal, and X. Zhang, "Spherical hyperlens for two-dimensional sub-diffractional imaging at visible frequencies," *Nat. Commun.* **1**, 143 (2010).



5<sup>th</sup> Publication:  
**Metacoatings for Wavelength-Scale,  
High-Numerical-Aperture Plano-Concave  
Focusing Lenses**

**Authors:** Mahin Naserpour, Carlos J. Zapata-Rodríguez, Carlos  
Díaz-Aviñó and Mahdieh Hashemi

Published in **Journal of the Optical Society of America B**,  
volume 33, pages 2120-2128, year 2016.

# Metacoatings for wavelength-scale, high-numerical-aperture plano-concave focusing lenses

MAHIN NASERPOUR,<sup>1,2</sup> CARLOS J. ZAPATA-RODRÍGUEZ,<sup>1,\*</sup> CARLOS DÍAZ-AVIÑÓ,<sup>1</sup> AND MAHDIEH HASHEMI<sup>3</sup>

<sup>1</sup>Department of Optics and Optometry and Vision Science, University of Valencia, Dr. Moliner 50, Burjassot 46100, Spain

<sup>2</sup>Department of Physics, College of Sciences, Shiraz University, Shiraz 71946-84795, Iran

<sup>3</sup>Department of Physics, College of Science, Fasa University, Fasa 7461781189, Iran

\*Corresponding author: carlos.zapata@uv.es

Received 7 June 2016; revised 8 August 2016; accepted 30 August 2016; posted 31 August 2016 (Doc. ID 267787); published 23 September 2016

We design plano-concave silicon lenses with coupled gradient-index plasmonic metacoatings for ultrawide apertured focusing utilizing a reduced region of  $\sim 20\lambda^2$ . The anomalous refraction induced in the planar input side of the lens and in the boundary of the wavelength-scale focal region boosts the curvature of the emerging wavefront, thus significantly enhancing the resolution of the tightly focused optical wave. The formation of a *light tongue* with dimensions approaching those of the concave opening is here evidenced. This scheme is expected to have potential applications in optical trapping and detection. © 2016 Optical Society of America

**OCIS codes:** (050.6624) Subwavelength structures; (110.2760) Gradient-index lenses; (240.6680) Surface plasmons.

<http://dx.doi.org/10.1364/JOSAB.33.002120>

## 1. INTRODUCTION

Tight focusing of electromagnetic waves is essential to a myriad of applications, such as photolithography and optical trapping, typically using dielectric thick lenses of high numerical aperture (NA). However, the unceasing miniaturization and integrability of photonic devices imposes severe restrictions on the implementation of such sorts of bulky pieces. In this context, concave positive lenses composed of meta-atoms to change the sign of its macroscopic refractive index might be incorporated in high-NA focusing platforms within a reduced region [1–4]. Epsilon-near-zero plano-concave lenses also prove a good performance prompted by the phenomenon of energy squeezing [5,6]. In particular, such architectures cannot operate at optical frequencies mainly due to material losses and demanding fabrication challenges.

Advances in current techniques for nanofabrication, some of them based on plasmonics, have opened new prospects for producing compact, planar focusing systems. Plasmonic flat lenses enabling a plane-wave efficient shaping into an output converging wavefront within a subwavelength interaction space have been developed using arrays of nanoholes [7,8], nanoslits [9,10], nanoparticles [11,12], corrugations [13], and nanoantennas [14,15]. In the previous examples, the mechanism set behind the control of the scattered light relies on the suitable spatial distribution of engineered, subwavelength phase shifters included on the active surface [16]. Therefore, a critical design

aspect of the focusing device is the choice of the elementary scatterers for obtaining the required phase distribution.

In the so-called metasurfaces, Mie resonances lead to controllable phase discontinuities, which are applied to administrate the beam shaping [15]. Alternatively, the phase of the electromagnetic field may change after passing through a subwavelength metal-dielectric structure on the basis of a modal coupling to the external radiation. Such a phenomenon is suitably explained in terms of an effective refractive index, and can be achieved with extremely high performance in transmission [17]. For instance, a set of metallic slits with controllable width can locally tune the effective index of refraction of the guided plasmonic modes [18]. These sorts of ultrathin nanostructures are here coined as graded-index metacoatings.

Flat metalenses offer some advantages accessibly to manufacture and integrate in complex devices; however, they suffer from severe geometrical restrictions to attain extremely high numerical apertures [19,20]. An alternative design relies on sculpturing a concave surface. In such a manner an aplanatic metasurface patterned on a spherical substrate has been proposed to focus light without coma and spherical aberrations [21]. The concept of metamaterials with engineered dispersion in curvilinear coordinates, with coaxial and concentric geometries, has been extensively exploited, for instance, in hyperlensing [22–24]

Previously we presented a design of nonplanar metacoatings composed of subwavelength metal-dielectric arrays to

accelerate optical waves in the near field [25–27]. These nanostructures allow us to grade ultrahigh indices of refraction together with high transmissivity, demonstrating controllable phase and amplitude responses over subwavelength propagation ranges for TM-polarized waves. Here, we utilize such a basic concept to engineer gradient-index ultrathin coatings, in a parallelizable assembly, as focusing elements with high efficiency. In fact, advantages of cascading a set of metasurfaces have been previously reported, for instance, as a polarization rotator [28], as an efficient cylindrical-vector-vortex beam generator [29], and as a polarization-controlled lens [30]. Conveniently implemented over the two sides of a plano–concave (divergent) dielectric microlens, we achieve miniaturized lenses with aberration-free high-numerical-aperture focalization.

### 2. LENS DESIGN

The medullary component of our focusing device is a bulky dielectric lens, which, without loss of generality, we consider as immersed in air. Light impinges over the flat surface of the lens, and the exit spherical surface has a short radius  $R > 0$ , whose center is set at a given point  $C$ , as depicted in Fig. 1. Here we consider that  $R$  remains in the scale of the wavelength, although our approach is not strictly restricted to such a regime. Under certain circumstances, this arrangement enables a high-aperture focusing of light emerging from

the concave surface of the lens. From the geometrical point of view, the optical power is carried by the second surface of the thick lens characterized by a paraxial focal length,

$$f = \frac{R}{1 - n}, \tag{1}$$

where  $n$  denotes the refractive index of the lens. If  $n > 1$  as occurs in natural dielectric materials, the lens is divergent with negative focal length,  $f < 0$ , disabling to focus light behind the concave surface, as illustrated in Fig. 1(a). Therefore, focusing is only available with a refractive index below the unity, which can be achieved by using metamaterials [6]. In the specific case of epsilon-near-zero metamaterials, setting  $n = 0$ , light is focused at the center of curvature of the concave exit surface, as shown in Fig. 1(b) [5]. This arrangement has recently been demonstrated experimentally in microwave frequencies and presents fascinating characteristics, such as reduced aberrations in configurations with numerical apertures close to unity [31]. An increased numerical aperture might be achieved by means of negative-index plano–concave lenses, as shown in Fig. 1(c). However, thick negative-index metamaterials in the near-infrared and visible frequency range exhibit a deficient performance mainly due to material Ohmic losses and inhomogeneities scattering.

Our approach is based on a transparent dielectric thick lens coated by graded-index ultrathin metasurfaces, as illustrated in Fig. 1(d). Therefore, material losses have a reduced impact in the lens performance. The coated metasurfaces, here coined metacoatings, are designed to compensate the negative optical power of the plano–concave dielectric lens. We propose a first metacoating set on the entrance flat surface to transform the incident plane wave into a spherical wave of center at  $F$ , coinciding with the center of curvature  $C$  of the concave surface in the lens. Such appropriate configuration reduces losses derived by reflections in the curved interface, and establishes a first numerical aperture in terms of the beam angle  $\Omega$ . In order to even further increase the numerical aperture of the lens, a second metacoating is placed in the concave surface. A controlled focal shift  $a < R$  leads to a magnified far-field angle of the resulting converging wave [32]. As a result, the transmitted wave field will focus at  $F'$  by free-space propagation, characterized by a numerical aperture  $NA' = \sin(\Omega')$ . Assuming that the focal point  $F'$  of the coupled metacoating thick lens is located closer to the concave surface than  $F$ , that is,  $a = \overline{FF'} > 0$ , the numerical aperture

$$NA' = \frac{NA}{\sqrt{1 + (a/R)^2 - 2(a/R) \cos \Omega}} \tag{2}$$

is also higher than the numerical aperture  $NA = \sin \Omega$  of the single-coated lens [32]. Specifically  $NA'$  reaches the unity when  $a = R \cos \Omega$ . Note that the transverse and on-axis resolutions are dependent on the overall numerical aperture of the focusing lens. In particular, this procedure leads to a critically improved axial resolution, which is determined by the inverse squared of the value of  $NA'$ .

Next we design the gradient-index metasurfaces, which are overlaid on the lens surfaces, taking over the wavefront management of the incident plane wave. Without loss of generality,

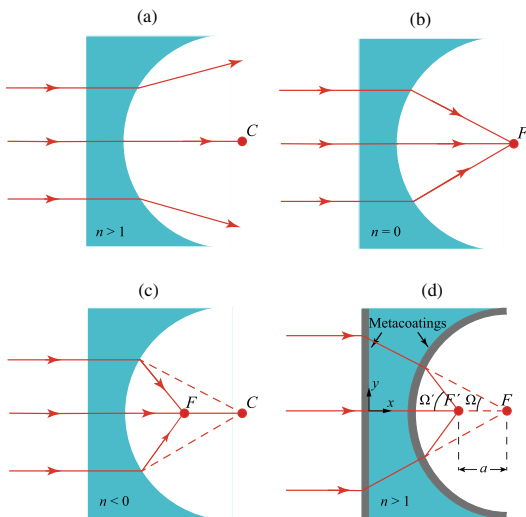


**Fig. 1.** Schematics based on optical rays of the focusing action of plano–concave dielectric lenses. (a) Transparent dielectrics with an index of refraction higher than unity lead to a diverging configuration. (b) An epsilon-near-zero metamaterial enables us to focus light at the center of curvature of the concave surface. (c) An increased numerical aperture is attained by using negative-index metamaterials. (d) Our proposal based on coupled metacoatings set at the entrance and exit surfaces of a transparent dielectric thick lens. A focused beam of semi-aperture angle  $\Omega$  will be generated by passing through the gradient-index flat metasurface. The converging wave field propagating inside the lens will be refocused at  $F'$  by means of the active curved metacoating, having an increased semiaperture angle  $\Omega'$ .

we will consider cylindrical lenses enabling a description of the problem in two dimensions. Note that the dielectric material of the thick lens having a refractive index  $n$  has a minor significance in the functioning of the focusing device. Following the Fermat's principle by evaluating equal optical path lengths, a normally incident plane wave passing through the first flat metacoating will be focused at the point  $F$ , found at a distance  $f_1$  and transversally centered at  $y = 0$ , provided that the phase shift produced by the gradient-index metasurface yields

$$\phi_1(y) = \phi_1(0) + nk \left( f_1 - \sqrt{y^2 + f_1^2} \right), \quad (3)$$

where  $k = 2\pi/\lambda$  is the wavenumber in vacuum,  $\phi_1(0)$  is an arbitrary phase, and  $y$  is the transverse coordinate indicating the distance from the optical axis. Assuming an ultrathin metacoating of width  $d$ , the gradient index is then given by  $n_1(y) = \phi_1(y)/kd$ . Of course, this approach disregards multiple reflections produced at the metacoating facets, and a more rigorous treatment will be implemented below.

As mentioned above, the cylindrical metacoating set at the back of the thick lens has a center of curvature  $C$  that is located exactly at the focal point  $F$ . Note that the constraint  $R < f_1$  must be considered, where  $f_1 - R$  stands for the vertex distance of the plano-concave lens. Therefore the wavefront of the impinging field remains concentric to the concave metacoating arriving at normal incidence. The induced phase shift on such a metasurface will reshape the incident wavefront by increasing its curvature. The field emerging from the nanolens then propagates in free space to focus at the point  $F'$  that is shifted a length  $a$  toward the rear metacoating. The dephase induced by the cylindrical metasurface is [32]

$$\phi_2(\theta) = \phi_2(0) + k \left[ (R - a) - \sqrt{R^2 + a^2 - 2aR \cos \theta} \right], \quad (4)$$

where  $\phi_2(0)$  is again an arbitrary phase term, and  $\theta$  is the azimuthal coordinate as measured from  $C$  and determining the angle from the optical axis. In practical terms,  $\phi_2$  will be operative in the range  $|\theta| \leq \Omega$ . If the width of the back metacoating is again  $d$ , the gradient index is now given by  $n_2(\theta) = \phi_2(\theta)/kd$ .

To illustrate the impact of ideal metacoatings, Fig. 2(a) shows the intensity distribution of the magnetic field,  $|H|^2$ , produced by a nonuniform magnetic surface current set on the front lens facet and having a phase distribution governed by the expression given in Eq. (3). The numerical simulations are calculated for a silicon plano-concave nanolens ( $n = 3.69$ ) of radius  $R = 3 \mu\text{m}$  at a wavelength  $\lambda = 800 \text{ nm}$  by using COMSOL Multiphysics, which is a finite element analysis software environment for modeling and simulation of electromagnetic systems. In Fig. 2(a), the length of the surface current is  $8 \mu\text{m}$ , and it is designed to focus light at a distance  $f_1 = 3.2 \mu\text{m}$ . In this way we generate a focused field around the center of curvature  $C$  with semiaperture angle  $\Omega = 51.3^\circ$ . The effect of the back metacoating on the nanolens focal field is simulated in Fig. 2(b), where we introduce a cylindrical surface current of curvature center set at  $C$  and with semiaperture angle  $\Omega$ . Additionally, a phase distribution of the surface current following Eq. (4), for a focal shift  $a = 1.5 \mu\text{m}$ , is implemented

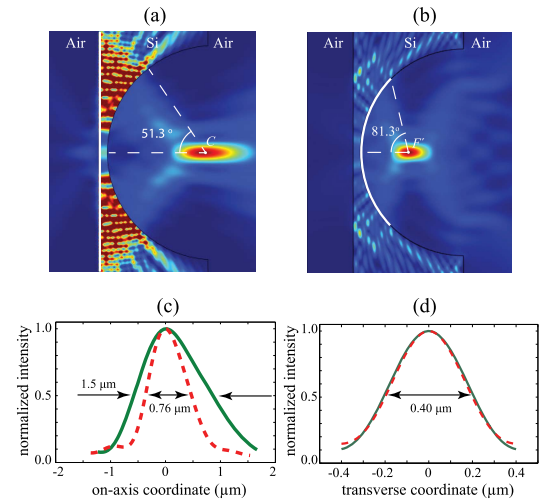


**Fig. 2.** (a) Intensity distribution  $|H|^2$  generated by a nonuniform surface current with modulated phase distribution given by Eq. (3) and set at the front surface of a plano-concave Si lens (sketched in white solid line), mimicking the effect of the designer metacoating. In (b) we set the surface current with phase distribution given by Eq. (4) at the back surface of the Si lens. Normalized intensity of the magnetic field in the focal volume of the flat (cylindrical) surface current, represented in green solid lines (red dashed lines) as measured along (c) the  $x$ -axis and (d) the  $y$ -axis. On-axis resolution critically improves with an active cylindrical surface while transverse resolution does not change significantly.

in the numerical simulation. It is evident that the shaped focal field is axially shifted from  $C$  to the focal point  $F'$ . In addition, an increased semiangular aperture  $\Omega' = 81.3^\circ$ , which is estimated with Eq. (2), will also make the numerical aperture  $\text{NA}'$  grow accordingly. Moreover, the enlarged numerical aperture leads to a resolution improvement in terms of the full width at half-maximum (FWHM) of the intensity, as measured along the  $x$ -axis, which is reduced from  $1.5$  to  $0.76 \mu\text{m}$ , as shown in Fig. 2(c). Finally, the transverse resolution experiences a negligible improvement of  $20 \text{ nm}$  (the FWHM yields  $0.40 \mu\text{m}$  with the back phased current), as evidenced in Fig. 2(d), due to its proximity to the diffraction limit.

### 3. ULTRATHIN GRADED-INDEX METACOATINGS

Next we proceed to design ultrathin metacoatings for the proper generation of the phase distribution  $\phi_1(y)$  and  $\phi_2(\theta)$ , given in Eqs. (3) and (4), respectively, all along the front surface and back surface of the plano-concave lens. A great variety of strategies can be found in the literature for such a purpose, for instance gradient metasurfaces utilizing the Pancharatnam-Berry phase elements [33,34], which in addition can provide a good efficiency. However, plano-concave cylindrical lenses may benefit from simplicity in the fabrication of the active metacoating if, for instance, their elementary units should not be patterned along the cylinder axis. A subwavelength metallic film of thickness  $d \ll \lambda$  including



nanoslits with controlled width proved to be good candidates for a tunable phase manipulation not only for spherical wavefronts [32] but also to accelerate focal beams and to create light capsules [25–27]. The resulting metacoating can be considered as a graded-index uniaxial metamaterial by simply altering the metal filling fraction  $f = w_m / (w_m + w_d)$  along the corresponding spatial coordinates,  $y$  and  $\theta$ , where  $w_d$  and  $w_m$  stand for the width of the slit and the metallic segment, respectively. Assuming that  $w_m$  remains below the penetration depth of the wave field inside the metal, the periodic array of metallic slits with nanoscale size optically behaves like an effective uniaxial crystal [35,36]. When light passes through the metallic slits, coupled surface plasmons are excited enabling wave propagation with characteristic propagation constant. In these circumstances, the multilayered metal–dielectric material behaves like a semitransparent effective medium exhibiting extreme anisotropy. Assuming that the incident plane wave is polarized perpendicularly to the nanoslits, the effective index of refraction of such metallodielectric metamaterial is approximately estimated as [37]

$$n_{\text{eff}} = \sqrt{\frac{\epsilon_d \epsilon_m}{f \epsilon_d + (1 - f) \epsilon_m}}, \quad (5)$$

where  $\epsilon_m$  and  $\epsilon_d$  denote the relative permittivities of the metal and the medium in the slits, respectively.

As illustration, we show in Fig. 3 the effective index of refraction evaluated for a gold metamaterial patterned by a uniform distribution of nanoslits of constant thickness,  $w_d = 15$  nm. For a convenient design of the metamaterial, we consider that the nanoslits are filled with silicon, a material that is also employed for the bulky plano–concave lens. Alternatively, one might propose a holey metacoating where the metallic slits are filled with air, but its lower index of refraction in comparison with Si critically limits the range of practical  $n_{\text{eff}}$ . At a wavelength  $\lambda = 800$  nm we set  $\epsilon_m = -23.36 + i0.77$  for Au and  $\epsilon_d = 13.64$  ( $= n^2$ ) for Si. An increasing metal filling fraction enables us to establish an ultra-high effective index  $n_{\text{eff}}$  that surpasses the refractive index of silicon. However, this is attained at the cost of growing Ohmic losses. For instance, a wave field propagating in an all-dielectric medium will gain a phase shift of  $\pi/2$  rad if, instead, the material now includes metallic components of

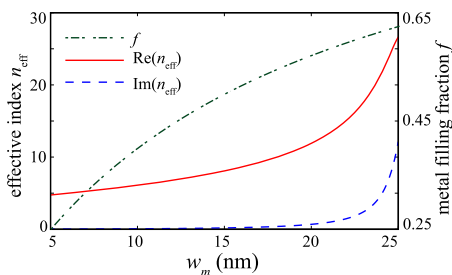


**Fig. 3.** Effective index of refraction evaluated with Eq. (5) for a gold-silicon periodic medium at a wavelength of  $\lambda = 800$  nm. Silicon layers are set with a fixed width  $w_d = 15$  nm. The metal filling fraction is governed by the Au films width  $w_m$ .

$w_m = 8.7$  nm ( $\text{Re}(n_{\text{eff}}) = 5.69 = n + \lambda/4d$ ), assuming a propagation length as short as  $d = 100$  nm. Incremental phase shifts of  $\pi/2$  rad can be obtained with Au elements of  $w_m = 14.2$  nm and  $w_m = 17.7$  nm, providing effective indices  $\text{Re}(n_{\text{eff}}) = 7.69$  and  $\text{Re}(n_{\text{eff}}) = 9.69$ , respectively.

Note that the giant modulation of the effective index of refraction of our nanogratings cannot be experienced by plane waves with TE polarization. In this case, the electric field is set along the nanoslits, and the real part of  $n_{\text{eff}}$  decreases when the metal filling factor grows [26,32]. For  $w_m$  higher than 9 nm, the multilayered metamaterial behaves like a metal with  $\text{Re}(n_{\text{eff}}) \approx 0$  and increasing  $\text{Im}(n_{\text{eff}})$ . As a consequence, the designed metacoating is highly sensitive to the polarization of the incident light, and can only be used for TM-polarized incoming light.

The estimation of such rapidly evolving phase shifts reached by wave fields in our Au-Si metamaterials is only approximate and more accurate evaluations are required to take into account, for instance, nonlocal effects [38], setting some bounds in the homogenization of the metallodielectric medium, and also cavity resonances derived from multiple reflections in the metacoating interfaces [37], as we will detail below. Figure 4 shows the phase shift gained by a TM-polarized plane

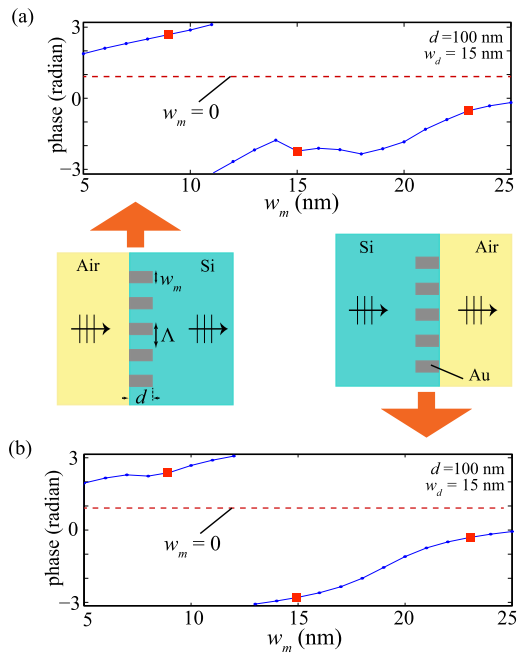


**Fig. 4.** Phase shift gained by a TM-polarized plane wave traversing through an Au-Si metacoating of thickness  $d = 100$  nm, as set in an air/silicon plane interface. For simplicity, we represent the phase shift in an interval ranging from  $-\pi$  to  $\pi$ . The slit width of the periodic nanostructure is fixed at  $w_d = 15$  nm and we vary the metal width  $w_m$ . In (a) the beam impinges from air, and in (b) from silicon. The red dashed line establishes the phase shift measured for an all-dielectric coating ( $w_m = 0$ ). Red squares illustrate that metamaterials with  $w_m = 9, 15,$  and  $23$  nm producing incremental phase shifts of approximately  $\pi/2$  rad with respect to a nonconducting film.

wave field of  $\lambda = 800$  nm after passing through a gold film of width  $d = 100$  nm including Si-filled nanoslits of thickness  $w_d = 15$  nm. The numerical simulations are again performed with COMSOL Multiphysics, which confirm (not shown in the figure) that the phase shift gained by the incident wave field is approximately proportional to the real part of  $n_{\text{eff}}$  as evaluated by Eq. (5), at least for metacoatings of moderate and low filling fraction where  $w_m$  remains below 15 nm. Figure 4(a) refers to the phase behavior of a nanopatterned film when a beam impinges from air and propagates in Si after passing through such an ultrathin device, as occurring in the front metacoating of a plano-concave lens. The simulations reproducing the conditions of the metacoating at the back of the plano-concave lens are depicted in Fig. 4(b). Note that for a high metal filling fraction, we found that Eq. (5) overestimates the effective index of refraction of the metal-dielectric metamaterial. Nevertheless, we verify from our results (not entirely shown in the figure) that changing the parameter  $w_m$ , which determines the metal filling fraction of the nanostructure, enables a phase detuning of the transmitted optical signal within the required range of  $2\pi$  rad.

Cavity resonances produced in the metacoating may lead to enhanced losses set in addition to Ohmic losses which are naturally present in the metal. This effect is illustrated in Fig. 5, where we evaluate the transmittance (also reflectance and absorbance) of our metacoatings of width  $d = 100$  nm and nanoslit thickness  $w_d = 15$  nm, employing our numerical solver based on the finite element method (FEM). Figure 5 evidences the relevance of absorption in the metamaterial for certain values of  $w_m$  and also the loss of transmitted intensity driven by reflections. Furthermore, nanostructures with values of  $w_m$  higher than 25 nm are opaque in practical terms, a length which roughly represents the penetration depth in the metal. We point out that surface plasmon resonances enabling extraordinary optical transmission, which is caused by the periodicity of the metallic nanostructure, are negligible in our case due to the deep subwavelength scale of  $\Lambda = w_m + w_d$  [39]. Now it is evident that a spatial modulation of the metal filling fraction in the metacoating leads not only to a graded-index  $n_{\text{eff}}$ , which modifies the phase of the transmitted field, but also contributes to the formation of gray zones where the intensity of the field can drop severely.

On the other hand, we may analytically estimate the amplitude and the phase transformation undergone by the scattered (magnetic) field after passing through the metallodielectric nanostructured film, by introducing the zero-order transmission amplitude: [37]

$$t = \frac{\tau_{12}\tau_{23} \exp(ikn_{\text{eff}}d)}{1 - \rho_{21}\rho_{23} \exp(2ikn_{\text{eff}}d)}. \quad (6)$$

Here,  $\tau_{12}$  and  $\tau_{23}$  are transmission coefficients at the front and back surface of the metacoating, respectively;  $\rho_{21}$  and  $\rho_{23}$  are reflection coefficients at the two ends of the nanostructure, in all cases containing both magnitude and phase. These coefficients are evaluated using  $\tau_{\alpha\beta} = n_\beta / (n_\alpha + n_\beta)$  and  $\rho_{\alpha\beta} = \tau_{\alpha\beta} - 1$ , where  $n_2 = n_{\text{eff}}$ . Transmittance is simply computed as  $T = |t|^2 (n_1/n_3)$ . Then our metamaterial reaches its optimal transmittance when  $\arg(\rho_{21}\rho_{23}) + 2kd \text{Re}(n_{\text{eff}})$

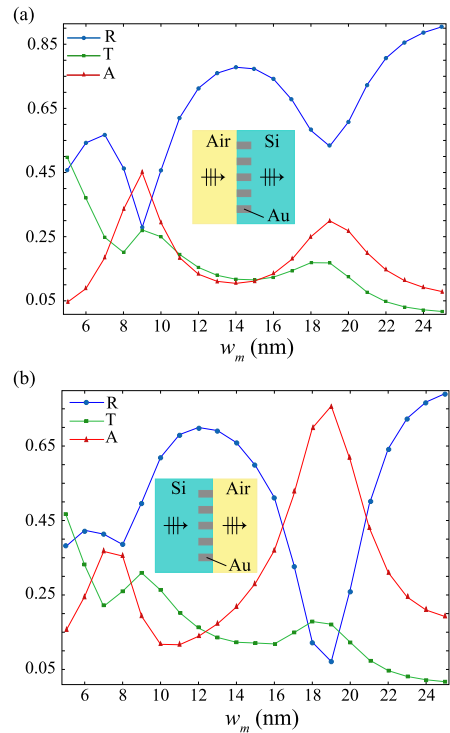


**Fig. 5.** Transmittance (T), reflectance (R), and absorbance (A) calculated for Au-Si metacoatings as described in Fig. 4, varying the width  $w_m$  of the metallic wires. The beam impinges from (a) air and from (b) Si.

satisfies the resonance condition reaching an entire multiple of  $2\pi$  rad.

From the analysis given above, it is apparent that an optimized response of the nanogratings in terms of the transmission efficiency might be achieved provided that the width of the Si layers in the multilayered nanostructure is not fixed but it can also vary appropriately. Nevertheless, further restrictions derived from fabrication tolerances in current nanotechnology support us to disregard narrower Si layers, enabling metamaterials with ultrahigh effective index of refraction, and also thinner metacoatings.

At this point we are in a position with the above-given analysis to design the elements of our graded-index metacoatings. From a practical point of view, it is appropriate to perform a discrete phase shift rather than to apply a continuous modulation of the incident wavefront. In this case, a finite number of metal-dielectric nanostructures are necessary to obtain the outlined phase range. In particular, we provide four periodic metallodielectric nanostructures producing incremental phase shifts of  $\pi/2$  rad, which has been proved to yield a satisfactory beam shaping [26]. We first consider an all-dielectric film ( $w_m = 0$ ), which demonstrates an optimal transmittance. In agreement with the results shown in Fig. 4, the remaining three Au-Si slit composites with prescribed dephases of  $\pi/2$  rad are

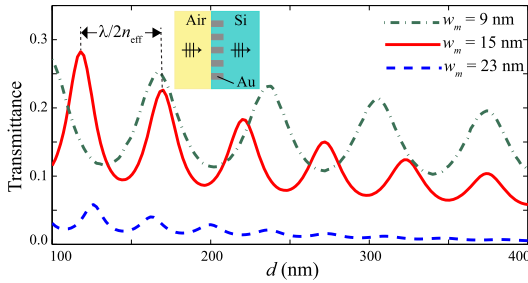


**Fig. 6.** Transmittance of metallic nanostructures with different Au wire width  $w_m$  as a function of thickness  $d$  of the metacoating, calculated at a wavelength  $\lambda = 800$  nm. Here we set  $w_d = 15$  nm.

then identified by  $w_m = 9, 15, 23$  nm, respectively, when the silicon layer width is kept fixed as  $w_d = 15$  nm. These values are highlighted in red squares in Fig. 4. It is worth noting that current technology allows us to assemble ultrathin, uniformly continuous metallic films of thicknesses of only 5 nm with reduced surface roughness of around 0.2 nm [40]. As a consequence, the values of  $w_m$  are here set as an integer in units of nanometers, and therefore the phase shift produced by these four elements of the graded-index metacoating are not exactly  $\pi/2$  rad; nevertheless, the produced deviation is small enough to be neglected.

Finally, we show the performance of our metallic gratings with different values of  $d$ . In Fig. 6 we illustrate the high-to-moderate transparency of gratings with  $w_m = 9, 15, 23$  nm and lengths  $d$  ranging from 100 to 400 nm. As expected, Fabry–Perot resonances with a periodic behavior governed by the effective index of refraction are responsible for the sinusoidal modulation of the transmitted field. Specifically, here we verify that Eq. (5) clearly overestimates  $n_{\text{eff}}$  in the case of  $w_m = 23$  nm. Finally, we recognize that our approach does not permit an engineered phase modulation coinciding with peak transmittances through the elements of the metacoating, at least for short lengths  $d$ .

#### 4. RESULTS AND DISCUSSION

Next we show some FEM-based numerical simulations to illustrate the validity of our approach, which relies on the use of coupled metacoatings set on the front and back surfaces of a wavelength-scale plano–concave lens thus enabling a plane wave to be tightly focused. As detailed above, the first metacoating is designed to convert a plane wavefront into a cylindrical wavefront that is concentric to the back surface at the point  $C$ , and the second metasurface further increases the angular aperture of the miniaturized lens. The metacoatings are composed of four types of zones, three of them constituted by metal–dielectric subwavelength gratings to induce controlled phase shifts in multiples of  $\pi/2$  with respect to bulk Si. We considered nanopatterned films of thickness  $d = 100$  nm with slits of  $w_d = 15$  nm, arranged in arrays of period  $\Lambda_1 = 24$  nm,  $\Lambda_2 = 30$  nm, and  $\Lambda_3 = 38$  nm. The phase pattern of the transmitted fields, approaching the continuous distribution given in Eqs. (3) and (4), are symmetric with respect

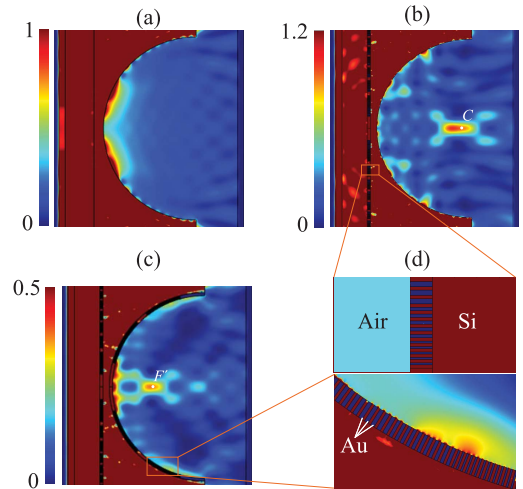


**Fig. 7.** FEM-based numerical simulations showing the intensity of the magnetic field when a monochromatic TM-polarized plane wave passes through a Si plano–concave lens of radius  $R = 3$   $\mu\text{m}$  and vertex distance of 200 nm: (a) without metacoatings, (b) including a single metacoating set on the flat front surface, and (c) with coupled metacoatings lying on the front and back surfaces of the lens. (d) Close-up of patterned Au nanoslit arrays in the flat (top) and concave (bottom) surfaces of the Si lens.

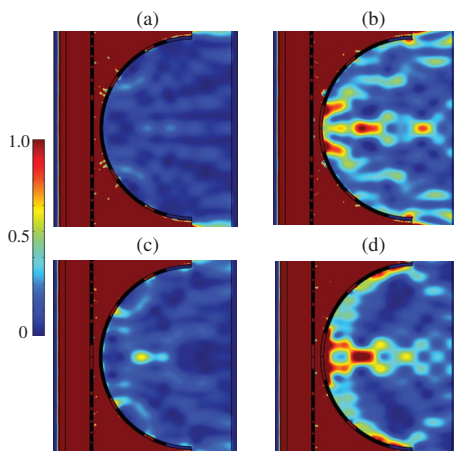
to the center of each metacoating, and therefore the designed metacoatings exhibit a mirror symmetry with respect to  $y = 0$ .

Figure 7(a) shows the refractive behavior of a bare Si plano–concave lens of radius  $R = 3$   $\mu\text{m}$  and vertex distance of 200 nm when a TM-polarized plane wave is used with  $\lambda = 800$  nm. Note that the effective area of the thick lens including the concave focal region is roughly  $A_{\text{eff}} = 2Rf_1$ , which represents an extent of only  $30\lambda^2$ . In agreement with Fig. 1(a), the beam spreads out by passing through the thick lens and it is unable to focus light. Figure 7(b) shows the performance of the same Si plano–concave lens but including a flat metacoating in its front surface to focus the beam at a distance of 3.2  $\mu\text{m}$  from it, exactly at the center point  $C$ . In particular, the central element of the metacoating (Si) has a semilength of 400 nm, followed by a nanograting of period  $\Lambda_3$  and total length of 304 nm (eight periods), an elementary grating of period  $\Lambda_2$  and 210 nm length (seven periods), and a metal–dielectric periodic nanostructure of period  $\Lambda_1$  and length of 192 nm (eight periods); this sequence of elementary gratings is repeated to gain the necessary phase shift  $\phi_1(y)$  given in Eq. (3). Comparing with Fig. 2(a), one can realize that the result of using elementary gratings to induce phase shifts of  $\pi/2$  rad is in a good agreement with the optimal designer metacoating producing a continuous phase distribution. Finally, we combine the action of a flat metacoating and a cylindrical metacoating set simultaneously, as shown in Fig. 7(c), thus obtaining a focal shift of  $a = 1.5$   $\mu\text{m}$  and consequently a superresolved focal spot. The arched metacoating has a central silicon piece of apical semiangle  $15^\circ$ , assembled to a periodic nanostructure of Au filling factor  $f = 0.61$  and aperture angle  $\Delta\theta = 11.7^\circ$

(16 periods), a cylindrical nanograting of  $f = 0.50$  and angle  $9.12^\circ$  (15 periods), a curved metamaterial of  $f = 0.38$  and angular range of  $7.9^\circ$  (17 periods), and so on to achieve the designed phase shift  $\phi_2(\theta)$ . In particular, the on-axis FWHM of the field intensity is decreased from  $1.12 \mu\text{m}$  for the case shown in Fig. 7(b) to  $0.84 \mu\text{m}$  measured from Fig. 7(c).

Here we point out that in spite of the low transmittance experienced by the elementary grating with  $w_m = 23 \text{ nm}$  in comparison with other metal–dielectric nanostructures, such a phase shifter is still applicable. The modulation undergone by the real amplitude of the scattered field has minimal effect regarding the construction of the focused wave, which might remind a Fresnel zone plate. It affects the energy efficiency of the lens and perhaps in the emergence of sidelobes and secondary peaks. It can be seen by comparing the resulting focal field in Fig. 2(b), where no amplitude modulation is applied, and Fig. 7(c).

Note that the metacoatings used in Fig. 7 are engineered to provide the maximum energy density at focus  $F'$ , a condition that is satisfied when the metal–dielectric gratings are symmetrically set off-axis. In this case, the central zone around  $y = 0$  shaping a major energy flux of the resultant focused field presents reduced losses derived by reflection and absorption, as shown in Fig. 5. To illustrate such an effect, in Fig. 8 we consider metacoatings whose central zone is formed by a metal–dielectric grating of period  $\Lambda = 38 \text{ nm}$ , which presents dramatic losses due to its high metal filling factor. In order to obtain the required phase shift described in Eqs. (3) and (4), the distribution of elementary metallodielectric gratings should be



**Fig. 8.** Intensity distribution produced in the focal region of a Si plano–concave lens including metacoatings with different arrangements of elementary metal–dielectric gratings. (a) A metallic grating of period  $\Lambda_3 = 38 \text{ nm}$  is used at the central zone of both metacoatings. Alternatively, we use an all-dielectric central zone for one metacoating and a metallic grating of period  $\Lambda_3$  in the center of (b) the cylindrical metacoating, and (c) the front flat metacoating. In (d) we reproduce Fig. 7(c), where the central zone of both metacoatings has no metallic components, but here using the same color map of previous subfigures.

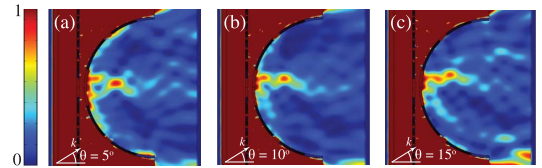


**Fig. 9.** Intensity distribution of focal waves produced by tilted TM-polarized plane waves with angles (a)  $\theta = 5^\circ$ , (b)  $10^\circ$ , and (c)  $15^\circ$ , all measured with respect to the optical axis  $y = 0$ .

permuted accordingly. When such lossy nanostructure is set in the central zone of the front metacoating and the back metacoating simultaneously, the plano–concave focusing lens is essentially opaque, as shown in Fig. 8(a). The impact of setting such lossy grating in the central zone is much notable on the cylindrical back metacoating rather than in the flat front metacoating, as depicted in Figs. 8(b) and 8(c). In the latter case, however, spurious spots appear in the focal volume, with special relevance of that located at the central point  $C$ . Finally, the noisy focal waves are clearly corrected when semitransparent phase shifters are set in the central zone of the coupled metacoatings, as shown in Fig. 8(d).

Our plano–concave lens with coupled metacoatings also presents a favorable performance under oblique incident illumination. For a comprehensive analysis of the refraction (and reflection) phenomenon involved in the interaction of monochromatic beams entering in metal–dielectric multilayered metamaterials, see Ref. [41]. As shown in Fig. 9, the beam is not focused at the focal point  $F'$  but the spot is laterally displaced as long as the impinging plane wave is tilted for paraxial angles ranging from  $\theta = 5^\circ$  to  $\theta = 15^\circ$ . The resulting focal wave does not present a significant atrophy of the beam shape and, consequently, the lateral and on-axis resolution remain practically unaltered.

In specific applications, such as particle trapping and sensing, it might be of interest to use high-numerical-aperture plano–concave lenses in the scale of the wavelength where  $R \gtrsim \lambda$ . In this case, the concave opening operates like an *optical mouth* within which it is possible to observe the formation of a focal wave in the form of a *light tongue* with appropriate dimensions. Here we explore the behavior of our proposal as pushed to such a limit. In Fig. 10 we show the intensity of a focused wave field performed by a metacoated plano–concave lens of inner radius  $R = 2 \mu\text{m}$  where the focal point shifted from  $C$  a distance  $a = 1 \mu\text{m}$ , again using a working wavelength of  $\lambda = 800 \text{ nm}$ . Since  $f_1$  is kept fixed for simplicity, the thickness of the Si lens increased from  $0.2$  to  $1.1 \mu\text{m}$ , which carries no impact in the generation of the focal wave. Here the effective area of the thick lens including the focal region decreases to  $A_{\text{eff}} = 20\lambda^2$ . As suggested above, an all-dielectric central zone is used to maximize the energy efficiency of the focusing device. The resultant focal spot again remains near the diffraction limit without a significant distortion in comparison with a virtually aberration-free focal wave. We may conclude that the reduction of the lens radius can be preceded in effect, however, limited by diffraction.

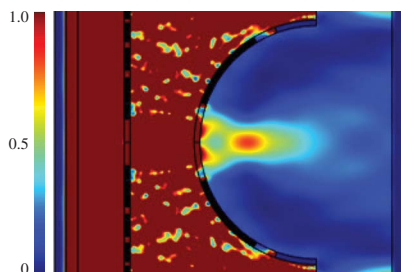


**Fig. 10.** Intensity of the magnetic field in the focal region of a meta-coated Si plano-concave lens of radius  $R = 2 \mu\text{m}$ , setting the focal shift parameter as  $a = 1 \mu\text{m}$ .

## 5. CONCLUSIONS

We designed cascaded metacoatings for the plano-concave surfaces of a wavelength-scale silicon lens to tightly focus light in the interior of the hollow opening in the form of a light tongue, which can shift laterally by controlling the tilt angle of the incident plane wave. The gradient-index metacoatings are here composed of a patterned gold film with engineered nanoslits, thus offering reduced Ohmic losses and efficient coupling to the exterior radiation. We point out that parallelization of metacoatings and alternatively metasurfaces might be carried out by means of auxiliary phase shifters like nanoholes and nanoantennas. Furthermore, suitable designs for terahertz and lower frequencies can also benefit from engineered metamaterials with ultrahigh index of refraction [42–44]. Mid-IR wavefront shaping can be carried out also using all-dielectric subwavelength high-index-contrast gratings offering a low-loss performance [45]. Finally, compact multifocal nanolenses might be developed following, for instance, the procedure of Refs. [46,47]. Implemented in a lenslet array, multifunctional platforms might be conceived for potential applications in sensing and optical trapping, where the light tongue is optically activated.

**Funding.** Spanish Ministerio de Economía y Competitividad (MINECO) (TEC2014-53727-C2-1-R).

## REFERENCES

- C. G. Parazzoli, R. B. Gregor, J. A. Nielsen, M. A. Thompson, K. Li, A. M. Vetter, M. H. Tanielian, and D. C. Vier, "Performance of a negative index of refraction lens," *Appl. Phys. Lett.* **84**, 3232–3234 (2004).
- P. Vodo, P. V. Parimi, W. T. Lu, and S. Sridhar, "Focusing by plano-concave lens using negative refraction," *Appl. Phys. Lett.* **86**, 201108 (2005).
- B. D. F. Casse, W. T. Lu, Y. J. Huang, and S. Sridhar, "Nano-optical microlens with ultrashort focal length using negative refraction," *Appl. Phys. Lett.* **93**, 053111 (2008).
- J. Xu, Y. Zhong, S. Wang, Y. Lu, H. Wan, J. Jiang, and J. Wang, "Focus modulation of cylindrical vector beams by using 1D photonic crystal lens with negative refraction effect," *Opt. Express* **23**, 26978–26985 (2015).
- M. Beruete, M. Navarro-Cía, M. Sorolla, and I. Campillo, "Planoconcave lens by negative refraction of stacked subwavelength hole arrays," *Opt. Express* **16**, 9677–9683 (2008).
- M. Navarro-Cía, M. Beruete, M. Sorolla, and N. Engheta, "Lensing system and Fourier transformation using epsilon-near-zero metamaterials," *Phys. Rev. B* **86**, 165130 (2012).
- H. Gao, J. K. Hyun, M. H. Lee, J.-C. Yang, L. J. Lauhon, and T. W. Odom, "Broadband plasmonic microlenses based on patches of nanoholes," *Nano Lett.* **10**, 4111–4116 (2010).
- S. Ishii, V. M. Shalaev, and A. V. Kildishev, "Holey-metal lenses: sieving single modes with proper phases," *Nano Lett.* **13**, 159–163 (2013).
- C. Ma and Z. Liua, "A super resolution metalens with phase compensation mechanism," *Appl. Phys. Lett.* **96**, 183103 (2010).
- L. Verslegers, P. B. Catrysse, Z. Yu, J. S. White, E. S. Barnard, M. L. Brongersma, and S. Fan, "Planar lenses based on nanoscale slit arrays in a metallic film," *Nano Lett.* **9**, 235–238 (2009).
- A. Ahmadi, S. Ghadarghadr, and H. Mosallaei, "An optical reflectarray nanoantenna: the concept and design," *Opt. Express* **18**, 123–133 (2010).
- Y. Huang, Q. Zhao, S. K. Kalyoncu, R. Torun, Y. Lu, F. Capolino, and O. Boyraz, "Phase-gradient gap-plasmon metasurface based blazed grating for real time dispersive imaging," *Appl. Phys. Lett.* **104**, 161106 (2014).
- P. Wróbel, J. Pniewski, T. J. Antosiewicz, and T. Szoplik, "Focusing radially polarized light by a concentrically corrugated silver film without a hole," *Phys. Rev. Lett.* **102**, 183902 (2009).
- F. Aieta, P. Genevet, M. A. Kats, N. Yu, R. Blanchard, Z. Gaburro, and F. Capasso, "Aberration-free ultrathin flat lenses and axicons at telecom wavelengths based on plasmonic metasurfaces," *Nano Lett.* **12**, 4932–4936 (2012).
- N. Yu, P. Genevet, F. Aieta, M. A. Kats, R. Blanchard, G. Aoust, J.-P. Tetienne, Z. Gaburro, and F. Capasso, "Flat optics: controlling wavefronts with optical antenna metasurfaces," *IEEE J. Sel. Top. Quantum Electron.* **19**, 4700423 (2013).
- A. Epstein and G. V. Eleftheriades, "Huygens' metasurfaces via the equivalence principle: design and applications," *J. Opt. Soc. Am. B* **33**, A31–A50 (2016).
- L. Verslegers, P. B. Catrysse, Z. Yu, and S. Fan, "Planar metallic nanoscale slit lenses for angle compensation," *Appl. Phys. Lett.* **95**, 071112 (2009).
- S. Ishii, A. V. Kildishev, V. M. Shalaev, K.-P. Chen, and V. P. Drachev, "Metal nanoslit lenses with polarization-selective design," *Opt. Lett.* **36**, 451–453 (2011).
- A. Arbabi, Y. Horie, A. J. Ball, M. Bagheri, and A. Faraon, "Subwavelength-thick lenses with high numerical apertures and large efficiency based on high-contrast transmitarrays," *Nat. Commun.* **6**, 7069 (2015).
- S. J. Byrnes, A. Lenef, F. Aieta, and F. Capasso, "Designing large, high-efficiency, high-numerical aperture, transmissive meta-lenses for visible light," *Opt. Express* **24**, 5110–5124 (2016).
- F. Aieta, P. Genevet, M. Kats, and F. Capasso, "Aberrations of flat lenses and aplanatic metasurfaces," *Opt. Express* **21**, 31530–31539 (2013).
- J. Rho, Z. Ye, Y. Xiong, X. Yin, Z. Liu, H. Choi, G. Bartal, and X. Zhang, "Spherical hyperlens for two-dimensional sub-diffractive imaging at visible frequencies," *Nat. Commun.* **1**, 143 (2010).
- Y. A. Barnakov, N. Kiriya, P. Black, H. Li, A. V. Yakim, L. Gu, M. Mayy, E. E. Narimanov, and M. A. Noginov, "Toward curvilinear metamaterials based on silver-filled alumina templates," *Opt. Mater. Express* **1**, 1061–1064 (2011).
- D. Lu and Z. Liu, "Hyperlenses and metalenses for far-field super-resolution imaging," *Nat. Commun.* **3**, 1205 (2012).
- M. Naserpour, C. J. Zapata-Rodríguez, A. Zakery, and J. J. Miret, "Highly localized accelerating beams using nano-scale metallic gratings," *Opt. Commun.* **334**, 79–84 (2015).
- M. Naserpour, C. J. Zapata-Rodríguez, A. Zakery, C. Díaz-Aviñó, and J. J. Miret, "Accelerating wide-angle converging waves in the near field," *J. Opt.* **17**, 015602 (2015).
- M. Naserpour, C. J. Zapata-Rodríguez, A. Zakery, and J. J. Miret, "Light capsules shaped by curvilinear meta-surfaces," *Appl. Phys. B* **120**, 551–556 (2015).
- C.-P. Huang, "Efficient and broadband polarization conversion with the coupled metasurfaces," *Opt. Express* **23**, 32015–32024 (2015).

29. X. Yi, X. Ling, Z. Zhang, Y. Li, X. Zhou, Y. Liu, S. Chen, H. Luo, and S. Wen, "Generation of cylindrical vector vortex beams by two cascaded metasurfaces," *Opt. Express* **22**, 17207–17215 (2014).
30. C. Pfeiffer and A. Grbic, "Cascaded metasurfaces for complete phase and polarization control," *Appl. Phys. Lett.* **102**, 231116 (2013).
31. V. Torres, B. Orzabayev, V. Pacheco-Peña, J. Teniente, M. Beruete, M. Navarro-Cía, M. S. Ayzá, and N. Engheta, "Experimental demonstration of a millimeter-wave metallic ENZ lens based on the energy squeezing principle," *IEEE Trans. Antennas Propag.* **63**, 231–239 (2015).
32. M. Naserpour, C. J. Zapata-Rodríguez, C. Díaz-Aviñó, M. Hashemi, and J. J. Miret, "Ultrathin high-index metasurfaces for shaping focused beams," *Appl. Opt.* **54**, 7586–7591 (2015).
33. D. Lin, P. Fan, E. Hasman, and M. L. Brongersma, "Dielectric gradient metasurface optical elements," *Science* **345**, 298–302 (2014).
34. F. Qin, L. Ding, L. Zhang, F. Monticone, C. C. Chum, J. Deng, S. Mei, Y. Li, J. Teng, M. Hong, S. Zhang, A. Alù, and C.-W. Qiu, "Hybrid bilayer plasmonic metasurface efficiently manipulates visible light," *Sci. Adv.* **2**, e1501168 (2016).
35. S. M. Rytov, "Electromagnetic properties of a finely stratified medium," *Sov. Phys. J. Exp. Theor. Phys.* **2**, 466–475 (1956).
36. E. Popov and S. Enoch, "Mystery of the double limit in homogenization of finitely or perfectly conducting periodic structures," *Opt. Lett.* **32**, 3441–3443 (2007).
37. P. Yeh, *Optical Waves in Layered Media* (Wiley, 1988).
38. J. Elser, V. A. Podolskiy, I. Salakhutdinov, and I. Avrutsky, "Nonlocal effects in effective-medium response of nanolayered metamaterials," *Appl. Phys. Lett.* **90**, 191109 (2007).
39. L. Martín-Moreno, F. J. García-Vidal, H. J. Lezec, K. M. Pellerin, T. Thio, J. B. Pendry, and T. W. Ebbesen, "Theory of extraordinary optical transmission through subwavelength hole arrays," *Phys. Rev. Lett.* **86**, 1114–1117 (2001).
40. W. Chen, M. D. Thoreson, S. Ishii, A. V. Kildishev, and V. M. Shalaev, "Ultra-thin ultra-smooth and low-loss silver films on a germanium wetting layer," *Opt. Express* **18**, 5124–5134 (2010).
41. C. Díaz-Aviñó, D. Pastor, C. J. Zapata-Rodríguez, M. Naserpour, R. Kotyński, and J. J. Miret, "Some considerations on the transmissivity of birefringent metamaterials," *J. Opt. Soc. Am. B* **33**, 116–125 (2016).
42. J. Shin, J.-T. Shen, and S. Fan, "Three-dimensional metamaterials with an ultrahigh effective refractive index over a broad bandwidth," *Appl. Phys. Lett.* **102**, 093903 (2009).
43. M. Choi, S. H. Lee, Y. Kim, S. B. Kang, J. Shin, M. H. Kwak, K.-Y. Kang, Y.-H. Lee, N. Park, and B. Min, "A terahertz metamaterial with unnaturally high refractive index," *Nature* **470**, 369–373 (2011).
44. S. Lee, "Colloidal superlattices for unnaturally high-index metamaterials at broadband optical frequencies," *Opt. Express* **23**, 28170–28181 (2015).
45. Y. Huang, Q. Zhao, S. K. Kalyoncu, R. Torun, and O. Boyraz, "Silicon-on-sapphire mid-IR wavefront engineering by using subwavelength grating metasurfaces," *J. Opt. Soc. Am. B* **33**, 189–194 (2016).
46. E. Mudry, E. L. Moal, P. Ferrand, P. C. Chaumet, and A. Sentenac, "Isotropic diffraction-limited focusing using a single objective lens," *Phys. Rev. Lett.* **105**, 203903 (2010).
47. M. Hashemi, A. Moazami, M. Naserpour, and C. J. Zapata-Rodríguez, "A broadband multifocal metalens in the terahertz frequency range," *Opt. Commun.* **370**, 306–310 (2016).

6<sup>th</sup> Publication:  
**Accelerating Wide-Angle Converging  
Waves in the Near Field**

**Authors:** Mahin Naserpour, Carlos J. Zapata-Rodríguez,  
Abdolnaser Zakery, Carlos Díaz-Aviñó and Juan J. Miret

Published in **Journal of Optics**, volume 17, 015602 (10pp), year  
2015.

# Accelerating wide-angle converging waves in the near field

Mahin Naserpour<sup>1,2</sup>, Carlos J Zapata-Rodríguez<sup>1</sup>, Abdolnaser Zakery<sup>2</sup>, Carlos Díaz-Aviñó<sup>1</sup> and Juan J Miret<sup>3</sup>

<sup>1</sup>Department of Optics, University of Valencia, Dr. Moliner 50, E-46100 Burjassot, Spain

<sup>2</sup>Department of Physics, College of Sciences, Shiraz University, Shiraz 71946-84795, Iran

<sup>3</sup>Department of Optics, Pharmacology and Anatomy, University of Alicante, P.O. Box 99, Alicante, Spain

E-mail: [carlos.zapata@uv.es](mailto:carlos.zapata@uv.es)

Received 16 September 2014, revised 4 November 2014

Accepted for publication 5 November 2014

Published 12 December 2014



## Abstract

We show that a wide-angle converging wave may be transformed into a shape-preserving accelerating beam having a beam-width near the diffraction limit. For that purpose, we followed a strategy that is particularly conceived for the acceleration of nonparaxial laser beams, in contrast to the well-known method by Siviloglou *et al* (2007 *Phys. Rev. Lett.* **99** 213901). The concept of optical near-field shaping is applied to the design of non-flat ultra-narrow diffractive optical elements. The engineered curvilinear caustic can be set up by the beam emerging from a dynamic assembly of elementary gratings, the latter enabling to modify the effective refractive index of the metamaterial as it is arranged in controlled orientations. This light shaping process, besides being of theoretical interest, is expected to open up a wide range of broadband application possibilities.

Keywords: invariant optical fields, artificially engineered materials, diffraction theory

PACS numbers: 42.25.Fx, 42.79.Dj, 61.05.jm, 78.67.Pt

(Some figures may appear in colour only in the online journal)

## 1. Introduction

Controlling wave fields at the nanoscale has opened up a vast range of novel phenomena that have been put to use in applications requiring ultra-compact photonic devices. Among these phenomena we find subwavelength imaging [1], optical cloaking [2], surface enhanced spectroscopy [3], and extraordinary optical transmission [4], to name a few. All of them are unique in conducting extremely localized wave fields, becoming evanescent in free space. This ability to govern a multichannel electromagnetic propagation within spaces below the wavelength allowed the design of diffractive optical elements (DOEs) with elementary scatterers being either optical antennas, plasmonic/metallic [5] or dielectric [6], corrugations [7] or nanoholes [8] with resolutions near the diffraction limit. Filters for colour printing [9, 10], polarization converters [11–13], lenses [14–16], and axicons [17, 18], are some of the optical devices that have benefited from this remarkable spatial confinement.

In the majority of these plasmonic devices submitted to date, the key proposal is the transformation of a plane wave that, by passing through a flat DOE, becomes a structured field with a tailored wavefront and polarization state. Notably, more sophisticated designs with non-planar geometries allow improved performance for the moulding of electromagnetic waves [19–22]. Thus it has been possible the focusing of wave fields with high numerical aperture, which results an essential factor to achieve a tight location with sizes close to the diffraction limit. Nevertheless, the control of monochromatic aberrations are inherently challenging in the near-field, limiting the potential applications of these DOEs accordingly.

An alternate route not presented so far, to the knowledge of the authors, may be found in the short conversion of a given high-aperture aberration-free focused beam by means of a DOE. However, if flat DOEs are employed in this case, inadequate beam shaping might result induced by optical aberrations [23, 24]. For this reason, a more advantageous procedure implies the use of diffracting arrangements having the same cylindrical or spherical symmetry of the impinging



focused beam, the latter being precedently generated in the far field.

Here we perform an exhaustive analysis of an optical method preliminary reported in [25] to shape high-aperture focal waves into diffraction-free nonparaxial beams with extreme spatial acceleration. Such Airy beams [26] with Bessel signature have been recently discussed in the literature, both from theoretical premises [27–29] and also with experimental evidences [30, 31]. This should not be understood as a nondiffracting Bessel beam with asymmetric transverse profile mimicking an Airy function recently analyzed in [32].

Let us point out that the controversial use of the term acceleration has its genesis in the paper of Berry and Balazs [33] where they illustrated the fact that an Airy wave packet, which is solution to the Schrödinger equation, exhibits a form-preserving probability density that continually accelerates, even though no force acts over the particles. Its optical analog in terms of time-harmonic beams rather than wave packets was first discussed in [34] keeping the original depiction.

In this context we highlight some previous schemes for generating Airy beams, which are based on the use of sub-wavelength metallic gratings [35, 36]. Nevertheless, the resulting nondiffracting beams exhibit moderate acceleration, greatly limited by their unequivocal paraxiality.

This paper is structured as follows. Since the scattered fields by the DOE are derived using the Debye diffraction integral, the latter is introduced in the next section. In section 3 we give a theoretical introduction to spatially accelerated beams, with particular emphasis on those exhibiting Bessel signature. This analysis will include the underlying mechanisms enabling the transformation of focal waves to accelerate beams with incomplete circular trajectories. In section 4 we will present a novel plasmonic nanoelement for acceleration of cylindrical beams in the vicinities of the focal region. The broadband response is also shown in detail. Section 5 analyzes some practical limitations of our proposals governed by the current nanotechnology, and we introduce some promising alternatives providing satisfactory results. Both dissipative effects and non-local effects are investigated in detail. Finally, the main conclusions of our study are outlined.

## 2. The Debye diffraction integral

In this section we will briefly consider the classical problem of diffraction in relation with a monochromatic converging wave that is diffracted by an aperture. Our purpose is to establish some suitable conditions for the transformation of a cylindrical wave into an accelerating beam. The schematic arrangement is depicted in figure 1(a). For simplicity, we will consider two-dimensional waves propagating in the  $zx$  plane, and therefore the magnetic field  $\mathbf{H}(z, x, t)$  of a given transverse-magnetic (TM) mode with time-domain frequency  $\omega$  can be set as  $H(z, x) \exp(-i\omega t) \hat{\mathbf{y}}$ ,  $\hat{\mathbf{y}}$  being the unitary vector pointing along the  $y$ -axis. Note that the validity of our

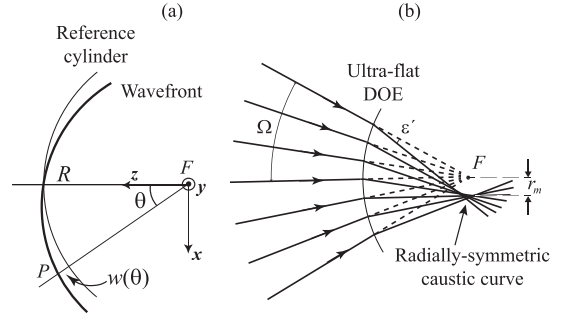


**Figure 1.** (a) Schematic arrangement representing the diffracted converging wave of focal point  $F$  as evaluated from the Debye diffraction integral (1). The emerging wavefront propagates in the  $xz$  plane and deviates from the reference cylinder by  $w(\theta)$ . (b) A focused beam of semi-aperture angle  $\Omega$  will be diffracted by an ultra-flat DOE set on the reference cylinder to induce a spatial acceleration by means of a transferred spatial frequency  $k \sin \epsilon'$ , that is also given by  $m/R$ , where  $R$  is the reference cylinder radius (also DOE radius). Wave localization will be observed along a caustic curve of radius  $r_m$  with center at focus  $F$ .

approach is straightforwardly extended to transverse-electric polarization by applying the duality theorem. Moreover, although uncommonly, our full-wave electromagnetic analysis is given in terms of the ‘scalar’ magnetic field  $H(\mathbf{r})$  since TM polarized waves enable to excite surface plasmon polaritons (SPPs) in metal–dielectric nanostructures, and thus to shape a beam using an ultra-flat plasmon-based DOE. In agreement with the diffraction theory of Debye, the wave field in the focal region might be estimated by means of the following diffraction integral, namely [37, 38]

$$H(\mathbf{r}) = \sqrt{\frac{kR}{2\pi i}} \exp(ikR) \int_{-\pi}^{\pi} H_S(\theta) \exp[-ik(\hat{\mathbf{q}} \cdot \mathbf{r})] d\theta, \quad (1)$$

where  $\mathbf{r} = (z, x)$ ,  $R$  is the radius of the diffracted cylindrical wave as taken over the reference cylinder (see figure 1(a)),  $k = \omega/c$  is the wave number, and  $H_S$  represents the magnetic field over the same reference cylinder. Finally,  $\hat{\mathbf{q}} = (\cos \theta, \sin \theta)$  is a unit vector pointing from the focus  $F$  in the direction of a given point  $P$  on the wavefront.

For the sake of clarity, the scattered wave field  $H_S(\theta)$ , which emerges from the ultra-flat DOE of radius  $R$  as illustrated in figure 1(b), will be expressed by means of a real and positive term,  $A(\theta)$ , and a phase only term  $\exp[iw(\theta)]$ , giving

$$H_S(\theta) = A(\theta) \exp[iw(\theta)]. \quad (2)$$

The apodization function  $A(\theta)$  takes into account the truncation of the converging field after passing through the diffracting optical element, and  $w(\theta)$  denotes deviations of the wavefront of the converging field from the reference cylinder representing monochromatic aberrations. In our case, the designed  $w(\theta)$  will be induced by a DOE in order to shape an aberration-free cylindrical wave. In our numerical simulations, we will consider a super-Gaussian apodization function

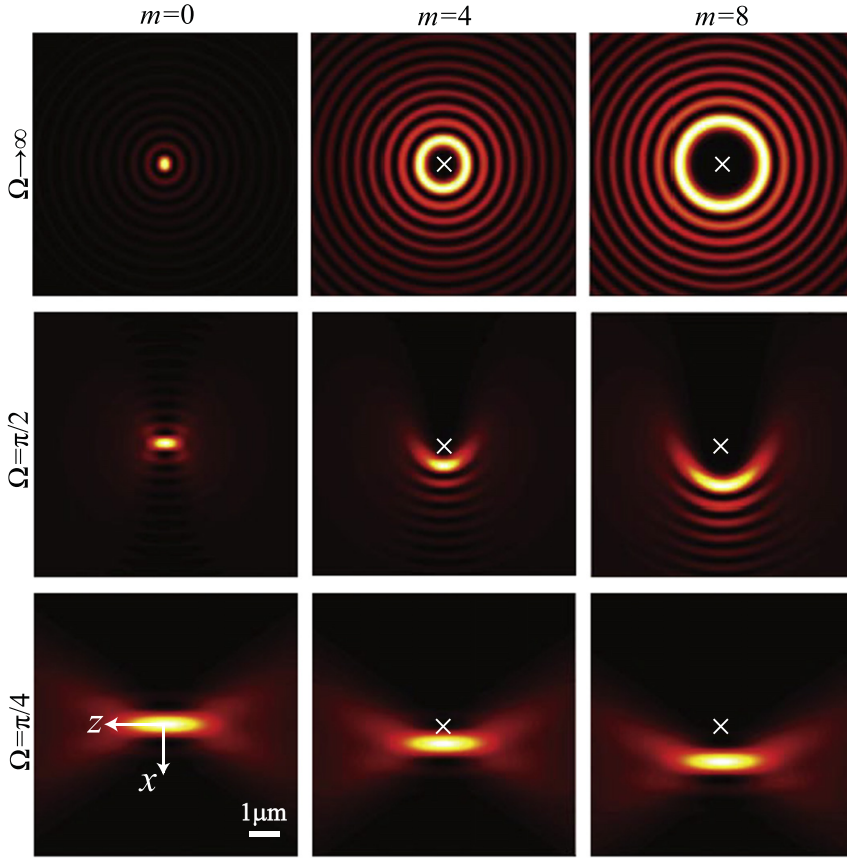


**Figure 2.** Intensity distribution  $|H(\mathbf{r})|^2$  derived by the Debye diffraction integral (1) for different semi-apertures  $\Omega$  and normalized radius  $m$ . White cross indicates the focal point of the converging beam.

rather than a customary flat-top profile, given by

$$A(\theta) = A_0 \exp\left[-(\theta/\Omega)^6\right], \quad (3)$$

of semi-aperture angle  $\Omega$ , enabling to minimize edge effects. We point out that the limits of integration in equation (1) makes the Debye diffraction wave fields practically unaltered for  $\Omega = \pi$  and higher values.

Furthermore we may consider a series expansion of  $w(\theta)$  in the vicinity of  $\theta = 0$ , a procedure that is commonly assumed to be adequate primarily in the paraxial regime. If we disregard defocusing and higher-order terms of the Taylor expansion, we finally set  $w(\theta) = m\theta$ , where we also neglected a constant term that will not contribute significantly in the diffraction integral (1). In fact, our DOE will be engineered to shape the wavefront of a converging field following a simple linear dependence in the coordinate  $\theta$ . Importantly, such a phase-only beam shaping will be necessarily performed over wide-angle converging waves, in contrast to the well-known method followed by Siviloglou *et al* [26]. Otherwise the diffracted field would yield an aberration-free off-axis focused beam, which is not spatially accelerated.

As a concluding remark, we make a further point of the validity of our procedure, which is not limited to the near field in agreement with the legitimacy of equation (1).

We point out that the parameter  $m$  governs the curvilinear trajectory of the focused field around the geometrical focus  $F$ , as depicted in figure 1(b). The converging wave locally carries a transverse spatial frequency given by  $m/R$  driving a wavefront tilt with angular deviation  $\epsilon'$  over the reference cylinder. In terms of optical rays, the resultant caustic curve will have a radius  $r_m = R \sin \epsilon'$ . As a consequence we may set  $r_m = |m|/k$ . Further agreement with diffraction patterns will be seen below within the regime of validity of the Debye formulation [37].

### 3. Focal waves with spatial acceleration

In figure 2 we show the field intensity  $|H(\mathbf{r})|^2$  for a converging wave field of different semi-apertures  $\Omega$  and values for the parameter  $m$  at a wavelength  $\lambda = 632.8$  nm. The values of the intensity are normalized to a maximum of unity so that the

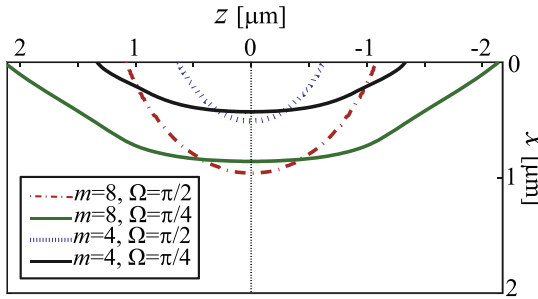


**Figure 3.** Trajectories for some of the wave fields whose intensity is shown in figure 2.

resulting profile becomes independent of the radius  $R$  of the cylindrical beam. We observe that the parameter  $m$  determines the distance from the geometrical focus  $F$  where the beam is localized, leading to a controlled acceleration of the focused beam. Before the beam spreads out, it takes a circular trajectory whose radius may be roughly estimated as  $r_m = |m|/k$  [29]. For instance, such radius for  $m = 4$  yields  $r_4 = 403$  nm, which is clearly subwavelength, however it is duplicated for  $m = 8$ . As a consequence, the curvature  $\kappa = 1/r_m$  of the trajectory governing the acceleration of the beam is inversely proportional to the parameter  $m$ . On the other hand, the length of such incomplete circular trajectory may be estimated under a geometrical basis. In this approach, the semi-aperture  $\Omega$  governs the length  $L_m$  of the accelerating-beam trajectory by means of the simple expression  $L_m = r_m \Omega$  [29].

Figure 3 illustrates the trajectories of different accelerating beams whose field intensity were previously shown in figure 2. Every trajectory is determined by points of maximum intensity  $|H(\mathbf{r})|^2$  by keeping fixed the polar angle  $\alpha$  of the position vector  $\mathbf{r}$ . Note that such a procedure differs from some other established ones where the intensity maximum is measured at different planes normal to the  $z$ -axis [26]. Before the wave packet is bent near the geometrical focus  $F$ , the intensity maximum of the beam determining its trajectory follows a linear equation. Subsequent to the accelerating course in the focal region, the beam restores its straight trajectory, however exhibiting a different slope. In agreement with the previous geometrical analysis,  $\Omega$  would determine the angle between these two linear trajectories inherently associated with the far field. However, we observe some discrepancies, especially for the lowest values of the parameter  $m$ . For instance, the trajectory gyration is  $94^\circ$  ( $64^\circ$ ) at  $m = 8$  and  $\Omega = \pi/2$  ( $\Omega = \pi/4$ ). Another aperture-dependent effect that is clearly seen in figure 3 is the position of the trajectory vertex. For the particular case of  $m = 8$  we observe that the vertex is on the focal plane,  $z = 0$ , at  $x = 0.96 \mu\text{m}$  ( $x = 0.86 \mu\text{m}$ ) for  $\Omega = \pi/2$  ( $\Omega = \pi/4$ ). Finally note that the incomplete circular trajectory is evident only for high angles  $\Omega$ , and that  $r_m = |m|/k$  predicts peak positions at radii slightly shorter than those observed in figure 3. In summary, the trajectory gyration decreases and its vertex shifts to the focal point  $F$  as long as the semi-aperture angle  $\Omega$  decreases. This

is in agreement with the fact that spatial acceleration ceases to occur for a low- $\Omega$  distribution where the beam falls into a rectangular symmetry [29, 39].

### 3.1. Bessel wave fields

Let us point out the existence of an analytical solution for the Debye integral equation (1), in the terms analyzed here, provided that  $\Omega \rightarrow \infty$ . In this case  $A(|\theta| \leq \pi) \rightarrow A_0$ , that is, there is no truncation of the focal field, which in addition has a plane-wave Fourier expansion with uniform angular distribution. In practical terms this occurs whenever  $\Omega > \pi$ . If we further assume that the normalized radius  $m$  is an integer, the magnetic field in equation (1) finally yields

$$H_B(\mathbf{r}) = (-i)^{m+1/2} A_0 \sqrt{2\pi k R} \exp(ikR + ima) J_m(kr), \quad (4)$$

where  $\alpha$  is the angle of the vector  $\mathbf{r}$  with respect to the positive  $z$ -axis, and  $J_m(\cdot)$  is the Bessel function of order  $m$ . The intensity distribution of these Bessel wave fields with different order  $m$  is shown in figure 2. Let us note that the phase distribution measured along the circular caustic curve of radius  $r_m$  is given by the term  $m\alpha = \pm kl$ , where  $l$  denotes the spatial coordinate  $l = r_m \alpha$ , and  $\pm$  is determined by  $\sigma_m = m/|m|$ ; this result indicates that the spatial frequency of the accelerating beam along its caustic curve is  $k$  coinciding with that of a plane wave in free space [40].

In the previously analyzed cases being  $\Omega < \pi$ , where the circular caustic curve is incomplete, the resultant accelerating beam resembles a Bessel wave field at least in regions neighboring such caustic curve. Explicitly, based on the principle of stationary phase, one might estimate a distribution of the field  $H(\mathbf{r}) = A(\alpha - \sigma_m \pi/2) H_B(\mathbf{r})/A_0$ , provided that  $|r| \approx r_m$  [29]. This represents a sector Bessel wave field centered on the positive (negative)  $x$ -axis for  $m > 0$  ( $m < 0$ ). For this reason, this sort of accelerating beams are also coined incomplete Bessel beams [27].

We point out that the FWHM, measured along the  $x$ -axis, of the high-numerical-aperture ( $\Omega = \pi/2$ ) focused beam that is associated with  $m = 0$  shown in figure 2 is equal to  $234$  nm, which is subwavelength ( $\lambda = 632.8$  nm) and approaching the diffraction limit. However, to generate an accelerating beam the parameter  $m$  has to be increased necessarily. This fact certainly leads to a wider main lobe. Note that the FWHM of the main peak of this sort of accelerating beams is approximately given by the width of the Bessel wave field driving its incomplete trajectory, which roughly follows the relation [29]

$$\text{FWHM} = C \lambda m^{1/3}, \quad (5)$$

where  $C = 0.220$ . This is illustrated in figure 4, where the asymptote set in solid red line and representing equation (5) provides accurate results for  $m > 10$ . To serve as an example, the FWHM of the main lobe for the incomplete Bessel wave field ( $\Omega = \pi/2$ ) of order  $m = 30$  is equal to  $425$  nm, however it drops to  $285$  nm if  $m = 8$  as depicted in figure 2. The accelerating beams remain subwavelength for these two values of  $m$ ; however according to equation (5) one can realize that further increments of the parameter  $m$  would lead

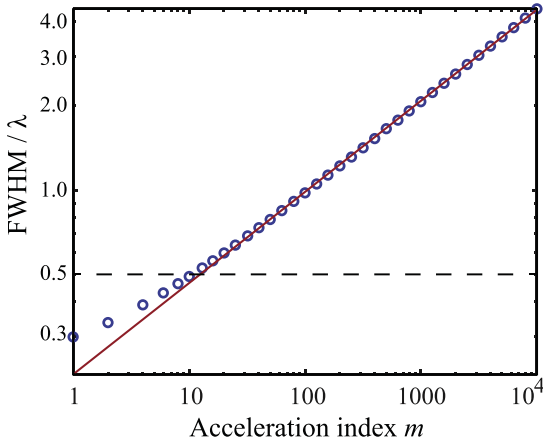


**Figure 4.** Normalized FWHM of a Bessel wave field ( $\Omega \rightarrow \infty$ ) as a function of the normalized radius  $m$ . The circles denote results given from numerical simulations, whereas the solid red line represents equation (5).

to beam widths surpassing  $\lambda$ . We finally conclude that generation of subwavelength accelerating beams is only possible by using low order Bessel precursors.

#### 4. Subwavelength DOEs for the acceleration of focal waves

By simple inspection of figure 2, particularly for  $\Omega = \pi/4$ , one can realize that the role of the phase-only term  $\exp(im\theta)$  appearing in the scattered wave field  $H_S$  is functionally identical to the phase term produced by a prism (also a blazed grating) achieving a focal shift at  $(m/k, 0)$ . Although not shown in figure 2, this is even more evident in the paraxial regime, that is for  $\Omega \ll 1$  [29]. Following this principle, an engineered curvilinear caustic can be set up by the beam emerging from a dynamic array of elementary DOEs, the latter enabling to modify the effective refractive index of the metamaterial and subsequently induce a given linear dephase of the incident wave field as it is arranged in controlled orientations. In case that the caustic curve exhibited a circular symmetry, as in our case, the graded DOE naturally has an annular shape.

Our purpose is the design of a nanostructured circular DOE inducing of a dephase with linear variation in the azimuthal coordinate  $\theta$  in a way that a convergent wave may be transformed into an accelerating beam. Since this transformation is preferably carried out in regions of reduced size typically of a few wavelengths, metallic nanoparticles are excellent candidates demonstrating to mold light below the wavelength. In addition, such DOE will be set in the vicinities of the focal region leading to a near-field shaping. For simplicity, we propose an optical system based on multilayer metal-dielectric stacks [41, 42]. Differently from the ordinary planar distribution, our nanostructure is arranged following a

circular pattern. We point out that analogous schemes have been reported for hyperlensing [21, 43].

Let us first reveal a proof of concept of the underlying beam shaping using graded DOEs with rectangular symmetry. It is widely known that the periodic array of metallic slits with nanoscale size optically behaves like an effective uniaxial crystal [44–46]. When light passes through the metallic slits, coupled surface plasmons are excited enabling propagation in semi-transparent effective media exhibiting extreme anisotropy. Under this long-wavelength regime, the dispersion equation of TM-polarized waves propagating in a multilayered nanostructure composed of a metal and a dielectric of relative electric permittivity  $\epsilon_m$  and  $\epsilon_d$  and deep-sub-wavelength width  $w_m$  and  $w_d$ , respectively, is given by

$$\frac{k_{\perp}^2}{\epsilon_{\parallel}} + \frac{k_{\parallel}^2}{\epsilon_{\perp}} = k^2, \quad (6)$$

where  $k_{\perp}$  and  $k_{\parallel}$  are the components of the wave vector propagating along a perpendicular and parallel direction of the layers, being the associated unit vectors  $\hat{\theta}_{\perp}$  and  $\hat{\theta}_{\parallel}$  respectively. Also the effective dielectric constant

$$\bar{\epsilon} = \epsilon_{\perp} \hat{\theta}_{\perp} \otimes \hat{\theta}_{\perp} + \epsilon_{\parallel} \hat{\theta}_{\parallel} \otimes \hat{\theta}_{\parallel} \quad (7)$$

finally is given by [47]

$$\epsilon_{\parallel} = \epsilon_m f + \epsilon_d (1 - f), \quad (8)$$

$$\epsilon_{\perp} = \frac{\epsilon_m \epsilon_d}{\epsilon_m (1 - f) + \epsilon_d f}, \quad (9)$$

where  $f = w_m/(w_m + w_d)$  is the metal filling factor. As a result, it can be used to induce a controlled phase delay.

Let us consider a wave field propagating along the metallic grating ( $k_{\perp} = 0$ ), which evolves with a spatial frequency (also known as propagation constant)  $k_{\parallel} = n_B k$ , and  $n_B = \sqrt{\epsilon_{\perp}}$  is the Bloch-mode refractive index. For the sake of clarity material losses are neglected in section 4 thus  $\epsilon_m, \epsilon_d, \epsilon_{\perp}$  and  $\epsilon_{\parallel}$  will be real permittivities. The wave field might experience a linear dephase distribution provided the effective refractive index

$$n_B(\theta_{\perp}) = n_0 + n_1 \theta_{\perp} \quad (10)$$

also varies linearly upon the transverse spatial coordinate  $\theta_{\perp}$ . The above assumption is valid for a slowly-varying refractive index, that is  $|n_1| \ll k$ . This effect can be achieved provided that the metal filling factor also varies upon the transverse spatial coordinate,

$$f(\theta_{\perp}) = \frac{\epsilon_m \left[ \epsilon_d - (n_0 + n_1 \theta_{\perp})^2 \right]}{(n_0 + n_1 \theta_{\perp})^2 (\epsilon_d - \epsilon_m)}, \quad (11)$$

as can be seen inserting equation (11) into equation (9). In this case, the effective permittivity  $\epsilon_{\perp}(\theta_{\perp})$  changes quadratically in space and  $\epsilon_{\parallel}$  in equation (8) will also vary, as shown in figure 5. In the latter figure we set  $\epsilon_d = 1$  for the dielectric and  $\epsilon_m = -10.77$  for the metal (gold at  $\lambda = 632.8$  nm and neglecting losses [48]) composing the inhomogeneous effective-uniaxial medium. In addition, the modal effective

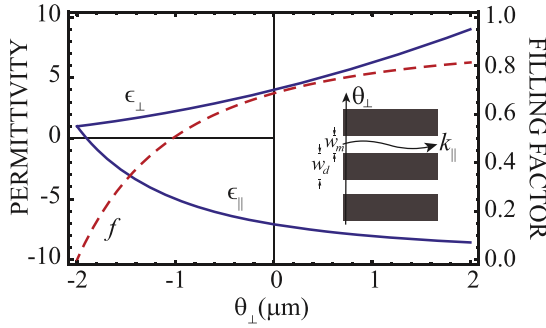


**Figure 5.** Spatial variation of the metal filling factor  $f$  and permittivities  $\epsilon_{\perp}$  and  $\epsilon_{\parallel}$  for an inhomogeneous MD nanostructure of effective index of refraction  $n_B = n_0 + n_1\theta_{\perp}$ , where  $n_0 = 2$  and  $n_1 = 0.5 \mu\text{m}^{-1}$ . Here we also consider  $\epsilon_d = 1$  and  $\epsilon_m = -10.77$ .

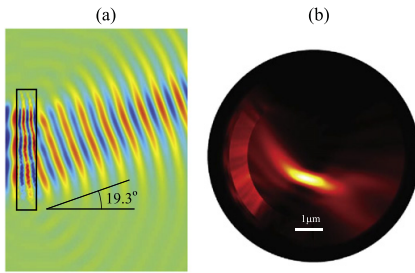


**Figure 6.** (a) Real part of the magnetic field  $H(z, x)$  for a plane wave scattered by our inhomogeneous anisotropic metamaterial with optical parameters given in figure 5. In (b) we represent the time-averaged energy density for an annular-shaped device with inner radius  $R_{ES} = 2.4415 \mu\text{m}$ .

index  $n_B$  is set to evolve linearly in  $\theta_{\perp}$  with  $n_0 = 2$  and  $n_1 = 0.5 \mu\text{m}^{-1}$ . However, bearing in mind that  $0 \leq f < f_{\infty}$ , this material processing can be achieved for  $\theta_{\perp} \geq -2 \mu\text{m}$ . Note that if  $f = 0$  then  $\epsilon_{\perp} = \epsilon_d$ ; on the other hand  $f_{\infty} = -\epsilon_m/(\epsilon_d - \epsilon_m)$  in the limit  $\theta_{\perp} \rightarrow \infty$  (that is  $\epsilon_{\perp} \rightarrow \infty$ ), which satisfies  $f_{\infty} < 1$ ; in our numerical example  $f_{\infty} = 0.915$ .

To illustrate the scattering behaviour of such inhomogeneous uniaxial metamaterial, figure 6(a) depicts the transmitted (and reflected) wave field of a collimated beam impinging on a planar thin film of thickness  $d = 660 \text{ nm}$  made of such plasmonic crystal with optical parameters given in figure 5. The numerical simulations were performed with a commercially-available program (COMSOL Multiphysics) based on the finite element method (FEM). Furthermore, a TM-polarized plane wave ( $\lambda = 632.8 \text{ nm}$ ) that is excited by a surface current is incident onto the left side of the nano-slit arrangement to prove the homogenized metamaterial. Perfectly matched layers were added to simulate electromagnetic waves that propagate into an unbounded domain. The dephase induced into the plane wave propagating within the metamaterial along the parallel direction of the composing

nanolayers is accurately estimated as

$$w(\theta_{\perp}) = n_B(\theta_{\perp})kd. \quad (12)$$

We observe in figure 6(a) that the normally incident field undergoes an angular deviation around  $e' = 19^{\circ}$ . We also note an unsatisfactory reflected signal that predominantly occurs when the optical path length difference  $2n_B d$  between each backscattered beam (of the Airy summation [47]) is  $\lambda/2$  plus an integer multiple of the wavelength; accordingly the dephase  $w(\theta_{\perp})$  of the transmitted optical signal equals  $\pi/2$  plus an integer multiple of  $\pi$  radians. This happens at four points in the working range  $|\theta_{\perp}| \leq 2 \mu\text{m}$  of our numerical example.

Note that there exists some limits in the DOE-based film thickness  $d$  for the wave field to emerge from the inhomogeneous metamaterial. In particular, the wave fields traveling inside the thin film gains a transverse spatial frequency that is given by  $n_1 kd$ , whose absolute value must be lower than  $k$  to subsequently propagate in free space. This constraint is set as  $d < |n_1|^{-1}$ ; in our numerical example  $d$  is lower than  $n_1^{-1} = 2 \mu\text{m}$ . Under these circumstances, the angle of the transmitted wave field is accurately estimated as  $e' = \sin^{-1}(n_1 d)$ , which in our numerical example reads  $e' = 19.3^{\circ}$ . The latter is in good agreement with our numerical simulations.

This analysis is carried out in a rectangular geometry, but also the circular arrangement being of major interest for us is also shown in figure 6(b). In the latter case, the dyadic permittivity is set as

$$\bar{\epsilon}(z, x) = \frac{1}{x^2 + z^2} \begin{bmatrix} z^2\epsilon_{\parallel} + x^2\epsilon_{\perp} & xz(\epsilon_{\parallel} - \epsilon_{\perp}) \\ xz(\epsilon_{\parallel} - \epsilon_{\perp}) & x^2\epsilon_{\parallel} + z^2\epsilon_{\perp} \end{bmatrix}, \quad (13)$$

in the Cartesian coordinate system. In figure 6(b) we show the time-averaged energy density of the wave field accelerated by the inhomogeneous uniaxial medium of permittivity given by equation (13) at  $\lambda = 632.8 \text{ nm}$ . The annular optical element is designed to convert a converging cylindrical wave into an accelerating beam with Bessel signature of order  $m = 8$ . An arc-shaped source surface current is set in front of the DOE to induce the focusing 2D field in the FEM-based simulations. For that purpose, and assuming that the index variation is governed by  $n_1 = 0.5 \mu\text{m}^{-1}$  and that the slab width is  $d = 660 \text{ nm}$  as in previous examples, the radius at the exit surface (ES) is estimated as  $R_{ES} = 2.4415 \mu\text{m}$ . The resultant incomplete Bessel beam is in good agreement with those shown in figure 2.

### 5. Practical implementation

To carry out the dephase process involved in this type of beam shaping, as discussed in detail in section 3, the thickness of the films comprising the metamaterial necessarily remains much shorter than the wavelength [45]. In the case of the stratified metal, in addition, its depth of penetration cannot be exceeded which is typically a few tens of nanometers in

the optical range. Otherwise, the long-wavelength approximation unequivocally provides wrong results [49, 50]. In addition, current technology allows to assemble ultra-thin, uniformly continuous metallic films of thicknesses of only 5 nm with reduced surface roughness of around 0.2 nm [51]. Nevertheless, lamellar composites including metallic nanofilms typically lead to a loss-enhanced effect [52]. As a consequence, optimal implementations of our inhomogeneous uniaxial metamaterial are based on nanostructures of metallic layers with a thickness close to its penetration depth.

A simple transfer matrix formulation may be used to achieve an analytical dispersion relation for waves propagating in the metal waveguide array with nanoscale size [47]. Importantly, this approach enables one to integrate the ohmic losses that inherently appear when using metallic elements in a metamaterial. Let us first consider the metal–dielectric multilayered medium in the simpler rectangular geometry. The phase  $w(x)$  gained by a Bloch mode propagating through the MD multilayered medium is specified by means of the modal index of refraction  $n_B = \text{Re}(k_{||})/k$ , where  $k_{||}$  is the complex propagation constant. The latter is computed from the dispersion relation applied to TM-polarized waves, which is derived from the Floquet–Bloch theorem, giving

$$\cos(k_B p) = \cosh(\eta_m) \cosh(\eta_d) + \frac{\epsilon_m^2 \kappa_{\perp d}^2 + \epsilon_d^2 \kappa_{\perp m}^2}{2\epsilon_m \epsilon_d \kappa_{\perp d} \kappa_{\perp m}} \sinh(\eta_m) \sinh(\eta_d), \quad (14)$$

where  $k_B$  is the Bloch wavenumber indicating the spatial frequency along a direction normal to the nanolayers,  $p = w_m + w_d$  is the *local* period of the nanostructure, and  $\eta_q = \kappa_{\perp q} w_q$  denotes the transverse decay of an on-axis homogeneous wave measured between the boundaries of either the metallic ( $q = m$ ) or the dielectric ( $q = d$ ) layer. Specifically

$$\kappa_{\perp q} = \sqrt{k_{||}^2 - \epsilon_q k^2}. \quad (15)$$

Again, by considering that the incident plane wave impinges normally to the metallic grating, and thus the Bloch mode also travels along such a direction, we solved equation (14) for  $k_B = 0$  (wave propagation along the slits). Finally, the relative permittivity of gold including losses is now  $\epsilon_m = -10.77 + 0.79i$  at the wavelength of interest,  $\lambda = 632.8$  nm [48].

Figure 7(a) shows a contour plot of the modal refractive index  $n_B$  for a Bloch wave field propagating along a given elementary grating with layer widths  $w_m$  and  $w_d$ . For  $w_m \leq 30$  nm and  $w_d \leq 100$  nm, no significant index mismatch is observed for invariant metal filling factor  $f = w_m/p$ , particularly for low and moderate  $f$ , a fact that is in excellent agreement with the effective medium approach [46]. Contrarily, setting the thickness of gold films unaltered,  $n_B$  changes abruptly as the air-loaded interspace  $w_d$  decreases, as it is shown in figure 7(b) for  $w_m = 25$  nm. This will be of help to map out a given phase distribution  $w(\theta_{\perp})$  since it depends in linear proportion to  $n_B$ .

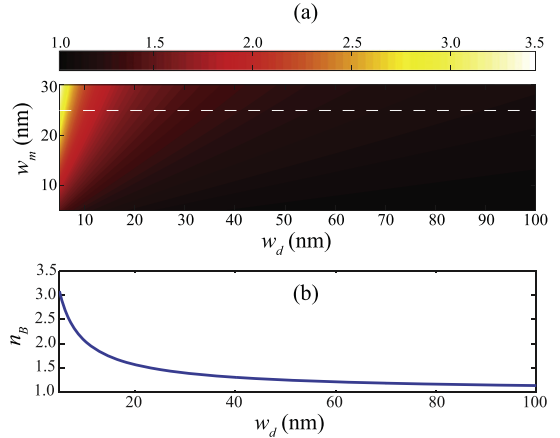


**Figure 7.** (a) Contour plot of the Bloch-mode refractive index  $n_B$  for different elementary Au gratings at  $\lambda = 632.8$  nm. In (b) we maintain the width of the Au layers fixed,  $w_m = 25$  nm, while the thickness of the slit  $w_d$  may varies. This case is also labeled in (a) with dashed lines.

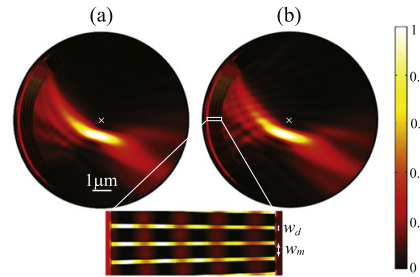


**Figure 8.** Time-averaged energy density of focal waves accelerated by means of a concentric graded grating made of gold at  $\lambda = 632.8$  nm. The width of gold layers is  $w_m = 25$  nm (at the exit surface) and the slit gap  $w_d$  ranges from 5 nm to 78 nm (a) continuously and (b) taking spacesteps higher than 1 nm. The centered cross determines the location of the focal point.

The dephase  $w(\theta_{\perp})$  gained by a Bloch mode is strongly dependent upon the air gap  $w_d$ , while here we assume that the width of Au layers is maintained at the ES, but importantly it is practically unaltered by fixing the metal filling factor. If the multilayered nanostructure changes its periodicity but its rate of metal is preserved, a Bloch mode propagating along the (non-parallel) interfaces will experience an invariant phase velocity in its trajectory. This happens for a converging Bloch mode travelling inside a concentric MD arrangement.

Next we will consider a subwavelength DOE in such a way that the metallic nanoelements are arranged over a circular sector. A converging super-Gaussian beam ( $\Omega = 2\pi/7$ ) impinges on the circular surface of higher radius, subsequently propagating inside the MD DOE for a distance of  $d = 660$  nm, as depicted in figure 8(a). The metal–dielectric interfaces are concentric to the focal point of the incident wave field, attached a X-shaped tag in the figure. At the ES, the profiled beam is still focused around the focus, which is

located at  $3.6 \mu\text{m}$ . However, a controlled variation of the width of the slits governing the local periodicity of the array will induce a selective dephase at different parts of the impinging wave field. Furthermore, the subwavelength DOE is designed to stamp a dephase on the converging beam to be transformed into an accelerating beam of order  $m = 8$  at  $\lambda = 632.8 \text{ nm}$ . The width of the metal layers is set as  $w_m = 25 \text{ nm}$  at the ES, and we determine  $w_d$  to achieve

$$n_B(\theta)kd = n_B(0)kd + m\theta, \quad (16)$$

starting from  $w_d = 5 \text{ nm}$ . Let us mention that current nanofabrication techniques enable values of  $w_d$  as low as  $50 \text{ nm}$  [15, 16], however theoretical studies go well beyond this limit [53]. Note that increasing  $w_d$  are found at decreasing angles  $\theta$ . In this modelling we neglect additional dephases induced by the impedance mismatching at the entrance and ESs of the metallic-slits arrangement, a procedure that is valid as proved in our numerical simulations and supported by theoretical studies [54].

In figure 8(a) we plot the time-averaged energy density of the converging wave transformed into an spatially-accelerated beam after passing through the designed subwavelength DOE. We made use of a finite element analysis solver and commercially available simulation software (COMSOL Multiphysics). This is in good agreement with the analysis based on the effective-medium approach given above, and the numerical simulations shown in figure 6(b). For extremely thin slits, particularly near the minimum of  $5 \text{ nm}$  previously established, ohmic losses manifested in a high absorption coefficient  $\text{Im}(k_{||})$  lead to limited transmission. In these cases, in addition, our design procedure may lead to an enhanced sensitivity when determining the values of  $w_d$ . In practice, however, we cannot consider a nanofabrication process with a limit of resolution below  $1 \text{ nm}$ . Under such constraints, a new subwavelength DOE is designed in such a way that the width  $w_d$  of the assembled metal waveguides takes integer values (in nanometers) at the ES. The resultant beam shaping is shown in figure 8(b). Spurious ripples near the DOE are evident, however, the main lobe of the accelerated focal wave remains nearly unchanged. For the sake of clarity, this constraint will not be considered here on.

As discussed previously, the transverse spatial frequency gained by the wave field at the DOE ES, governing the acceleration of the emerging beam, is in direct proportion to the width  $d$  of the transforming metamaterial. From equations (10) and (16) we infer that the normalized radius of the transmitted field yields

$$m = n_1 kdR_{ES}, \quad (17)$$

where the radius of the ES,  $R_{ES} = 3.6 \mu\text{m}$  in our numerical simulations (also  $n_1 = 0.339 \mu\text{m}^{-1}$ ). One can infer that a subwavelength DOE longer than  $d = 660 \text{ nm}$  leads to an enhanced acceleration, and vice versa. In figure 9 we show the resultant beam shaping when  $d$  is varied, which is in good agreement with our analysis. Importantly, the radius  $r_m = |m|/k$  of the accelerating beam with Bessel signature must be shorter than the radius of the ES, which is equivalent

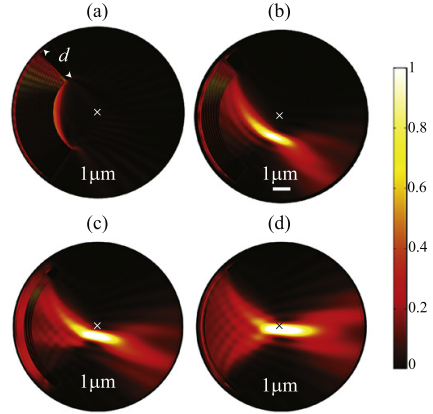


**Figure 9.** Accelerating beams generated by the designed subwavelength DOEs but increasing its thickness: (a)  $d = 3.0 \mu\text{m}$ , (b)  $d = 1.0 \mu\text{m}$ , and also decreasing it: (c)  $d = 0.4 \mu\text{m}$ , and (d)  $d = 0.1 \mu\text{m}$ . For simplicity, the circular working window has a given radius but varying linear scale. The focal point of the impinging converging wave is set at the window center with a cross-shaped tag.

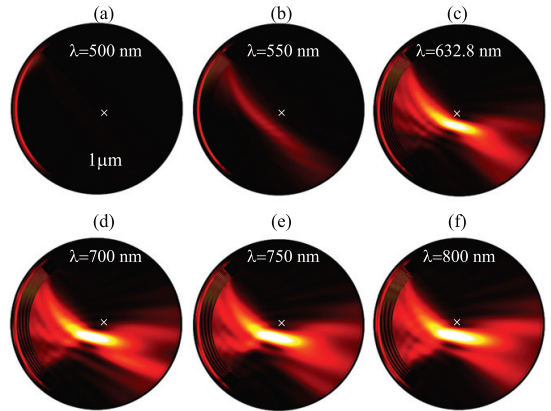


**Figure 10.** Time-averaged energy density of focal waves accelerated by the subwavelength DOE designed for a working wavelength of  $632.8 \text{ nm}$ . Particularly, the gold films have a length of  $660 \text{ nm}$ . The radiation wavelength is varied from  $500 \text{ nm}$  to  $800 \text{ nm}$ .

to the constraint  $d < |n_1|^{-1}$  inferred above. In our FEM-based simulations this means that a value of  $d$  higher than  $n_1^{-1} = 2.95 \mu\text{m}$  as occurs in figure 9(a) leads to an effect of total internal reflection at the ES.

## 6. Broadband response

The designed subwavelength DOE also exhibits a broadband response. In figure 10 we plot the beam shaping produced at wavelengths above and below the reference  $\lambda = 632.8 \text{ nm}$ . In agreement with equation (17), one can expect that the normalized radius  $m$  decreases when shifting to the near infrared,

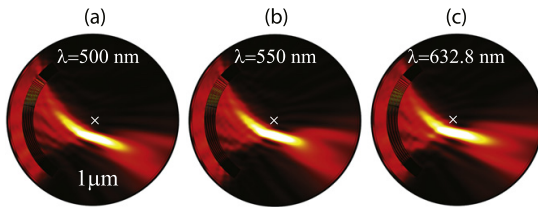


**Figure 11.** Numerical simulations of accelerating beams of different wavelengths and molded by a silver DOE. Again, the thickness of the gratings is 660 nm.

that is for decreasing  $k$ . In this case, however, the trajectory radius of the accelerating beam is not necessarily shorter, since it exclusively depends on the dispersive nature of  $|n_1|$ . In particular, a fast drop of the dispersive (real part of the) permittivity for gold leads to a marginally-decreasing modal refractive index  $n_B$ , and also the value of  $|n_1|$ . This minor effect takes place with a critical increasing of the FWHM of the focal waves, which is driven by diffraction, as evidences figure 10(f) at  $\lambda = 800$  nm. On the contrary, the acceleration of the converging beam is not produced at shorter wavelengths. In this case,  $n_B$  clearly deviates from its optimal linear dependence upon  $\theta$ , producing an spurious defocusing of the accelerating beam. In addition, the metamaterial opacity that is caused by a dominant imaginary part of  $\epsilon_m$  prevents from achieving an intense transmitted signal.

For broadband applications in a spectral range below  $\lambda = 632.8$  nm we propose the use of silver instead of gold. Gold nanolayers provide improved chemical stability as compared to silver nanolayers, but at the cost of higher losses for the propagating SPPs. Note that at such wavelength,  $\epsilon_m = -18.3 + i0.48$  for silver [55]. Figure 11 depicts the time-averaged energy density of focal waves accelerated by a subwavelength DOE specifically designed for its use with Ag films of thickness  $w_m = 25$  nm at the ES and length  $d = 660$  nm, at a working wavelength  $\lambda = 632.8$  nm. At lower wavelengths, the beam shaping results in a satisfactory acceleration of the converging beam.

## 7. Conclusions

We designed a nanostructured DOE to induce a dephase with linear variation in the azimuthal coordinate in a way that a convergent wave will accelerate around its geometrical focus  $F$ . Such near-field shaping is carried out only a few wavelengths far from this focal point, enabled by multilayer metal-dielectric stacks. A controlled variation of the assembled waveguide width governing the local periodicity of the array will induce a selective dephase at different parts of the impinging wave field. This proves that an engineered curvilinear caustic can be set up by the beam emerging from a dynamic array of elementary DOEs, the latter modifying the effective refractive index of the metamaterial and subsequently inducing a given linear dephase of the incident wave field as it is arranged in controlled orientations.

In particular, the subwavelength DOE was designed to stamp a dephase on the converging beam to be transformed into an accelerating beam of Bessel signature with order  $m = 8$  at  $\lambda = 632.8$  nm. Before the wave packet is bent near  $F$ , the intensity maximum of the beam determining its trajectory follows a linear equation. Subsequent to the accelerating course in the focal region, the beam restores its straight trajectory, however exhibiting a different orientation. We demonstrated that the generation of near-diffraction-limited beams accelerating along an incomplete circular caustic curve is only possible by using low order Bessel precursors. Furthermore, the trajectory gyration decreases and its vertex shifts to the focal point  $F$  as long as the semi-aperture angle of the converging wave field decreases. Importantly, total internal reflection might be observed at the ES of the sub-wavelength DOE whether its width surpasses  $|n_1|^{-1}$ . This is in good agreement with the analysis we fulfilled based on the effective-medium approach treating the MD arrangement as an inhomogeneous uniaxial metamaterial.

This annular DOE also exhibits a broadband response. When shifting to the near infrared, the trajectory radius of the accelerating beam is marginally decreasing. This minor effect takes place with a critical increasing of the FWHM driven by diffraction. For broadband applications in a spectral range below  $\lambda = 632.8$  nm we propose the use of silver instead of gold. Gold nanolayers provide improved chemical stability as compared to silver nanolayers, but at the cost of higher losses for the propagating SPPs. The presented results may bring about new possibilities for studying self-acceleration in integrated optics, using them to generate new structured plasma channels, and exploring nonlinear optical processes.

## Acknowledgments

This research was funded by the Spanish Ministry of Economy and Competitiveness under the project TEC2011-29120-C05-01. M Naserpour, acknowledges financial support from the Ministry of Science, Research and Technology of Iran.

## References

- [1] Fang N, Lee H S, Sun C and Zhang X 2005 *Science* **308** 534–7
- [2] Ergin T, Stenger N, Brenner P, Pendry J B and Wegener M 2010 *Science* **328** 337–9
- [3] Alonso-González P *et al* 2012 *Nat. Commun.* **3** 684
- [4] Ebbesen T W, Lezec H J, Ghaemi H F, Thio T and Wolf P A 1998 *Nature* **391** 667–8
- [5] Mühlischlegel P, Eisler H J, Martin O J F, Hecht B and Pohl D W 2005 *Science* **308** 1607–8
- [6] Albella P, Poyli M A, Schmidt M K, Maier S A, Moreno F, Sáenz J J and Aizpurua J 2013 *J. Phys. Chem. C* **117** 13573–84
- [7] Raether H 1988 *Surface Plasmons on Smooth and Rough Surfaces and on Gratings* (Berlin: Springer)
- [8] Martín-Moreno L, García-Vidal F J, Lezec H J, Pellerin K M, Thio T, Pendry J B and Ebbesen T 2001 *Phys. Rev. Lett.* **86** 1114–7



- [9] Kumar K, Duan H, Hegde R S, Koh S C W, Wei J N and Yang J K W 2012 *Nat. Nanotechnology* **7** 557–61
- [10] Roberts A S, Pors A, Albrektsen O and Bozhevolnyi S I 2014 *Nano Lett.* **14** 783–7
- [11] Wang F, Chakrabarty A, Minkowski F, Sun K and Wei Q H 2012 *Appl. Phys. Lett.* **101** 023101
- [12] Yu N, Aieta F, Genevet P, Kats M A, Gaburro Z and Capasso F 2012 *Nano Lett.* **12** 6328–33
- [13] Luo J, Yu H, Song M and Zhang Z 2014 *Opt. Lett.* **39** 2229–31
- [14] Wróbel P, Pniowski J, Antosiewicz T J and Szoplik T 2009 *Phys. Rev. Lett.* **102** 183902
- [15] Verslegers L, Catrysse P B, Yu Z, White J S, Barnard E S, Brongersma M L and Fan S 2009 *Nano Lett.* **9** 235–8
- [16] Ishii S, Kildishev A V, Shalaev V M, Chen K P and Drachev V P 2011 *Opt. Lett.* **36** 451–3
- [17] Aieta F, Genevet P, Kats M A, Yu N, Blanchard R, Gaburro Z and Capasso F 2012 *Nano Lett.* **12** 4932–6
- [18] Yu N, Genevet P, Aieta F, Kats M A, Blanchard R, Aoust G, Tettiene J P, Gaburro Z and Capasso F 2013 *IEEE J. Sel. Top. Quantum Electron.* **19** 4700423
- [19] Yin L, Vlasko-Vlasov V K, Pearson J, Hiller J M, Hua J, Welp U, Brown D E and Kimball C W 2005 *Nano Lett.* **5** 1399–402
- [20] Liu Z, Lee H, Xiong Y, Sun C and Zhang X 2007 *Science* **315** 1686
- [21] Barnakov Y A, Kiriy N, Black P, Li H, Yakim A V, Gu L, Mayy M, Narimanov E E and Noginov M A 2011 *Opt. Mater. Express* **1** 1061–4
- [22] Wu G, Chen J, Zhang R, Xiao J and Gong Q 2013 *Opt. Lett.* **38** 3776–9
- [23] Mahajan V N 1984 *Appl. Opt.* **22** 3042–53
- [24] Zapata-Rodríguez C J, Pastor D, Martínez L E and Miret J J 2012 *J. Opt. Soc. Am. A* **29** 1992–8
- [25] Naserpour M, Zapata-Rodríguez C J, Zakery A and Miret J J 2015 *Opt. Commun.* **334** 79–84
- [26] Siviloglou G A, Broky J, Dogariu A and Christodoulides D N 2007 *Phys. Rev. Lett.* **99** 213901
- [27] Kaminer I, Bekenstein R, Nemirovsky J and Segev M 2012 *Phys. Rev. Lett.* **108** 163901
- [28] Alonso M A and Bandres M A 2012 *Opt. Lett.* **37** 5175–7
- [29] Zapata-Rodríguez C J and Naserpour M 2014 *Opt. Lett.* **39** 2507–10
- [30] Courvoisier F, Mathis A, Froehly L, Giust R, Furfaro L, Lacourt P A, Jacquot M and Dudley J M 2012 *Opt. Lett.* **37** 1736–8
- [31] Zhang P, Hu Y, Cannan D, Salandrino A, Li T, Morandotti R, Zhang X and Chen Z 2012 *Opt. Lett.* **37** 2820–2
- [32] Kotlyar V V, Kovalev A A and Soifer V A 2014 *Opt. Lett.* **39** 2395–8
- [33] Berry M and Balazs N 1979 *Am. J. Phys.* **47** 264–7
- [34] Siviloglou G A and Christodoulides D N 2007 *Opt. Lett.* **32** 979–81
- [35] Choi D, Lim Y, Lee I M, Roh S and Lee B 2012 *IEEE Photonics Technol. Lett.* **24** 1440–2
- [36] Tang X M, Li L, Li T, Wang Q J, Zhang X J, Zhu S N and Zhu Y Y 2013 *Opt. Lett.* **38** 1733–5
- [37] Visser T D and Wiersma S H 1992 *J. Opt. Soc. Am. A* **9** 2034–47
- [38] Zapata-Rodríguez C J 2007 *J. Opt. Soc. Am. A* **24** 675–86
- [39] Chamorro-Posada P, Sánchez-Curto J, Aceves A B and McDonald G S 2013 arXiv:1305.3529
- [40] Zapata-Rodríguez C J, Pastor D and Miret J J 2012 *Opt. Express* **20** 23553–8
- [41] Feng S, Elson M and Overfelt P 2005 *Phys. Rev. B* **72** 085117
- [42] Maier S A and Atwater H A 2005 *J. Appl. Phys.* **98** 011101
- [43] Lu D and Liu Z 2012 *Nat. Commun.* **3** 1205
- [44] Rytov S M 1956 *Sov. Phys.—JETP* **2** 466
- [45] Yariv A and Yeh P 1977 *J. Opt. Soc. Am.* **67** 438–48
- [46] Smith D R and Pendry J B 2006 *J. Opt. Soc. Am. B* **23** 391–403
- [47] Yeh P 1988 *Optical Waves in Layered Media* (New York: Wiley)
- [48] Lide D R 2007 *CRC Handbook of Chemistry and Physics* 88th edn (Boca Raton, FL: CRC Press)
- [49] Elser J, Podolskiy V A, Salakhutdinov I and Avrutsky I 2007 *Appl. Phys. Lett.* **90** 191109
- [50] Chebykin A V, Orlov A A, Vozianova A V, Maslovski S I, Kivshar Y S and Belov P A 2011 *Phys. Rev. B* **84** 115438
- [51] Chen W, Thoreson M D, Ishii S, Kildishev A V and Shalaev V M 2010 *Opt. Express* **18** 5124–34
- [52] Zapata-Rodríguez C J, Miret J J, Sorni J A and Vuković S 2013 *IEEE J. Sel. Top. Quantum Electron.* **19** 4601408
- [53] Verslegers L, Catrysse P B, Yu Z and Fan S 2009 *Appl. Phys. Lett.* **95** 071112
- [54] Chen S, Jin S and Gordon R 2014 *Opt. Express* **22** 13418–26
- [55] Johnson P B and Christy R W 1972 *Phys. Rev. B* **6** 4370–9